UNIVERSITY OF CALIFORNIA

Santa Barbara

# Remote sensing of plant species using airborne hyperspectral visible-shortwave infrared and thermal infrared imagery

A dissertation submitted in partial satisfaction of the

requirements for the degree Doctor of Philosophy

in Geography

by

Susan Kay Meerdink

Committee in charge:

Professor Dar Roberts, Chair

Professor Jennifer King

Professor Kelly Caylor

Professor Paul Gader, University of Florida

December 2018

The dissertation of Susan Kay Meerdink is approved.

_____

Paul Gader

_____

Kelly Caylor

_____

Jennifer King

_____

Dar Roberts, Committee Chair

December 2018

Remote sensing of plant species using airborne hyperspectral visible-shortwave infrared and thermal infrared imagery

# Acknowledgements

I have been fortunate enough to have many people help and support me throughout this dissertation work. It is hard to summarize how much I appreciate these individuals who got me through the program. First, I would like to start by thanking Dar Roberts, my advisor, for selecting me as a graduate student and seeing me through the six years of my graduate career. I have learned an immense amount of information from you, which has fully prepared me for a career in vegetation remote sensing. I was also very lucky to have Jennifer King, Kelly Caylor, and Paul Gader rounding out my UCSB dissertation committee. Jennifer, thank you for serving on my committee from the beginning and sticking with me throughout my master's and Ph.D. I thoroughly appreciate your attention to detail and willingness to tackle new research topics. Kelly, thank you for your willingness to join my committee in the last year of my Ph.D. Lastly, thank you, Paul, for always finding time to talk research even with the three-hour time difference and for helping me secure my postdoc position at the University of Florida. Your mentorship and positive support ensured I remained focused and driven to finish my dissertation.

The Viper Lab has been a wonderful community to work in for the past six years. I have thoroughly enjoyed getting to know all the current and past Viper graduate students. Your willingness to socialize and share research ideas has been crucial to the completion of my Ph.D. Specifically, I would like to send a big thank you to my office mates, Sarah Shivers and Seth Peterson. Thank you, Sarah, for being office-mate extraordinaire who was always willing to talk and give valuable feedback. I am extremely grateful to Seth, who is the foundation of the Viper Lab and most always providing the solution to the current problem. Two other Vipers need to be individually recognized for their help and support over the

years. The first is Keely Roth, who I only overlapped for a year or two in the program, but without her help in my first year, I would never have finished my master's degree. Thank you, Keely, for continuing to be extremely generous with your support, advice, and research ideas. The second is Erin Wetherley, who has been my partner in crime since Day 1 of our graduate program. There are no words to express my gratitude for what you have done for me throughout our time at UCSB. I would not have made it through our classes and the program if you had not been there for me.

I would be amiss if I did not thank the Geography Department's Outreach and Visibility committee. The members of this committee have also been a wonderful community for me throughout my time at UCSB. I am so grateful to Kitty Currier and Heather Frazier for being my friends and teaching me how to be a successful member of a team. You reminded me that there was more to graduate school and we could make a difference by volunteering. I am also grateful to Sari Blakeley and Rafael Ramos for helping me sustain the committee after the graduation of Kitty and Heather. Your enthusiasm and dedication to our volunteer work were inspiring and contagious. I am so lucky that our friendship evolved out of the committee work because you two have been absolutely wonderful to hang out with over the past couple of years.

Before arriving at UCSB, I was extremely fortunate enough to have wonderful mentors at the University of Northern Iowa. Dr. Maureen Clayton was the first faculty member to mentor me and initiated my research skills. Thank you so much for taking a chance on me and supporting me throughout my undergraduate career. I also am extremely grateful to Dr. Andrey Petrov who was an excellent mentor and shaping me into the researcher I am today. Thank you for the large amount of time you spent teaching and

advising me. I would not be successfully completing my Ph.D. without your influence and support throughout my undergraduate career.

Last, but not least, I would like to thank my parents and sisters for their undying support and patience. You were always willing to listen to my highs and lows even if you did not quite understand the situation. Thank you for always having my back so that I could feel more comfortable following the twists and turns of graduate school. The true hero of my Ph.D. is my loving husband, Zan Preston. Thank you so much for supporting me emotionally and financially throughout my Ph.D. I firmly believe that you could have your master's in remote sensing after reading all my papers and providing edits. I would never have completed my Ph.D. without your help. I am so eternally grateful for what you have done for me and so lucky to have you in my life.

# Curriculum Vitae

# Susan Kay Meerdink

## Education

| | |
|---|---|
| 2014 – 2018 | Ph.D. Geography, University of California Santa Barbara |
| 2012 – 2014 | M.A. Geography, University of California Santa Barbara |
| 2007 – 2012 | B.S. Geographical Information Science, University of Northern Iowa, *Summa Cum Laude* |
| 2007 – 2012 | B.A. Ecology & Systematics Honors Research, University of Northern Iowa, Thesis: Analyzing Taimyr wild reindeer and calving grounds dynamics *Magna Cum Laude* |

## Professional Appointments

| | |
|---|---|
| 2016 – 2018 | Graduate Research Assistant, NASA Jet Propulsion Laboratory |
| 2014 – 2018 | Graduate Research Assistant, University of California Santa Barbara |
| 2017 – 2017 | Geospatial Remote Sensing Intern, The Climate Corporation |
| 2012 – 2015 | Teaching Assistant, University of California Santa Barbara |
| 2011 – 2012 | Undergraduate Research Assistant, University of Northern Iowa |
| 2010 – 2012 | Technical Assistant, University of Northern Iowa Botanical Center |
| 2009 – 2011 | Field Technician, Iowa Department of Natural Resources |

## Refereed Publications

**Meerdink, S.K.,** Roberts, D.A., King, J. Y., Roth, K. L., Dennison, P. E., Amaral, C. H., & Hook, S. J. (2016). Linking seasonal foliar traits to VSWIR-TIR spectroscopy across California ecosystems. Remote Sensing of Environment, 186, 322-338.

**Meerdink,** S.K. (2014). Linking seasonal foliar traits to VSWIR-TIR spectroscopy across California ecosystems (Published master's thesis). Available from ProQuest Dissertations and Theses database.

### *Manuscripts in preparation*

**Meerdink, S.K.,** Roberts, D.A., Roth, K.L., King, J.Y., Gader, P., & Koltunov, A. (submitted). Classifying California plant species temporally using airborne hyperspectral imagery. Remote Sensing of Environment.

**Meerdink, S.K.,** Roberts, D.A., Hulley, G., Pisek, J., Raabe, K., King, J.Y., & Hook, S.J. (submitted). Plant species' spectral emissivity and temperature using the

Hyperspectral Thermal Emission Spectrometer (HyTES) sensor. Remote Sensing of Environment.

**Meerdink**, S.K., Hook, S.J., Abbott, E.A., & Roberts, D.A. (submitted). The ECOSTRESS Spectral Library 1.0. Remote Sensing of Environment.

Dennison, P., Kokaly, R., Thompson, D.R., Qi, Y., Daughtry, C., **Meerdink, S.K.,** Quemada, Gader, P., M., Roberts, D.A., & Wetherley, E.B. (submitted). Comparison of Methods for Modeling Fractional Cover using Simulated Satellite Hyperspectral Imager Spectra. Remote Sensing of Environment.

Roberts, D.A., Roth, K.L., Wetherley, E.G., **Meerdink, S.K.**, and Perroy, R.L., (in press), 1 Hyperspectral Vegetation Indices, Chapter 1 in in P.S. Thenkabail, J.G. Lyon and A. Huete (ed), Hyperspectral Remote Sensing of Vegetationm, 2nd edition, Volume 2. CRC Press, in press.

**Meerdink, S.K.**, Roberts, D.A., King, J. Y., Roth, K. L., Dennison, P. E., Amaral, C. H., & Hook, S. J. (2016). Linking seasonal foliar traits to VSWIR-TIR spectroscopy across California ecosystems. Remote Sensing of Environment, 186, 322-338.

## Honors, Grants, & Fellowships

2018 Jack Estes Remote Sensing Memorial Award, $500
2018 Department of Geography Summer Research Grant, $2400
2017 NASA Earth and Space Science Fellowship (NESSF), *Discriminating California plant species and evaluating temperature relations across seasons within drought impacted ecosystems*, $30000
2017 Jet Propulsion Laboratory Subcontract, *Plant species mapping, water, and LMA using HyTES*, $35000
2017 UCSB Graduate Student Association Travel Grant, $200
2017 UCSB Academic Senate Travel Grant, $900
2016 Jet Propulsion Laboratory Subcontract, *Plant species mapping, water, and LMA using HyTES*, $35000
2016 NASA Earth and Space Science Fellowship (NESSF), *Discriminating California plant species and evaluating temperature relations across seasons within drought impacted ecosystems*, $30000
2016 Department of Geography Dangermond Travel Award, $500
2015 Department of Geography Dangermond Travel Award, $500
2015 NASA Earth and Space Science Fellowship (NESSF), *Discriminating California plant species and evaluating temperature relations across seasons within drought impacted ecosystems*, $30000
2014 American Geophysical Union Outstanding Student Paper Award
2012 AAG International Geographic Information Fund Student Travel Grant, $500

2011 CW Lantz Scholarship
2011 Irene Thompson Scholarship
2011 Pudil Environmental Scholarship
2011 NASA Iowa Space Grant, *Taimyr Wild Reindeer calving grounds dynamics*, $10500
2010 NASA Iowa Space Grant, *Taimyr Wild Reindeer calving grounds dynamics*, $10500
2010 Pudil Environmental Scholarship
2010 La Duke Family Scholarship
2009 NASA Iowa Space Grant, *Long-term implications of the "Ethanol Boom"*, $7000
2009 University of Northern Iowa Pond and Water Scholarship
2008 NASA Iowa Space Grant, *Ecological niche model of Glyptemys insculpta in Iowa*, $7000
2008 Vivian Wisemen Fuller Scholarship
2008 University of Northern Iowa Distinguished Scholar

## Scholarly Presentations & Posters

2017 **Meerdink, S.K.**, Roberts, D.A., Gader, P., King, J., Roth, K., Tane, Z., Koltunov, A. (2017). *Discriminating California plant species throughout the drought using airborne VSWIR and TIR imagery*. Ecological Society of America Annual Meeting. Portland, OR. (Presentation)

2017 **Meerdink, S.K.**, Roberts, D.A., Hook, S.J. *Exploring spectral emissivity features of plants from leaf to canopy levels*. American Geophysical Union Fall Meeting. New Orleans, LA. (Presentation)

2017 **Meerdink, S.K.**, Hook, S.J., Abbott, E.A., Roberts, D.A. *The ECOSTRESS Spectral Library*. HyspIRI Science Workshop. Pasadena, CA. (Presentation)

2017 Dennison, P., Kokaly, R., Thompson, D.R., Daughtry, C. Gader, P., **Meerdink, S.K.,** Quemada, M., Roberts, D.A., Wetherley, E.B. *Comparing methods for mapping fractional cover using simulated HyspIRI spectra.* HyspIRI Science Workshop. Pasadena, CA. (Presentation)

2016 **Meerdink, S.K.**, Roberts, D.A., Hook, S. *Spectral emissivity features of plants: Prospects for the Hyperspectral Thermal Emission Spectrometer (HyTES) sensor*. American Geophysical Union Fall Meeting. San Francisco, CA. (Poster)

2016 **Meerdink, S.K.**, Roberts, D.A., Hook, S.J. *Spectral emissivity features of plants: Prospects for the Hyperspectral Thermal Emission Spectrometer (HyTES) sensor*. HyspIRI Science Workshop. Pasadena, CA. (Presentation)

2016 **Meerdink, S.K.**, Roberts, D.A., Roth, K. *Differentiating California plant species across seasons using airborne VSWIR and TIR imagery*. Invited talk, University of Florida Department of Geography Colloquium. Gainesville, FL. (Presentation)

2016 **Meerdink, S.K.**, Roberts, D.A., Roth, K. *Differentiating California plant species across seasons using airborne VSWIR and TIR imagery*. Association of American Geographers Annual Meeting. San Francisco, CA. (Presentation)

2015 **Meerdink, S.K.**, Roberts, D.A., Roth, K. *Discriminating plant species across California's diverse ecosystems using airborne VSWIR and TIR imagery*. American Geophysical Union Fall Meeting. San Francisco, CA. (Poster)

2014 **Meerdink, S.**, Roberts, D.A., Roth, K., Amaral, C., Hook, S., King, J. *Linking seasonal foliar chemistry to VSWIR-TIR spectroscopy across California ecosystems*. American Geophysical Union Fall Meeting. San Francisco, CA. (Presentation)

2014 **Meerdink, S.**, Roberts, D.A., Roth, K., Amaral, C., Hook, S., King, J. *Linking seasonal foliar chemistry to VSWIR-TIR spectroscopy across California ecosystems.* HyspIRI Science Workshop. Pasadena, CA. (Presentation)

2014 Cooney, M.D., Petrov, A.N., Kolpashchikov, L., **Meerdink, S**.K. *Understanding long-term spatiotemporal dynamics of the Taimyr reindeer herd in a changing environment.* Association of American Geographers Annual Meeting. Tampa, FL. (Presentation)

2013 **Meerdink, S.**, Roberts, D.A., Amaral, C., Hook, S., King, J. *Linking seasonal foliar chemistry to VSWIR-TIR spectroscopy across California ecosystems*. HyspIRI Science Workshop. Pasadena, CA. (Presentation)

2012 **Meerdink, S**., Petrov, A.N., Kolpashchikov, L., Pestereva, A.V. *Taimyr wild reindeer spatial fidelity and calving grounds dynamics in a changing climate*. International Polar Year Conference. Montréal, Canada. (Presentation)

2012 **Meerdink, S**., Petrov, A.N., Kolpashchikov, L., Pestereva, A.V. *Taimyr wild reindeer spatial fidelity and calving grounds dynamics in a changing climate*. Association of American Geographers Annual Meeting. New York, NY. (Presentation)

2011 **Meerdink, S**., Petrov, A.N., Voss, M., Sugumaran, R. *Long-term implications of the "ethanol boom" for American agriculture: Iowa case study*. Association of American Geographers Annual Meeting. Seattle, WA. (Presentation)

## Professional Service

| | |
|---|---|
| 2012 – 2018 | Chair of UCSB Geography Department's Visibility and Outreach Committee |
| 2017 & 2018 | Planned a Trivia Night for UCSB Geography Department faculty, graduate, and undergraduate students |
| 2016 | Planned a Scavenger Hunt for UCSB Geography faculty and students |
| 2014 – 2018 | Planned, organized, and presented a workshop at AAUW Tech Savvy geared at attracting girls 6 - 9 grades into STEM fields. |

| | |
|---|---|
| 2015 | Session chair and organizer: The Quest to Map Plant Species. In, *Association American Geographers Annual Meeting, 2015*. San Francisco, CA. |
| 2014 – 2015 | Vice President of UCSB Student Chapter of the American Society for Photogrammetry and Remote Sensing (ASPRS) |
| 2012 – 2018 | Planned and attended tabling events at local K - 9 school's Science Nights |
| 2012 – 2018 | Planned and executed Geography Awareness Week in November where UCSB Geography Department faculty and students attend local K-12 schools to share their perspective and love of geography. As part of this, I also presented at local school sharing my research. |

# Abstract

Remote sensing of plant species using airborne hyperspectral visible-shortwave infrared and thermal infrared imagery

By

Susan Kay Meerdink

In California, natural vegetation is experiencing an increasing amount of stress due to prolonged droughts, wildfires, insect infestation, and disease. Remote sensing technologies provide a means for monitoring plant species presence and function temporally across landscapes. In this his dissertation, I used hyperspectral visible shortwave infrared (VSWIR), hyperspectral thermal (TIR), and hyperspectral VSWIR + broadband TIR imagery to derive key observations of plant species across a gradient of environmental conditions and time frames. In Chapter 2, I classified plant species using hyperspectral VSWIR imagery from 2013 - 2015 spring, summer, and fall. Plant species maps had the highest classification accuracy using spectra from a single date (mean kappa 0.80 – 0.86). The inclusion of spectra from other dates decreased accuracy (mean kappa 0.78 - 0.83). Leave-one-out analysis emphasized the need to have spectra from the image date in the classification training, otherwise classification accuracy dropped significantly (mean kappa 0.31 – 0.73). In Chapter 3, I used hyperspectral TIR imagery to determine the extent that high precision spectral emissivity and canopy temperature can be exploited for vegetation research at the canopy level. I found that plant species show distinct spectral separation at the leaf level, but separability among species is lost at the canopy level. However, species' canopy temperatures exhibited different distributions among dates and species. Variability in canopy

temperatures was largely explained by LiDAR derived canopy structural attributes (e.g. canopy density) and the surrounding environment (e.g. presence of pavement). In Chapter 4, I used combined hyperspectral VSWIR and broadband TIR imagery to monitor plant stress during California's 2013 – 2015 severe drought. The temperature condition index (TCI) was calculated to measure plant stress by using plant species' surface minus air temperature distributions across dates. Plant stress was not evenly distributed across the landscape or time with lower elevation open shrub/meadows, showing the largest amount of stress in June 2014, and August 2015 imagery. Plant stress spatial variability across the study area was related to a slope's aspect with highly stressed plants located on south or south-southwest facing slopes. Overall, this dissertation quantifies the ability to temporally study plant species using hyperspectral VSWIR, hyperspectral TIR, and combined VSWIR+TIR imagery. This analysis supports a range of current and planned missions including Surface Biology and Geology (SBG), Environmental Mapping and Analysis Program (EnMAP), National Ecological Observatory Network (NEON), Hyperspectral Thermal Emission Spectrometer (HyTES), and ECOsystem Spaceborne Thermal Radiometer Experiment on Space Station (ECOSTRESS).

# Table of Contents

# 1. Introduction

Plant species' responses to climate change are already clearly visible throughout the world's ecosystems (Walther et al., 2002). For example, increasing air temperature and decreasing precipitation in Southern California have already caused distribution shifts in ten plant species (Kelly and Goulden, 2008). With changes already occurring, it has never been more critical to establish baseline conditions and the means for monitoring changes in species' distributions in response to climate. Remote sensing technology allows for the investigation of ecological processes and systems across landscapes and temporal scales, but current spaceborne systems cannot detect the needed level of detail to determine the magnitude and direction of change (Cohen and Goward, 2004; Ustin et al., 2004).

The NASA's Hyperspectral Infrared Imager (HyspIRI) spaceborne mission[1] would address a significant gap in our knowledge by providing comprehensive information on plant species composition, biochemistry, and temperature with global coverage (Lee et al., 2015). A unique feature of HyspIRI is the inclusion of two instruments that measure wavelengths in the combined range of 0.38 – 12 μm: an imaging spectrometer measuring the Visible Near Infrared/Shortwave Infrared spectrum (VSWIR) and a multi-spectral imager measuring the Thermal (TIR; Lee et al., 2015). Very little is known about the potential of combined VSWIR spectroscopy and broadband TIR for ecological research. However, integration of the VSWIR and TIR could allow researchers to utilize the strengths of each spectral region and answer research questions that cannot be answered with existing spaceborne sensors

[1] The HyspIRI mission has transitioned to the Surface Biology and Geology (SBG) mission, but will be referred to as HyspIRI throughout the remainder of this dissertation. The HyspIRI mission explicitly includes simultaneous VSWIR and TIR observations, while the SBG mission may not.

(Ribeiro Da Luz and Crowley, 2007). In order to evaluate the potential of HyspIRI data for ecosystem monitoring at the plant species level across landscapes and seasonal extents, we first need to quantify the extent of plant species separation across each electromagnetic domain.

HyspIRI's hyperspectral VSWIR imager is able detect to subtle spectral shifts between species that are caused by differences in chemistry, physiology, and structure, thus making discrimination of plant species possible (Roberts et al., 2004). Plant species maps provide a baseline for monitoring ecosystem changes with specific applications for monitoring invasive species expansion (Dubula et al., 2016; Somers and Asner, 2012; Underwood et al., 2003), monitoring wildfire disturbance recovery (Riaño et al., 2002; Schwartz et al., 2015), and detecting the effect of pathogens on vegetation, such as insects (Guarín and Taylor, 2005; Lawrence and Labus, 2003; Tane et al., 2018a). While plant species discrimination has been successful for many ecosystems, current hyperspectral VSWIR imagers are limited to airborne platforms, resulting in plant species distributions for a single season and small spatial extent (Garcia and Ustin, 2001). Due to this limited data availability, our understanding of species discrimination over large temporal and spatial scales is restricted and is not representative of HyspIRI's capabilities. Very few studies have temporally classified species over time, but regional studies have shown that seasonal and inter-annual changes in plant spectra can be important for separating some plant species (Dennison and Roberts, 2003; Dudley et al., 2015). However, these studies were restricted to a single year and a small geographic area which does not address the ability to classify species over multiple years.

Recent studies employing hyperspectral TIR emissivity have found that plant species are spectrally distinct using hyperspectral TIR emissivity, which could augment plant species discrimination (Ribeiro Da Luz and Crowley, 2010; Ullah et al., 2012a). Laboratory hyperspectral TIR measurements have demonstrated that separability of plant species increases with decreasing water content, suggesting that the inclusion of TIR imagery during seasonal senescence will improve species discrimination (Meerdink et al., 2016; Ullah et al., 2012b). Previous studies demonstrate the successful application of TIR emissivities for the study of leaf characteristics (Arshad and Ali, 2018; Fabre et al., 2011; Neinavaz et al., 2016b), but they include the caveat that these relationships may not translate to the canopy scale. To our knowledge, only one study has used airborne hyperspectral TIR imagery to discriminate plant species using airborne hyperspectral TIR imagery (Ribeiro Da Luz and Crowley, 2010). Due to the small number of sensors available, we have a limited understanding of plant species canopy spectral response in the TIR domain using hyperspectral measurements. Without knowledge of plant species response at fine spectral and spatial scale for TIR, it is difficult to fully understand broadband TIR measurements.

Based on HyspIRI's ability to measure the TIR, it is possible to obtain land surface temperature (LST), thus providing a way to monitor ecosystem function and health. Leaf temperature is important for many aspects of functional plant ecology as it influences transpiration, sensible heat flux, photosynthesis, and respiration (Leuzinger et al., 2010). Integrated over a canopy, vegetation temperature is strongly couple to atmospheric conditions, making it important for local and global climate (Leuzinger et al., 2010). Leuzinger and Körner (2007) found that rather than the mean canopy temperature, it is the fine-scale temperature distributions which determine heat and gas fluxes. These fine-scale

temperature distributions are the result of differences in species' anatomical, physical, and biological traits (Leuzinger et al., 2010). In support of this finding, Roberts et al. (2015) found that plant species in Santa Barbara, California form unique clusters when comparing LST and the amount of green vegetation present. Large-scale canopy temperature can be estimated using current satellite infrared images, but the spatial resolution of such data is too coarse spatial resolution to account for differences between species (Soer, 1980). HyspIRI is the only mission that could decipher canopy temperature variations by species and increase our limited knowledge of how these relationships change both temporally and spatially.

The overarching goal of my research is to evaluate the potential of HyspIRI data for ecosystem monitoring at the plant species level for larger spatial and seasonal extents. In this study, I will use hyperspectral VSWIR and TIR imagery separately for the purposes of plant species classification and then exploit synergies between the VSWIR and TIR to determine our ability to map plant species stress for a diverse set of ecosystems during a period of increasing water stress. In the second chapter, I use hyperspectral VSWIR imagery collected during the HyspIRI airborne campaign in the spring, summer, and fall seasons of 2013 – 2015 to generate a plant species classification map that is temporally resistant. The third chapter uses hyperspectral TIR imagery over the Huntington Gardens to determine the extent to which plant species have significantly different spectral and temperature patterns. Lastly, the fourth chapter uses the combined VSWIR and TIR imagery available from the HyspIRI airborne dataset to examine plant species' response through California's 2013 – 2015 drought. By developing these techniques and products, I will provide insight into ecosystem physiological functions through plant species' variation in canopy temperature over time and over large areas.

In Chapter 2, I use hyperspectral VSWIR imagery to develop methods for classifying dominant plant species across annual and seasonal variation. I develop spectral libraries of species' spectra from single and multiple dates to test the spectral similarity across 2013 – 2015 during spring, summer, and fall. I also developed leave-one-out (LOO) spectral libraries to test the transferability of spectra across image dates. I used canonical discriminant analysis (CDA) as a dimensionality reduction technique followed by linear discriminant analysis (LDA) as a classifier. I then compare image date classifications produced with the different spectral libraries to evaluate the ability to classify plant species temporally using hyperspectral VSWIR imagery.

In Chapter 3, I use hyperspectral TIR imagery to determine if high spectral resolution emissivity and fine spatial resolution LST can be exploited for plant species research at the canopy level. I quantify plant species separability in the TIR domain at leaf and canopy levels to determine the scalability of leaf measurements to the canopy using a simple physical scaling model. At fine spatial resolutions, plant species' temperature variability is examined between dates and evaluated for significantly different distributions. In order to understand temperature distribution differences, variability is correlated with tree structural attributes and neighborhood characteristics derived from LiDAR.

In Chapter 4, I use hyperspectral VSWIR with LST imagery to evaluate plant species' temperature relations across seasons within drought impacted ecosystems. Using 158 images at 36 m spatial resolution across nine dates, I conduct a large-scale analysis of plant species' annual and seasonal temperature variability throughout a prolonged drought. I developed a plant species specific Temperature Condition Index (TCI) that maps plant stress across the

landscape and identifies areas that experienced prolonged stress. Plant stress was correlated with topographic attributes to better understand the environment's effect on plant stress.

# 2. Classifying California plant species temporally using airborne hyperspectral imagery


## Abstract

Accurate knowledge of seasonal and inter-annual distributions of plant species is required for many research and management agendas that track ecosystem health. Airborne imaging spectroscopy data have been used successfully to map plant species, but often only in a single season or over a limited spatial extent due to data availability. NASA's Hyperspectral Infrared Imager (HyspIRI) preparatory airborne campaign flew an imaging spectrometer during 2013- 2015, capturing a severe drought and thus providing the opportunity to evaluate species discrimination over an extreme range in environmental conditions. Here we evaluate the portability of image-based training data and accuracy of species discrimination. Imagery was acquired in the spring, summer, and fall seasons of 2013 - 2015 with the Airborne Visible/Infrared Imaging Spectrometer (AVIRIS). Reference spectral libraries were developed with three sets of spectra: spectra from a single image date, combining spectra from multiple dates (by season, by year, and from all dates), and creating leave-one-out libraries (LOO) that pooled spectra from all dates but one. Canonical discriminant analysis (CDA) was used to reduce dimensionality of spectra, and classification was performed using linear discriminant analysis (LDA). When only spectra from the same image date were used, plant species were classified with a mean kappa accuracy ranging between 0.80 – 0.86 for the nine dates. Seasonal and annual spectral libraries had comparable accuracies with mean kappa 0.79 – 0.83 and 0.78 – 0.83, respectively. Seasonal libraries did perform slightly better than annual libraries for species because they better incorporated changes in spectra due to

phenology. Spectral libraries were not transferable across dates, with mean kappa accuracies dropping to 0.31 – 0.73 for LOO spectral libraries. These results emphasize that spectral libraries built from previously collected imagery may not be able to accurately map plant species over new images. Specifically, our results highlight the need to use reference spectra that adequately represent the biophysical status of the plant species within an image for accurate mapping. Our research provides relevant insight for advanced species-mapping techniques across large spatial and temporal scales using imagery from sensors like HyspIRI.

## 2.1 Introduction

Plant species maps provide a baseline for monitoring the world's ecosystems, which are already responding to climate change (Walther et al., 2002). Globally, researchers have documented shifts in plant phenology that provide compelling evidence of species being influenced by environmental change (Cleland et al., 2007). For example, in Southern California, increasing air temperature and decreasing precipitation have already caused distribution shifts in ten widely distributed plant species (Kelly and Goulden, 2008). In order to quantify these changes, plant species maps are crucial for many applications, including monitoring invasive species expansion (Underwood et al., 2003), tracking wildfire disturbance recovery (Riaño et al., 2002), and detecting vegetation disturbances such as insect infestation (Lawrence and Labus, 2003; Tane et al., 2018a).

There are many techniques for developing species maps, including ground-based approaches, but remote sensing technology allows for the investigation of ecological processes and systems on larger spatial and temporal scales. Imaging spectroscopy, or hyperspectral remote sensing, makes discrimination of plant species possible because the hundreds of narrow bands can be used to detect subtle spectral shifts between species that are

caused by differences in chemistry, physiology, and structure (Asner and Martin, 2008; Roberts et al., 2004). Using sensors such as the airborne visible/infrared imaging spectrometer (AVIRIS) or HYperspectral Digital Imagery Collection Experiment (HYDICE) sensor, plant species in diverse ecosystems have been classified successfully (Clark et al., 2005; Martin et al., 1998; Roth et al., 2015b; van Aardt and Wynne, 2007). While these studies demonstrate the ability to classify plant species, until now most research has been temporally restricted to a single image date.

Very few studies have addressed these temporal limitations due to the availability of airborne hyperspectral imagery. However, in order to capture ecosystem changes over time, it is necessary to develop remote sensing techniques that incorporate a plant's annual and seasonal variability. Classification rules developed for a given date may not be applicable to other dates due to changes in species' spectral response throughout the season and from year to year (Peñuelas and Filella, 1998). In regional studies, seasonal and inter-annual changes in plant spectra have been shown to be important for separating plant species during a drought and from invasive species (Burkholder et al., 2011; Dennison et al., 2003). Dudley et al. (2015) incorporated a single year's phenology into species classifications and found that multi-temporal spectral libraries achieved similar overall classification accuracy compared to single-date libraries. However, Dudley et al. (2015) was restricted to a single year and a small geographic area which does not address the ability to classify species over multiple years.

Plant species mapping research has been restricted to airborne platforms because current space-borne systems cannot generate the level of spectral detail needed to map species (Cohen & Goward, 2004; Ustin et al., 2004). Promising new sensor systems, such as

the proposed Hyperspectral Infrared Imager (HyspIRI) mission, would be able to quantify the plant species distributions and physiological functions required to address this need (Lee et al., 2015). The HyspIRI mission would provide hyperspectral imagery with global coverage of Earth's ecosystems every 16 days, at 30 m spatial resolution, resulting in a significantly larger dataset with which to develop species maps through time. While the need for this instrumentation was identified in the 2017 decadal survey, no launch date has been announced (National Academies of Sciences and Medicine, 2018).

To develop precursor datasets in advance of the HyspIRI mission, the National Aeronautics and Space Administration (NASA) flew airborne instruments starting in 2013. The goal of this three-year campaign was to demonstrate the range of important scientific applications that can be uniquely addressed with the HyspIRI mission (Lee et al., 2015). Flying over large swaths of California and capturing the worst drought on record for the state, this campaign has been leveraged by multiple studies (Bell et al., 2015; Coates et al., 2015; He et al., 2015; Palacios et al., 2015; Tane et al., 2018b; Wang et al., 2015; Wetherley et al., 2017).

Our study leverages this unique dataset collected during the HyspIRI airborne preparatory campaign to explore the capabilities of seasonal and annual plant species classification. Collecting reference spectra, for the purpose of classifying plant species, is time consuming and expensive, even more so for ecosystems with rugged terrain. Ideally, for efficient processing of future datasets, spectral libraries would incorporate temporal variability for the purpose of maintaining accuracy when applied to newly collected imagery or locations. Our study determines and quantifies the extent plants' temporal spectra can be used to generate accurate plant species classification maps. To establish baseline

classification capabilities, we developed spectral libraries from a single image date to classify 26 plant species and land cover classes. We then combined seasonal and annual spectra to evaluate our ability to map plant species with increased seasonal or annual spectral variability. Finally, we used leave-one-out libraries (LOO), that pooled spectra from all dates but one, to determine how transferable libraries are across image dates. Our overarching objective is to determine how effectively spectra collected from seasonal or annual imagery can be used to classify species over multiple years and over a 12980 km² area. Specifically, we asked the following questions:

1. What is the capability of classifying California plant species between 2013 – 2015 during the spring, summer, and fall?
2. Can a multiple-date spectral library be used to map species annually and seasonally?
3. How transferable are spectral libraries across dates for species classifications?

## 2.2 Methods

### *2.1 Study site and image acquisition*

Imagery was collected with the AVIRIS sensor as part of the HyspIRI Airborne Preparatory Campaign. AVIRIS measures 224 bands of radiance between 360 and 2500 nm with a full width at half-maximum of 10 nm (Green et al., 1998). The sensor was flown on the NASA ER-2 aircraft at an altitude of 20 km over six flightboxes in California to simulate future satellite imagery from HyspIRI (Lee et al., 2015). This study uses a spatial subset of imagery from the Santa Barbara flightbox, which includes ten of the eleven flightlines that were acquired with a 35º northeast-southwest orientation (Figure 2.1). These ten flightlines cover a diverse landscape that is approximately 12980 km². Coastal Santa Barbara county,

with its Mediterranean climate is captured along the southern portions of the flightlines. The elevation increases from sea level to a peak of 2,697 m with the imagery capturing the transition from shrubland to conifer forests located in the Los Padres National Forest. The campaign flew three times per year, thus capturing April, June, and November or August imagery during 2013, 2014, and 2015 (Table 2.1). Two flightlines were excluded and two replaced with another date due to technical errors when collecting the data, resulting in 88 AVIRIS images used in our analysis.

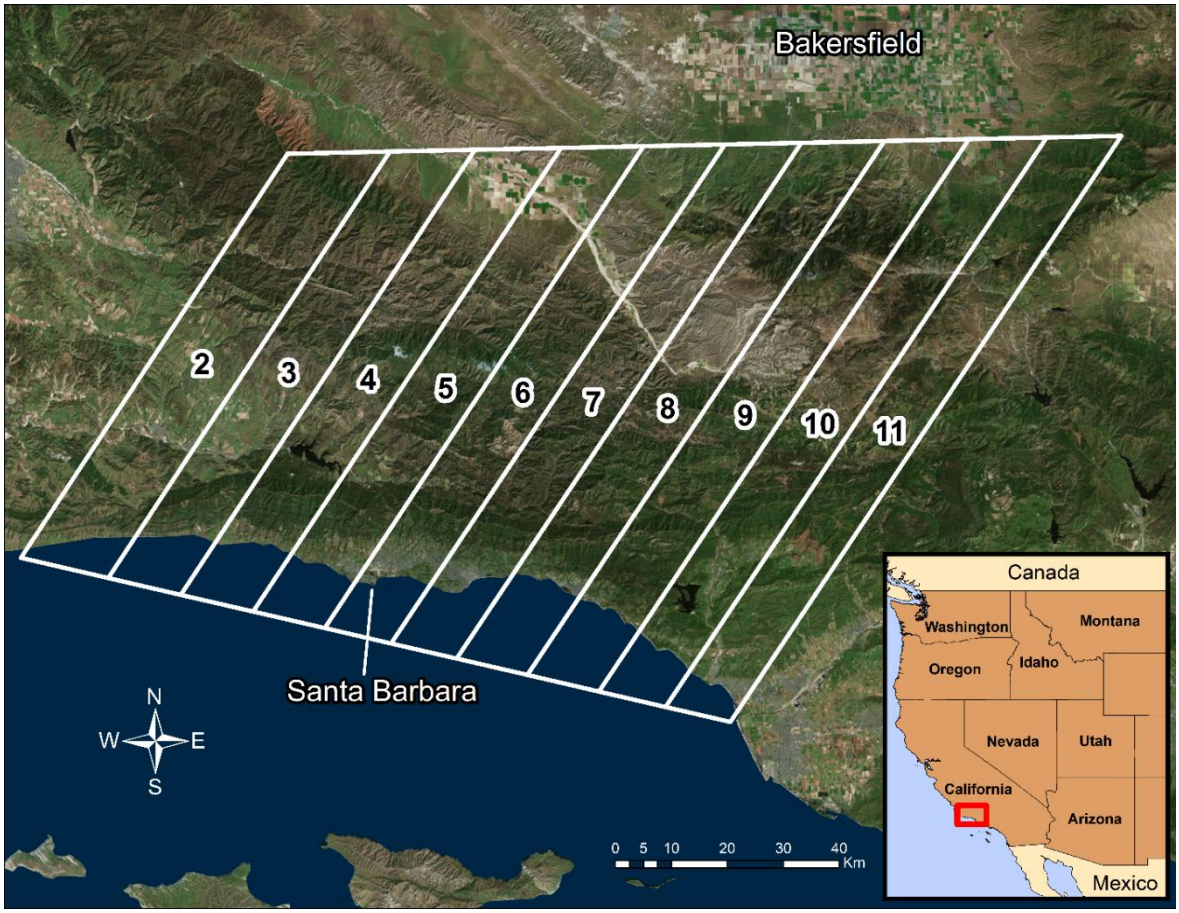


*Figure 2.1. Santa Barbara flight box and the HyspIRI Airborne Preparatory campaign flightlines used in study.*

*Table 2.1. Dates and flightlines covered for the Santa Barbara flight box. The * symbol denotes deviations from other flightline dates.*

| | FL02 | FL03 | FL04 | FL05 | FL06 | FL07 | FL08 | FL09 | FL10 | FL11 |
|---|---|---|---|---|---|---|---|---|---|---|
| 2013 Spring | 04/11/13 | 04/11/13 | 04/11/13 | 04/11/13 | 04/11/13 | 04/11/13 | 04/11/13 | 04/11/13 | 04/11/13 | 04/11/13 |
| 2013 Summer | 06/06/13 | 06/06/13 | 06/06/13 | 06/06/13 | 06/06/13 | 06/06/13 | 06/06/13 | 06/06/13 | 06/06/13 | 06/06/13 |
| 2013 Fall | 11/25/13 | 11/25/13 | 11/25/13 | N/A | 11/25/13 | 11/25/13 | 11/25/13 | 11/25/13 | 11/25/13 | 11/25/13 |
| 2014 Spring | 04/16/14 | 04/16/14 | 04/16/14 | 04/16/14 | 04/16/14 | 04/16/14 | 04/16/14 | 04/16/14 | 04/16/14 | 04/16/14 |
| 2014 Summer | 06/06/14 | 06/06/14 | 06/06/14 | 06/06/14 | N/A | 06/04/14* | 06/06/14 | 06/06/14 | 06/04/14* | 06/06/14 |
| 2014 Fall | 08/29/14 | 08/29/14 | 08/29/14 | 08/29/14 | 08/29/14 | 08/29/14 | 08/29/14 | 08/29/14 | 08/29/14 | 08/29/14 |
| 2015 Spring | 04/16/15 | 04/16/15 | 04/16/15 | 04/16/15 | 04/16/15 | 04/16/15 | 04/16/15 | 04/16/15 | 04/16/15 | 04/16/15 |
| 2015 Summer | 06/02/15 | 06/02/15 | 06/02/15 | 06/02/15 | 06/02/15 | 06/02/15 | 06/02/15 | 06/02/15 | 06/02/15 | 06/02/15 |
| 2015 Fall | 08/24/15 | 08/24/15 | 08/24/15 | 08/24/15 | 08/24/15 | 08/24/15 | 08/24/15 | 08/24/15 | 08/24/15 | 08/24/15 |

*2.2 Image processing*

NASA's Jet Propulsion Laboratory (JPL) provided 18 m spatial resolution HyspIRI-like reflectance products simulated using AVIRIS imagery (Thompson et al., 2015). In order to use the AVIRIS dataset across flight dates, a series of additional preprocessing steps were required. The custom source code developed for this study and used to process AVIRIS imagery is available at https://github.com/susanmeerdink/AVIRIS-Image-Preprocessing. The preprocessing steps, described below, can be summarized as registration across dates, geolocation refinement, and relative radiometric normalization.

Although initially geolocated by the JPL, the AVIRIS images exhibited significant systematic spatial misalignment at the scale of multiple pixels. Therefore, the first preprocessing step registered the images across dates to approach a subpixel level alignment required for multi-date studies. Because using manually selected control points rarely delivers subpixel accuracy and due to the large number of images needing to be registered, we applied an automated registration algorithm (Koltunov et al., 2012) that was successfully used in previous multi-temporal AVIRIS studies involving spectral unmixing (e.g. Khanna et

al., 2017, 2013; Tane et al., 2018a) and other change detection research (Koltunov et al., 2016, 2009). This algorithm represents band-wise iterations of relative radiometric normalization between the reference and the source images, followed by a gradient-based video-sequence stabilization method (Irani, 2002) that estimates the unknown parameters of a chosen between-image motion model. Each image was visually inspected to determine which band and model (affine or shift) resulted in highest performing registration. In this process, one date of flightlines is used as a reference for all other dates. The 16 Apr 2014 flightlines were selected as the reference images for registration because all ten flightlines were available and no cloud cover was present.

During the second step, the registered images were georeferenced to correct absolute georefencing error. The National Agriculture Imagery Program (NAIP) digital orthophotos acquired in the spring and fall of 2012 were utilized as a basemap for this process. The orthophotos were mosaicked and resampled to 18 m spatial resolution and then used to collect ground control points for the 16 Apr 2014 flightlines. Because all images were co-registered in the previous step, the image coordinates for the control points in 16 Apr 2014 flightlines were applied for all other image dates.

The final processing step was a relative radiometric normalization on the image products. During 2013 – 2015, the HyspIRI simulated reflectance product was actively undergoing development which made it difficult to compare spectra across flight dates. To compensate for atmospheric artifacts and noise, a linear correction was developed for each date and applied to the corresponding images (Clark et al., 2002; Wetherley et al., 2018). This was done by creating a band-by-band ratio of reflectance values using an invariant target's field and image spectra (Figure A.1). The roof of the United States Postal Service

distribution center in Goleta, CA was selected as the invariant target (Thompson et al., 2015). On 2 May 2014, spectra were collected on the roof using an Analytical Spectra Device Full Range spectrometer which covers the 0.3 – 2.5 μm range with a sampling interval of 1 nm (Analytical Spectra Devices, Inc., Boulder, CO USA). Image spectra were collected from 15 – 20 pixels for each of the nine image dates. The invariant target fell on flightline 5 or 6, depending on flight date. This approach assumes that ground targets are temporally invariant and reflectance retrieval errors are systematic for all flightlines acquired on the same date.

*2.3 Reference data*

Reference data on the spatial distribution of dominant species and land cover types were collected both in the field and using AVIRIS and NAIP imagery. In the field, we used a composition estimation method where patches of dominant plant species and their relative composition were collected using a high-power spotting scope and laser range finder from remote vantage points (Meentemeyer et al., 2001). Patches having greater than 75% single species composition were recorded and digitized on the AVIRIS flightline. These patches were stored with location and metadata as polygons in a shapefile. Species consistently found growing in mixed patches were treated as a single class (e.g. ARCA-SALE and ATCA-ERNA, Table 2.2). In this study, 700 references polygons were collected to cover new species and locations not previously covered in other studies. This was in addition to approximately 400 polygons collected previously (Roberts et al., 2015; Roth et al., 2015b). Reference polygons were used to extract spectra from imagery, and only pixels completely falling into a reference polygon were used to develop spectral libraries. The species codes, total number of polygons, and pixels for each class are shown in Table 2.2.

*Table 2.2. Dominant classes mapped with corresponding abbreviations, polygon, and pixel counts.*

| Species | Code | Polygons | Pixels |
|---|---|---|---|
| Adenostoma fasciculatum | ADFA | 75 | 2063 |
| Agricultural Residue | AGRES | 59 | 1359 |
| Artemisia californica and Salvia leucophylla | ARCA-SALE | 61 | 1702 |
| Arctostaphylos spp. | ARGL | 53 | 1276 |
| Atriplex canescens and Ericameria nauseosa | ATCA-ERNA | 36 | 659 |
| Baccharis pilularis | BAPI | 19 | 323 |
| Brassica nigra | BRNI | 47 | 1357 |
| Ceanothus cuneatus | CECU | 24 | 462 |
| Ceanothus megacarpus | CEME | 55 | 1544 |
| Ceanothus spinosus | CESP | 31 | 867 |
| Citrus spp. | CISP | 30 | 628 |
| Eriogonum fasciculatum | ERFA | 30 | 989 |
| Eucalyptus spp. | EUSP | 44 | 1257 |
| Irrigated Grasses | IRGR | 35 | 538 |
| Juniperus californica | JUCA | 15 | 178 |
| Mediterranean Annual Grasses and Forbs | MAGF | 58 | 3075 |
| Persea Americana | PEAM | 60 | 2187 |
| Pinus jeffreyi | PIJE | 16 | 226 |
| Pinus monophylla | PIMO | 36 | 531 |
| Pinus sabiniana | PISA | 34 | 854 |
| Pseudotsuga menziesii | PSMA | 11 | 261 |
| Quercus agrifolia | QUAG | 42 | 1152 |
| Quercus berberidifolia | QUBE | 36 | 426 |
| Quercus douglasii | QUDO | 37 | 1115 |
| Rock | ROCK | 26 | 463 |
| Soil | SOIL | 40 | 835 |
| Umbellularia californica | UMCA | 27 | 817 |

*2.4 Library development, dimensionality reduction, and classification*

Altogether, 25 spectral libraries were developed and used to classify the nine image dates (Table 2.3). There were three categories of spectral libraries: single date, multiple date, and leave-one-out (LOO). There were nine single date spectral libraries that were developed using spectra from a single image date. There were seven multiple date spectral libraries in which three were developed from seasonal images, three were developed from yearly images, and one was developed from all images. The seasonal spectral libraries had spectra from a

season across the three years of image dates (e.g. Spr-All, Sum-All, Fall-All). The yearly spectral libraries also had spectra from three image dates that were restricted to a single year (e.g. 2013-All, 2014-All, 2015-All). The last multiple date library was the All-Dates library developed using all nine image dates. The last spectral library category, leave-one-out (LOO) cross validation spectral libraries, tested whether spectra from all other dates could accurately classify an image. In these libraries, one date was left out from the spectral library. Table 2.3 specifies which image dates were used in the development of each spectral library.

*Table 2.3. Spectra from image dates used to develop spectral libraries. Note that fall 2013 imagery was collected in November, while 2014 and 2015 fall dates were collected in August.*

| | Library Name | Spectra from Image Dates | | |
|---|---|---|---|---|
| Single-Date Libraries | Spr-2013 | 04/11/2013 | | |
| | Sum-2013 | 06/06/2013 | | |
| | Fall-2013 | 11/25/2013 | | |
| | Spr-2014 | 04/16/2014 | | |
| | Sum-2014 | 06/06/2014 | | |
| | Fall-2014 | 08/29/2014 | | |
| | Spr-2015 | 04/16/2015 | | |
| | Sum-2015 | 06/02/2015 | | |
| | Fall-2015 | 08/24/2015 | | |
| Multiple Date Libraries | Spr-All | 04/11/2013 | 04/16/2014 | 04/16/2015 |
| | Sum-All | 06/06/2013 | 06/06/2014 | 06/02/2015 |
| | Fall-All | 11/25/2013 | 08/29/2014 | 08/24/2015 |
| | 2013-All | 04/11/2013 | 06/06/2013 | 11/25/2013 |
| | 2014-All | 04/16/2014 | 06/06/2014 | 08/29/2014 |
| | 2015-All | 04/16/2015 | 06/02/2015 | 08/24/2015 |
| | All-Dates | All 9 image dates | | |
| Leave-One-Out (LOO) Libraries | LOO-Spr13 | All dates except 04/11/2013 | | |
| | LOO-Sum13 | All dates except 06/06/2013 | | |
| | LOO-Fall13 | All dates except 11/25/2013 | | |
| | LOO-Spr14 | All dates except 04/16/2014 | | |
| | LOO-Sum14 | All dates except 06/06/2014 | | |
| | LOO-Fall14 | All dates except 08/29/2014 | | |
| | LOO-Spr15 | All dates except 04/16/2015 | | |
| | LOO-Sum15 | All dates except 06/02/2015 | | |
| | LOO-Fall15 | All dates except 08/24/2015 | | |

For each spectral library, data were split into training and validation (Figure 2.2). For each species, 70% of the reference polygons were randomly selected to be used in training. For each of those selected training polygons, a maximum of ten pixels were randomly selected until the total number of training pixels exceeded 350. This was implemented to create a balanced training dataset because not all species had the same number of polygons or pixels (Table 2.2; Roth et al., 2012). Random selection was repeated for 50 iterations. If a polygon fell on two flightlines, spectra from both flightlines were included. The multiple date and LOO libraries used the same training pixels as the single dates. This resulted in each date having an even number of spectra and larger libraries compared to single date libraries.

Each spectral library underwent dimensionality reduction using canonical discriminant analysis (CDA), a technique that was previously found to achieve the best species-level separation for a library (Alonzo et al., 2013; Roth et al., 2015a, 2015b). CDA reduces the data by finding orthogonal components while deriving functions that maximize linear separation among groups (e.g., plant species; Klecka, 1980). The number of functions derived is equal to the number of groups minus one. CDA coefficients were calculated for the 50 iterations of training pixels. These 50 coefficients were averaged and applied to the spectra for dimensionality reduction (Cruz-Castillo et al., 1994). The averaged CDA coefficients were applied to the validation spectra libraries.

Linear discriminant analysis (LDA) was run using CDA-transformed spectra to classify plant species. LDA derives linear combinations of the canonical variables which best correlate with class membership (Fisher, 1936). LDA was trained using the same 50 iterations to develop CDA coefficients. LDA was applied to the validation polygons, where the class was defined by the pixel majority of the polygon. If the class matched the validation

polygon plant identification, the polygon was considered correct. Class separability was evaluated using the kappa coefficient (Congalton, 1991), overall accuracy, and class-level producer's and user's accuracies. The kappa coefficients between classifications were evaluated for statistical significance using one-way analysis of variance (ANOVA). All 225 classifications with overall and kappa accuracy can be found in Table A.1 – A.3.

```
FOR each iteration
        FOR each species
                Randomly select 70% of polygons for training
                Set number of training pixels to 0
                FOR each polygon selected for training
                        IF polygon has more than 10 pixels
                                Randomly select 10 pixels in polygon
                        ELSE
                                Select all pixels in polygon
                        END
                        Add indices and number of training pixels selected
                        IF training pixel count is greater than 350
                                continue onto next species
                        END
                END
        END
END
```

*Figure 2.2. Pseudocode describing the process of splitting reference polygons into training and validation.*

## 2.3 Results

### *2.3.1 Single Date Spectral Libraries*

Spectral libraries developed from a single image date were used to develop baseline capabilities for classifying the plant species in this study (Table 2.4). Overall, the 24 plant species in this study were successfully classified with high accuracies across dates and

diverse ecosystem using single date spectral libraries. Single date spectral libraries classifying the corresponding image date, such as the Spr-2013 library applied to the Spring 2013 imagery, resulted in the highest classification accuracies, ranging from 0.80 – 0.86 kappa across the nine image dates. Single date libraries used to classify an unrelated image, such as the Spr-2013 library applied to the Summer 2013 imagery, performed poorly with all kappa accuracies below 0.5. Species spectra distributions were significantly different between image dates, which produced lower accuracies when classifying an image with a spectral library from different date.

*Table 2.4. Average classification kappa accuracy for each image date using single date spectral libraries. Averaged kappa accuracy is calculated from 50 iterations. Bold designates spectral libraries that contain image date spectra. Rows report the spectral library, while columns report image dates.*

| | **Image Date** | | | | | | | | |
|---|---|---|---|---|---|---|---|---|---|
| | **Spr 2013** | **Sum 2013** | **Fall 2013** | **Spr 2014** | **Sum 2014** | **Fall 2014** | **Spr 2015** | **Sum 2015** | **Fall 2015** |
| Spr-2013 | **0.85** | 0.41 | 0.26 | 0.42 | 0.13 | 0.21 | 0.29 | 0.26 | 0.22 |
| Sum-2013 | 0.35 | **0.84** | 0.26 | 0.36 | 0.25 | 0.37 | 0.34 | 0.37 | 0.37 |
| Fall-2013 | 0.24 | 0.18 | **0.80** | 0.19 | 0.12 | 0.30 | 0.27 | 0.28 | 0.32 |
| Spr-2014 | 0.06 | 0.07 | 0.19 | **0.84** | 0.20 | 0.36 | 0.39 | 0.43 | 0.34 |
| Sum-2014 | 0.14 | 0.22 | 0.14 | 0.22 | **0.85** | 0.29 | 0.38 | 0.19 | 0.26 |
| Fall-2014 | 0.01 | 0.06 | 0.10 | 0.40 | 0.13 | **0.85** | 0.41 | 0.48 | 0.54 |
| Spr-2015 | 0.03 | 0.03 | 0.09 | 0.35 | 0.14 | 0.29 | **0.83** | 0.29 | 0.29 |
| Sum-2015 | 0.09 | 0.13 | 0.19 | 0.36 | 0.18 | 0.29 | 0.34 | **0.86** | 0.38 |
| Fall-2015 | 0.04 | 0.09 | 0.09 | 0.32 | 0.19 | 0.35 | 0.33 | 0.35 | **0.85** |

For single date image classification, accuracies were not consistent across seasons or years (Figure 2.3). The 2013 and 2014 spring imagery had the highest classification accuracy (kappa mean of 0.84). These two image dates captured new seasonal leaf growth for many of

the species studied. The image classification of 2013 spring imagery shows the expected plant species distributions with conifer forests found northeast in the Los Padres National Forest and the southern edge containing the chaparral communities traditionally found in this region (Figure 2.4). The 2013 fall imagery had the lowest accuracy, but only marginally with a kappa mean of 0.80. However, the classification errors are visually apparent in the image compared to other dates, with conifers (PSMA and PIJE) having much lower accuracies (Figure 2.5). Classification of 2013 Fall imagery was difficult for two reasons: plants were fully senescent which reduces spectral separability, and the imagery was collected particularly late in the year (November) causing lighting geometry to adversely impact the plant species classification. The 2014 summer image deviated the most from expected plant species distributions despite having high accuracies with library classification (Figure 2.5). Flightline 2 (extreme western flightline) had the most pronounced cross track variation due to bidirectional reflectance distribution function (BRDF) effects. These effects are also present in other images, but less so due to a collection time closer to solar noon. Zoomed in portions of the classification show how distributions shift across images dates (Figure 2.6; Figure 2.7). The other image date classifications can be found in Figure A.2- A.10.

Examining the user and producer's accuracies for individual species shows marked differences between species and dates (Figure 2.8; Figure A.11 – A.14). Classification accuracy was not consistent across seasons and years for species with overall low accuracies, while species with high accuracies resulted in little variation across dates (Figure 2.9). For example, the seasonal differences and range of accuracies for JUCA and PIMO (the two species with the lowest accuracies) are much larger than for QUDO and ARCA-SALE (the two species with the highest accuracies). These four species and species-combinations

illustrate how canopy geometry and morphology influence species classification accuracies. While common on the landscape, JUCA grows dispersed with, at times, meters of bare substrate or grass between individuals. Evergreen trees, such as PIMO, have sparse canopies and therefore tend to have spectra that are highly influenced by substrate. On the other hand, ARCA-SALE form dense canopies of individuals with limited influence of substrate on the spectra. QUDO is a broadleaf tree with canopies larger than the 18 m spatial resolution, so pixel spectra are not influenced by any other species. Species that tend to grow interspersed with other species, such as ARGL, also have lower accuracies and are often confused in the classifier with their respective interspersed species, such as ADFA.

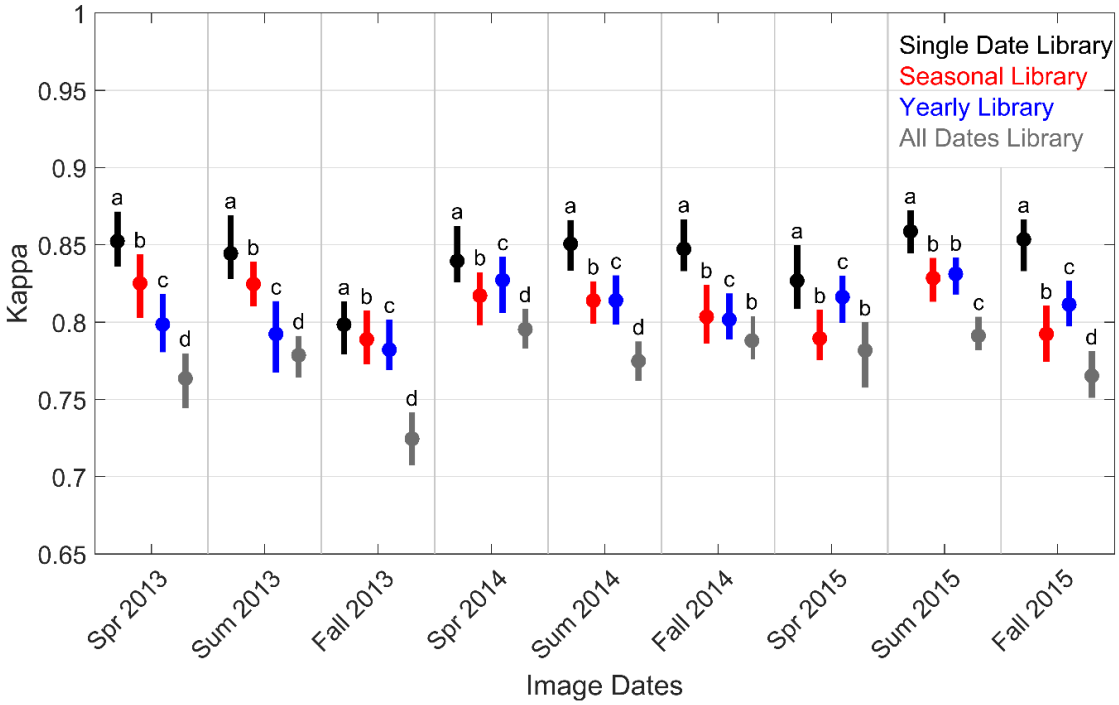


*Figure 2.4. Classification accuracy of all nine images using four different spectral libraries. Dots represent mean classification accuracy with the top and bottom of bars marking the maximum and minimum accuracies. Letters designate libraries that are significantly different for each date ($p < 0.05$).*

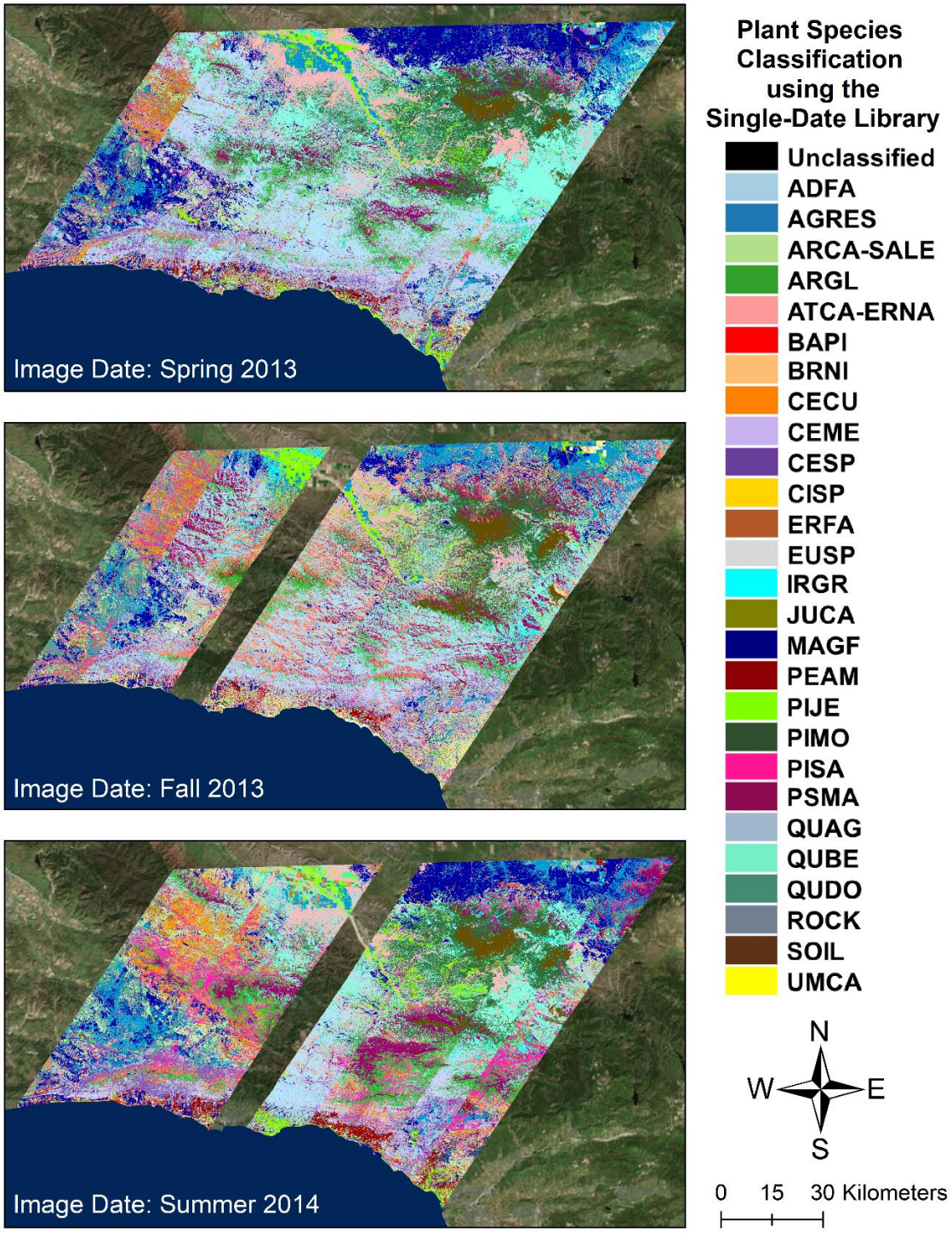


*Figure 2.5. Plant species classification of Spring 2013, Fall 2013, and Summer 2014 imagery using the corresponding single date spectral library. Other image classifications can be found in Figures A.2 – A.10.*

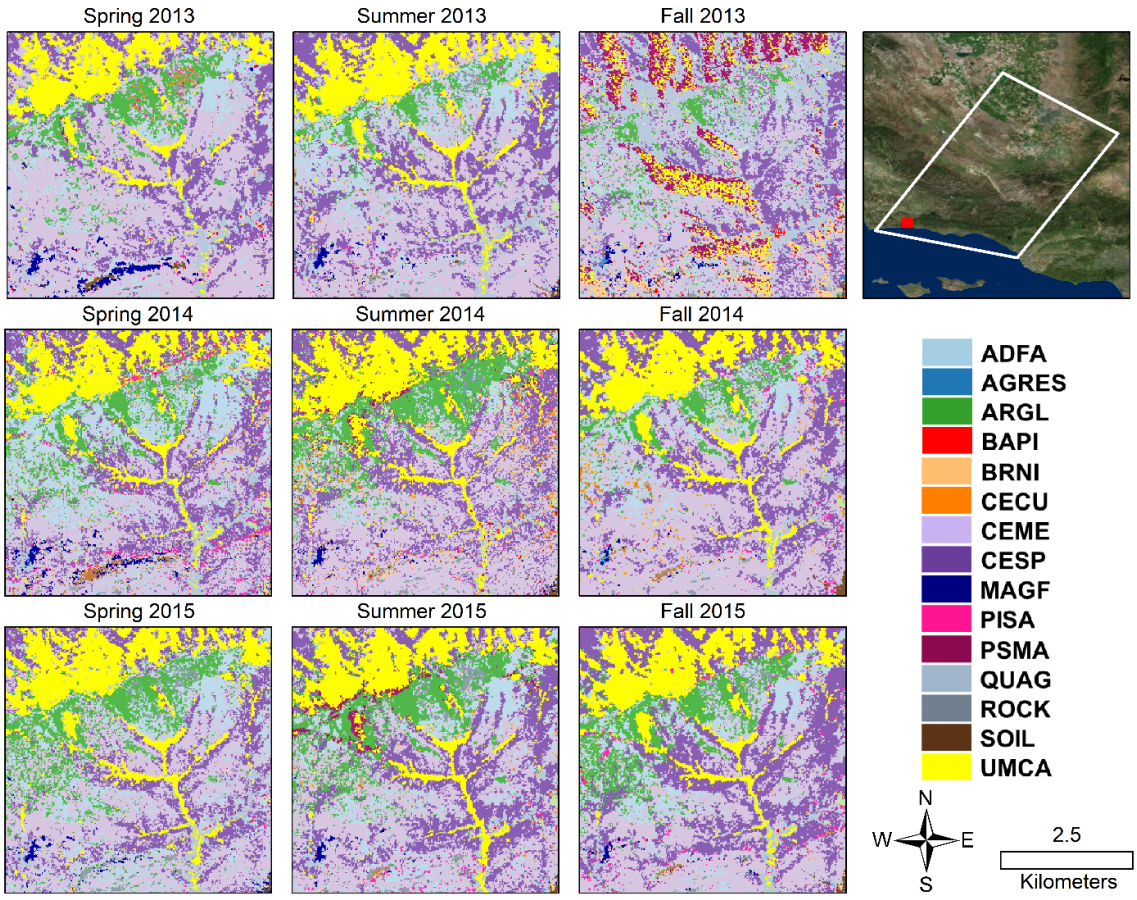


*Figure 2.6. Plant species classifications zoomed in on a portion of the Santa Ynez Mountain foothills. Only species and classes present in this subset are included in the legend.*

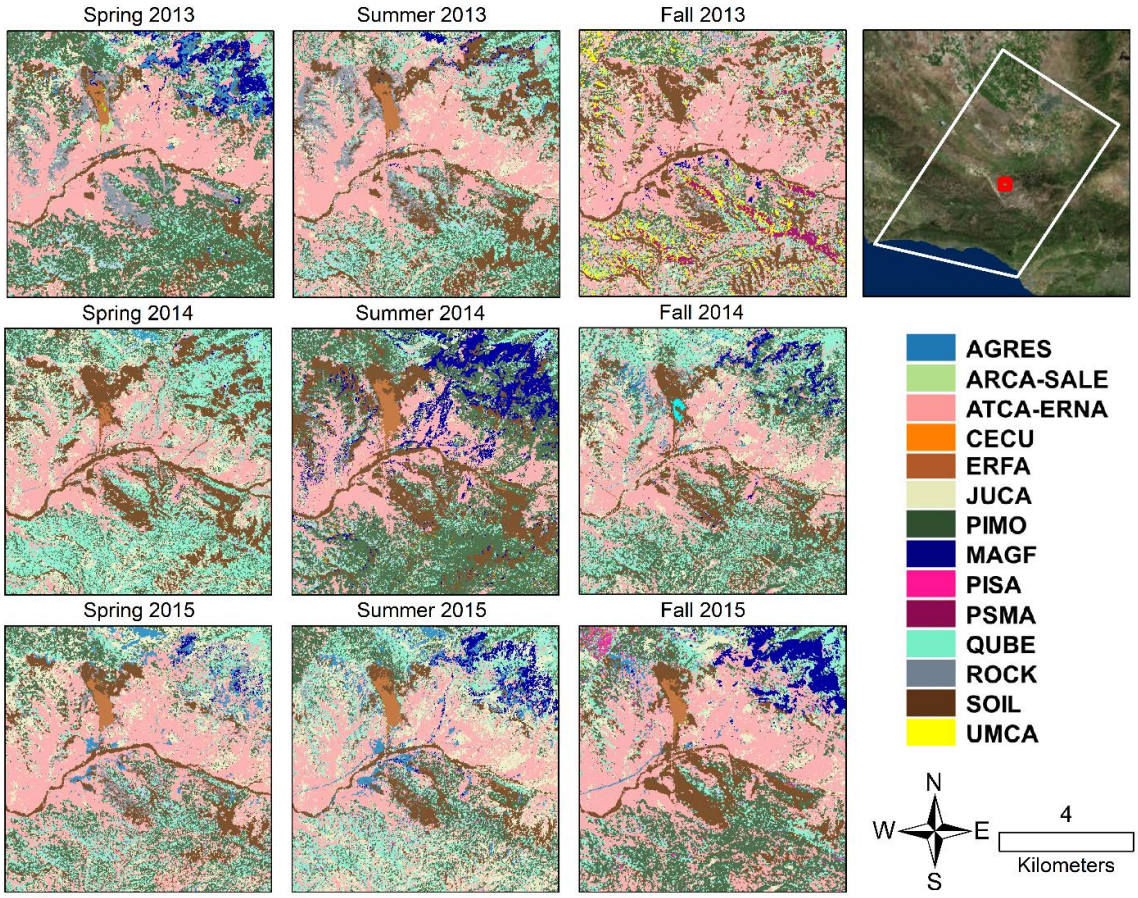


*Figure 2.7. Plant species classifications zoomed in on a portion of the Los Padres National Forest. Only species and classes present in this subset are included in the legend.*

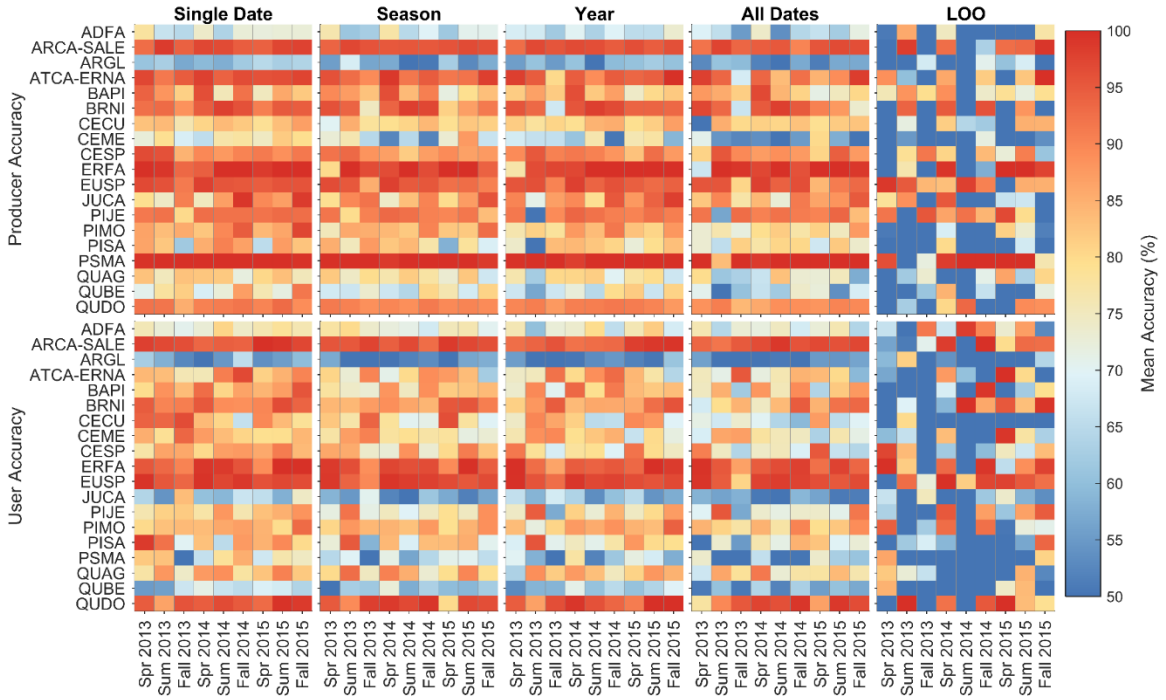


*Figure 2.8. Mean producer and user's accuracies using different spectral libraries on the nine image dates. Classes missing from figure are AGRES, CISP, IRGR, MAGF, PEAM, ROCK, SOIL, and UMCA. All classes' accuracies found in Figures A.11 – A.14.*

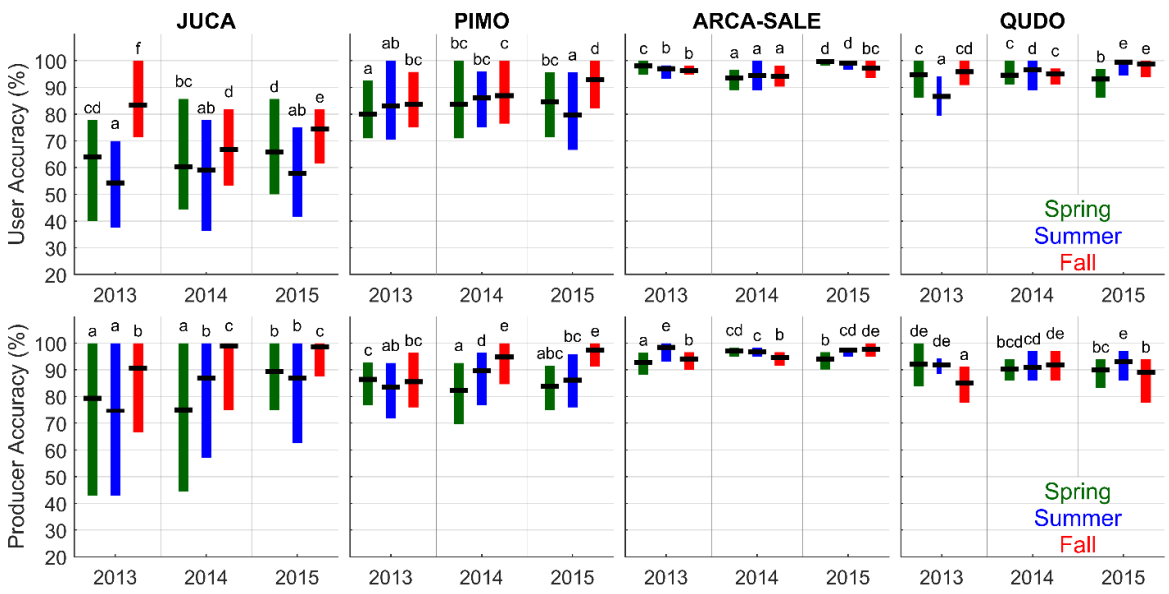


*Figure 2.9. Comparison of four classes' user and producer accuracies across image dates using single date spectral libraries. JUCA and PIMO were the lowest performing and ARCA-SALE and QUDO were the highest performing classes. Dots are mean accuracy with the top and bottom of bars marking the maximum and minimum accuracies seen across 50 iterations. Letters designate dates that are significantly different ($p < 0.05$).*

### *2.3.2 Multiple Date Spectral Libraries*

In order to test our capability of classifying plant species across a time series, multiple-date spectral libraries were developed (Table 2.5). Image dates were classified satisfactorily if the spectral library contained spectra from that specific image date. For example, the Spring 2013 imagery was classified accurately with the Spr-All (0.83 mean kappa) and 2013-All (0.80 mean kappa) spectral libraries, but had low accuracies with Fall-All (0.20 mean kappa) and 2015-All (0.09 mean kappa) spectral libraries. Seasonal and yearly differences in spectra made classification difficult when using spectral libraries derived exclusively from other image dates.

*Table 2.5. Average classification kappa accuracy for each image date using multi-date spectral libraries. Averaged kappa accuracy is calculated from 50 iterations. Bold designates spectral libraries that contain image date spectra.*

| | **Image Date** | | | | | | | | |
|---|---|---|---|---|---|---|---|---|---|
| | **Spr 2013** | **Sum 2013** | **Fall 2013** | **Spr 2014** | **Sum 2014** | **Fall 2014** | **Spr 2015** | **Sum 2015** | **Fall 2015** |
| Spr-All | **0.83** | 0.62 | 0.36 | **0.82** | 0.27 | 0.38 | **0.79** | 0.55 | 0.42 |
| Sum-All | 0.38 | **0.82** | 0.34 | 0.57 | **0.81** | 0.65 | 0.47 | **0.83** | 0.58 |
| Fall-All | 0.20 | 0.51 | **0.79** | 0.37 | 0.16 | **0.80** | 0.41 | 0.52 | **0.79** |
| 2013-All | **0.80** | **0.79** | **0.78** | 0.30 | 0.14 | 0.36 | 0.42 | 0.30 | 0.35 |
| 2014-All | 0.28 | 0.42 | 0.31 | **0.83** | **0.81** | **0.80** | 0.58 | 0.64 | 0.66 |
| 2015-All | 0.09 | 0.10 | 0.17 | 0.59 | 0.20 | 0.52 | **0.82** | **0.83** | **0.81** |
| All-Dates | 0.76 | 0.78 | 0.72 | 0.80 | 0.77 | 0.79 | 0.78 | 0.79 | 0.77 |

For all image dates, the single date spectral library outperformed all non-inclusive multiple date libraries (Figure 2.4). However, the corresponding seasonal or yearly libraries were comparable to single-date kappa values. The inclusion of other seasonal and annual spectra dropped the accuracy by 0.01 – 0.06 kappa compared to single-date classification's kappa. In general, the season-based spectral libraries (0.79 – 0.83 mean kappa) performed similar to year-based spectral libraries (0.78 – 0.83 mean kappa). The spectral library containing all image dates, performed consistently low across all nine dates. The inclusion of spectra from all nine dates with the All-Dates library dropped classification accuracy by 0.03 – 0.10 kappa compared to the single date library. However, it is worth noting for Fall 2014 and Spring 2015 imagery, the performance of the All-Dates spectral library was not significantly different than that of the seasonal library.

Producer and user's accuracies for individual species also decreased with the use of multiple-date spectral libraries (Figure 2.8). For seasonal libraries, approximately 58% of

species' accuracies were negatively impacted compared to single date libraries with producer and user accuracies dropping by 3.8 and 4% on average. Yearly libraries had a similar response with 59% of species having lower accuracies, with user accuracy dropping by 4.1% and producer accuracy by 4% on average. Use of the All-Dates spectral library for classification increased the number of species negatively impacted to 67%. User accuracies dropped on average by 7.4% and producer accuracies by 7.7% compared to single date classifications. While a majority of species across dates were negatively impacted with the inclusion of additional spectra, others experienced an increase in classification accuracy using multiple-date libraries or were not significantly different. Approximately 25% of the species for seasonal and yearly libraries and 19% of the species for All-Dates library did not have significantly different accuracies compared to the single date spectral library. Figure 2.8 shows an example of the variation described above for three species in two image dates. We did not find a single species across dates or an image date across species that consistently performed better or worse using multiple date spectral libraries.

*2.3.3 LOO Spectral Libraries*

In order to test the transferability of spectral libraries, we developed leave-one-out cross validation (LOO) spectral libraries to classify image dates (Table 2.6). Classification accuracies of images using these libraries were significantly lower than single date or multiple date spectral libraries. An image was not classified well unless spectra from that image was contained in the spectral library. The best performing LOO spectral library was the 2015 Summer imagery with a mean kappa of 0.73, but this was still significantly lower than single date or multiple date spectral libraries' classification accuracies (mean kappa range from 0.78 – 0.86). The lowest performing was the 2014 Summer imagery with a mean

kappa of 0.31, demonstrating that spectra from this image date were the least similar to other dates.

*Table 2.6. Mean classification kappa accuracy for each image date using leave-one-out (LOO) spectral libraries. Mean kappa accuracy is calculated from 50 iterations. Bold designates spectral library that does not contain image date spectra.*

| | **Image Date** | | | | | | | | |
|---|---|---|---|---|---|---|---|---|---|
| | **Spr 2013** | **Sum 2013** | **Fall 2013** | **Spr 2014** | **Sum 2014** | **Fall 2014** | **Spr 2015** | **Sum 2015** | **Fall 2015** |
| LOO-Spr13 | **0.47** | 0.78 | 0.74 | 0.79 | 0.77 | 0.79 | 0.78 | 0.79 | 0.77 |
| LOO-Sum13 | 0.78 | **0.61** | 0.73 | 0.79 | 0.78 | 0.78 | 0.78 | 0.79 | 0.77 |
| LOO-Fall13 | 0.78 | 0.79 | **0.44** | 0.80 | 0.79 | 0.79 | 0.79 | 0.81 | 0.78 |
| LOO-Spr14 | 0.77 | 0.78 | 0.73 | **0.67** | 0.77 | 0.80 | 0.79 | 0.79 | 0.77 |
| LOO-Sum14 | 0.77 | 0.78 | 0.73 | 0.80 | **0.31** | 0.79 | 0.78 | 0.79 | 0.77 |
| LOO-Fall14 | 0.77 | 0.78 | 0.73 | 0.79 | 0.77 | **0.59** | 0.78 | 0.79 | 0.76 |
| LOO-Spr15 | 0.77 | 0.78 | 0.74 | 0.80 | 0.78 | 0.79 | **0.61** | 0.79 | 0.77 |
| LOO-Sum15 | 0.76 | 0.78 | 0.73 | 0.80 | 0.78 | 0.79 | 0.78 | **0.73** | 0.76 |
| LOO-Fall15 | 0.77 | 0.78 | 0.74 | 0.80 | 0.78 | 0.79 | 0.78 | 0.79 | **0.64** |

In general, the loss of classification accuracy was also true for individual plant species' user and producer accuracies (Figure 2.8; Figure A.11 – A.14). Compared to the single date spectral libraries, approximately 73% of species across dates had lower classification accuracies using LOO spectral libraries. Only 10% of species did not have significantly different accuracies, but none had any that were improved compared to single date libraries. We found that Spring 2013 and Summer 2014 image classification suffered the most when using LOO spectral libraries. Spring 2015 imagery was the least impacted using LOO libraries, but was only marginally better than other image dates. While most species generally performed worse using LOO spectral libraries, the magnitude of loss depended on the image date and species. For example, for ARCA-SALE, a top performing species for

other libraries, the mean classification accuracy dropped by 40% from Spring 2013 to Fall 2013 imagery using the LOO spectral libraries (Figure 2.10). However, for Summer 2015 and Fall 2015 imagery the classification accuracies only differed by 5%.

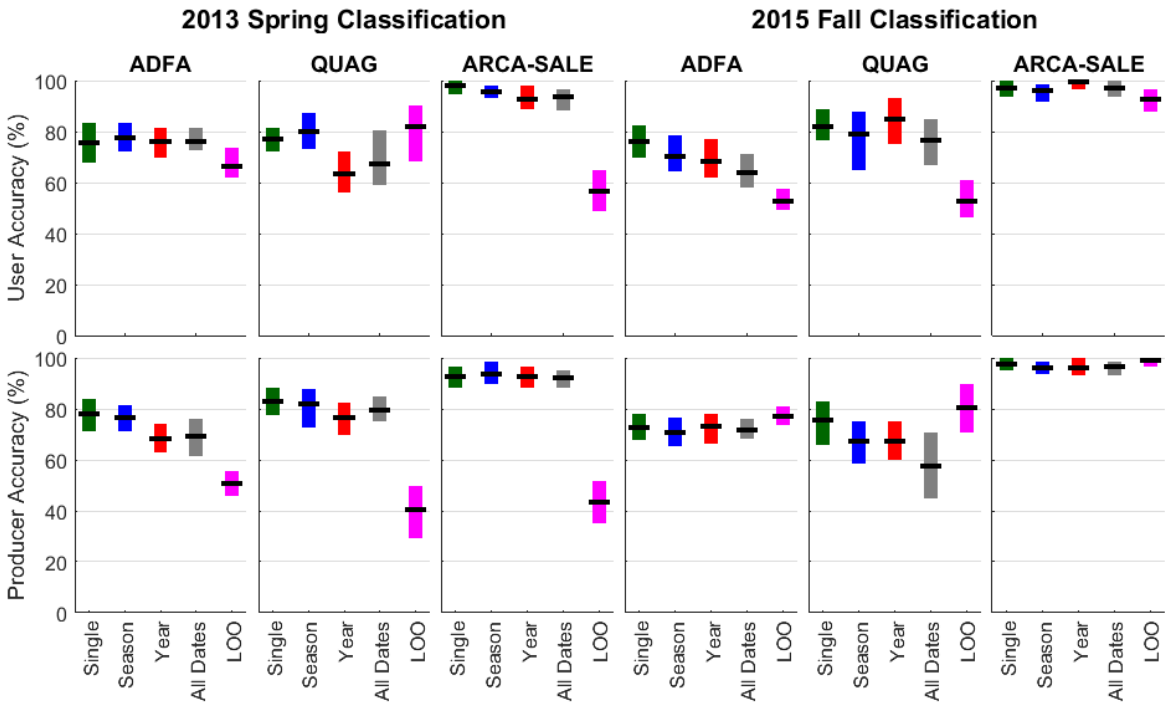


*Figure 2.10. Comparison of three species' producer and user accuracies for two image dates using five different spectral libraries. Horizontal black lines mark mean accuracy with the top and bottom of bars marking the maximum and minimum accuracies seen across 50 iterations.*

## 2.4. Discussion

### *2.4.1 Classifying plant species*

To establish baseline classification capabilities, we classified plant species using spectra from a single image date. We found that plant species can be classified across this diverse landscape with a mean kappa accuracy ranging from 0.78 – 0.84 over the nine image

dates. These results demonstrate that California species, often found in remote and rugged terrain, can be classified accurately using hyperspectral remote sensing. Additionally, this study was able to classify species with user and producer's accuracies >75%, even though most represent less than ideal characteristics for remotely classifying. The species analyzed in this study were predominantly chaparral shrubs or conifers, for which many individuals are required to fill a single 18 m pixel. Many of these species grow in heterogeneous patches with individuals from other species influencing the spectrum. Some species in this study are dispersed on the landscape or do not form dense canopies, which introduces substrate influence into the spectrum. In contrast, classification studies focusing on broadleaf tree species often have a single individual that can fill an entire pixel, resulting in a spectrum composed of solely that individual. For example, *Juniper californica* (JUCA), a shrub with open canopies that do not fill an entire 18 m pixel, had a mean producer and user accuracy of 79.4 and 63.9% for Spring 2013 imagery. While *Quercus douglassii* (QUDO) had a mean producer and user accuracy of 94.7 and 92.1% for Spring 2013 imagery because it is a broadleaf large canopy tree and filled the entire pixel.

Other studies have also had success mapping plant species using a single date spectral library. In a subset of our study area, Roth et al. (2015) classified 23 dominant chaparral plant species with a 0.84 mean kappa accuracy, also using CDA-LDA as a classifier. Roberts et al. (2015) also classified 22 of the same classes as reported in this study with a kappa accuracy of 0.73 using Multiple Endmember Spectral Mixture Analysis (MESMA). In other ecosystems, a single date spectral library has been used to classify plant species with a range of success using different methodologies. For example, three southern pine species in North America were mapped with 83% accuracy (van Aardt and Wynne, 2007), eleven eastern

broadleaf tree species in North America were classified with 75% accuracy (Martin et al., 1998), and seven tropical rainforest species were classified with 92% accuracy (Clark et al., 2005). The results of this study complement the above mentioned studies and establish our capabilities for classifying plant species using airborne datasets. The next step in determining the possibility of classifying species with future hyperspectral satellites is evaluating our classification capabilities across time.

*2.4.2 Annual and seasonal classification of plant species*

We explored the potential for using a multi-temporal spectral library for classification that would be better suited for capturing the variability anticipated by the HyspIRI sensor. The seasonal and annual spectral libraries performed similar to single-date spectral library classifications with a slight decrease in accuracy. In general, seasonal libraries performed better than yearly libraries, demonstrating that matching phenology plays a dominant role in species classification. Including spectra from all nine image dates further decreased kappa classification by adding too much seasonal and annual spectral variability. In other disciplines, an increased amount of data results in more accurate or representative models whereas in vegetation remote sensing it does not. While species do exhibit unique spectral characteristics due to biochemical and structural composition, individuals can deviate from the normal, creating a distribution of potential spectra for a species (Asner and Martin, 2009). These distributions can overlap other species' spectral distributions, particularly as the variability of seasonal and year-to-year changes in a species' spectral response are added. In our study, that added variability ultimately reduced spectral separability between classes and confused the classifier.

Very few studies have explored plant species classification through seasons or years at the canopy scale. However, phenological patterns have been found to be important factors at the leaf level with hyperspectral measurements. In tropical forests, Hesketh and Sánchez-Azofeifa (2012) found that classification of trees and lianas at the leaf level dropped from approximately 80% accuracy for a single season to 20% across seasons. Burkholder et al. (2011) found that the ability to separate invasive and native species at the leaf level peaked in July and August where optimum band selection shifted between each sampling period. When discriminating reed species, Fernandes et al. (2013) found that species are only spectrally distinct during the senescent period. These studies emphasize the importance of capturing species distributions as they change across seasons and years, not only in a single observation.

Only four published studies have classified plant species across multiple dates. Using five water deficit image dates, Dennison and Roberts (2003) found that the amount of variation in non-photosynthetic materials increased confusion between species and ultimately decreased accuracy by 8–16%. Conversely, additional research found that the inclusion of monthly spectra increased detection by 0.11 – 0.29 kappa for invasive tree species in Hawaii using Earth Observing-1 Hyperion data (Somers and Asner, 2013, 2012). Dudley et al. (2015), using five image dates from a single year, found that seasonally-mixed spectral libraries achieved similar overall classification accuracies compared to single-date libraries, and in some cases, resulted in improved classification accuracies. While similar to our study, Dudley et al. (2015) had key differences including a smaller study area, finer spatial resolution (10.9 – 16.7 m), and imagery only from a single year. Our research expands the research to include a 12980 km² area, 18 m spatial resolution, and three years of imagery.

*2.4.3 Transferability of plant species classification*

The collection and processing of reference spectra is time consuming and expensive. Ideally, reference spectra that can be shared across geographies and dates would vastly improve the efficiency of remote sensing applications. Our analysis use LOO spectral libraries to test the transferability of spectral libraries. We found that classification accuracy dropped severely if spectra from the image date were not included in the spectral library. The LOO spectral libraries decreased mean kappa accuracy to 0.31 – 0.73 compared to the single date spectral library with a mean kappa of 0.80 – 0.86. The variability in classification accuracy across the 50 iterations also increased significantly compared to other libraries. For this study area and dates observed, we found that spectral libraries were not transferrable across dates. However, this might be due to the airborne dataset being acquired over 4 – 6 hours with variable sun-sensor geometry and captured increasing drought conditions. Perhaps under similar conditions, such as soil moisture and lighting, spectral libraries would be transferrable across dates. Additionally, the limited ability to transfer spectral libraries across dates is restricted to biotic materials. Abiotic materials, e.g. rocks, minerals, and urban materials, have shown to be portable across time because they are generally invariant (Herold et al., 2004; Herold and Roberts, 2005).

The scientific community has been developing databases of spectra to assist remote sensing applications. Most spectral libraries focus on leaf or canopy spectra collected with a handheld spectrometer, but a couple of libraries contain image-derived spectra. One of the most recently developed spectral libraries is the NASA-funded Ecosystem Spectral Information System (EcoSIS) spectral library that hosts spectra uploaded by researchers which are publicly available for download (https://ecosis.org/). From our research, it is

apparent that image derived spectra will likely not be transferrable to a new image date, meaning that existing spectral libraries will not yield accurate plant species classifications. Instead, we believe there is a need for starting a public geodatabase of reference polygons and locations of species and classes that can be used for any research application, sensor, or time period. The development of such a database would provide a validation and training dataset that can be used across all remote sensing platforms for any application.

*2.4.4 Opportunities when using airborne hyperspectral imagery*

While this study is a reasonable representation of the data that will be available with HyspIRI, there are some additional considerations to take into account, specifically including spatial resolution, georeferencing, and atmospheric correction. Currently, the proposed spatial resolution of HyspIRI is 30 m pixels, while this study used 18 m pixels. Spatial resolution has been found to affect classification accuracy and would need to be further investigated (Roth et al., 2015a; Schaaf et al., 2011). Furthermore, at the HyspIRI scale, spaceborne missions tend to deliver stable image geolocation at a subpixel level, which is not available with airborne passive remote sensing. To mitigate these differences, we made extensive efforts to reference AVIRIS images to known ground locations and also aligned the images between dates. However, geolocation errors are still present in the dataset due to residual misalignment. Finally, the reflectance retrieval algorithm was evolving as the campaign progressed, and influenced the stability in reflectance between images. We attempted to correct for spectral differences between dates and flightlines by using an invariant reflectance target, but some spectral differences that are caused by the reflectance retrieval, and not species phenology, may still exist. BRDF effects on imagery are a common issue with airborne platforms and were shown to greatly impact this and other studies using

this dataset, further exacerbated by multi-hour imaging campaigns required to cover each flight box (Tane et al., 2018a; Wetherley et al., 2017). In HyspIRI images spaced by 19 days, the fixed viewing geometry and rapid image acquisition will reduce BRDF differences within a scene and across dates, thus potentially improving classification accuracy compared to the HyspIRI-like airborne imagery.

Identifying capabilities of mapping plant species presents opportunities for sensors currently or soon-to-be deployed in addition to HyspIRI. For example, scheduled to launch in 2019, the Environmental Mapping and Analysis Program (EnMAP) mission sponsored by Germany is an imaging spectrometer that will provide measurements at 420 - 1000 nm and 900 - 2450 nm (Stuffler et al., 2007). This mission would provide global coverage with a revisit time of 27 days, and would significantly increase hyperspectral data volume for temporal classification of species. In addition, the National Ecological Observatory Network (NEON) airborne mission flies an imaging spectrometer once a year over 47 terrestrial field sites (Kampe et al., 2010). Sponsored by the National Science Foundation, this program is expected to continue for 30 years which will yield the largest imaging spectroscopy dataset with continuous measurements for individual locations. The results of this study provide a link between existing research and future possibilities for classifying plant species across seasons over years using datasets such as HyspIRI, EnMAP, and NEON.

## 2.5 Conclusion

Our study quantifies the potential for classifying seasonal and yearly distributions of plant species, specifically for the HyspIRI sensor. We set out to answer three questions. First, we asked how accurately can plant species be classified across spring, summer, and fall in 2013 – 2015 using single date spectral libraries. We found that the 24 species and land covers

in this study were classified with high accuracies across the nine dates (mean kappa 0.80 – 0.86). Species with open canopies had the lowest user and producer accuracies because of the influence of substrate on spectra. Second, we explored the use of multiple date spectral libraries for classification to capture a broader range of phenological conditions that would be present in the repeat acquisitions of the HyspIRI mission. We found that the increased spectral variability due to changes in plant phenology and drought conditions, and perhaps the combined errors of various preprocessing steps that are unique to the airborne image data used, resulted in a loss of classification accuracy. However, accuracies were still comparable to single date libraries with seasonal libraries having a mean kappa 0.79 – 0.83 and annual libraries having a mean kappa 0.78 – 0.83. Finally, we asked how transferable vegetation spectral libraries are across dates using LOO spectral libraries. We found that LOO libraries resulted in a significant decrease in classification accuracy (mean kappa 0.31 – 0.73) and did not yield species maps that would be accurate enough for future research. However, this might not be true for satellite based measurements as it will have smaller range of sun-sensor geometries compared to the airborne dataset.

Instead of developing image based vegetation spectral libraries, we recommend that the science community develop a geodatabase containing reference locations of species that can then be applied to any image or sensor. Such a database would allow researchers flexibility in addressing science questions. This flexibility is exceptionally important as temporal hyperspectral datasets grow exponentially with ongoing airborne campaigns and proposed spaceborne missions. The proposed HyspIRI mission would be uniquely poised to globally capture plant species distributions with a 19-day revisit time. Thus, it is important to

expedite development of robust multi-temporal species classification techniques capable of extracting new information from the temporal dimension of hyperspectral data.

# 3. Plant species' spectral emissivity and temperature using the Hyperspectral Thermal Emission Spectrometer (HyTES) sensor


## Abstract

The thermal domain (TIR; 2.5 – 15 μm) delivers unique measurements of plant characteristics that are not possible in other parts of the electromagnetic spectrum. However, these TIR measurements have largely been restricted to laboratory leaf level or coarse spatial resolutions due to the lack of suitable data from airborne and spaceborne instruments. The airborne Hyperspectral Thermal Emission Spectrometer (HyTES) provides an opportunity to retrieve high spectral resolution emissivity and land surface temperature (LST) that can be exploited for canopy level vegetation research. This study is a small-scale spatial resolution analysis of plant species' emissivity and LST using HyTES imagery acquired in the Huntington Botanical Gardens on 2014 July 5 and 2016 Jan 1. Leaf and canopy emissivity variation was identified among 24 plant species and used to determine leaf to canopy scaling capabilities. HyTES LST patterns among species and dates were quantified and correlated to LiDAR derived tree canopy attributes. At the leaf scale, one third of the species showed distinct spectral separation from other species. However, at the canopy scale most species were not spectrally separable. A simple physical scaling model, using leaf inclination and leaf area index, did not accurately reproduce canopy emissivities; suggesting other variables are necessary for scaling such as blackbody cavity effects. LST data, derived from TIR measurements, showed that species exhibited significantly different distributions between dates and species. These distributions were largely explained by canopy structure (e.g. tree height and canopy density) and composition of neighboring pixels (e.g. presence of pavement

versus trees). While species do not exhibit unique emissivity signatures at the canopy, the LST variation among species provides a stronger understanding of LST variability in coarser resolution TIR imagery. This study represents the first look at vegetation characteristics using the NASA's HyTES TIR sensor, opening the door for future remote sensing vegetation studies including the recently launched ECOsystem Spaceborne Thermal Radiometer Experiment on Space Station (ECOSTRESS) mission.

### 3.1 Introduction

The thermal domain (TIR; 2.5 – 15 μm) affords two unique measurements of plant characteristics through emissivity and land surface temperature (LST) that are not possible using the visible-shortwave infrared spectrum (0.35 – 2.5 μm). These measurements are being used for vegetation research at multiple scales including the determination of leaf water content (Fabre et al., 2011; Ullah et al., 2012b), plant evaporation rates (Anderson and Kustas, 2008; Otkin et al., 2014), and large-scale drought monitoring (Kogan, 1995; Liu and Kogan, 1996). The increased availability of TIR sensors and technological advances have now made it increasingly possible to examine vegetation characteristics using emissivity and LST measurements.

TIR emissivity signatures are unique from the visible-shortwave infrared because of how light interacts with the leaf. Due to the low energy of TIR wavelengths, leaves appear opaque because energy does not penetrate leaf surfaces (Gates and Tantraporn, 1952; Salisbury, 1986; Salisbury and Milton, 1988). Measured spectral emissivity for a leaf is the product of light interactions with the outer layers of the leaf (Elvidge, 1988; Salisbury, 1986; Wong and Blevin, 1967). In contrast, spectra in the visible-shortwave infrared domain are the product of light interactions with the internal leaf structure and biochemical components

because the high energy wavelengths of this domain can penetrate leaf surfaces (Curran, 1989). Ribeiro da Luz (2006) conducted one of the first studies to investigate vegetation characteristics in the TIR and found that leaves display complex absorption features related to organic constituents of leaf surfaces. Since then, high spectral resolution TIR laboratory measurements have been leveraged to quantify leaf water content using a variety of methods (Arshad and Ali, 2018; Buitrago et al., 2016; Fabre et al., 2011; Meerdink et al., 2016; Ullah et al., 2014, 2013, 2012b). Other studies have leveraged this domain for plant species classification at the leaf level (Buitrago et al., 2018; Harrison et al., 2018; Ullah et al., 2012a) or leaf area index estimation (Neinavaz et al., 2016a). These studies demonstrate the successful application of TIR emissivities for the study of leaf characteristics, but with the caveat that these relationships may not translate to canopy scale and are only relevant for high spatial resolution sensors at the few meter scale.

Ultimately, to address the broader science and remote sensing questions, it is necessary to scale these studies to the canopy. Ribeiro Da Luz and Crowley (2007) were the first ones to address this knowledge gap by making measurements at increasing distances from natural canopies with a field spectrometer. Other studies have also used high spectral resolution TIR imaging under controlled laboratory conditions to measure canopy changes due to water stress (Gerhards et al., 2016) and to develop a relationship with leaf area index (Neinavaz et al., 2016a). Ribeiro Da Luz and Crowley (2010) provide the only study, to our knowledge, that has used airborne hyperspectral TIR imagery to study plant characteristics. Using Spatially-Enhanced Broadband Array Spectrograph System (SEBASS; Hackwell et al., 1996) imagery, the research identified spectral differences between species located in the

State Arboretum of Virginia. TIR emissivity measurements at the canopy level have been few in number due to lack of sensors and low signal to noise ratios in the sensors available.

TIR LST measurements are unique because of the relationship between plant temperatures and plants' response to the environment. As plants close stomata to maintain their carbon-water balance, plant temperatures increase due to a decrease in evapotranspiration rates (Jones, 2014). This relationship has long been recognized in plant ecology and used as an indicator of plant water relations and stress (Calderón et al., 2013; Grant et al., 2007; Jackson et al., 1988; Jones and Leinonen, 2003). Leaf or field level LST measurements have been used for developing irrigation and crop health indices (Fuchs, 1990; Fuchs and Tanner, 1966; Jackson et al., 1981, 1977; Jones and Leinonen, 2003; Jones and Schofield, 2008), estimating stomatal conductance (Jones, 1999; Jones et al., 2002; Leinonen et al., 2006), calculating evapotranspiration rate (Anderson et al., 2008; Fisher et al., 2008), or measuring an evaporative stress index (Anderson et al., 2016; Otkin et al., 2014, 2013). Satellite level LST measurements have been used for global or regional drought monitoring ( Kogan, 1995; Liu and Kogan, 1996; Singh et al., 2003).

While these studies have successfully used temperature as a proxy for plant water status, many other factors can influence a plant's canopy temperature. Leuzinger and Körner (2007) found that leaf dimensions and stomatal conductance alone could not capture canopy temperatures, but that canopy architecture has a strong influence on canopy LSTs. Additionally, the presence or absence of key taxa or plant functional types influences the temperature distribution of a forest and an urban environment (Leuzinger et al., 2010; Leuzinger and Körner, 2007). In these studies, leaf type (broad vs. needle), leaf size (small vs. large), and substrate (grass vs. concrete) interacted to create unique temperature

distributions and sensitivity among tree species (Leuzinger et al., 2010, 2005; Leuzinger and Körner, 2007). Our understanding of plant LST patterns are especially limited at the canopy level, mainly due to the coarse spatial resolution of satellite measurements and the lack of plant structural variability available in agriculture field measurements.

The Hyperspectral Thermal Emission Spectrometer (HyTES) is a recent sensor developed using new technologies from the National Aeronautics and Space Administration (NASA) Jet Propulsion Laboratory (JPL). This sensor presents a unique opportunity to study vegetation properties at the canopy level with a 2 m spatial resolution at a nominal flight altitude of 1 km. HyTES measures 256 radiance bands in the 7.5 – 12 µm spectral domain at 17 nm spectral sampling (Hook et al., 2013). High spatial resolution (2 – 10 m) temperature and emissivity data are currently available to order from https://hytes.jpl.nasa.gov/order for science campaigns over the Southwestern USA and Hawaii from 2013 – 2018. Using a temperature emissivity separation algorithm developed by JPL, this sensor is able to retrieve surface temperatures with an error of <1 ºC and 186 emissivity bands in the TIR window region between 8-12 µm (Hook et al., 2013). This sensor has been used in a variety of research projects including methane/trace gas detection and quantitative retrievals (Hulley et al., 2016; Johnson et al., 2014; Kuai et al., 2016) and geological composition (Iqbal et al., 2018; Kruse, 2015). High spectral resolution and fine spatial resolution TIR imagery has not been widely used for vegetation due to the lack of suitable measurements and the subtle features of plants (Ribeiro Da Luz and Crowley, 2010). However, the HyTES sensor presents an opportunity to examine canopy properties at these resolutions.

The purpose of our study was to explore the possibility of using HyTES imagery for measuring plant species' canopy characteristics. HyTES's 186 TIR emissivity bands provide

a unique opportunity to study patterns of TIR canopy signatures that were previously only possible with a limited number of sensors (e.g. SEBASS). The high accuracy LST retrievals at fine spatial resolutions allow for the examination of patterns across species and dates. We investigate drivers of LST variability using LiDAR derived canopy attributes. Specifically, we asked the following questions:

1) What TIR spectral variation among plant species is present at the leaf scale?
2) Using HyTES imagery, do plant species exhibit unique TIR emissivity signatures at the canopy scale?
3) What are the leaf to canopy scaling capabilities for TIR emissivities?
4) How do LST patterns vary among species, canopy attributes, and dates?

## 3.2 Methods

### *3.2.1 Study Site*

The Huntington Botanical Gardens, located in San Marino, CA, USA, is a collections-based research and educational institution established in 1919 (Figure 3.1). It covers approximately 48.6 hectares and contains about 15,000 documented plant varieties, most of which are tagged and identified. In order to best relate laboratory spectra to canopy spectra, plants with canopies having at least a 12-meter diameter were identified using a database provided by the Huntington Gardens, high-resolution imagery, and field assessment. Out of these species, 24 species with three or more individuals were selected (Table 3.1). Each selected individual identified had fresh leaf samples taken for laboratory measurements (see Section 3.2.2). Only tree canopies with a diameter larger than 12 meters were chosen for this analysis to ensure there were multiple pixels for each individual tree. The polygons of individual trees were used to extract emissivity and LST values from HyTES imagery (see

Section 3.2.3) and also LiDAR variables (see Section 3.2.6). Only pixels completely falling into a reference polygon were used to avoid the edge of tree canopies. The number of pixels differed between image sources due to different spatial resolutions. Table 3.1 lists the 24 plant species sampled in this study with the number of pixels associated for each with 2014 and 2016 imagery.

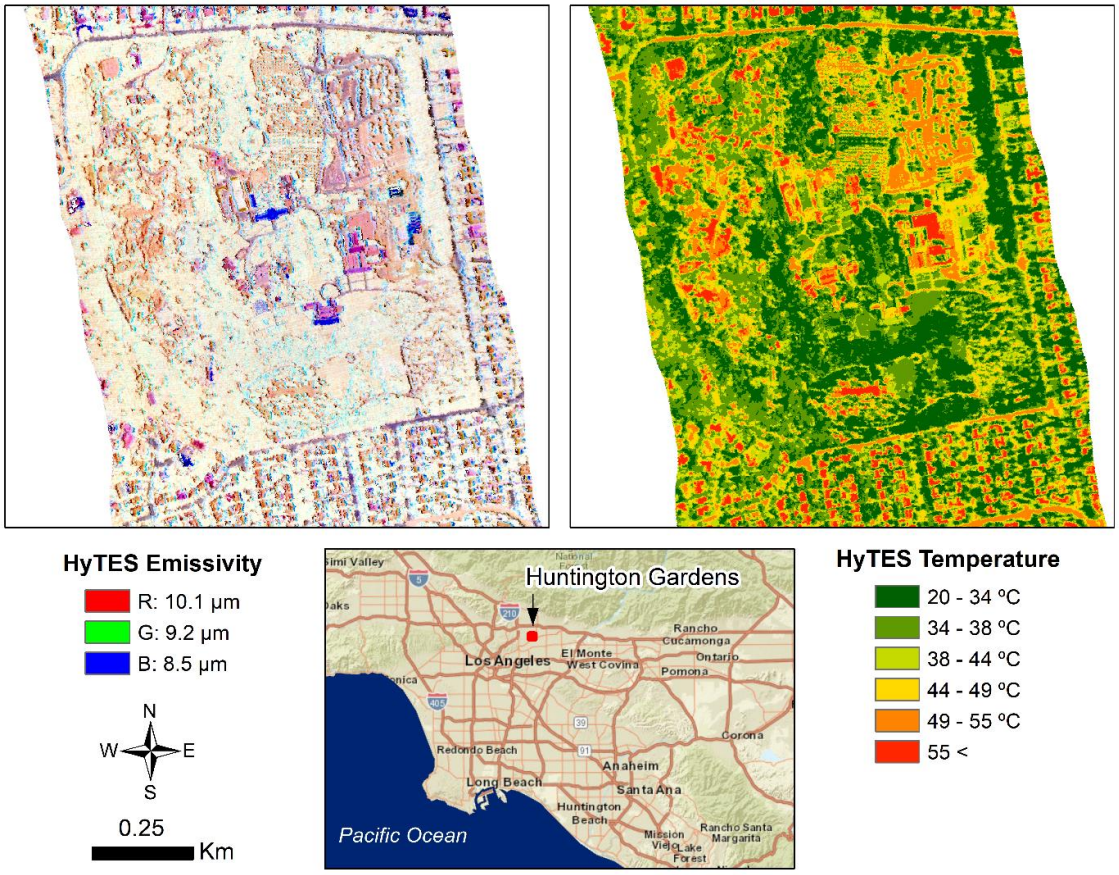


*Figure 3.1 HyTES imagery at 2m resolution (1,100 AGL flight altitude) from 2014 July 5 showing emissivity and Land Surface Temperature (LST). Emissivity is displayed with bands 10.1 µm as red, 9.2 µm as green, and 8.5 µm as blue. Other panels show the location of Huntington Gardens study area near Pasadena in San Marino, California, USA.*

*Table 3.1. Summary of plant species sampled in this study with associate sample sizes.*

| Plant Species | Acronym | Common Name | *N* for Nicolet | *N* for HyTES 2014 | *N* for HyTES 2016 |
|---|---|---|---|---|---|
| *Aloe arborescens* | ALAR | Candelabra Aloe | 3 | 23 | 24 |
| *Bambusa beecheyana* | BABE | Beechey Bamboo | 6 | 35 | 44 |
| *Bambusa tuldoides* | BATU | Punting Pole Bamboo | 3 | 42 | 44 |
| *Brachychiton discolor* | BRDI | Lacebark | 3 | 52 | 58 |
| *Brachychiton rupestris* | BRRU | Queensland Bottle | 3 | 37 | 53 |
| *Caesalpinia cacalaco* | CACA | Cascalote | 3 | 20 | 30 |
| *Cassia leptophylla* | CALE | Golden Medallion | 3 | 40 | 42 |
| *Cedrus deodara* | CEDE | Deodar Cedar | 3 | 43 | 53 |
| *Chorisia insignis* | CHIN | White Silk Floss | 3 | 34 | 36 |
| *Chorisia speciosa* | CHSP | Silk Floss | 3 | 40 | 45 |
| *Ficus columnaris* | FICO | Moreton Bay Fig | 3 | 32 | 38 |
| *Ficus thonningii* | FITH | Stranger Fig | 3 | 46 | 53 |
| *Jacaranda mimosifolia* | JAMI | Jacaranda | 3 | 30 | 34 |
| *Lagerstroemia indica* | LAIN | Crape Myrtle | 3 | 47 | 55 |
| *Magnolia grandiflora* | MAGR | Southern Magnolia | 3 | 39 | 46 |
| *Melaleuca linariifolia* | MELI | Snow-in-summer | 3 | 38 | 42 |
| *Peltophorum africanum* | PEAF | Weeping Wattle | 3 | 35 | 37 |
| *Podocarpus gracilior* | POGR | Fern Pine | 3 | 57 | 65 |
| *Quercus agrifolia* | QUAG | Coast Live Oak | 3 | 65 | 80 |
| *Quercus ilex* | QUIL | Holly Oak | 3 | 31 | 40 |
| *Quercus robur* | QURO | English Oak | 3 | 27 | 34 |
| *Quercus suber* | QUSU | Cork Oak | 3 | 24 | 25 |
| *Quercus virginiana* | QUVI | Southern Live Oak | 3 | 41 | 49 |
| *Salix babylonica* | SABA | Weeping Willow | 3 | 45 | 53 |
| *Tipuana tipu* | TITI | Tipu | 3 | 42 | 54 |

### *3.2.2 Leaf Measurements*

Fresh leaf samples were harvested in the field, and spectral measurements conducted in the lab. Samples were collected on February 2, October 3, and October 6, 2016. Samples were collected from tree species using pole clippers and from shrub species using pruning shears. Multiple leaves were collected from individual plants, with leaves randomly selected from the highest accessible part of the canopy. For taller individuals this means that sampled

leaves received full sun for part of the day, whereas leaf samples from shorter individuals were collected from the top of the canopy in full sun exposure. The leaves were wrapped in damp paper towels and placed in polyethylene bags to be stored in a cooler at ~10 °C with a towel to prevent direct contact with ice. In order to preserve the integrity of the samples, spectra were measured at the NASA JPL within 48 hours of collection.

Before spectral analysis, leaves were removed from polyethylene bags and excess moisture was wiped off. If a single leaf did not fill the lab spectrometer field of view, multiple leaves from the same individual were clustered while minimizing gap and overlap between leaves. Leaves were placed on aluminum foil to minimize background effects that may be present from gaps. A Nicolet 520FT-IR Spectrometer fitted with a Labsphere gold coated integrating sphere (model RSA N1 700D) was used to measure reflectance from 2.5 – 15.4 μm (Thermo Electron Corp., Madison, WI, USA). This sensor uses a single EverGlo infrared light source that has a bulb temperature of 1140 °C to output constant radiation. To reduce the impact of moisture in the air on the spectra, dry air was sent into the external sphere. Gold was measured once every hour and used as a standard to calibrate the Nicolet spectrometer. Distilled water was used to check the calibration and accuracy of reflectance products. The Nicolet spectrometer has a sampling interval of 0.001 μm, and each spectrum was determined from 300 scans, which took approximately three minutes to collect. Each plant sample was an average of three spectra, which were collected in one of two ways. First, a single set of leaves was measured and rotated three times. Second, three sets of different leaves from the same individual were measured.

Nicolet spectrometer spectra also underwent quality assurance through visual assessment and were averaged using code located at https://github.com/susanmeerdink/ASD-

Nicolet-Spectra-Processing. Measurements were used to calculate emissivity by using Kirchhoff's Law (ε=1−R), which in turn, enables comparisons to be made between the laboratory spectral measurements and HyTES emissivity images. The uncertainty associated with the Nicolet FT-IR emissivities is 0.002 (0.2 %) (Korb et al. 1999). Measurements were then convolved to HyTES bands using a Gaussian model with a 0.1 μm full width half max (FWHM) and HyTES band center wavelengths that ranged from 8.3 to 11.5 μm (Hook et al., 2013). Examples of leaf emissivities resampled to HyTES wavelengths are shown in Figure 3.2. All references to leaf emissivities in this paper are the resampled to HyTES wavelengths spectra.

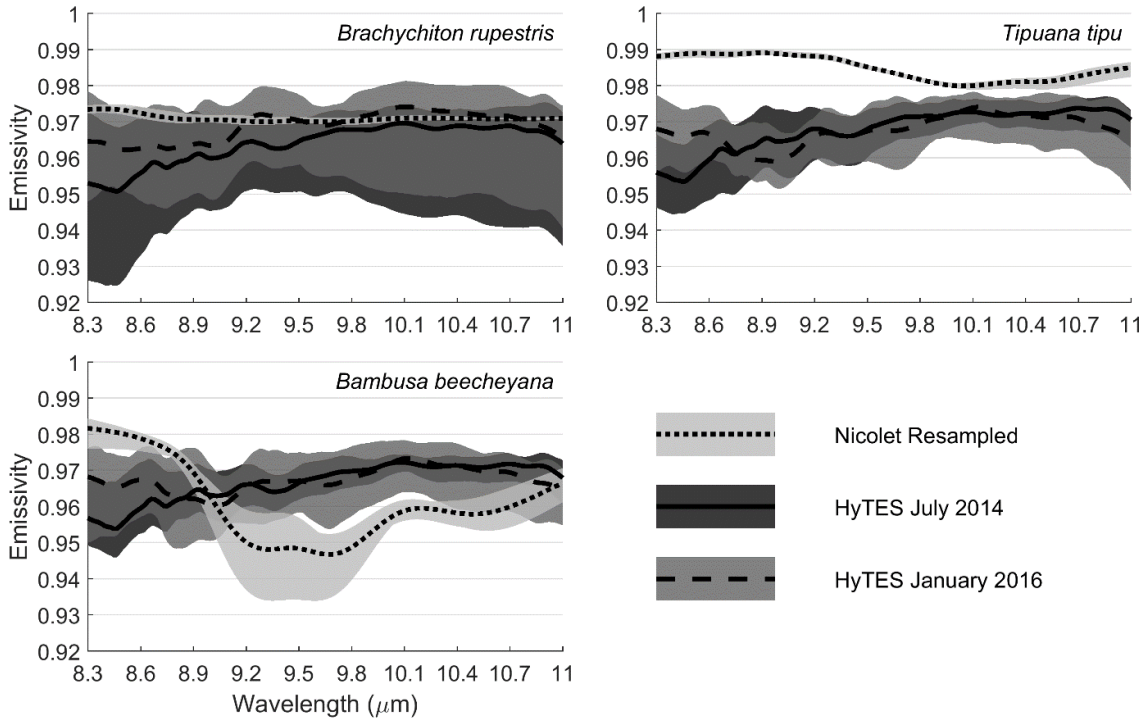


*Figure 3.2 Emissivities of three select species from three sources: Leaf emissivities resampled from Nicolet spectrometer, canopy emissivity from July 2014 HyTES imagery, and canopy emissivity from January 2016 HyTES imagery. Colored areas designate the minimum and maximum emissivity observed.*

*3.2.3 Canopy Measurements*

HyTES is a hyperspectral airborne sensor that measures radiance across 256 bands in the 7.5 - 12 μm spectral range (Hook, Johnson, & Abrams, 2013). The HyTES sensor was flown on the Twin Otter plane on two dates: July 5, 2014 and January 25, 2016 (Figure 3.1). The HyTES sensor can be flown at various altitudes above the ground surface that provides the flexibility to obtain data at different spatial resolutions. The 2014 flightline was flown at 17h42m UTC with a spatial resolution of 1.7 meters and the 2016 flightline was flown at 22h36m UTC with a spatial resolution of 1.9 meters. Air temperatures during flights were 31ºC and 22 ºC for July 2014 and January 2016, respectively. Examples of canopy emissivities from 2014 and 2016 are shown in Figure 3.2. Details of the HyTES L2 TES algorithm are available in an algorithm theoretical basis document (ATBD) and is available upon request. It should be noted that while HyTES has 256 bands, a surface emissivity cannot be retrieved from all of them since some bands are in regions with strong atmospheric absorption.

*3.2.4 Leaf to Canopy Scaling*

In order to evaluate the potential of scaling leaf emissivities to the canopy, a simple physical model was used to calculate apparent emissivities as adopted from Guoquan and Zhengzhi (1993). This model calculates apparent emissivity as a function of leaf emissivity, soil emissivity, leaf inclination, and leaf area index (LAI). The apparent emissivity ($\varepsilon_c$) of a vegetation canopy is determined using Kirchhoff's Law:

$$\varepsilon_c = 1 - A$$

Where the estimated canopy reflectance (*A)* and calculated as:

$$A = \left[\left(1 - \sqrt{\varepsilon_l}K^{-1}\right)\left(2\sqrt{\varepsilon_l}K^{-1} + \varepsilon_s - \varepsilon_s\sqrt{\varepsilon_l}\right)e^{LAI\sqrt{\varepsilon_l}K} - \left(1 + \sqrt{\varepsilon_l}K^{-1}\right)\left(-2\sqrt{\varepsilon_l}K^{-1} + \varepsilon_s + \varepsilon_s\sqrt{\varepsilon_l}K^{-1}\right)e^{-LAI\sqrt{\varepsilon_l}K}\right]/Y \quad (1)$$

This algorithm incorporates the influence of leaf inclination angle on apparent emissivity of a vegetation canopy by assuming a constant leaf angle:

$$K = [1 + (1 - \varepsilon_l)cos^2\theta_o]^{\frac{1}{2}} \quad (2)$$

The extinction and backscattering coefficients for diffuse flux are incorporated as:

$$Y = \left(1 + \sqrt{\varepsilon_l}K^{-1}\right)\left(2\sqrt{\varepsilon_l}K^{-1} + \varepsilon_s - \varepsilon_s\sqrt{\varepsilon_l}K^{-1}\right)e^{LAI\sqrt{\varepsilon_l}K} - \left(1 + \sqrt{\varepsilon_l}K^{-1}\right)\left(-2\sqrt{\varepsilon_l}K^{-1} + \varepsilon_s + \varepsilon_s\sqrt{\varepsilon_l}K^{-1}\right)e^{-LAI\sqrt{\varepsilon_l}K} \quad (3)$$

Where $\theta_o$ is the constant leaf inclination angle, *LAI* is the leaf area index, $\varepsilon_s$ is the substrate soil emissivity, and $\varepsilon_l$ is the leaf emissivity.

In our model calculations, resampled Nicolet spectra were used as leaf emissivities. For substrate soil emissivity, an Alfisol soil spectrum matching the soil type of the Huntington Gardens was selected from the ECOSTRESS spectral library, previously known as the ASTER spectral library (Baldridge et al., 2009; Meerdink et al., in prep). The soil spectrum was also resampled to HyTES wavelengths using the same method described in Section 2.2. LAI was not measured for these tree species, and a range of LAI values from 0.5 to 3 were tested (Figure B.1).

Leaf inclination angle distributions information for eight of the studied tree species (BRDI, BRRU, FICO, QUAG, QUIL, QURO, QUSU, SABA) were obtained either directly in the Huntington Gardens on December 9, 2012, or came from measurements carried in other locations including the University of California Botanical Garden, Berkeley, CA, USA (37.87° N, 122.24° W); the Botanical Gardens in Monaco (43.73° N, 7.424° E); Bergius

Botanical Garden, Stockholm, Sweden (59.37° N, 18.05° E); Castelporziano, Italy (41.71° N, 12.38° E), Kaisaniemi, Finland (60.17° N, 24.95° E); and Montado, Portugal (38.11° N, 8.576° W).

The leaf inclination angles were measured using the leveled digital camera method introduced by Ryu et al. (2010). A series of images were taken of the tree crowns in windless conditions; the images were visually inspected for the presence of leaves with their surfaces oriented perpendicularly to the viewing direction of the digital camera and the leaf inclination angles were measured manually from such images (see Raabe et al. (2015) for details). Approximately 100 leaves were measured for each species – a sufficient amount to determine leaf angle distribution at the whole crown level (Pisek et al., 2013).

*3.2.5 Spectral Analysis*

Mann-Whitney U Test (MWU), also known as the Wilcoxon Test, was used to determine significant differences in species pairs because the distributions of emissivities were non-parametric. MWU is performed at each wavelength comparing species pairs, emissivities and is summarized in two ways: per wavelength and per species pair. For each wavelength, we report the total number of species pairs that were significantly different from a single species' emissivity distribution. This identifies wavelengths where a species is significantly unique from the 23 other species analyzed. For each species pair, we report the total number of wavelengths that are significantly different. This identifies which species are more spectrally similar or dissimilar from each other. In addition, species separability was tested using spectral angle mapper (SAM) which calculates the spectral angle between two spectral vectors that have a common origin (Kruse et al., 1993). SAM measures differences in spectral shape across all wavelengths, while MWU measures differences in emissivity at a

single wavelength. The statistical difference in species LST distributions was analyzed using ANOVA.

*3.2.6 LiDAR Imagery*

Light Detection and Ranging (LiDAR) terrain data were collected over the Huntington Gardens in 2014 through the Los Angeles Region Imagery Acquisition Consortium (LARIAC4; *LARIAC Product Guide 2006-07*, 2006). The spatial resolution is 10.2 cm with vertical accuracy of 27.7 cm at a 95% confidence level. Multiple LiDAR products were used to derived canopy structural attributes and properties (Table 3.2). Polygons of individual trees, described in Section 2.1, were used to extract tree height statistics, including mean, maximum, minimum, standard deviation, and range of heights. These polygons were also used to extract the total number of returns for a tree canopy and calculate tree canopy size. To determine a tree's neighbors, the LARIAC4 land cover classification product was used. This product has an overall accuracy of 97.86% with seven land cover classes, including tree, grass/shrub, bare soil, water, buildings, roads/railroads, and other pavement. The water and building classes were not included because <2% of trees had these classes as neighbors. A 5-meter buffer around tree individuals was used to extract the surrounding land cover pixels to determine tree neighbors. Information derived from the LiDAR products was summarized for each individual and correlated with mean, maximum, and minimum canopy LSTs.

*Table 3.2. Descriptive and statistical metrics extracted from the LiDAR data.*

| | Variable Name | Variable Description |
|---|---|---|
| Height Above Ground | Mean | Mean height above ground for a tree canopy |
| | Min | Minimum height above ground for a tree canopy |
| | Max | Maximum height above ground for a tree canopy |
| | Std | Standard deviation of height above ground for a tree canopy |
| | Range | Range of heights above ground for a tree canopy |
| Neighbors | Other Trees | Number of pixels classified as trees within 5m buffer of tree canopy |
| | Grass/Shrub | Number of pixels classified as grass/shrub within 5m buffer of tree canopy |
| | Bare Soil | Number of pixels classified as bare soil within 5m buffer of tree canopy |
| | Roads | Number of pixels classified as roads within 5m buffer of tree canopy |
| | Other Pavement | Number of pixels classified as other pavement within 5m buffer of tree canopy |
| Other | Tree Size | Tree canopy size ($m^2$) |
| | Num. of Returns | The total number of returns for a tree canopy |

## 3.3 Results

### *3.3.1 Leaf emissivity*

Spectral angles identified separability between the plant species pairs for leaf emissivities based on spectral shape (Figure 3.3a). Among the most spectrally distinct were two species from the *Bambusa* family (BABE and BATU), which are known to have strong silica content expressed as a strong absorption feature. Other notable species that were distinct with spectral angles above 0.1 radians included QURO and FITH. However, most species pairs had relatively small spectral angles even at the leaf level demonstrating that spectral shapes between species are too similar for separability.

While spectral angle determines separability based on spectral shape, Mann-Whitney-U (MWU) tests determine separability based on the number of wavelengths containing significantly different emissivities. For MWU tests, the majority of species pairs had more

than 75% of wavelengths exhibit significantly different emissivities (Figure 3.4a). Among the most spectrally distinct species were CEDE, PEAF, POGR, and TITI. This analysis also can determine which species might be spectrally confused with each other. For example, POGR was spectrally distinct from most species, but not from PEAF and QUIL. Other species, such as ALAR and CEDE, were not spectrally distinct from most, but compared to a single species had > 75% significantly different wavelengths.

Another aspect of MWU analysis is the ability to determine which wavelengths contain the largest discriminating power for plant species (Figure 3.5a*;* Figure B.2. – B.5). At the leaf level, the 24 species are categorized into three groups: a) species that were different spectrally from 8.3 – 11.5 µm; b) species that were spectrally different for a subset of wavelengths; or c) species that were not spectrally distinct. There were three species (CEDE, POGR, TITI) that were spectrally distinct from other species across the measured TIR spectrum. Eight species (BABE, BATU, BRRU, CALE, FICO, FITH, MAGR, and PEAF) had portions of their emissivities that were distinct from other species. For example, BABE was similar to 20% of the species pairs in the 4 – 6 µm range, but was similar to 80% of the species pairs between 8 – 10 µm. However, the majority of species fell into the final category where their emissivities were not spectrally distinct in the 2.5 – 11.5 µm range. These species, such as SABA and ALAR, had emissivities that were the least separable with only 10 - 20% significant pairs.

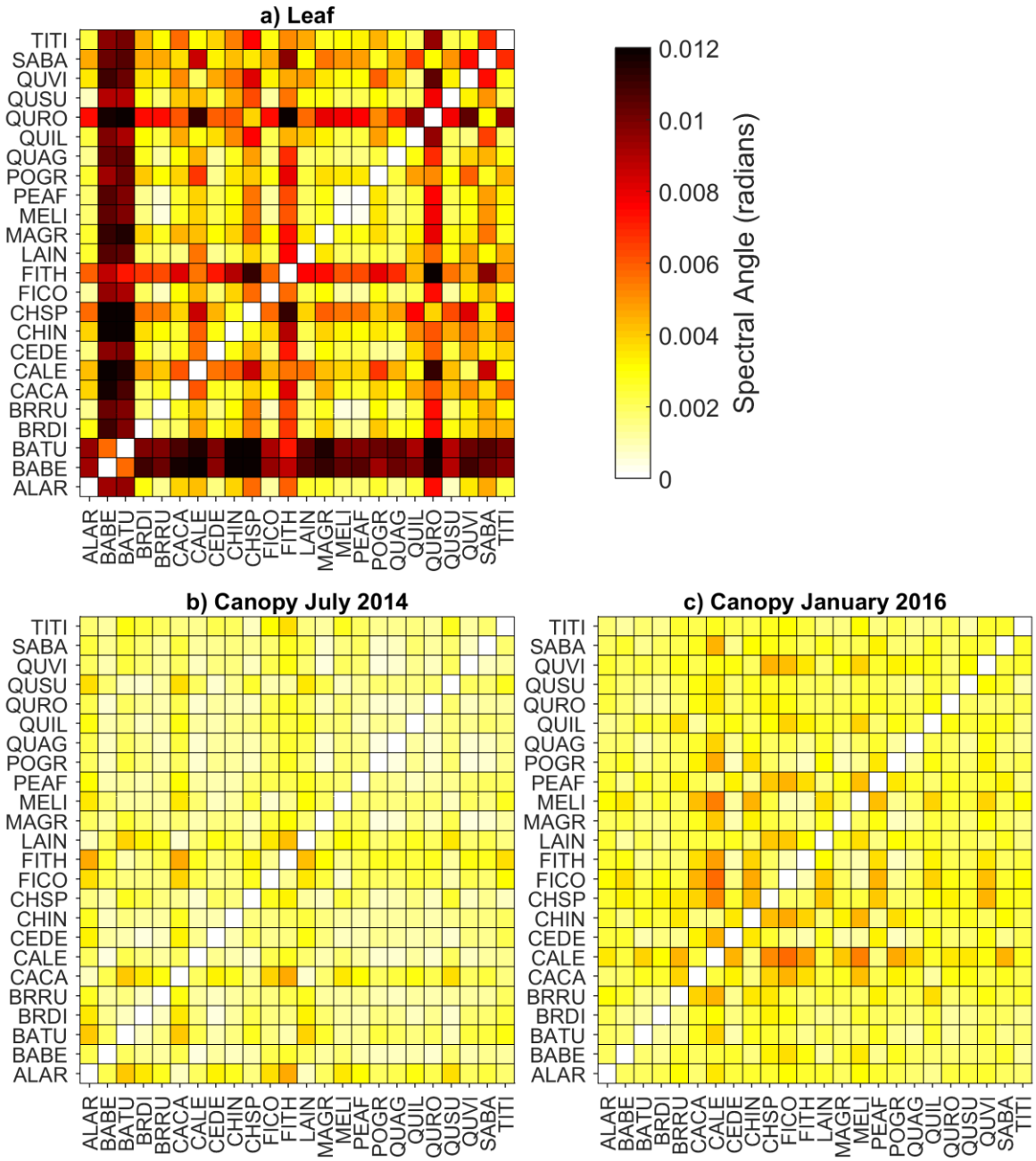


*Figure 3.3. The spectral angle between species for emissivities collected from (a) leaf, (b) leaf resampled to HyTES wavelengths, (c) canopy July 2014, and (d) canopy January 2016 imagery.*

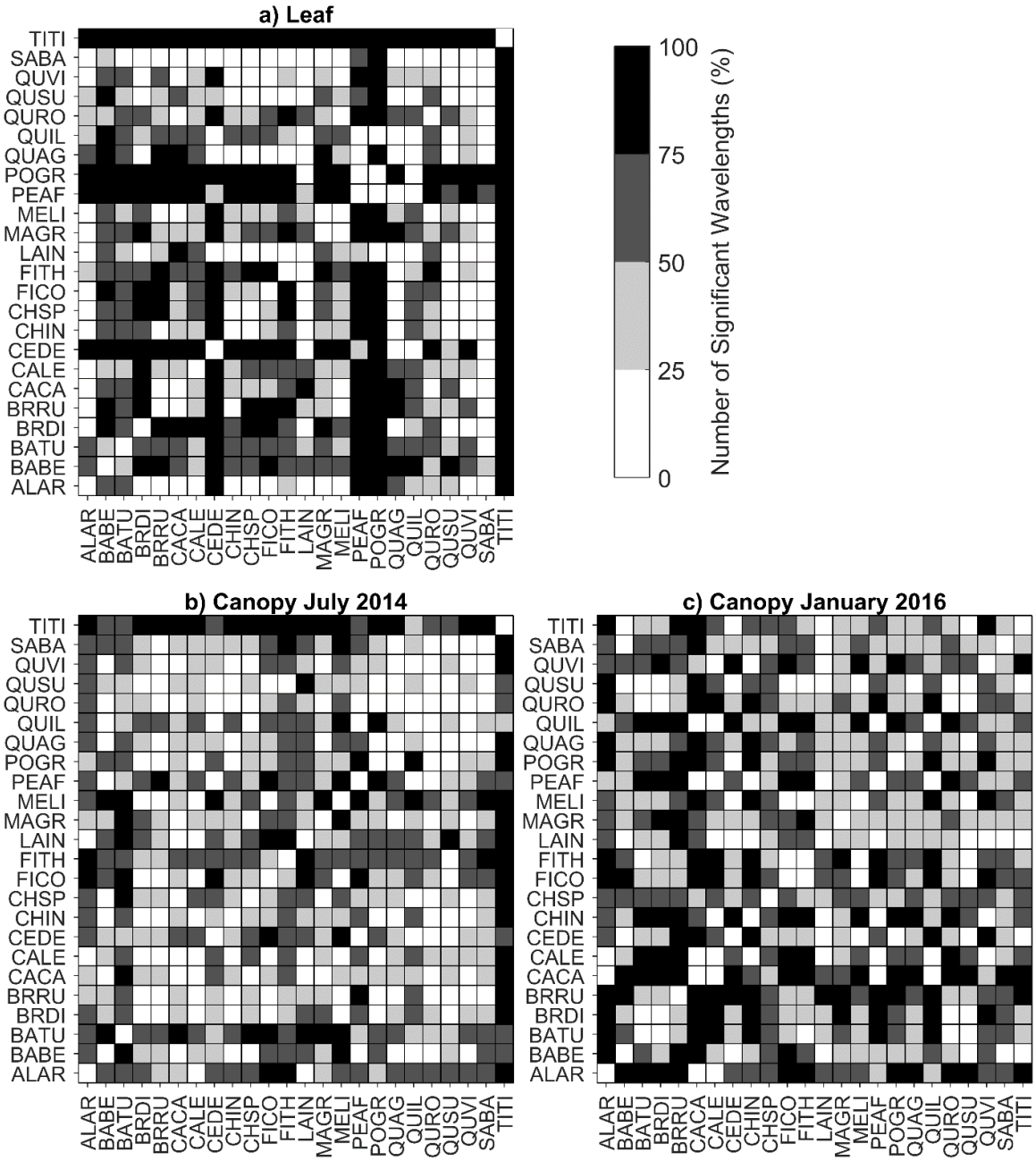


*Figure 3.4. The percent of wavelengths that are significant different ($p < 0.05$) between species pair for (a) leaf emissivity, (b) canopy July 2014 emissivity, and (c) canopy January 2016 emissivity.*

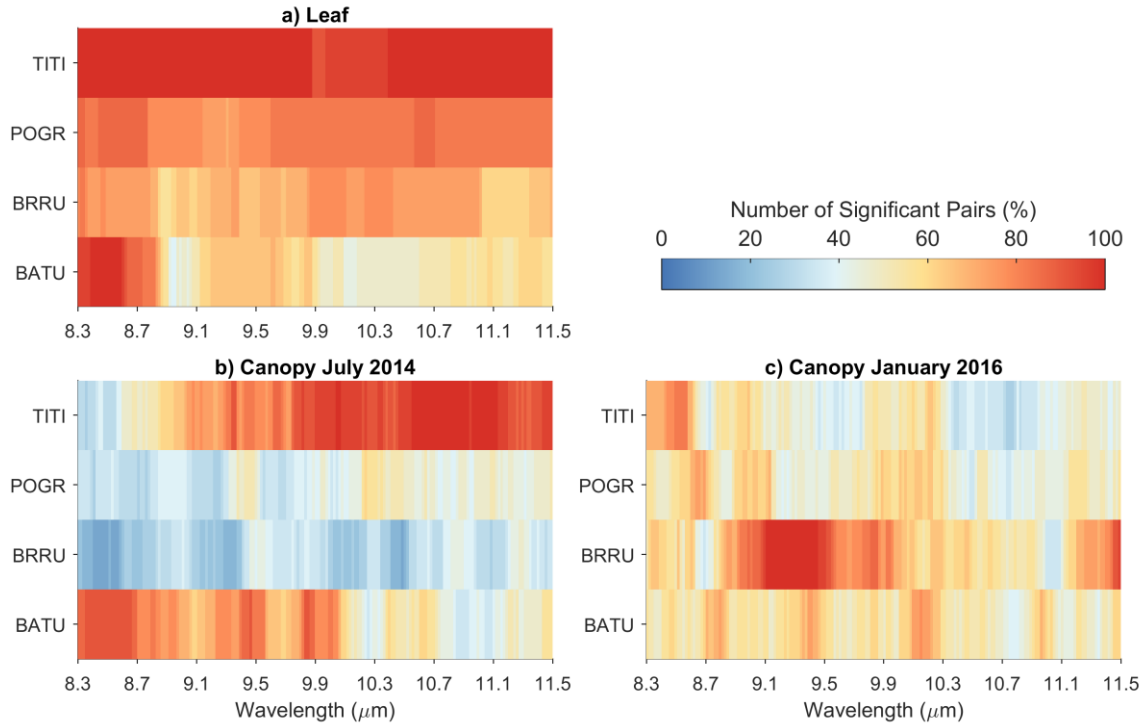


*Figure 3.5. The percent of significantly different pairs at each wavelength identified by Mann Whitney U (MWU) tests for plant species emissivities from the (a) leaf, (b) canopy July 2014, and (c) canopy January 2016. For other species' significant wavelengths, see Figure B.2 – B.5.*

### *3.3.2 Canopy emissivity*

Separability of species based on spectral shape was very low for both of the canopy emissivity dates compared to leaf emissivities (Figure 3.3b & c). Spectral angles showed that January 2016 canopy emissivities had slightly more separation between species, but separability was marginal. For both dates, spectral angles between species pairs were consistently low, with only a couple of species in 2016 (CALE and PEAF) showing more separability with higher spectral angles across dates. The smaller spectral angles observed for

canopy emissivities compared to leaf emissivities demonstrate that the spectral variability among species observed at the leaf scale did not translate to the canopy.

Analyzing the number of wavelengths that were significantly different between species pairs reveals a similar pattern at the canopy level (Figure 3.4b & c). Compared to leaf spectra, both dates had a higher number of species pairs with only 0 –50% of wavelengths being significantly different. While leaf emissivities only had 129 pairs in this low distinguishability category, July 2014 had 170 pairs and January 2016 had 145 pairs emphasizing that many species became more spectrally similar when scaled to the canopy. This analysis also highlights seasonality differences when separating species spectrally. In general, canopy emissivities were more spectrally distinct in January 2016 than July 2014. Some species pairs, such as ALAR and TITI, remained spectrally distinct from each other over the two time periods while most experienced changes in separability strength.

Similar to leaf emissivities, species exhibited different sets of influential wavelengths at the canopy level which shifted between the two image dates (Figure 3.5b & c). However, unlike leaf emissivities, no species were spectrally distinct for the entire 8.3 – 11.5 µm range. The majority of the 24 species for both dates were not spectrally distinct in any portion of the electromagnetic spectrum. There were nine species in July 2014 and five species in January 2016 that were spectrally distinct in a subset of the measured TIR spectrum. These were not the same species for each date due to seasonality differences in emissivity. For example, TITI was spectrally distinct compared to other species from 10 – 11.5 µm in July 2014 while in January 2016 most of that spectrally separability was lost.

*3.3.3 Comparison of leaf and canopy emissivities*

As previously mentioned, laboratory leaf emissivities were significantly different from canopy emissivities for most wavelengths of the 24 species in July 2014 and January 2016 (Figure 3.6). In general, species' emissivities at the leaf and canopy were least similar between 9.9 – 10.5 µm. Across 8.3 – 11.5 µm, at least 12 of the 24 species were significantly different between leaf and canopy emissivities. These 12 species had canopy attributes that are known to decrease the ability to retain leaf spectral information at the canopy. One of those species, TITI, commonly has an open canopy which will increase the influence of substrate in canopy emissivity. BABE has canopies composed of diverse leaf orientations which retain less spectral information due to multiple scattering that occurs in canopies. However, there were some species with canopy emissivities more similar to measured leaf emissivities. For example, CHIN and CHSP had 73% of wavelengths that were spectrally similar between the two levels. These two species were broadleaf planophile trees, which are able to retain leaf spectral information due to favorable geometries. Leaf emissivities for these species might be representative of canopy emissivities for portions of the TIR. However, for most species, leaf emissivities were not representative of canopy emissivities. Leaf level could not be directly translated to canopies without additional scaling algorithms.

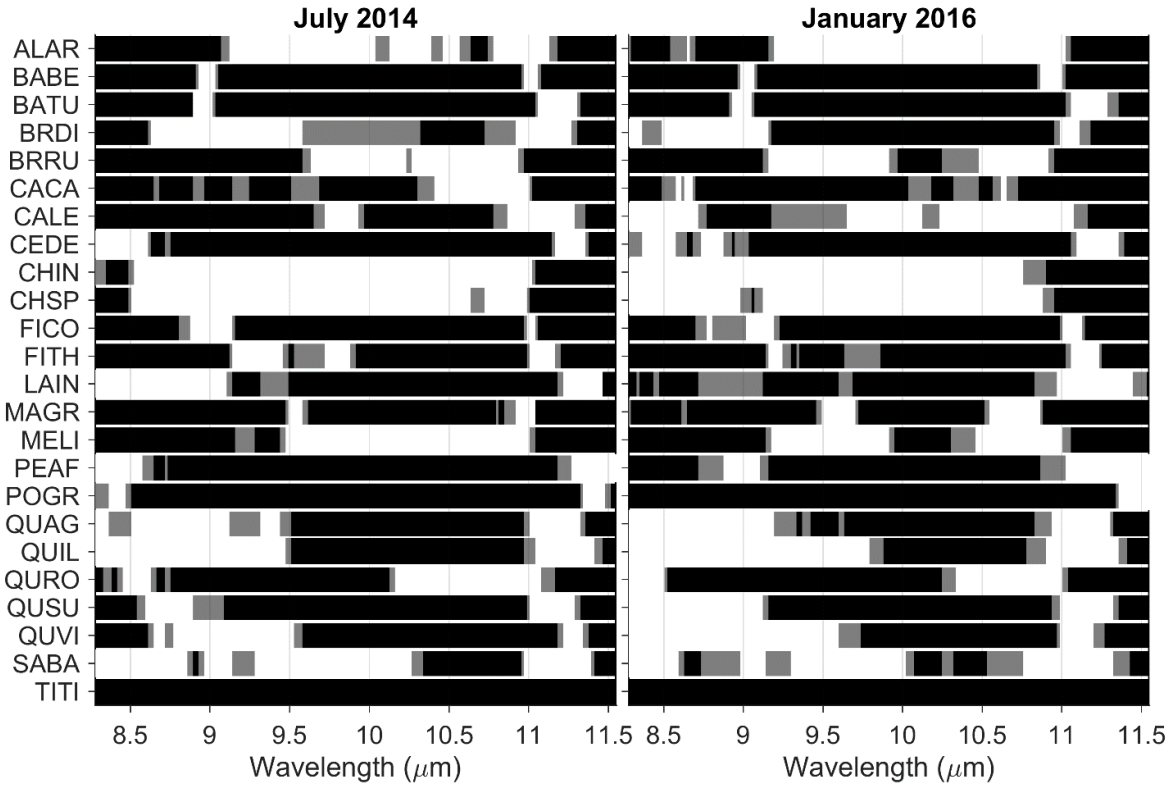


*Figure 3.6 Wavelengths that were significantly different between leaf emissivities and canopy emissivities from 2014 (left) and 2016 (right). Gray designates wavelengths at significance of $p < 0.05$ and black designates significance at $p < 0.01$.*

To scale leaf emissivities to the canopy, a simple physical model was used to calculate apparent emissivity for eight species (Figure 3.7). As leaf emissivities are scaled to the canopy, multiple scattering emissions fill in any spectral features and cause a general increase in canopy level emissivity similar to a graybody. Some species, such as SABA and QURO, retain spectral features, although features become subtler. Other species, such as BRRU and QUSU, became gray bodies with no spectral features. HyTES emissivities collected from July 2014 and January 2016 imagery have lower emissivity compared to modelled apparent emissivity and in many cases did not match the modelled spectrum shape.

A simple model using leaf area index (LAI), emissivities of leaf and soil, and leaf inclination angle is not sufficient for the calculation of canopy emissivities.

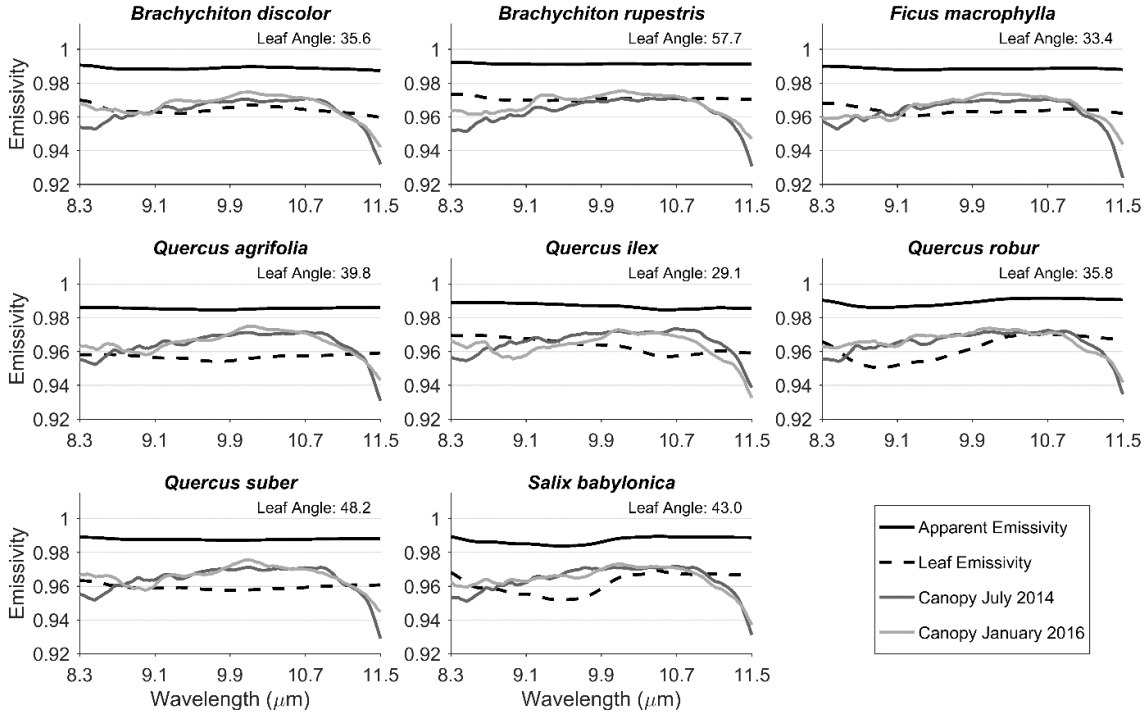


*Figure 3.7 Comparison of apparent emissivity (using LAI 3.0), leaf emissivity, and canopy emissivity from 2014 and 2016 HyTES imagery for eight selected species.*

### *3.3.4 Canopy LST*

Canopy LST distributions for species in July 2014 and January 2016 HyTES imagery were very different (Figure 3.8). As expected, due to warmer air conditions, July 2014 had a higher range of observed LSTs compared to January 2016. When comparing species distributions between the two dates 20 out of 24 species had significantly different distributions. Comparing species pairs, LST distributions also revealed significant differences between dates (Figure 3.9). In 2014, 48 more species pairs were significantly different compared to 2016 data. In 2014, five species (ALAR, FICO, FITH, MELI, PEAF)

were very distinct from the other nineteen species. In contrast, 2016 had only two species (CHSP and SABA) that were very distinct from the other species. Species with similar canopy architecture did not have significantly different LST distributions, such as two bamboo species (BABE and BATU) with uniform canopies and the two Ficus species (FICO and FITH) with closed dense canopies.

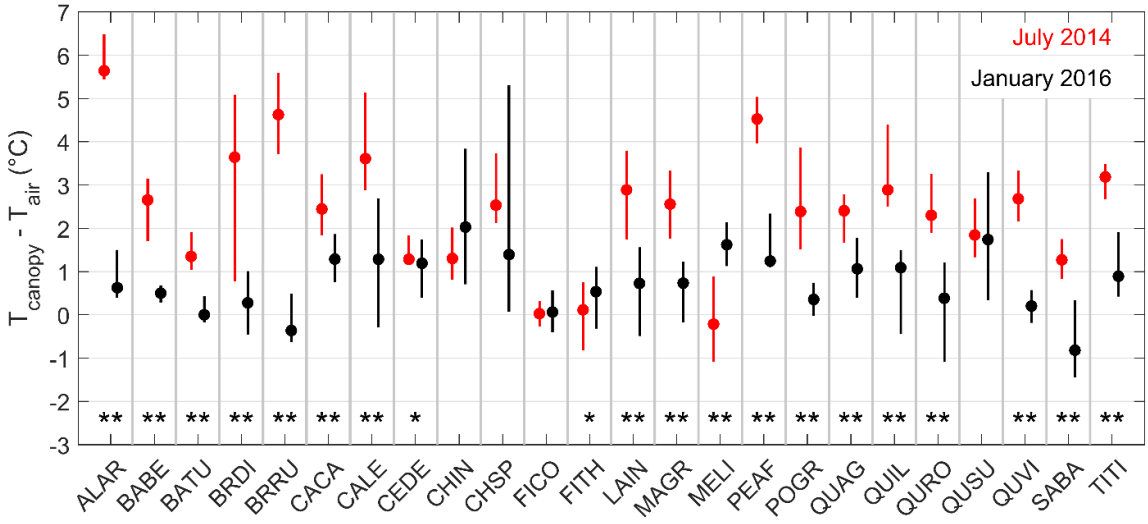


*Figure 3.8. 2014 and 2016 canopy LST distributions (canopy LST minus air temperature) for each species. Circles are median LSTs with the top and bottom of bars marking the 25$^{th}$ and 75$^{th}$ quartiles. Asterisks designates significant differences between 2014 and 2016 LST distributions (* $p < 0.05$, ** $p < 0.01$).*

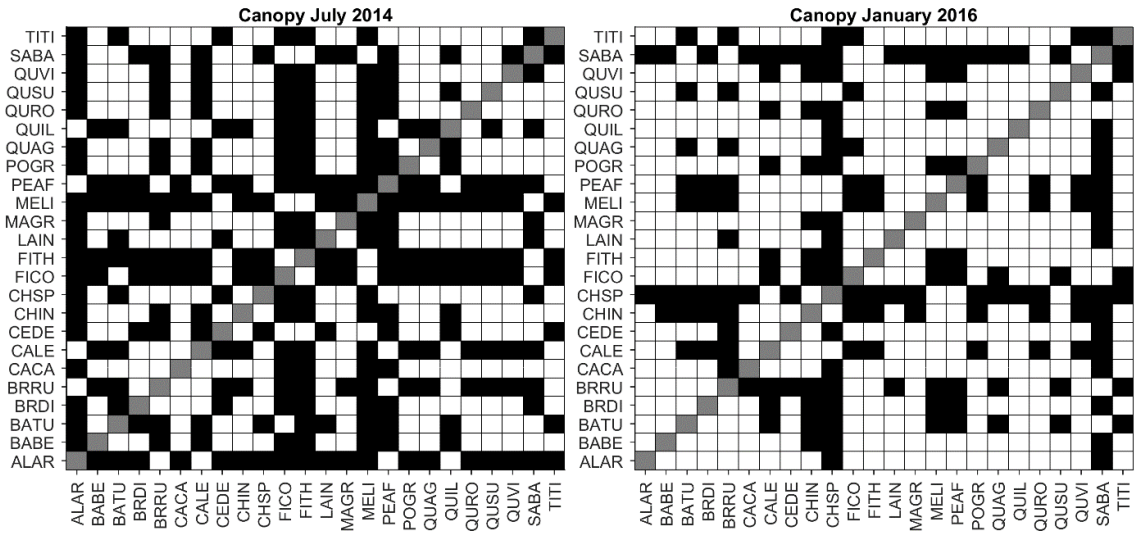


*Figure 3.9. LST comparison between species pairs for 2014 (left) and 2016 (right) imagery. Black squares designate significant differences between species LST distributions ($p < 0.05$).*

Variables derived from the LiDAR dataset were found to correlate strongly with LST distributions in 2014 and 2016 (Figure 3.10). A tree's neighbors within a 5 m radius were strongly correlated with the tree's canopy LST. Specifically, the presence of pavement in the neighborhood resulted in higher canopy LSTs because of the sensible heat release from dark asphalt pavements. However, if the tree was surrounded by other trees the canopy LST was lower, presumably due to the increase in latent heat flux. In July 2014, increased presence of grass/shrub, bare soil, and roads as neighbors were correlated with higher canopy LSTs. However, this correlation was not present in January 2016, which was flown in cooler ambient temperatures. Tree height was found to be significantly negatively correlated with 2014 and 2016 LSTs. As the only shrub in this study, ALAR's LSTs were measured from multiple individuals that formed a large aloe patch on the side of a hill. Due to the architecture and height of these plants, ALAR had the highest LST for July 2014 compared

to other species. FICO, the tallest species in this study, experienced LST values that did not vary much from air temperatures on either date.

Canopy density, as measured by the number of LiDAR returns, was also found to impact canopy LSTs, but more so in warm ambient air conditions. Dense, closed canopies (e.g. FICO, BABE, and BATU) had cooler LSTs and a smaller range of LST, even on the hot 2014 July day. Low density canopies have a larger substrate influence and experienced higher LSTs, especially if the substrate was man-made and ambient conditions were warm. Species with open tree canopies had warmer LSTs and experienced a larger range of LSTs, mainly caused by the influence of the substrate below the canopy. For example, in January CHSP and CHIN species had dropped their leaves for the season exposing the substrate beneath. In July, CHSP and CHIN had a closed canopy and LST distributions were not significantly different from most species.

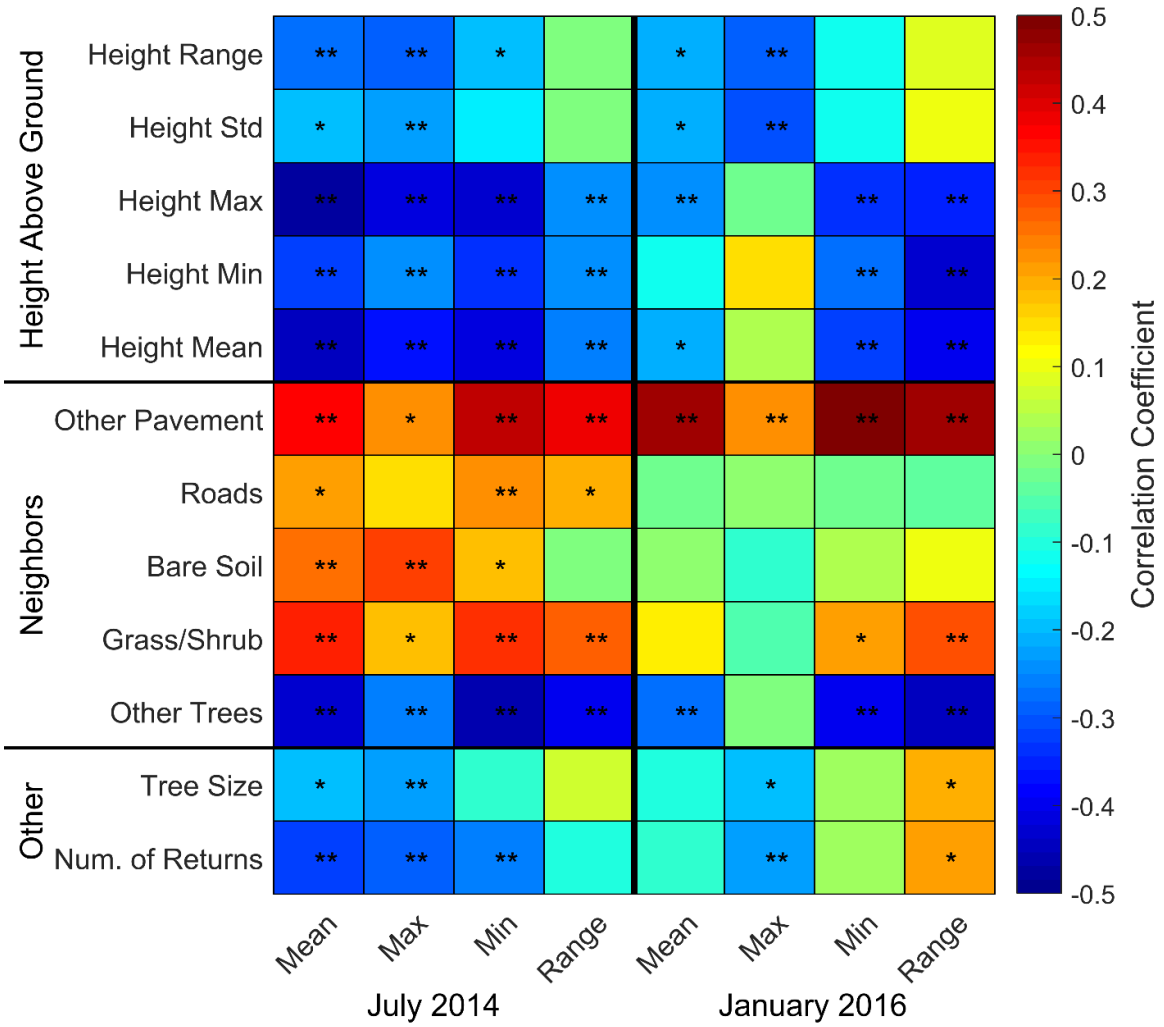


*Figure 3.10. Correlations between 2014 and 2016 LST statistics (x-axis) and LiDAR derived variables (y-axis). Asterisks designate significant differences in correlations (* $p < 0.05$, ** $p < 0.01$).*

## 3.4 Discussion

### *3.4.1 Plant species' leaf emissivity variability*

In this study, we quantified the spectral separability of plant species' leaf level emissivities. We found that leaf emissivities were unique for approximately one third of the 24 plant species analyzed in this study. This remained true even when leaf emissivities were

resampled from over 177 wavelengths to HyTES's 155 wavelengths between 8 – 11 µm. Thirty out of 276 species pairs were separable based on spectral shape, while 91 species pairs were separable based on the total number of wavelengths that were significantly different. Our results show that some plant species exhibit unique spectral features at the leaf level that distinguishes them spectrally. However, not all species in this study were spectrally unique. In contrast, other researchers have found that most of the species they studied are spectrally separable. Using 13 common garden species in the Netherlands, Ullah et al. (2012a) found that 76 out of 78 species pairs had significantly different Jefferies Matusita distances. In a direct comparison to the previous study, Rock et al. (2016) classified eight species with 92% overall accuracy but stipulated high signal-to-noise ratio was necessary. Another study successfully classified 19 species with a kappa of 0.94 (Buitrago et al., 2018). However, there are a few studies that also found confusion between species. In a study mirroring results similar to ours, Harrison et al. (2018) classified 26 tropical species and found most species were spectrally similar with the exception of five. Lastly, a study classified 32 species at the canopy with an overall accuracy of only 83%, but also found that leaf emissivities contained more spectral separability then the canopy (Ribeiro da Luz, 2006).

When discussing the separability of plant species in the TIR, it is common to identify wavelengths that contain the most discriminating power. The largest discriminating power among species was found at the 2.5 – 8 µm wavelengths, which has been identified for containing key information for species discrimination or leaf trait retrieval (Buitrago Acevedo et al., 2017; Buitrago et al., 2018, 2016; Meerdink et al., 2016). However, HyTES does not measure between 2.5 – 8 µm because this region is complicated due to the long wavelength edge of the solar radiation curve, strong water vapor absorption, and the short

wavelength edge of the terrestrial emittance curve (Gates et al., 1965). The range of emissivities retrieved from HyTES in the atmospheric window region (8 – 11 μm) did not contain as much spectral discrimination for species in our study. As in other studies, plant species tend to be featureless in this region with weaker absorption features (Elvidge, 1988). In the HyTES measured TIR spectrum, our study identified key wavelengths at 8.5, 10.04, and 11.2 μm, which are related to known features of water absorption and cellulose (Elvidge, 1988). While we did not relate leaf emissivities to leaf traits, other studies suggest that leaf traits expressed in the TIR promote species identification at the leaf level and potentially at the canopy (Riberio da Luz and Crowley, 2010).

*3.4.2 Plant species' canopy emissivity variability*

We found, for the same set of species, that canopy emissivity for July 2014 and January 2016 HyTES imagery does not contain the magnitude of separability among species as seen at the leaf level. No species showed clear separability based on spectral shape and only 29 and 54 out of 276 species pairs had more than 80% of wavelengths significantly different for July 2014 and January 2016, respectively. When determining influential wavelengths for species discrimination, ten out of 24 species had regions of the TIR that were significantly different. Species had more variability within species than between which easily confused species discrimination. Although images were collected in different seasons and years, the canopy emissivities showed limited variation for evergreen species.

Very few studies have examined canopy spectral emissivity, mainly due to the lack of data at desired spectral and spatial resolutions. In controlled laboratory settings, canopy emissivities have been found to be significantly different for four species and that increases in LAI correspond to increases in emissivity (Neinavaz et al., 2016a). Also in laboratory

settings, stress studies have found that increasing water stress causes emissivity to increase due to blackbody cavity effects (Buitrago et al., 2016; Gerhards et al., 2016). While these studies demonstrate opportunities for canopy emissivity, they have been restricted to fine spatial resolution imagery collected in controlled settings. Only one study, to our knowledge, has examined canopy emissivity characteristics collected using airborne imagery. Ribeiro Da Luz and Crowley (2010) successfully classified approximately 25 species using 1 m spatial resolution imagery from the SEBASS sensor. However, this was only half of the species studied, with the remainder not being spectrally separable.

*3.4.2 Scaling emissivities from leaf to canopy*

We scaled leaf emissivities using a simple physical model to determine if the inclusion of leaf area index, emissivities of leaf and soil, and leaf normal inclination angle would result in representative canopy emissivities. We found that the calculated apparent emissivities were not representative of canopy emissivities even with compensating for LAI and inclination angle. This may be related to the fact that the leaf inclination angles were partly measured in different locations and at different times compared to the emissivity measurements. It has been previously shown that, depending on the species, leaf inclination angles can vary strongly with season and exposure to light (Raabe et al., 2015). Direct measurements from the same site and for the same date with the airborne observations would be more reliable and might provide a more accurate representation of the canopy structure.

It is not surprising that canopy emissivities do not reflect the same spectral features as leaf emissivities, because the same problem presents itself in other regions of the electromagnetic spectrum. In the visible-shortwave infrared spectrum, leaf spectra deviate from canopy spectra due to the influence of canopy structure, the presence of non-

photosynthetic vegetation, background substrate, and multiple scattering within the canopy (Asner and Martin, 2008; Ollinger, 2011; Roberts et al., 2004; Verhoef, 1984). In the TIR domain, scaling is complicated due to several factors that weaken already subtle plant features including canopy voids, leaf angle, canopy structure, and errors in temperature emissivity separation (Ribeiro Da Luz and Crowley, 2010, 2007; Salisbury, 1986). Ribeiro Da Luz and Crowley (2007) confirmed the complication of scaling when taking measurements from a field of view of 6.4 cm to 44 cm and experienced progressive attenuation of the spectral emissivity features. Ribeiro Da Luz and Crowley (2010) found that canopy geometry and composition including leaf morphology, leaf disposition (e.g. planophile or erectophile), canopy closure, and size of canopy were the largest controlling factors. Radiative transfer models could be used to account for the scattering and absorption of radiation inside canopies when scaling (Francois et al., 1997; Jacob et al., 2017; Olioso, 1995; Snyder and Wan, 1998; Verhoef et al., 2007). These models incorporate additional variables including directional gap fraction, angular cavity effect coefficients, and better incorporation of soil contribution. Without the use of radiative transfer models, relationships developed using leaf emissivities will not be directly translatable to the canopy for future airborne or spaceborne missions.

*3.4.3 Land surface temperature (LST) pattern among species*

Finally, temperature patterns across species were significantly different between the July 2014 and January 2016 HyTES imagery, corresponding to ambient air temperatures that were 31 ºC and 22 ºC respectively. In the warmer ambient air conditions experienced in July 2014 imagery, species' LST distributions were found to be significantly different in 129 out of 276 species pairs. In cooler ambient air conditions, only 81 species pairs were significantly

different. Other studies have also found species-specific differences in LST distributions. For example, Leuzinger et al. (2010) found that small leafed trees were cooler than large leaf trees while Meier and Scherer (2012) showed that deciduous trees had higher LST variation in the canopy compared to conifers. Urban tree canopy LSTs depend on species-specific properties and the location of the tree (Leuzinger and Körner, 2007; Meier and Scherer, 2012).

We found that LST distributions were highly correlated with a tree's neighboring pixel land cover type. Other trees and pavement as neighbors had the highest influence on canopy LSTs. This corresponds to a study that found that substrate can impact the tree temperature where grass is cooler than a sealed surface like asphalt or concrete (Kjelgren and Montague, 1998; Leuzinger et al., 2010; Montague and Kjelgren, 2004). In our study, the added complexity of a tree's architecture and tree height were negatively correlated with LST. In our study site and a mixed deciduous forest in NW Switzerland, open canopies exhibited mean canopy leaf temperatures close to air temperature and dense canopies exhibited warmer than air temperatures (Leuzinger and Körner, 2007).

*3.4.4 Considerations*

This study explored the application of HyTES imagery for plant species' emissivity and LST research. Our findings expose the limitations to be considered for future research. In this study, leaf samples were not collected at the same time as the imagery, so differences between leaf and canopy might be related to phenology differences. The stability of leaf emissivities over the season and years has not been studied, so it cannot be said how influential phenology is on emissivity. Additionally, we had a small sample size for leaf measurements due to time constraints and the number of individuals available in the

Huntington Gardens. A more comprehensive and systematic sampling is required to fully study the scaling of leaf emissivities to canopies, including the measurement of tree characteristics such as leaf area index. Additionally, errors may be present in canopy emissivity and LST products. These products are calculated through an iterative Temperature Emissivity Separation (TES) algorithm developed by NASA JPL, which has been adapted to HyTES's 256 radiance bands. However, due to the relatively new deployment of this sensor, the algorithm is undergoing refinement to improve atmospheric correction accuracy, especially as new applications are presented that require emissivity retrievals with high accuracy.

While our study found that species classification using TIR is difficult at the canopy level, this study does present opportunities for a mission recently deployed. In June 2018, the ECOsystem Spaceborne Thermal Radiometer Experiment on Space Station (ECOSTRESS) was launched with the primary goal of measuring plant temperatures in order to understand how much water plants need and how they respond to stress. The sensor was installed on the International Space Station providing data with a 38-m in-track by 69-m cross-track spatial resolution, five spectral bands in the 8 – 12.5 μm range, and a predicted temperature sensitivity of ≤0.1 K (Lee et al., 2015). This study directly supports future ECOSTRESS research questions for vegetation emissivity and LST. For example, the ECOSTRESS mission will be delivering an evapotranspiration product for the continental USA and over key biomes around the world. A key assumption of the evapotranspiration models requires that vegetation emissivity does not vary by species. This analysis gives insight into the amount of error introduced into models that calculate evapotranspiration.

### 3.5 Conclusions

The development of NASA's HyTES hyperspectral thermal sensor has opened up the possibility of using high spectral resolution emissivity and fine spatial resolution LST for vegetation research. In this study we set out to answer four questions. First, we asked if plant species were spectrally separable using leaf level emissivities. We found that 20 out of 24 plant species were spectrally separable through spectral shape or the number of wavelengths containing significantly different emissivities. Second, we asked if this species variability extended to canopy emissivities collected from July 2014 and January 2016 HyTES imagery. We found that plant species lost most of the spectral separability seen at the leaf level when scaled to canopy emissivities. Third, we asked what were the capabilities of scaling leaf emissivities to canopy emissivities to support relationships developed at leaf levels. We found that using a simple scaling algorithm that incorporates LAI, leaf inclination, and soil emissivity does not accurately scale leaf emissivities to the canopy. Finally, we asked what LST patterns do plant species exhibit across dates and how does the variability relate to canopy attributes. We found that species' canopy LSTs displayed unique distributions across dates and among species. Many of these distributions could be explained by canopy geometry, with tree density and height playing key roles. Additionally, species canopy temperatures were highly influenced by a tree's surrounding environment, with neighboring trees creating cooler LST and pavement creating warmer LST conditions.

Our study fills in knowledge gaps in the TIR domain for both emissivity and LST. Previously, only one study has examined plant species using high spectral resolution airborne TIR imagery. Our results demonstrate that only a few spectrally distinct species in the Huntington Gardens were separable at the canopy and that leaf level relationships derived

empirically in the lab will not directly translate to the canopy. Most of the unique spectral characteristics measured in laboratory conditions are not retained at the canopy due to multiple scattering which involves emission, reflection, and absorption. However, the HyTES fine spatial resolution LST imagery has provided a deeper understanding of LST variability across plant species which exhibit different canopy attributes. LST is primarily used to measure plant stress, but we found that plant species still exhibit variability in temperature distributions even in ideal water conditions.

With the launch of the ECOSTRESS mission and continued image collection of HyTES, more TIR imagery will become available to the scientific community. This study begins to explore the application of such a dataset for the purposes of vegetation research, specifically how much variability there is among plant species. As research expands in the TIR domain, our understanding of plants' variability in TIR spectral signatures and LST will become increasingly important. Advancing this research for vegetation canopies may enable new types of remote sensing observations that are distinct from other portions of the electromagnetic spectrum.

# 4. Monitoring water stress of Southern California plant species during the 2013 – 2015 drought


## Abstract

From 2012 to 2015, California experienced the most severe drought conditions since 1895 causing natural vegetation throughout the state to become water stressed. With many areas in California being inaccessible and extremely rugged terrain, remote sensing provides a means for monitoring plant stress across a large landscape. Airborne hyperspectral and thermal imaging captured the drought in the spring, summer, and fall of 2013 – 2015 across 11,640 $km^2$ of Southern California. This study provides a large scale analysis of plant species' annual and seasonal temperature variability throughout a prolonged drought. We developed a species specific Temperature Condition Index (TCI) that maps plant stress across the landscape and identifies areas that experienced prolonged water stress. Lastly, in order to better understand the environment's effect on plant stress we relate topographic attributes to plant stress. Overall, 68 – 82% of species pairs exhibited significantly different temperature distributions across the nine dates. Plant stress was not evenly distributed across the landscape or time with lower elevation open shrub/meadows, June 2014, and August 2015 imagery capturing the largest amount of stress. Highly stressed plants were correlated with south or south-southwest facing slopes, while other topographic attributes were weakly correlated with TCI. Our results show that by using thermal and hyperspectral measurements we can monitor plant stress temporally and across ecoregions. This work supports improved monitoring of natural landscapes especially for areas prone to continued drought and high risk of wildfires.

## 4.1 Introduction

From 2012 to 2015, California experienced conditions that resulted in the most severe drought over the past 1200 years (Griffin and Anchukaitis, 2014). During this time, the state's 12-month accumulated precipitation was less than 34% of average, resulting in the hottest and driest on annual period record since 1895 (Mann and Gleick, 2015; Swain et al., 2014). The resulting water shortage lead to a wide range of impacts on natural systems including tree mortality (Young et al., 2017), bark beetle infestation (Guarín and Taylor, 2005; Tane et al., 2018a), and canopy water content loss (Asner et al., 2016). Extreme events, such as this drought, are projected to become more frequent and intense with the advancement of climate change (Mann and Gleick, 2015; Mastrandrea et al., 2011; Mastrandrea and Luers, 2012). Developing and perfecting the ability to monitor plant water stress on a regional scale will be necessary not only for vegetation management through a drought but also for planning and preparation got drought related impacts such as wildfires.

Many parts of California are extremely remote and have rugged terrain making it difficult to access and monitor through field efforts. Remote sensing technologies enable the monitoring of natural landscapes that are not normally accessible. The technology most commonly used for the purpose of monitoring plant water stress is thermal remote sensing, specifically using land surface temperature ($T_s$) as it has been long recognized as an indicator for plant water availability (Gates, 1968). This is due to the relationship between leaf-air temperature differential and leaf conductance (Jones, 2014). Stomata are sensitive to plant water status and respond by minimizing imposed changes in the balance between water supply and evaporative demand. With decreasing leaf or soil water potential, stomata will close thus decreasing the amount of transpiration occurring which causes leaf temperatures to

rise. The availability of handheld infrared thermometers allowed for the first coupling of plant conductance and temperatures instead of leaf measurements with embedded temperature probes (Monteith and Szeicz, 1962; Tanner, 1963). With the increasing availability of sensors, monitoring water stress using temperature has become possible at multiple scales but has been most commonly executed at field and regional scales.

At the plot level, researchers working on agriculture applications have been utilizing the relationship between plant temperature and water stress for five decades to improve irrigation techniques and increase crop yields. This focus has resulted in the development of various indexes still commonly used today including the Crop Water Stress Index (CWSI; Idso et al., 1981; Jackson et al., 1981), Degrees Above Non-Stressed Canopy (DANS; Taghvaeian et al., 2014), and the ratio of canopy temperature to non-stress crop ($T_c$ ratio; Bausch et al., 2011). These indices have been successfully used to manage irrigation practices (Thomson et al., 2012), but generally require in-situ meteorological data or previously derived stress baselines. Additionally, because they have been developed for agricultural fields, the studies predominately use handheld infrared thermal radiometers or unmanned aerial vehicles (UAVs) with mounted infrared thermal imaging to collect data (Costa et al., 2013). Due to these prerequisites, these methodologies cannot be easily scaled for natural landscapes that are inaccessible and cover thousands of kilometers.

To monitor vegetation stress at larger scales, researchers quantify stress using temperature calculated from spaceborne sensors such as the Advanced Very High Resolution Radiometer (AVHRR), the Moderate Resolution Imaging Spectroradiometer (MODIS), or the Landsat Thematic Enhanced Thematic Mapper (ETM+). The use of these sensors has resulted in the development of temperature based indices for monitoring drought such as the

Temperature Condition Index (TCI; Kogan, 1995; Kogan, 1997) and indices based on a combination of temperature and vegetation index such as the Vegetation Temperature Condition (VTC; Wan et al., 2004), the Vegetation Health Index (VHI; Kogan, 1997; Kogan et al., 2004), and the Drought Severity Index (DSI; Bayarjargal et al., 2006). These indices have been used to monitor and capture plant water stress during droughts in many places including India (Bhuiyan et al., 2006; Singh et al., 2003; Sruthi and Aslam, 2015), the United States (Felix N. Kogan, 1995; Wan et al., 2004), and Mongolia (Bayarjargal et al., 2006; Karnieli et al., 2006; Kogan et al., 2004). With spatial resolutions of 1 km or larger, these studies generally focus on global or large regional patterns of plant stress due to drought. These methodologies would provide a broader overview of plant stress during California's 2012-2015 drought, but would not give a detailed enough prospective for county-level management of vegetation.

A NASA Hyperspectral Infrared Imager (HyspIRI) airborne campaign captured Southern California's extreme drought conditions during 2013 – 2015 spring, summer, and fall (Lee et al., 2015). This campaign flew two instruments collecting a unique dataset of hyperspectral and thermal imagery at 18 and 36 m spatial resolution, respectively. This dataset provides an opportunity to examine natural vegetation plant stress across nine dates at a finer spatial resolution than possible with satellite-based sensors. In this study, we leveraged this dataset to analyze plant species' stress during the California's recent drought across 11,640 $km^2$ of Southern California. We subtracted surface temperature from air temperature ($T_s$-$T_a$) to construct plant species temperature and stress response annually and seasonally. We developed a species-specific temperature condition index (TCI) for monitoring plant stress using a plant species classification developed from the hyperspectral

imagery and scaled species temperature responses to the study area. We produced a map of vegetation plant stress variability across nine dates and investigated explanatory variables of plant stress. Specifically, we ask the following questions:

1. How do plant species surface temperature ($T_s$) and surface temperature minus air temperature ($T_s$-$T_a$) vary over spring, summer, and fall seasons with an increasing drought signal from 2013 - 2015?
2. What spatial and temporal patterns of plant stress are present across the landscape?
3. Is variability in plant stress spatial distributions explained by topographic attributes?

## 4.2 Methods

### *4.2.1 Study area*

The study area includes 11,640 km² of natural vegetation in Southern California comprising seven ecoregion subsections (Figure 4.1). The majority of this area falls into the Los Padres National Forest (LPNF), while the remainder is privately owned land or urbanized. The elevation increases from sea level to a peak of 2,697 m with the imagery capturing the transition from chaparral shrubland to conifer forests located in the LPNF. The entire study area experiences a Mediterranean climate characterized by wet, cool winters and dry, hot summers. Annual precipitation for the area ranges from 250 to 1000 mm with 95% falling between November and March (Davis and Michaelsen, 1995; Diamond et al., 2013). However, during the time period studied (2013 – 2015) this area experienced an extreme drought (Griffin and Anchukaitis, 2014; Swain et al., 2014). Figure 4.2 shows the daily precipitation for 2013 – 2015 at three stations: Santa Barbara Airport (elevation 2.7 m),

Gibraltar Dam (elevation 475 m), and Pine Mountain Club (elevation 1834 m). Locations of these three stations are shown in Figure 4.1.

This area is also characterized by frequent wildfires that have been increasing in severity (Davis and Michaelsen, 1995; Moritz, 1997; Syphard et al., 2011). The LPNF has been actively suppressing wildfires since the 1900s, but suppression efforts became more effective after 1950 due to the use of large air tankers (Davis and Michaelsen, 1995). Even with fire suppression, the time since last fire is under 10 years for a large portion of the LPNF although many areas have not burned in 75 or more years (Figure 4.3). The California Department of Forestry and Fire Protection (CalFire) develops fire hazard severity maps, which designates zones with varying degrees of fire hazard based on factors such as fuel, slope, and fire weather. These zones represent the likelihood that an area will burn over a 30 – 50 year period. Based on these zones, the majority of the study area falls into a very high fire hazard severity zone (Figure 4.3).

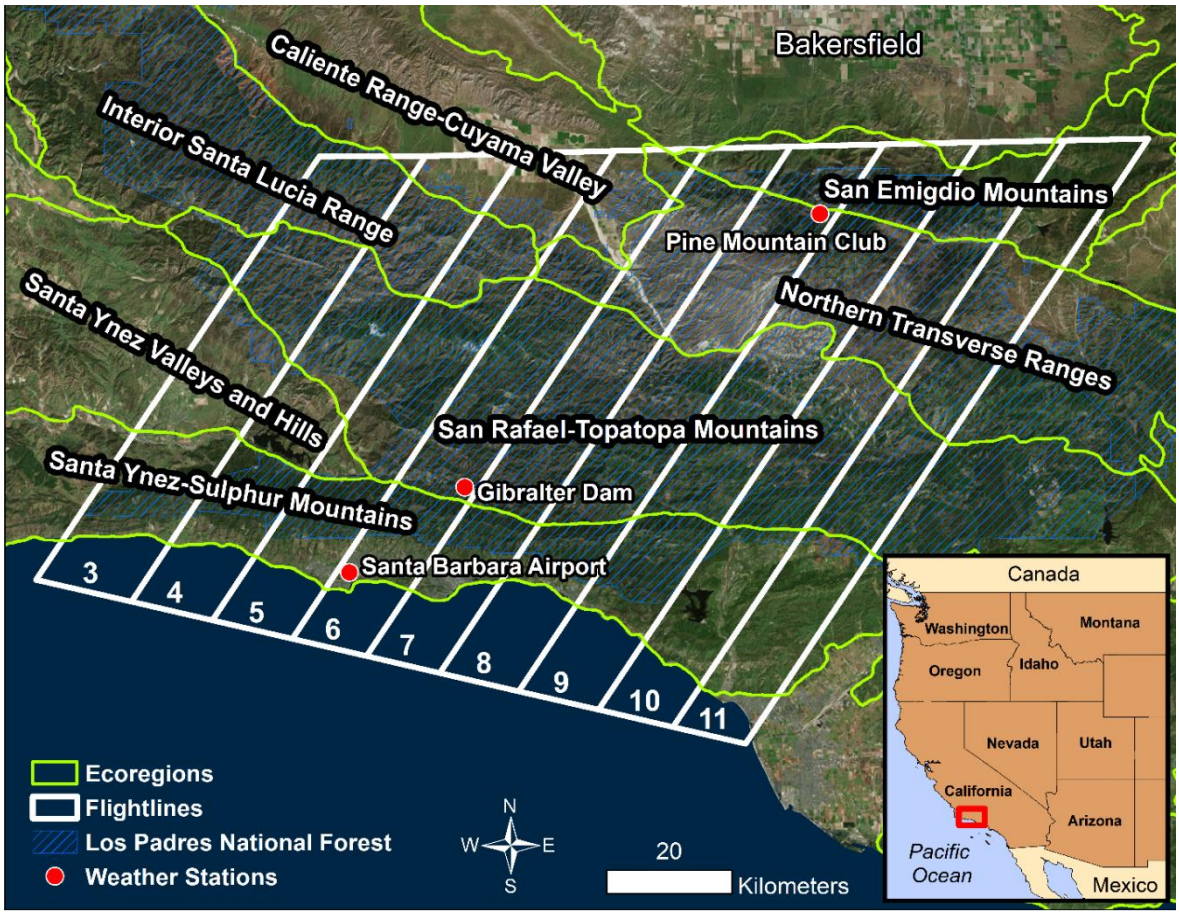


*Figure 4.1. The flightlines (white) and ecoregions (yellow-green) in the Santa Barbara flight box used from the HyspIRI Airborne Preparatory campaign.*

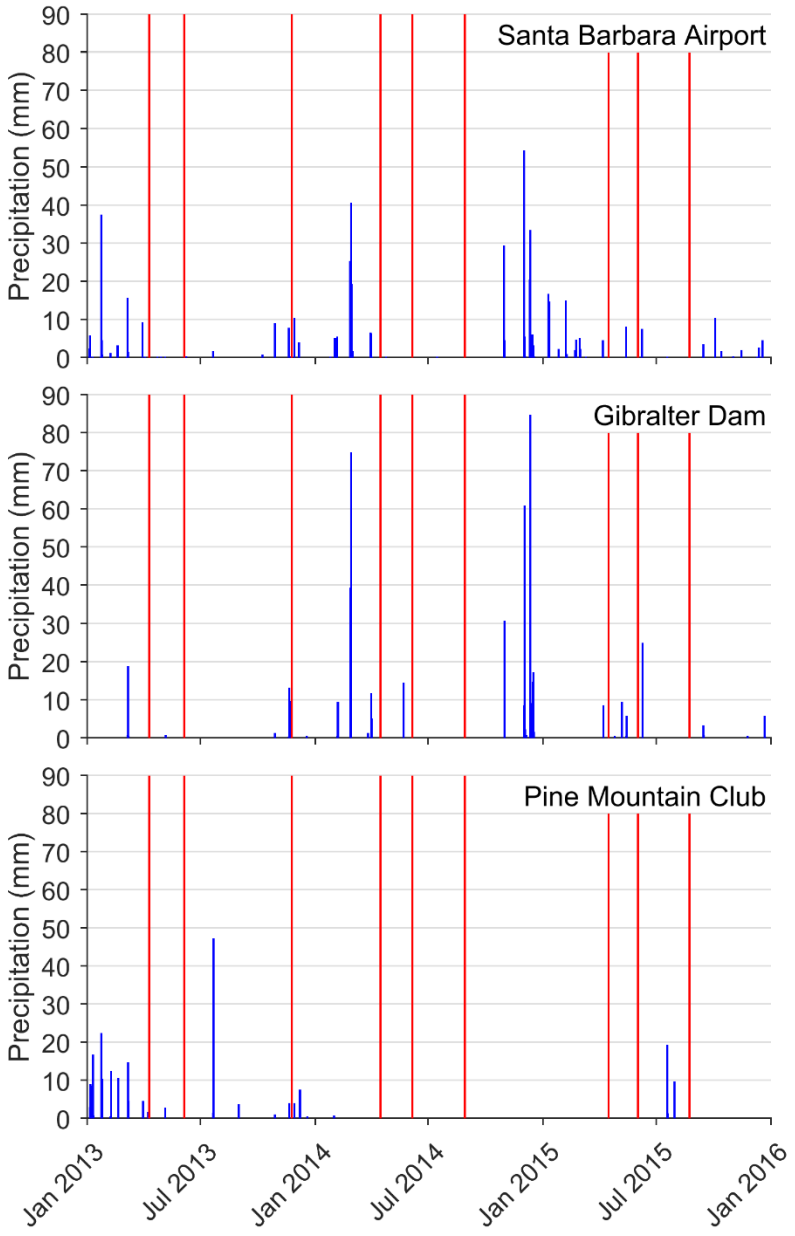


*Figure 4.2. Daily precipitation (blue) from January 2013 to January 2016 for three weather stations in the study area. Locations of the three stations are shown in Figure 1. Red lines designate flight dates: 2013 Apr 11, 2013 June 6, 2013 Nov 23, 2014 Apr 16, 2014 June 6, 2014 Aug 29, 2015 Apr 16, 2015 June 2, and 2015 Aug 24.*

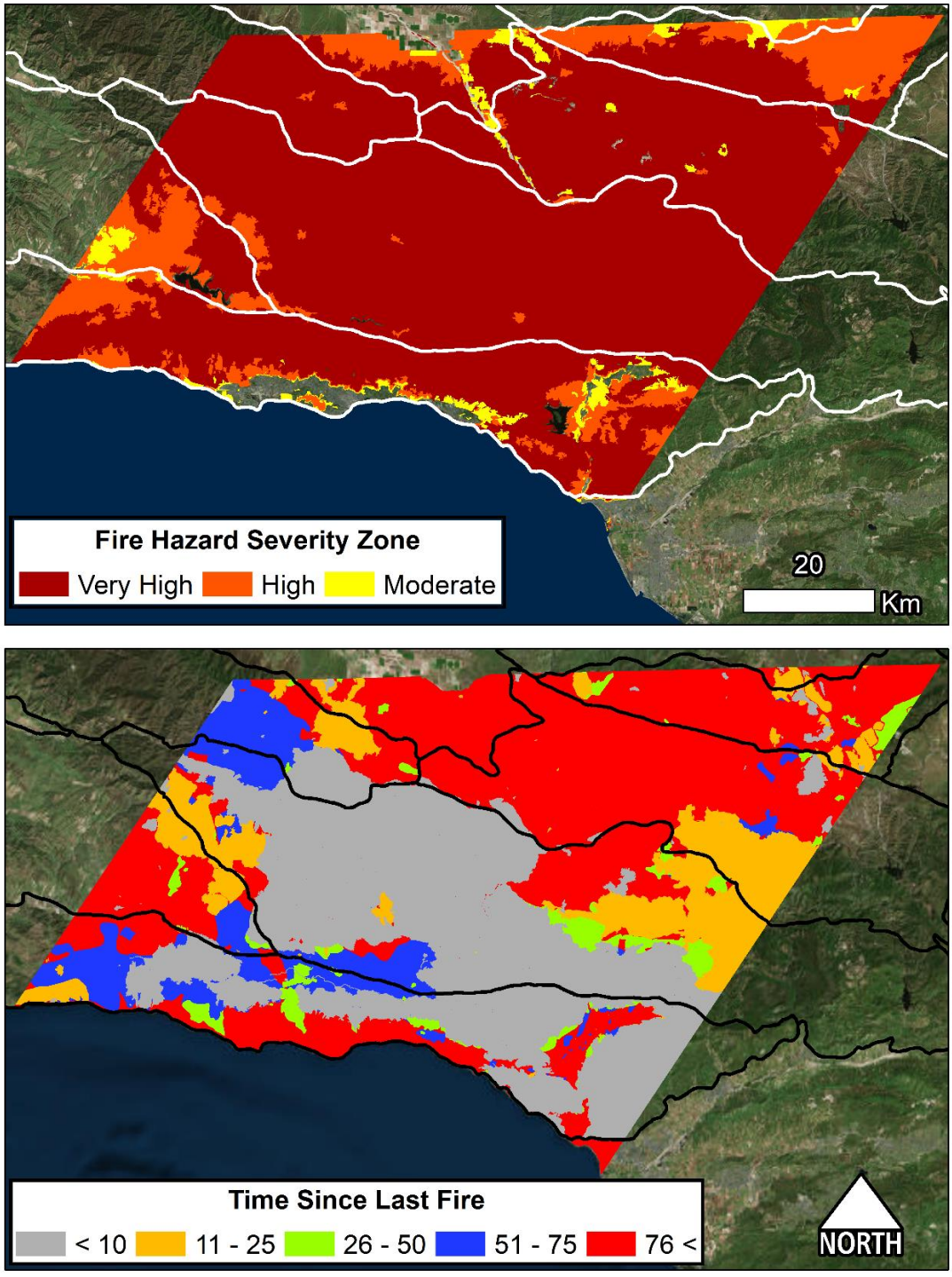


*Figure 4.3. The fire hazard severity rating determined by CalFire (top) and the time since last fire provided by United States Forest Service (bottom) for study area. Time since last fire was last updated December 2017.*

*4.2.2 Remotely sensed data*

Remotely sensed imagery of the study area was collected with the Airborne Visible/Infrared Imaging Spectrometer (AVIRIS) and MODIS-ASTER Airborne Simulator (MASTER) sensor as part of the NASA Hyperspectral Infrared Imager (HyspIRI) Airborne Preparatory Campaign (Green et al., 1998; Hook et al., 2001). These sensors were flown simultaneously on the NASA ER-2 aircraft at an altitude of 20 km over six flight boxes in California to simulate future satellite imagery from HyspIRI (Lee et al., 2015). This study uses a spatial subset of imagery from the Santa Barbara flight box that includes nine of the eleven flightlines that were acquired with a 35º northeast-southwest orientation (Figure 4.1). Imagery was collected on 2013 Apr 11; 2013 June 6; 2013 Nov 23; 2014 Apr 16; 2014 June 6; 2014 Aug 29; 2015 Apr 16; 2015 June 2; and 2015 Aug 24. Some flightlines were excluded or replaced due to technical errors when collecting the data, resulting in 79 AVIRIS and 79 MASTER images being used in the analysis presented here. NASA's Jet Propulsion Laboratory (JPL) provided HyspIRI-like AVIRIS and MASTER products. For AVIRIS, this entails HyspIRI simulated reflectance products measuring 224 bands between 0.38 and 2.5 µm with a 18 m spatial resolution (Thompson et al., 2015). For MASTER, the product was delivered with five emissivity bands and a land surface temperature ($T_s$) band at a 36 m spatial resolution (Gillespie et al., 1998; Hook et al., 2001; Hulley and Hook, 2011). The $T_s$ retrievals have an overall accuracy $\leq$ 0.33 K and a noise equivalent differential temperature (NEdT) ranging from 0.15 – 0.74 K per band (Wetherley et al., 2018).

In order to use AVIRIS and MASTER datasets together across flight dates, a series of additional preprocessing steps were required. AVIRIS products underwent additional pre-processing steps detailed in Meerdink et al. (in prep). MASTER images were georeferenced

to correct locational errors of the entire multi-temporal image sequences. Acquired in the spring and fall of 2012, the National Agriculture Imagery Program (NAIP) digital orthophotos were used as a reference source for the world coordinates. These orthophotos were mosaicked and resampled to 36 m spatial resolution for MASTER and then used to collect ground control points. After pre-processing of AVIRIS and MASTER images was completed, the AVIRIS and MASTER images were layered into a single file. With an AVIRIS swath width of ~12km and MASTER swath width of ~40 km, any spatial areas that were not covered by both sensors were removed. The majority of clouds were manually masked out, but cirrus clouds still remain in some flightlines.

*4.2.3 Plant Species Information*

Reference data on the spatial distribution of dominant species and land cover types were collected both in the field and using AVIRIS and NAIP imagery and are detailed in Meerdink et al. (in prep) (Table 4.1). Reference polygons were used to extract $T_s$ and topographic attributes from imagery and only pixels completely falling into a reference polygon were used to develop spectral libraries. Some species used in the aforementioned research were not included in this work due the coarser spatial resolution of MASTER imagery reducing the number of samples. Some species are consistently found growing in mixed patches and were treated as a single class (e.g. ARCA-SALE and ATCA-ERNA). The plant species classification was developed using the classifications derived in Meerdink et al. (in prep). This paper uses the plant species classifications from Spring 2013, Summer 2013, Spring 2014, Spring 2015, and Summer 2015 imagery developed using spectral libraries from the same image date. These image dates were selected because overall classification accuracies were above 0.8 kappa and all flightlines were available. To develop a single plant species

classification map, the classification value mode for each pixel was determined using the five dates. To match MASTER spatial resolution, this classification map was resampled to 36 m spatial resolution using the mode for pixels to be aggregated.

*Table 4.1. Classes and plant species used in study with corresponding abbreviation and plant functional type.*

| Species | Code | Leaf Duration | Leaf Form | Plant Form |
|---|---|---|---|---|
| *Adenostoma fasciculatum* | ADFA | Evergreen | Needleleaf | Shrub |
| Agricultural Residue | AGRES | Annual | N/A | Herb |
| *Artemisia californica* and *Salvia leucophylla* | ARCA-SALE | Deciduous and Deciduous | Needleleaf and Broadleaf | Shrub |
| *Arctostaphylos spp.* | ARGL | Evergreen | Broadleaf | Shrub |
| *Atriplex canescens* and *Ericameria nauseosa* | ATCA-ERNA | Deciduous and Deciduous | Broadleaf and Broadleaf | Shrub |
| *Baccharis pilularis* | BAPI | Evergreen | Broadleaf | Shrub |
| *Brassica nigra* | BRNI | Annual | N/A | Herb |
| *Ceanothus cuneatus* | CECU | Evergreen | Broadleaf | Shrub |
| *Ceanothus megacarpus* | CEME | Evergreen | Broadleaf | Shrub |
| *Ceanothus spinosus* | CESP | Evergreen | Broadleaf | Shrub |
| *Citrus spp.* | CISP | Evergreen | Broadleaf | Tree |
| *Eucalyptus spp.* | EUSP | Evergreen | Broadleaf | Tree |
| Irrigated Grasses | IRGR | Annual | N/A | Herb |
| *Juniperus californica* | JUCA | Evergreen | Needleleaf | Tree |
| Mediterranean Annual Grasses and Forbs | MAGF | Annual | N/A | Herb |
| *Persea Americana* | PEAM | Evergreen | Broadleaf | Tree |
| *Pinus jeffreyi* | PIJE | Evergreen | Needleleaf | Tree |
| *Pinus monophylla* | PIMO | Evergreen | Needleleaf | Tree |
| *Pinus sabiniana* | PISA | Evergreen | Needleleaf | Tree |
| *Pseudotsuga menziesii* | PSMA | Evergreen | Needleleaf | Tree |
| *Quercus agrifolia* | QUAG | Evergreen | Broadleaf | Tree |
| *Quercus berberidifolia* | QUBE | Evergreen | Broadleaf | Tree |
| *Quercus douglasii* | QUDO | Deciduous | Broadleaf | Tree |
| *Umbellularia californica* | UMCA | Evergreen | Broadleaf | Tree |

*4.2.4 Temperature Products*

It is common in the literature to use $T_s$-$T_a$ as a proxy for plant stress (Moran et al., 1994; Vidal et al., 1994; Vidal and Devaux-Ros, 1995). In order to develop a land surface

temperature minus air temperature ($T_s$-$T_a$) product, it was necessary to estimate air temperature within a 15-minute window for each image pixel. AVIRIS Level 1B products generated by JPL include an image with each pixel's observation time. This observation time image was resized to 36 m spatial resolution and georeferenced. Air temperature was obtained from 800 weather stations available through the National Oceanic and Atmospheric Administration (NOAA) Meteorological Assimilation Data Ingest System (MADIS). Air temperature for the nine flight dates was binned into 15 minute intervals between the hours of 16:00 and 21:00 UTC, which corresponds to the range of flight times seen in observation time imagery. The station point data were interpolated using topographically informed interpolation in order to exploit the relationship between air temperature and elevation by using the environmental lapse rate (Willmott and Matsuura, 1995). Obtained through the NOAA Earth System Research Laboratory (ESRL), the environmental lapse rate for the image date was calculated using radiosonde data from the Vanderburg Air force base. The environmental lapse rate for the nine dates varied between 2.42 X $10^{-3}$ $^{o}$C $m^{-1}$ and 3.81 X $10^{-3}$ $^{o}$C $m^{-1}$. The estimated sea level air temperature at each station *i* was estimated from

$$ {}_sT_i = T_i + \Gamma z_i \quad (4) $$

where Γ is the environmental lapse rate for the image date, $z_i$ is the elevation at station *i* obtained the station data, and ${}_sT_i$ is the estimated air temperature at sea level for station *i*. Using the estimated sea level air temperature, simple kriging with spherical variograms was used to generate an air temperature image for each time-step and date. Every pixel's collection time was matched to the closest air temperature time step and the corresponding estimated sea level air temperature. Air temperature at each pixel was estimated using elevation from the National Elevation Dataset (NED) according to

$$ {}_sT_i = T_i - \Gamma z_j \quad (5) $$

where $z_j$ is the NED elevation at pixel $j$. The estimated air temperature for each pixel was then subtracted from MASTER's $T_s$ product to generate a $T_s$-$T_a$ image. An example of the surface temperature, air temperature, and $T_s$-$T_a$ image for 2015 June 2 is shown in Figure 4.4.

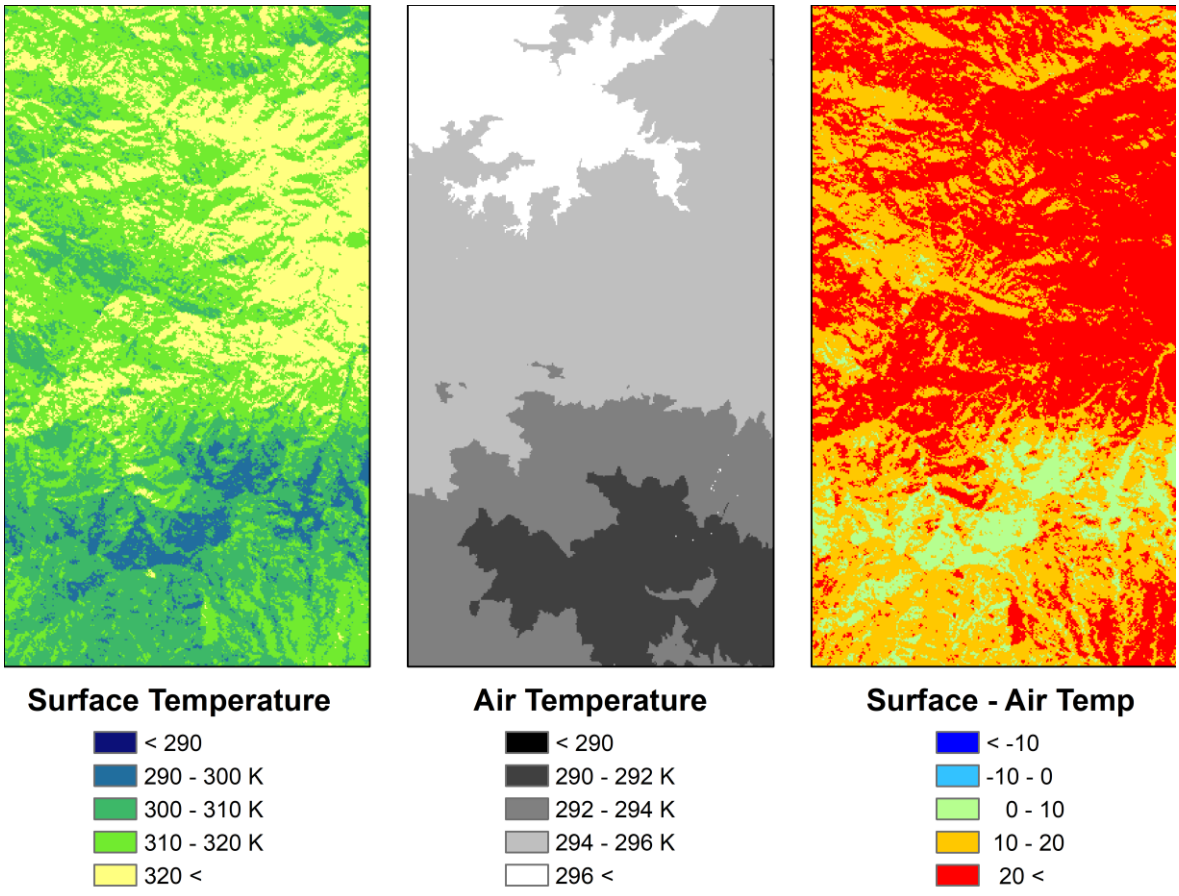


*Figure 4.4. A geographic subset from the 2015 June 2 date of surface temperature derived from MASTER imagery, estimated air temperature using station data, and the surface minus air temperature ($T_s$-$T_a$) product.*

The Temperature Condition Index (TCI) has been used successfully to monitor drought-related vegetation stress in India, Mongolia, United States, and globally (Bayarjargal et al., 2006; Bhuiyan et al., 2006; F. N. Kogan, 1995; Kogan, 1997; Sholihah et al., 2016;

Singh et al., 2003). This index was originally developed for the Advanced Very High Resolution Radiometer (AVHRR) and uses brightness temperature from 1985 - 1993. We altered the index for MASTER imagery over nine image dates. TCI was calculated for each species as:

$$TCI = 1 - \frac{(T_{max} - T)}{(T_{max} - T_{min})} \quad (3)$$

Where $T_{max}$ and $T_{min}$ are the maximum and minimum $T_s$-$T_a$ value over the nine image dates for each species and $T$ is the $T_s$-$T_a$ for each pixel. Given this equation, the highest stress case is TCI = 1 and the lowest stress case is TCI = 0. This date and species specific TCI value was applied to the plant species classification image, resulting in a TCI distribution image with nine bands corresponding to each image date. The statistical difference in plant species $T_s$ and TCI distributions were analyzed using ANOVA.

*4.2.5 Topographic Calculations*

In order to determine which topographic attributes are associated with stressed plants, nine topographic attributes were calculated for correlation analysis with TCI distributions (Table 4.2). The National Elevation Dataset (NED), assembled by the United States Geological Survey (USGS), is a ~10m spatial resolution raster product that was used to calculate the topographic attributes. The NED was used to calculate elevation in meters, slope in percent, and aspect in degrees. The elevation product was used to calculate the terrain ruggedness index (TRI) which provides a quantitative measure of topographic heterogeneity (Riley et al., 1999). For each pixel, the TRI value is calculated by the sum change in elevation between a grid cell and its eight neighbor pixels. The elevation and slope product was used to calculate the topographic wetness index (TWI) which is commonly used to quantify topographic control on hydrological processes (Beven and Kirkby, 1979). Using

ArcGIS, a flow direction raster was calculated using elevation. The flow direction raster was then used to calculated flow accumulation raster which finds the upslope contributing area for each pixel. TWI was then calculated using the flow accumulation and slope raster, adjusted by spatial resolution.

While elevation and slope were used directly in the correlation, aspect was not because it is expressed as circular degrees clockwise from 0º to 360º, thus is difficult to quantitatively compare. Instead, three attributes were calculated from aspect imagery: north to south slope orientation (N-S; Cooper, 1998), west to east slope orientation (W-E; Cooper, 1998), north-northeast to south-southwest orientation (NNE-SSW; Roberts and Cooper, 1989). Values of N-S and W-E range from -1 to 1 and represent the extent to which a slope faces north (N-S = 1), south (N-S = -1), east (W-E = 1), or west (W-E = -1). NNE-SSW represents the extent to which a slope faces the typically cooler and wetter north-northeast orientation (NNE-SSW = -1) versus the hotter and dryer south-southwest orientation (NNE-SSW = 1). It has been argued that aspect should not be considered without taking into account the interactions with slope (Stage, 1976). To account for this interaction, three additional attributes were calculated from aspect and slope imagery: cosine transformation (N-S A+S; Stage, 1976), sine transformation (W-E A+S; Stage, 1976), and cosine transformation adjusted for aspect (NNE-SSW A+S). Positive values of W-E A+S are associated with east facing slopes and negative values with west facing slopes. For N-S A+S, positive values are north facing slopes with negative values for south facing slopes. N-S A+S and W-E A+S will have a zero value for pixels on flat ground, but pixels on steep ground will have high weights for the sine and cosine of aspect. The last slope and aspect attribute is a combination of cosine transformation and the NNE-SSW aspect attribute. The aspect was

adjusted for north-northeast to south-southwest orientation and then the cosine transformation was applied. This results in positive values being associated with north-northeast facing slopes and negative values south-southwest facing slopes.

*Table 4.2. Topographic attributes extracted from the National Elevation Dataset. α is aspect in radians and θ is percent slope. For TRI, $x_{ij}$ is the elevation of each neighbor cell to cell $x_{00}$. For TWI, As is the specific catchment area and β is the slope. For more details, see Section 4.2.6.*

| Metric | Full Name | Formula | References |
|---|---|---|---|
| Elevation | Elevation (m) | | |
| Slope | Slope (%) | | |
| N-S | North–south slope orientation | $\cos \alpha$ | (Cooper, 1998) |
| W-E | West–east slope orientation | $\sin \alpha$ | (Cooper, 1998) |
| NNE-SSW | North–northeast – south–southwest orientation | $\cos(\alpha - 30)$ | (Roberts and Cooper, 1989) |
| N-S A+S | Cosine Transformation | $\theta * \cos \alpha$ | (Stage, 1976) |
| W-E A+S | Sine Transformation | $\theta * \sin \alpha$ | (Stage, 1976) |
| NNE-SSW A+S | Cosine Transformation with north–northeast – south–southwest orientation | $\theta * \cos(\alpha - 30)$ | (Stage, 1976) |
| TRI | Terrain Ruggedness Index | $\left[\sum((x_{ij} - x_{00})^2)\right]^{\frac{1}{2}}$ | (Riley et al., 1999) |
| TWI | Topographic Wetness Index | $\ln\left(\frac{As}{\tan \beta}\right)$ | (Beven and Kirkby, 1979) |

## 4.3 Results

### *4.3.1 Temperature Measures*

Species exhibited significantly different $T_s$ distributions across seasons and among species (Figure 4.5). The majority of plant species pairs (59%) were significantly different for seven to nine of the image dates. Only BRNI and ADFA exhibited $T_s$ distributions across all nine dates that were not significantly different. The November 2013 image date showed

the smallest number of significantly different species pairs with 60.9%. The April 2014 image date showed the highest number of significantly different species pairs with 77.5%. Species pairs that did not have significantly different temperature distributions tended to share the same leaf duration: evergreen, deciduous, and annual. While species pairs that were significantly different tended to have different structure (herb vs. shrub vs. tree) and slightly less importantly leaf shape (needleleaf vs. broadleaf).

The seasonal and species patterns expressed in $T_s$ are accentuated for $T_s$-$T_a$ and TCI. Figure 4.6 shows mean seasonal $T_s$, $T_s$-$T_a$, and TCI values for the three coolest and warmest plant species across the nine image dates. The three warmest plant species are JUCA, MAGF, and ATCA-ERNA with $T_s$ around 45ºC while the three coolest plant species are PIJE, CESP, and UMCA with $T_s$ around 30ºC. CESP and UMCA, two of the coolest species, are generally found in close proximity of the ocean on mesic north facing slopes, while PIJE grows at high elevations (>2000 m). The warmest species grow in exposed warm locations that do not experience the cooling effect of the ocean due to distance. There are also consistent seasonal and annual patterns across all species. For example, the November 2013 imagery was consistently cooler than any other date captured due to the very late seasonal collection date.

The differences between these species become more pronounced when the air temperature is taken into account, with the warmest species having $T_s$-$T_a$ temperatures around 20ºC, while the coolest species exhibit $T_s$-$T_a$ around 5ºC. When air temperature is considered it becomes apparent that plant species are experiencing less transpiration in June compared to August due to larger deviations in air temperature. While June consistently displays larger $T_s$-$T_a$, April and August dates do not show a consistent pattern across species.

In the case of JUCA, August dates show less stress compared to April dates while UMCA experiences the opposite. In addition to being warmer, JUCA, MAGF, and ATCA-ERNA also experience a larger range of $T_s$-$T_a$ throughout the year compared to the coolest species.

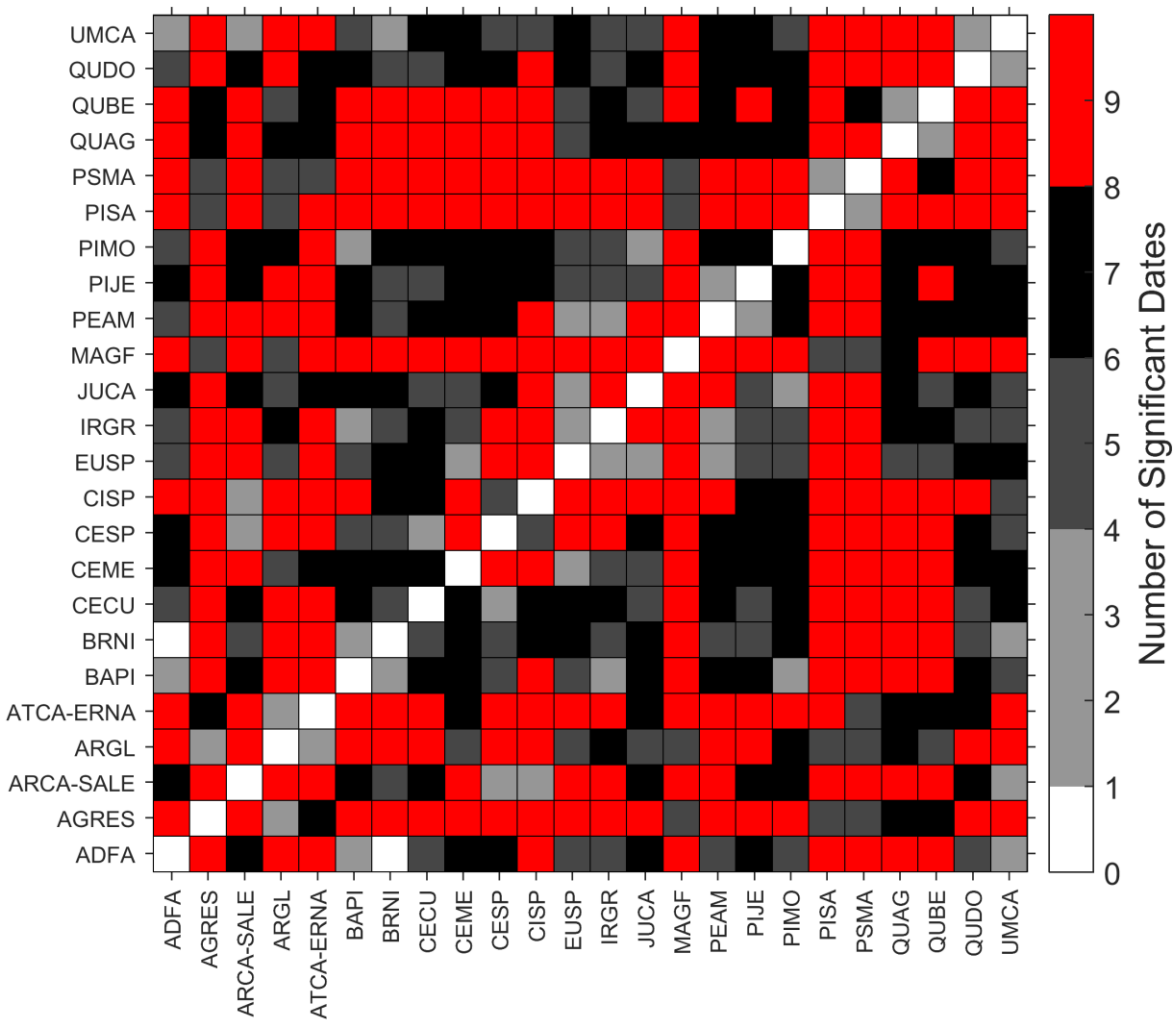


*Figure 4.5. The number of significantly different land surface temperature ($T_s$) distributions across nine image dates.*

Developed using $T_s$-$T_a$, perhaps unsurprisingly the mean seasonal TCI values display similar patterns to $T_s$-$T_a$. Scaled from least amount of stress (0) to most amount of stress (1), this index shows how a particular date compares to the minimum and maximum amount of

stress across all dates. The minimum $T_s$-$T_a$ to calculate TCI for each species was found in the November 2013 imagery for the majority of species, while the maximum $T_s$-$T_a$ was found for most species in the June 2013 and June 2014 imagery. In general, April TCI values were much more consistent across years for a species compared to summer or fall imagery. For all species, the November 2013 imagery showed plants the least stressed, while June dates for all years showed the largest amount of stress.

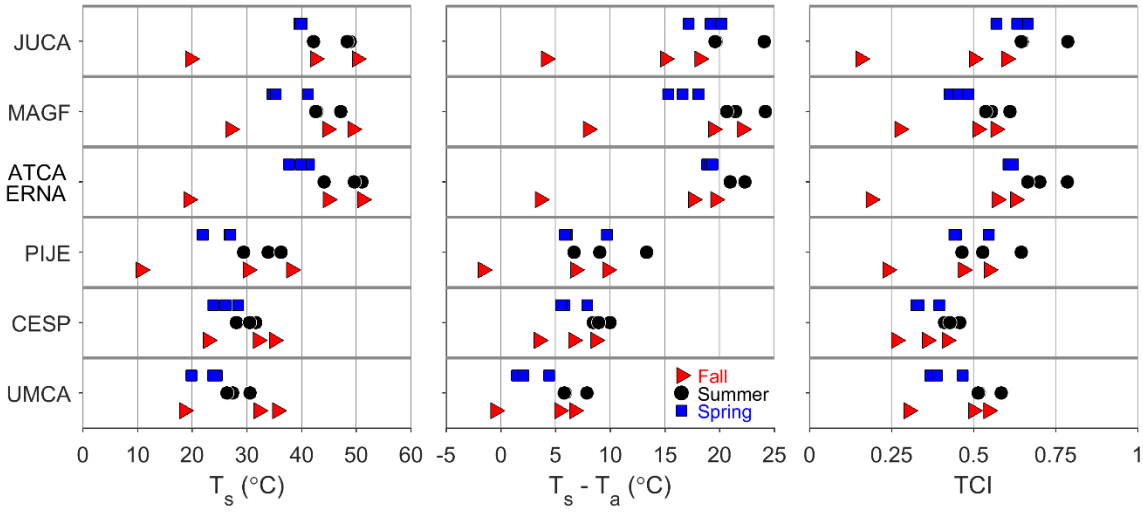


*Figure 4.6. Seasonal mean land surface temperature ($T_s$), $T_s$-$T_a$, and Temperature Condition Index (TCI) values for three coolest (PIJE, CESP, and UMCA) and three warmest (JUCA, MAGF, and ATCA-ERNA) plant species.*

### *4.3.2 Temperature Condition Index (TCI) Spatial Distribution*

TCI distributions fluctuated across seasons, years, and flightlines (Figure 4.7). Seasonally, June image dates have the highest TCI values and April image dates have the lowest. The November 2013 date had the lowest TCI values of all nine dates, which is due to later image collection. After three years of severe drought, the 2015 images had more stressed vegetation compared to 2013 and 2014. The distribution of TCI values across a

single date show flightline edges, which is due to the fact that airborne imagery was collected over a four-hour period. This range of collection times captures changes in sun angle and also diurnal patterns in plant temperatures.

TCI distributions were not equally distributed across the landscape and were highly dependent on the ecoregion. The Santa Ynez – Sulphur Mountain ecoregion, which has the closest proximity to the ocean, had generally less stressed vegetation compared to other ecoregions. The San Emigdio Mountain ecoregion, a high-elevation conifer forest, also had consistently low TCI plants across seasons and years. The Caliente Range – Cuyama Valley ecoregion, the farthest ecoregion from the ocean, had consistently higher TCI values and more stressed plants across all nine image dates. The largest ecoregion in the study area was the San Rafael – Topatopa Mountains which experienced the largest range in TCI values and plant stress levels. Consistently the central portion to western half of the ecoregion had more stressed plants compared to the eastern half. The central region of the San Rafael – Topatopa Mountains, an extremely remote and rugged area, shows elevated TCI values for all dates compared to other regions.

The majority of TCI pixel values fell between 0.25 – 0.75 across the nine dates (Figure 4.8). The highest TCI values (0.75 – 1.00), which indicate high stress, are found in the June 2014 and August 2015 image dates. Compared to other dates and particularly fall dates, August 2015 had elevated TCI values with the majority of pixels falling into the 0.50 – 0.75 range. Out of all nine dates captured, June 2014 experienced the most stress with approximately 75% of pixels having TCI values from 0.50 – 1.00. June 2014 also had the highest daily maximum air temperature experienced out of all nine dates. November 2013 experienced the lowest stress with 92% of pixels having 0.00 – 0.50 TCI values. This is also

captured the frequency in which a pixel had a TCI greater than 0.75 (Figure 4.9 top) and greater than 0.5 (Figure 4.9 bottom) highlighting geographic areas that have been perpetually stressed. Approximately 1.25% of pixels had 7 to 9 dates with TCI values greater than 0.75, but this number jumps to 29.4% with TCI values greater than 0.50. The majority of highlighted stressed areas are located within the Los Padres National Forest. The exceptions are stressed areas in the Santa Ynez Valleys and Hills and Caliente Range – Cuyama Valley ecoregions which are owned mostly by private individuals.

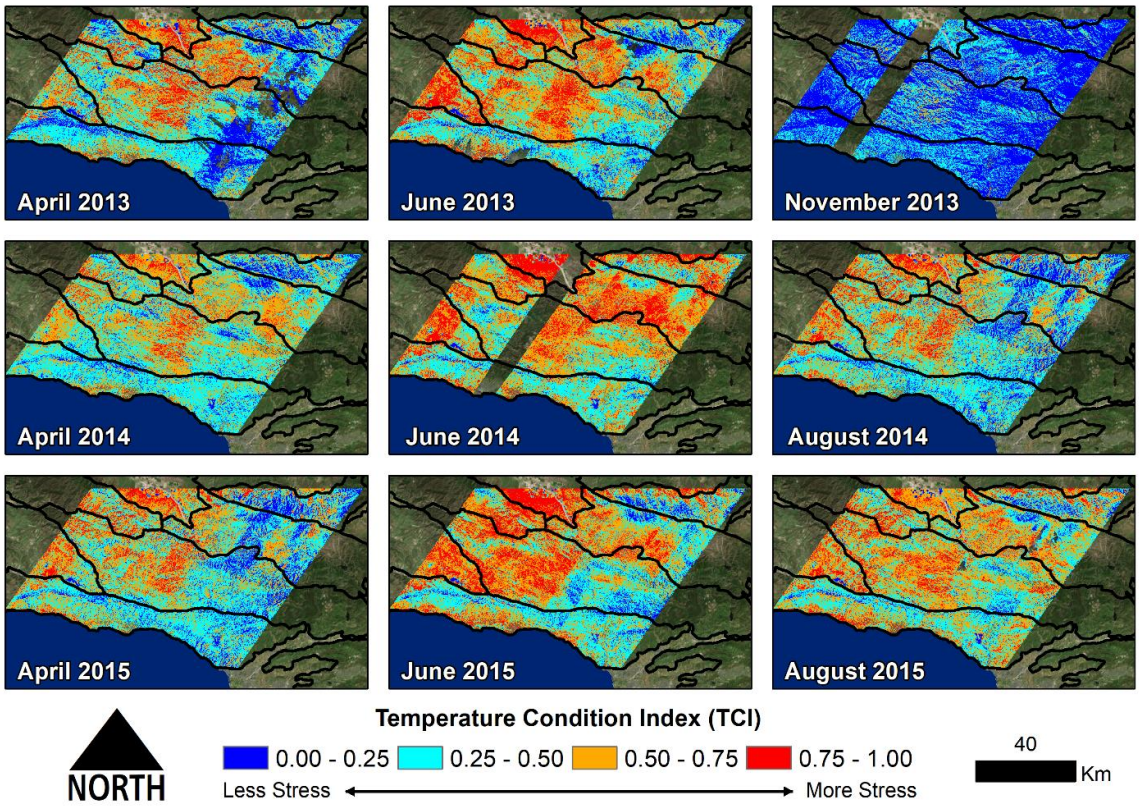


*Figure 4.7. Temperature condition index (TCI) for nine image dates with ecoregion's boundaries are shown in black.*

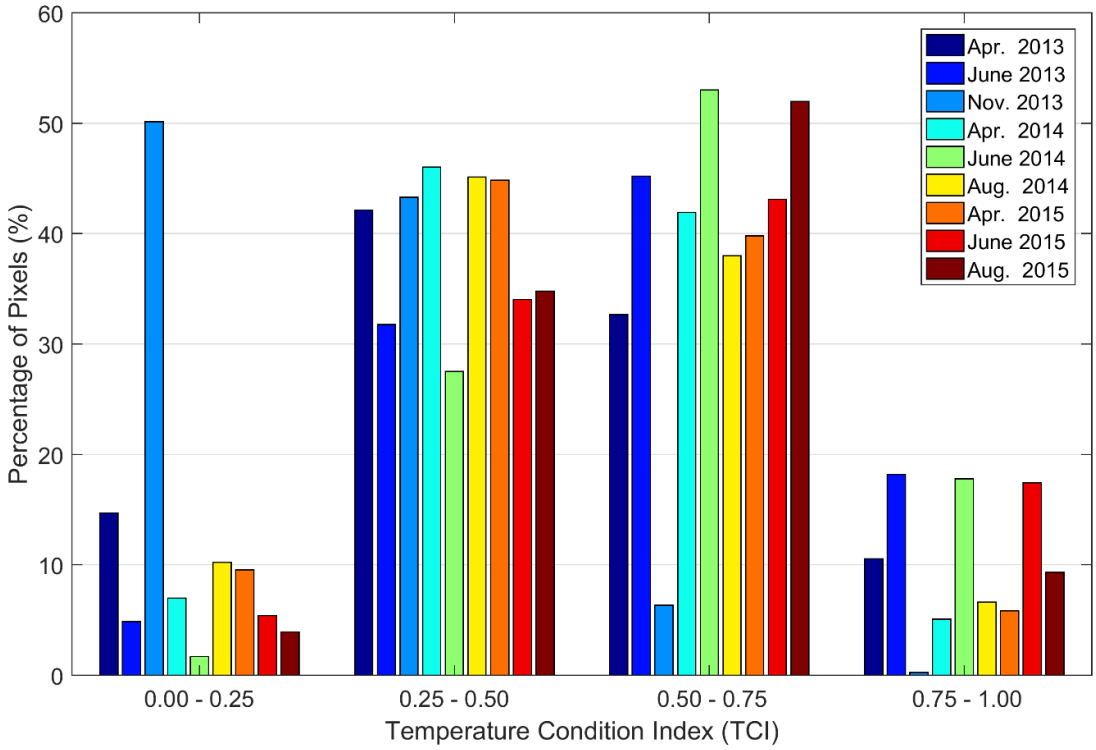


*Figure 4.8. For each of the nine dates, percent of pixels falling into the four categories of temperature condition index (TCI) ranges.*

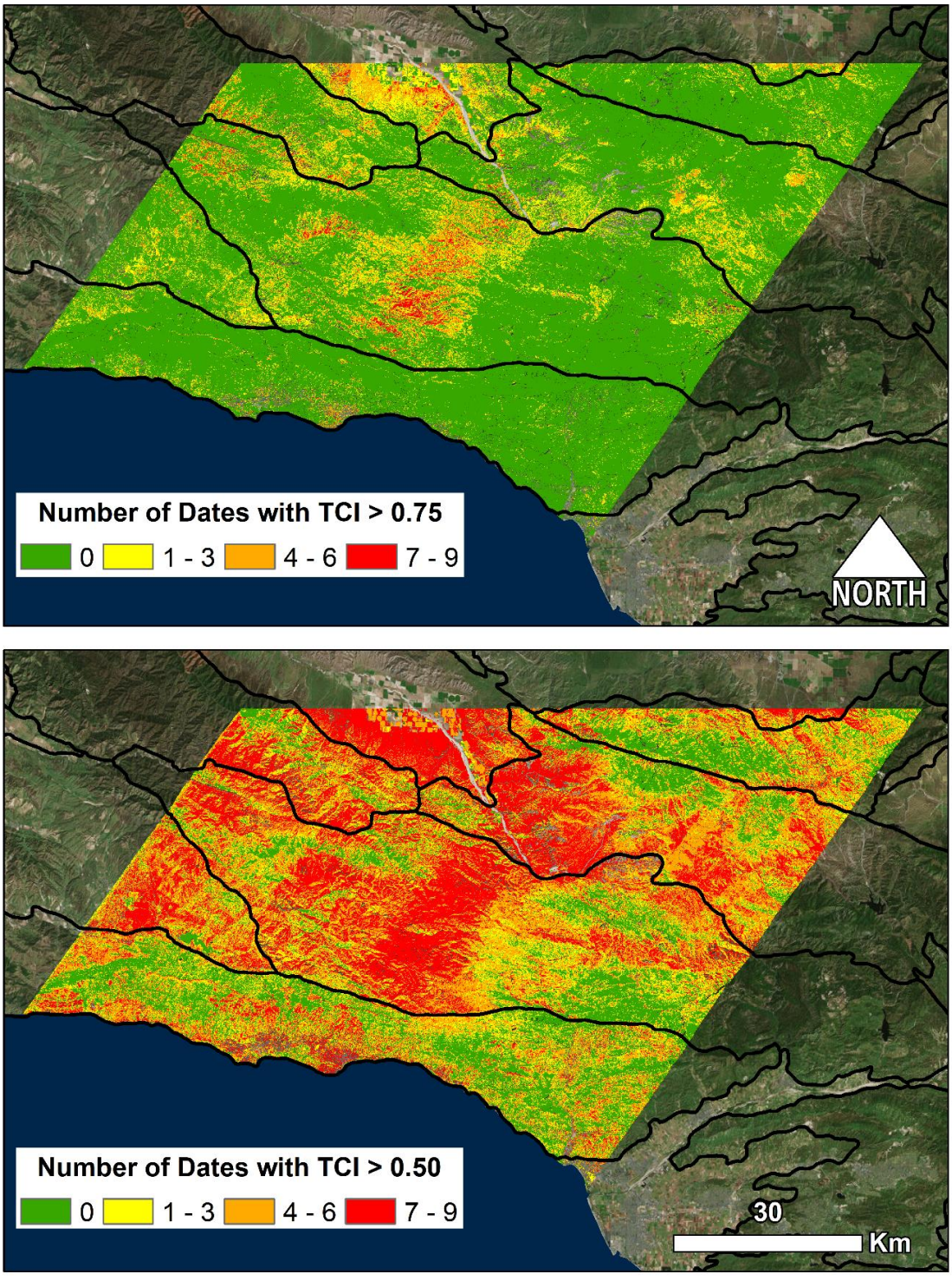


*Figure 4.9. The number of image dates a pixel exceeded a temperature condition index (TCI) value of 0.75 (top) and 0.50 (bottom).*

*4.3.3 Topographic effects*

In an attempt to explain why particular areas were more or less stressed, TCI was correlated with collection time and topographic attributes that vary across a landscape (Figure 4.10). Out of the nine topographic attributes calculated, the attributes with the strongest correlation to TCI values were related to N-S and NNE-SSW facing slopes. A south or south-southwest facing slope is associated with high stress plants. The interaction between slope and aspect, as measured with A+S attributes, was not more strongly correlated than aspect alone showing that the relationship between stress and topographic attributes is mainly driven by aspect. For aspect attributes, the August 2015 date represents a unique departure from other dates collected. The W-E attribute was positively correlated with TCI, while the NNE-SSW attribute lost correlation strength showing that east facing slopes were strongly correlated with high stress plants more than south-southwest facing slopes.

The other terrain attributes did not have strong correlations with distributions of TCI, but the correlations were found to be significant. Slope was found generally to have a negative correlation, so that steeper slopes experience lower stress. The TWI had a weak positive relationship with stress showing that areas with higher catchment have more stress. However, this is probably more attributable to the fact that high TWI values are associated with low slopes which has a stronger correlation with TCI. The terrain ruggedness index (TRI) had a weak correlation with TCI values, except for November 2013 where there was a strong negative correlation associating high ruggedness with low stress. The strongest correlation between elevation and TCI was found for the April 2014 and June 2014 dates where higher elevation was associated with higher stress. In addition to topographic attributes, we correlated a pixel's collection time with the resulting TCI value. The image

collection time had a strong negative correlation with temperature variation on June 2013 and 2015 where later (~22 UTC or 3 pm PST) collection times resulted in lower stress. Image collection time had a strong positive correlation with TCI on August 2014 where later collection times resulted in higher stress. However, on this date collection times ended earlier in the day around 20 UTC or 1 pm PST.

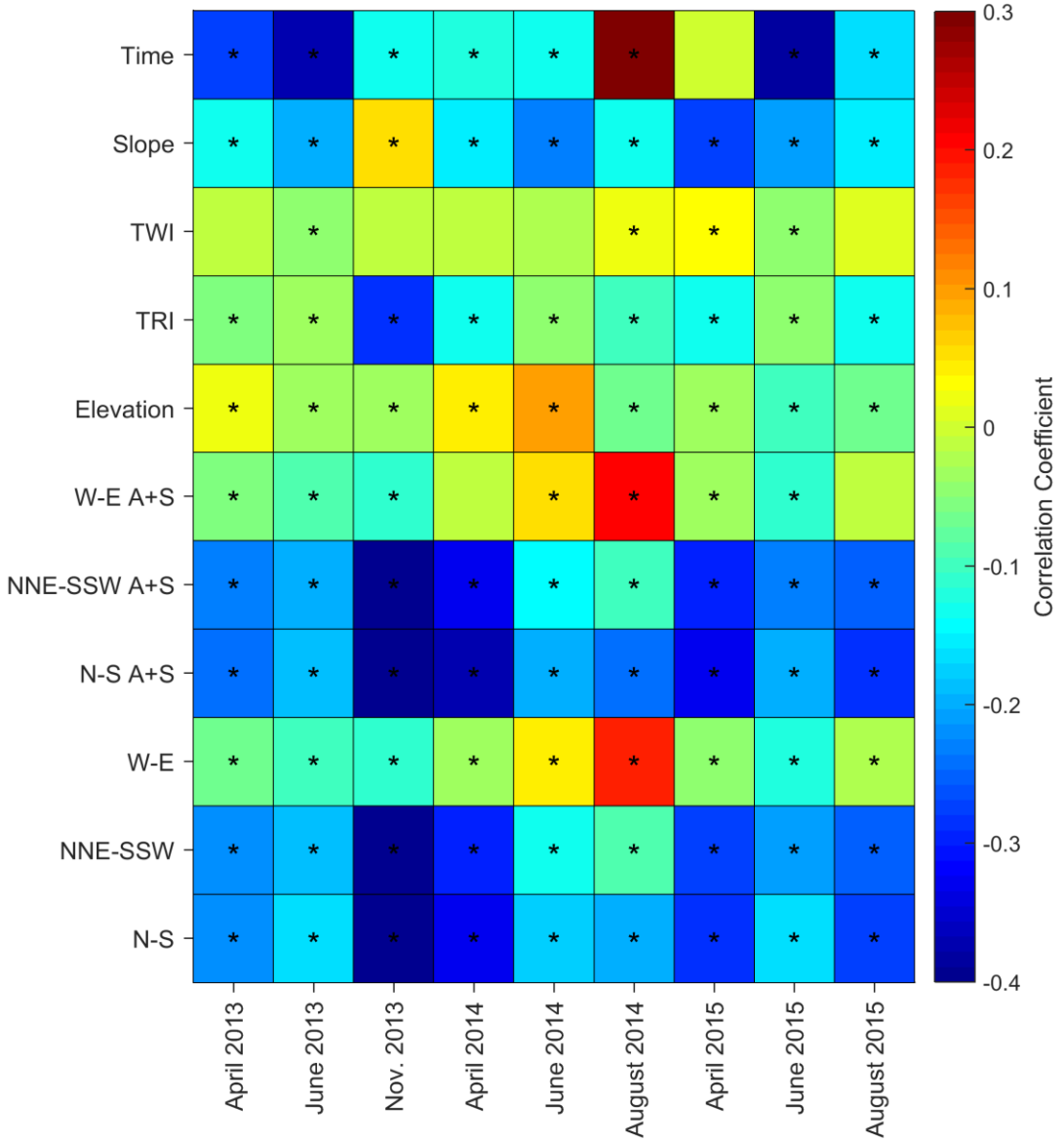

*Figure 4.10. Correlations of topographic attributes and temperature condition index (TCI). Asterisk (*) denotes significance at $p < 0.05$.*

## 4.4 Discussion

### *4.4.1 Patterns of plant species seasonal temperature distributions*

In order to understand how plant species are responding to drought conditions, we characterize dominant species temperature distributions. This produced an assessment of how species $T_s$ and $T_s$-$T_a$ varies annually throughout a prolonged drought and across seasons. These species have evolved adaptations that are common in a Mediterranean climate where precipitation is the limiting growth factor (Meentemeyer et al., 2001) and summer drought can result in 2 -11 months of water deficit (Pavlik, 1991). Within this study area are two ecoregion provinces: 1) chaparral forest/shrub and 2) open woodland, shrub, coniferous forest/meadow. These ecoregion provinces have different plant communities that have different adaptations for surviving prolonged periods of water stress, which we see reflected in the temperature distributions across dates.

The chaparral forest and shrub province covers the Santa Ynez-Sulphur Mountains and Santa Ynez Valleys and Hills sub-regions (Figure 4.1). These provinces had consistently lower TCI distributions across the nine dates. Chaparral plant species are adapted to withstand xylem cavitation and mechanical stresses that occur during the annual rainless period (Jacobsen et al., 2007). In fact, chaparral species have key physiological adaptions that maximize the capture and utilization of water and light which evolved as resistance to cavitation, thick evergreen leaves, and root to shoot ratios (Jacobsen et al., 2007; Kummerow et al., 1977; Meentemeyer et al., 2001). These adaptions translate into lower plant temperatures and less stress over the dates observed. In general, chaparral species, such as

CESP, had the lowest $T_s$-$T_a$ distributions. While all chaparral species have heightened resistance, species do vary in their extent to withstand extended dry conditions by having different biomechanical properties such as stem mechanical strength, root depth, fiber properties, and post-fire regeneration (Canadell et al., 1996; Jacobsen et al., 2007). These biomechanical differences among species have been found to be expressed in canopy temperature in deciduous tree forests (Scherrer et al., 2011). For these chaparral species, the biomechanical differences translate into significantly different temperature distributions. For example, two chaparral shrubs, *Baccharis pilularis* (BAPI) and *Adenostoma fasciculatum* (ADFA) have a rooting depth maximum of 3.2 and 7.6 m respectively (Canadell et al., 1996; Hellmers et al., 1955). BAPI experienced mean $T_s$-$T_a$ values greater than 15ºC for three dates, while ADFA did not have any mean $T_s$-$T_a$ values exceeding 13ºC. A greater rooting depth allows plants to access deeper water and allows them to keep stomata open, reducing plant temperatures and extending growth into the dry season (Gardner, 1983).

The open woodland, shrub, coniferous forest/meadow province covers the San Rafael-Topatopa Mountains, Interior Santa Lucia Range, Northern Transverse Ranges, Caliente Range-Cuyama Valley, and San Emigdio Mountains sub-regions (Figure 4.). This province has a large elevation gradient ranging from 800m to 2700m and is not in close proximity to the ocean. Due to this large elevation gradient, species at elevations < 1400 m exhibit very different adaptations to water and heat stress than species in the chaparral forest and shrub province. The three species with the largest $T_s$-$T_a$ difference (MAGF, ATCA-ERNA, JUCA) belong to this province at lower elevations. For Mediterranean annual grasses and forbs (MAGF), the start and end of the growing season is completely dictated by rainfall patterns (Bartolome et al., 2007; Xu and Baldocchi, 2004), with peak biomass generally

occurring during late spring when most of the available soil moisture has been used (George et al., 2001). By late summer, MAFG appears highly stressed according to the TCI but has actually fully senesced and is no longer transpiring. For annual species, such as MAGF and BRNI, the TCI index is misleading because it is unable to determine when a plant has actually died instead of being water stressed. As a halophyte, *Atriplex canescens* (ATCA) uses the saline soils in this area to lower leaf area and growth rate, which decreases the rate at which soil water is depleted, ultimately increasing the longevity of plants (Flowers and Yeo, 1986; Glenn and Brown, 1998). *Juniperus californica* (JUCA) is found on semi-arid leeward slopes with open crowns (Minnich, 2007) and belongs to a genus that is considered among the most resistant in the world to water-stress induced xylem cavitation (Maherali et al., 2004; Willson et al., 2008).

Found in elevations greater than 1400m, the open woodland, shrub, coniferous forest/meadow province also has one of the species that experienced minimal differences in $T_s$-$T_a$, *Pinus jeffreyi* (PIJE). Restricted to high elevations to achieve preferred growing conditions, this species is deeply rooted allowing for the species to access bedrock water throughout the growing season (Hubbert et al., 2001; Rose et al., 2003). Access to a reliable water supply has been linked to relatively high values and small fluctuations of predawn xylem pressure potential which results in PIJE being considered one of the most drought tolerant conifers (Delucia et al., 1988; Delucia and Schlesinger, 1991). PIJE did not experience prolonged periods of stress in this study area or time frame, but in other regions of Southern California this species' response to climatic factors has been a concern. In the San Bernardino mountains, leeward south-facing slopes of PIJE stands have been experiencing mass mortality that is likely due to climate forcing (Minnich et al., 1995).

Additionally, in the adjacent Santa Rosa mountain range, PIJE distributions increased in elevation by 28 m from 1977 to 2007 due to climate shifts (Kelly and Goulden, 2008). While conifers such as PIJE are drought tolerant, species such as JUCA are able to outcompete conifers by maintaining high maximum leaf conductance at very low soil water potentials which can strongly deplete soil water to a depth of 2 m (Delucia et al., 1988).

*4.4.2 Mapping plant stress*

Using imagery collected over California's 2013 – 2015 drought, we developed a temperature condition index (TCI) to capture plant species water stress across the landscape. Approximately 30% of the study area experienced high stress for seven to nine of the dates observed. Our analysis showed that June 2014 and August 2015 contained the highest amount of stress based on TCI values. In this region it would be expected that plant would experience more stress in August compared to June increase water deprivation. However, TCI is only a snapshot of a plant's current stress and leaf temperatures are highly influenced by the environmental conditions of that day (Gates, 1968; Jones, 2014). It is not a direct indication of repeated or cumulative stress. For example, 2014 August 29 and 2015 August 24 had similar daily maximum air temperatures around 26ºC, but 2014 had higher wind speeds (13 m/s vs. 3.6 m/s; NOAA MADIS). Although plant temperature and environmental conditions have complex feedbacks, laboratory experiments found that leaf temperatures decrease with increasing wind speeds and at the plant this may result in a decrease of water usage (Gates, 1968). So while the August dates had similar air temperatures and probably similar water availability, plants in the 2014 date experienced less stress then 2015 due to different wind speeds on that particular day measured.

Not only does plant stress increase a plant's susceptibility to insects and disease (Jackson, 1986; Schoeneweiss, 1975), but repeated water stress on plants has been linked to an increase in fire risk for the landscape (Dennison et al., 2003; Maselli et al., 2003; Verbesselt et al., 2007). Plant stress alone is not an indication of fire risk for an area because of the complex interaction of human, ecological, and climatic factors (Vidal et al., 1994). However, this area is already prone to wildfires with many areas having a time since last fire of less than 10 years (Figure 2; Moritz, 1997). Additionally, the frequency and size of fires has been increasing in the Los Padres National Forest (Moritz, 1997; Syphard et al., 2011). In our analysis, June 2014 and August 2015 dates showed the highest amount of stress across the landscape. Since June to September is the maximum fire danger period for this area, higher vegetation dryness due to water stress becomes a major predisposing factor for fire occurrence (Maselli et al., 2003).

Due to the increased fire risk in Mediterranean ecosystems (Fernandez-manso et al., 2016; Moritz, 1997; Mouillot et al., 2002; Vidal et al., 1994) and the predicted increase in wildfires due to climate change (Mastrandrea and Luers, 2012; Moriondo et al., 2006; Scholze et al., 2006), there has been a strong effort to predict the occurrence of wildfires. The statistical relationship between stress indices similar to TCI and fire frequency has been experimentally confirmed by several works. Maselli et al. (2003) found using NOAA Advanced Very High Resolution Radiometer (AVHRR) imagery that Normalized Difference Vegetation Index (NDVI) decreases in Mediterranean areas were linked to increased probability of fire occurrence during summer months. Using the Landsat imagery and an index based on the combination of vegetation index and $T_s$-$T_a$, researchers successfully located areas where fire risk was high and predicted fire events (Vidal and Devaux-Ros,

1995). Plant stress indices, such as TCI, may provide opportunities for parameterizing climate models or fire weather monitoring.

*4.4.3 Effects of topography on plant stress*

Topography, such as aspect, slope, and elevation, are useful surrogates for the spatial and temporal distributions of factors such as solar radiation and precipitation (Stage and Salas, 2007). This is especially true in Southern California where ecosystems are water-limited (Meentemeyer et al., 2001). The amount of solar radiation and precipitation an area receives during the year controls plant distributions, composition, and richness (Somers et al., 2015). Due to these relationships, we correlated topographic attributes to distributions of TCI across dates to assess the strength of their relationship to varying amounts of stress.

In our study, aspect was found to be highly correlated with plant stress which strongly impacts the amount of solar radiation a surface receives (Jones, 2014; Nunez, 1980). Ultimately the amount of solar radiation a surface receives impacts soil temperatures (Jones, 2014). In the northern hemisphere, south-southwest facing slopes receive more solar radiation compared to north-northeast facing slopes (Dubayah and Rich, 1995; Nunez, 1980). In agreement with this study, other studies have found that stressed plants were largely associated with south-southwest facing slopes (Guarín and Taylor, 2005; Paz-Kagan et al., 2017; Stephenson, 1998). In southern California, this association becomes more pronounced during the spring and summer due to a larger difference in energy balance and potential evapotranspiration between north and south facing slopes (Miller and Poole, 1983). In our analysis, April and June dates expressed a stronger correlation between TCI and N-S values. Plants located on south facing exposures are not only more stressed, but are also most susceptible to fire due to an increased likelihood of ignition caused by lower soil moisture

content and when burned experience the highest burn severity (Ireland and Petropoulos, 2015). North facing exposures, in addition to being less stressed, also recover faster when burned due to more favorable moisture conditions (Ireland and Petropoulos, 2015).

While aspect was found to have the strongest correlation with plant stress, expressions of aspect that incorporate interactions with slope also had strong correlations. These topographic attributes capture the effect aspect has on the amount of solar radiation a surface receives with increased slopes (Jones, 2014; Stage, 1976). In the literature, slope steepness displays diverse patterns since steep slopes may be related to high runoff and shallower slopes are related to low runoff and poor water drainage (Bennett et al., 2015; Guarín and Taylor, 2005). Additionally, for steeper slopes the slight advantage of a decrease in incoming solar radiation is likely offset by decreasing soil depth (Stage, 1976). Southwest and west facing aspect with shallow slopes were found to have high tree mortality in southern Sierra Nevada (Paz-Kagan et al., 2017). While another study in the Sierra Nevada found that the density of dead trees was higher on north slopes compared to south slopes (Guarín and Taylor, 2005).

*4.4.4 Considerations when using airborne thermal imagery*

An unavoidable characteristic of using large airborne thermal datasets is the temporal variation in image collection. Throughout the day, a plant's rate of evaporation and transpiration varies (Jones, 1999; Jones and Leinonen, 2003; Jones and Schofield, 2008). It is more efficient for a plant to restrict periods of open stomata and rapid photosynthesis to those times when potential evaporation is low, particularly in the morning, and close stomata during mid-day/afternoon which will improve water use efficiency (Jones, 2014). As stomata close and evaporation rates decrease to conserve water, a plant's temperature increases

(Jones and Leinonen, 2003; Jones and Schofield, 2008). Because of this relationship, diurnal patterns of plant temperatures and the difference in plant temperatures and air temperature are not static throughout the day. Plants are rarely at air temperature and are often warmer than the air during the day and cooler at night (Tanner, 1963). This is captured in diurnal patterns of latent heat flux with an increase throughout the morning and a peak around mid-day (Anderson et al., 1984; Verma et al., 1989, 1986). In our analysis, we captured this diurnal pattern in plant temperatures and found the timing of pixel collection was correlated with $T_s$ and, ultimately, plant stress measured with TCI. Since flightlines were not all collected at the same time, patterns of plant stress captured with TCI will include hourly variability in transpiration rates.

In our analysis, we restricted our analysis to natural vegetation and assumed that vegetation or plant species compose an entire 36 m pixel. However, when using coarser resolution thermal imagery, $T_s$ has been shown to be highly influenced by sub-pixel materials (Coates et al., 2015; Wetherley et al., 2018). The presence of soil, rock, or manmade surfaces can be a key source in $T_s$ variability due to material properties such as albedo, thermal conductivity, moisture content, and structure (Oke, 1988). Variability within a plant species' temperature has been found to be linked to the percent of green vegetation present in a pixel (Coates et al., 2015; Roberts et al., 2015). The Vegetation Condition Index (VCI) and Vegetation Temperature Condition (VTC) incorporate percent green vegetation fractional cover by using Normalized Difference Vegetation Index (NDVI) in addition to temperature (Kogan, 1997; Singh et al., 2003; Wan et al., 2004). While NDVI has been shown to be strongly correlated with percent green vegetation, it does not directly determine the sub-pixel materials or amounts (Carlson and Riziley, 1997; Jiang et al., 2006; Montandon and Small,

2008). Instead future works should include incorporating percent green vegetation by using a spectral mixture analysis (Settle and Drake, 1993).

The data used in this study is a precursor to the future Hyperspectral Infrared Imager (HyspIRI) mission, as it was identified in the 2017 decadal survey (National Academies of Sciences and Medicine, 2018). The HyspIRI mission would provide hyperspectral and thermal imagery with global coverage of Earth's ecosystems every 16 days (Lee et al., 2015). Additionally, the ECOsystem Spaceborne Thermal Radiometer Experiment on Space Station (ECOSTRESS) was launched in June 2018 with the primary goal of measuring plant temperatures in order to understand how much water plants need and how they respond to stress. The sensor was installed on the International Space Station (ISS) providing data with a 38-m in-track by 69-m cross-track spatial resolution and a predicted temperature sensitivity of ≤0.1 K (Lee et al., 2015). Our dataset only captures a snapshot of plant stress which is highly influenced by the environmental characteristics of that day and does not capture continued and prolonged stress throughout a year. The HyspIRI revisit time would allow researchers to monitor yearly trends of plant stress while accounting for the daily variability seen in plants' $T_s$. With the unique orbit of the ISS, composite ECOSTRESS data can be used to develop patterns of daily changes $T_s$ and evapotranspiration rates. These unprecedented datasets would allow for the continuous monitoring of plant stress at the species level, which can ultimately become a tool for managing natural vegetation across generally inaccessible areas or preparing and protecting communities from wildfires.

### 4.5 Conclusion

In this study, we answered three questions surrounding plant species during the extreme Southern California drought that ranged from 2012 – 2015. First, we asked whether

plant species exhibit significantly different temperature distributions across nine dates in 2013 - 2015. We found that 68 – 82% of species pairs were significantly different among each other across spring, summer, and fall imagery. Species pairs with different structures (herb vs. shrub vs. tree) resulted in the largest temperature distribution differences. Second, we asked how is plant stress distributed across that landscape during the extreme drought. Using plant species classification maps derived from hyperspectral data, we found that stress was not evenly distributed across the landscape. Open shrub/meadow ecoregion provinces had larger $T_s$-$T_a$ distributions compared to chaparral ecoregion provinces, which are generally located within closer proximity to the ocean. The June 2014 and August 2015 imagery contained the largest amount of stress across the landscape. Finally, we asked if topographic attributes were associated with patterns of high stress. We found that south and south-southwest facing slopes had the strongest correlation with high stress TCI values across all nine dates, while other topographic attributes were not strongly correlated to plant stress.

Together these findings suggest that we can use hyperspectral and land surface temperature data to monitor plant species' response to drought conditions across the landscape. During 2012 – 2015, California experienced an extreme drought in which the implications are still forthcoming. This research captured the spatial and temporal patterns of plant stress in Southern California, which can be used to help manage and monitor natural vegetation that is generally inaccessible and remote. Continuing to develop and refine methods for evaluating temporal patterns of plant species' stress is a necessary step towards a deeper, quantitative understanding of the functioning natural environment.

# 5. Conclusion

## 5.1 Summary of Research

Based on these results, synergies between hyperspectral VSWIR and TIR imagery can be used to extract crucial information about temporal and spatial distributions of plant species and stress. In Chapter 2, I found that hyperspectral VSWIR imagery could be used to discriminate plant species accurately across annual and phenological changes. Overall, classification accuracy was affected by a species' temporal spectral variability. Spectral libraries of single dates performed better than multiple date libraries, likely because they decreased within-class variance by reducing phenological variability that occurs across time. Spectral libraries that did not contain spectra from the classified image performed poorly, which indicates the limited applicability of transferring existing spectral libraries to future work. This research advances techniques for monitoring species across large spatial and temporal scales using proposed sensors like HyspIRI and ultimately supports many research agendas that are tracking ecosystem health and changes as a result of climate.

In Chapter 3, I found that hyperspectral TIR imagery could not be used to discriminate plant species at the canopy level, but species' canopy temperatures did exhibit significantly different distributions. Using laboratory leaf measurements, I found that approximately one third of the species showed distinct spectral separation from other species. However, at the canopy scale most species were not spectrally separable. A simple physical scaling model, using leaf inclination and leaf area index, did not accurately reproduce canopy emissivities, suggesting other variables are necessary for scaling leaf measurements to the canopy. While emissivity measurements do not appear to be useful for plant species research, the canopy temperature retrieved from the TIR imagery do show promise for future

vegetation research. We found that species canopy LSTs displayed unique distributions across dates and among species. Many of these distributions could be explained by canopy geometry with tree density and height playing key roles. Additionally, species canopy temperatures were highly influenced by a tree's surrounding environment with neighboring trees creating cooler LST and pavement creating warmer LST conditions. This study represents the first look at vegetation characteristics using NASA's HyTES TIR sensor, opening the door for future remote sensing vegetation studies including the recently launched ECOsystem Spaceborne Thermal Radiometer Experiment on Space Station (ECOSTRESS) mission.

In Chapter 4, I found the combined use of hyperspectral VSWIR and surface temperature imagery can be used to monitor plant species' stress throughout California's 2013 – 2015 drought. Using the fused imagery, the temperature condition index (TCI) was calculated to measure plant stress by using plant species' surface minus air temperature distributions across dates. Overall, 68 – 82% of species pairs exhibited significantly different temperature distributions across the nine dates of imagery covering the drought. Plant stress was not evenly distributed across the landscape or time with lower elevation open shrub/meadows and June imagery capturing the largest amount of stress. Highly stressed plants were correlated with south or south-southwest facing slopes, while other topographic attributes were weakly correlated with TCI. Our results show that by using thermal and hyperspectral measurements we can monitor plant stress temporally and across ecoregions. This work supports improved monitoring of natural landscapes, with emphasis on areas prone to continued drought and high risk of wildfires.

## 5.2 Ongoing research and future directions

The results of this dissertation can be immediately employed in a variety of ongoing and planned science missions including Surface Biology and Geology (SBG), Environmental Mapping and Analysis Program (EnMAP), National Ecological Observatory Network (NEON), Hyperspectral Thermal Emission Spectrometer (HyTES), and ECOsystem Spaceborne Thermal Radiometer Experiment on Space Station (ECOSTRESS). There is considerable room for growth in plant species characterization using either hyperspectral VSWIR imagery, hyperspectral TIR imagery, or fused hyperspectral VSWIR and broadband TIR imagery.

In Chapter 2, we successfully used hyperspectral VSWIR imagery to classify plant species across nine dates. However, we only used one classification method and there are many other types of classifiers available. In particular, future research should include classifiers that are capable of handling non-gaussian data due to the nature of VSWIR vegetation signatures. These classifiers could include support vector machine (SVM; Colgan et al., 2012; Jones et al., 2010) or generative adversarial networks (Han et al., 2017; He et al., 2017). Additionally, our research found that spectral libraries are not portable across dates. Future research needs to be directed towards handling large temporal hyperspectral datasets so that comparisons across years and seasons would be feasible. Perhaps under similar conditions, such as soil moisture and lighting, spectral libraries would be transferrable across dates. Another way to handle temporal classification is to move away from the use of spectral libraries and instead rely on reference polygons. We believe there is a need for starting a public geodatabase of reference polygons and locations of species and classes that can be used for any research application, sensor, or time period. The development of such a

database would provide a validation and training dataset that can be used across all remote sensing platforms for any application.

Chapter 3 demonstrated the abilities of the HyTES sensor for characterizing plant species. To our knowledge, our work is only the second study to examine plant species' high spectral resolution emissivities using airborne imagery (Ribeiro Da Luz and Crowley, 2010). Most hyperspectral TIR research is restricted to the leaf level and currently relationships developed using leaf emissivities will not be directly translatable to the canopy for future airborne or spaceborne missions (Ribeiro Da Luz and Crowley, 2007). Future research should explore the use of radiative transfer models to scale leaf level measurements to canopy level in the TIR domain (Francois et al., 1997; Jacob et al., 2017; Olioso, 1995; Snyder and Wan, 1998; Verhoef et al., 2007). In our research, we found the species exhibit unique temperature distributions that are linked to canopy structure and surrounding attributes. However, it is necessary to have a thorough examination of the seasonality and magnitude of drivers for species' canopy temperature, which would be of particular interest to urban tree planning and modelling (Leuzinger et al., 2010, 2005; Leuzinger and Körner, 2007).

In Chapter 4, we monitored plant stress across California's severe 2013 – 2015 drought. Variability within a plant species' temperature has been found to be linked to the percent of green vegetation present in a pixel (Coates et al., 2015; Roberts et al., 2015). Future research should incorporate the percent of non-photosynthetic vegetation in pixels for a more robust characterization of drought patterns. For example, the Vegetation Condition Index (VCI) and Vegetation Temperature Condition (VTC) incorporate percent green vegetation fractional cover by using Normalized Difference Vegetation Index (NDVI) in

addition to temperature (Kogan, 1997; Singh et al., 2003; Wan et al., 2004). Instead of using a vegetation index to approximate percent green vegetation, AVIRIS imagery can be used with a spectral mixture analysis (SMA) to estimate composition (Roberts et al., 1998). This research was performed on a regional scale, but could be scaled globally with the launch of a spaceborne hyperspectral sensor. The proposed SBG satellite mission would be equipped to discern the plant species distributions and physiological functions. Combined with existing platforms that measure canopy temperatures, such as ECOSTRESS, this research could be scaled to monitor drought conditions globally.

Based on these results, I conclude that the combined use of hyperspectral VSWIR and TIR imagery can produce unique insights into plant species' temporal and spatial variability over a period of increasing water stress. Research indicates that only 30 years of warmer temperatures has already affected the phenology, distribution, range, dynamics, and composition of plant species (Walther et al., 2002). Furthermore, predictions of future climate change are highly variable which exacerbates our uncertainty about future trajectories for ecosystems. Due to these pressing changes, it is important to develop techniques that utilize spaceborne platforms to quantify and characterize ecosystems at the plant species level (Ustin, 2013). Generating maps of plant species using a global imaging spectrometer and multi-spectral TIR sensor gains the scientific community knowledge of composition and spatial extent of dominant plant species within an ecosystem. This information is necessary for many research agendas that are tracking ecosystem health and changes (Lawrence and Labus, 2003; Riaño et al., 2002; Tane et al., 2018a; Underwood et al., 2003). Furthermore, greater understanding of the spatial and temporal variability of canopy temperature will increase our knowledge of vegetation energy balance and functions.

Analysis of canopy temperature will aid global ecosystem modeling efforts by decreasing uncertainties of model inputs (Goodenough et al., 2006; Schimel et al., 2014). Fusing hyperspectral VSWIR and TIR imagery together will improve efforts to monitor ecosystems at large spatial and temporal scales and ultimately contribute to our understanding of how climate change is affecting the world's ecosystems.

# A. Appendix: Supplementary materials for Chapter 2: Classifying California plant species temporally using airborne hyperspectral imagery

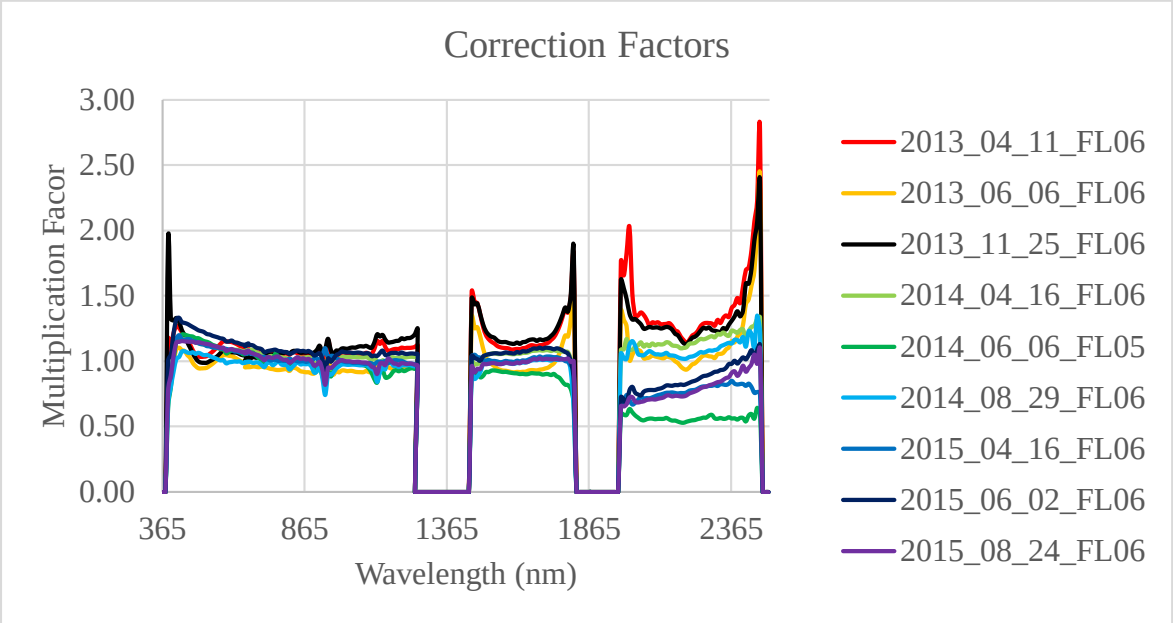


*Figure A.1. Spectral correction factors applied to imagery for radiometric normalization.*

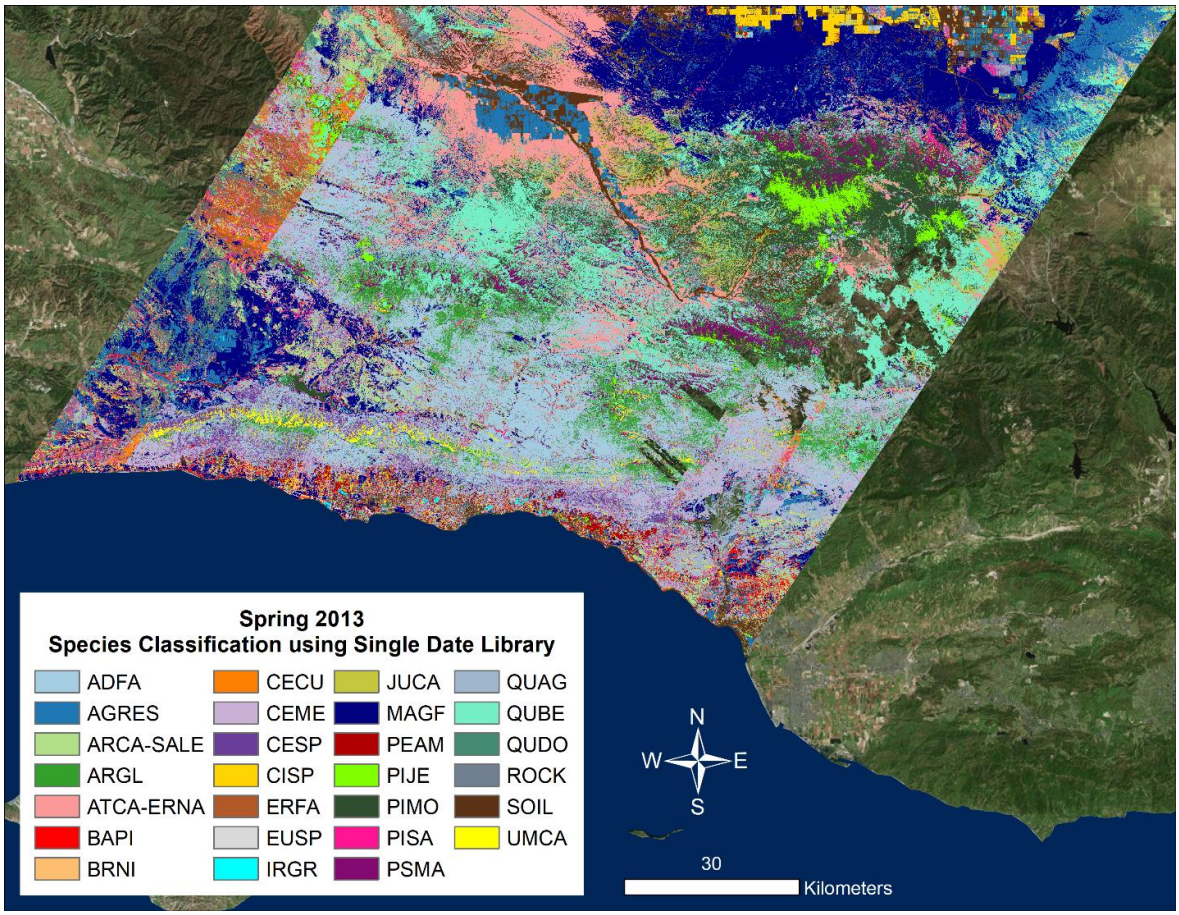


*Figure A.2. Plant species classification using single date spectral library for 2013 spring imagery.*

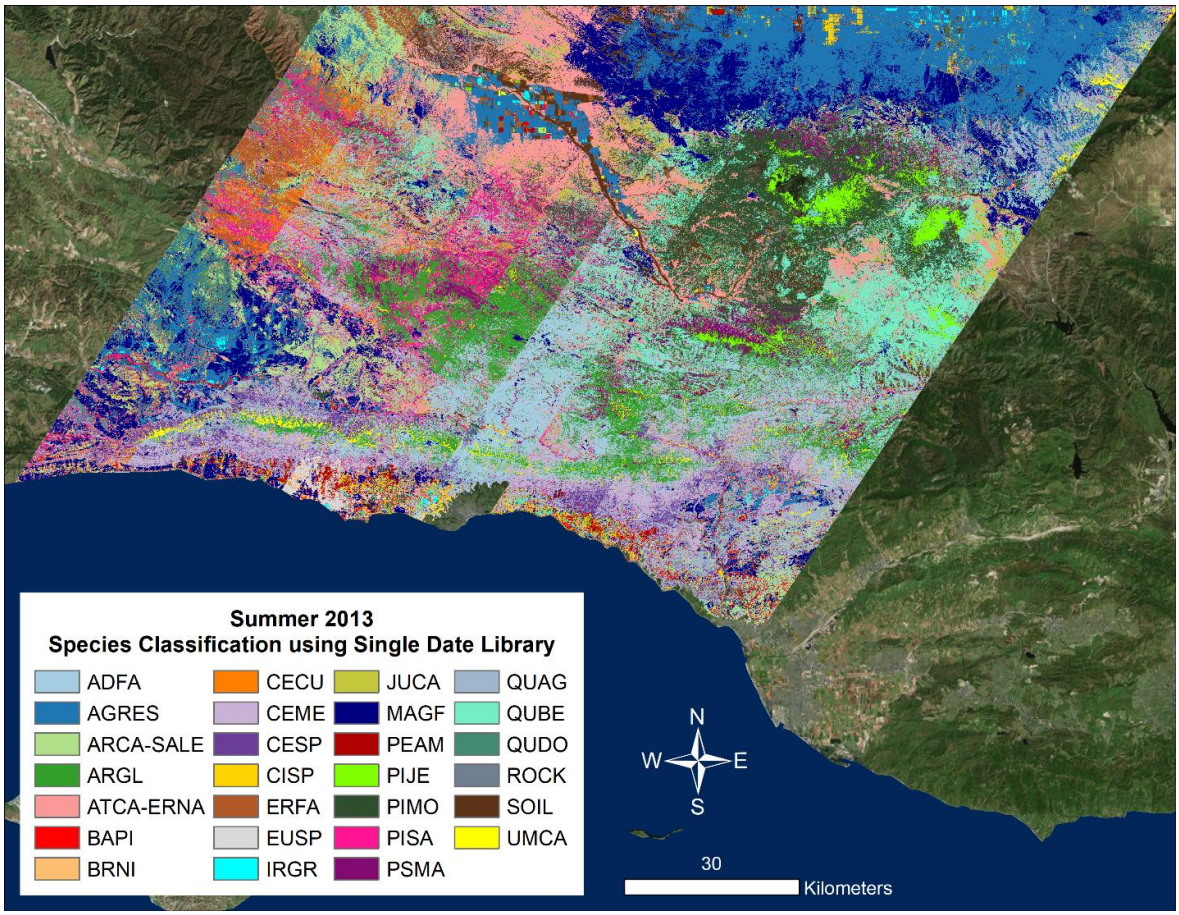


*Figure A.3. Plant species classification using single date spectral library for 2013 summer imagery.*

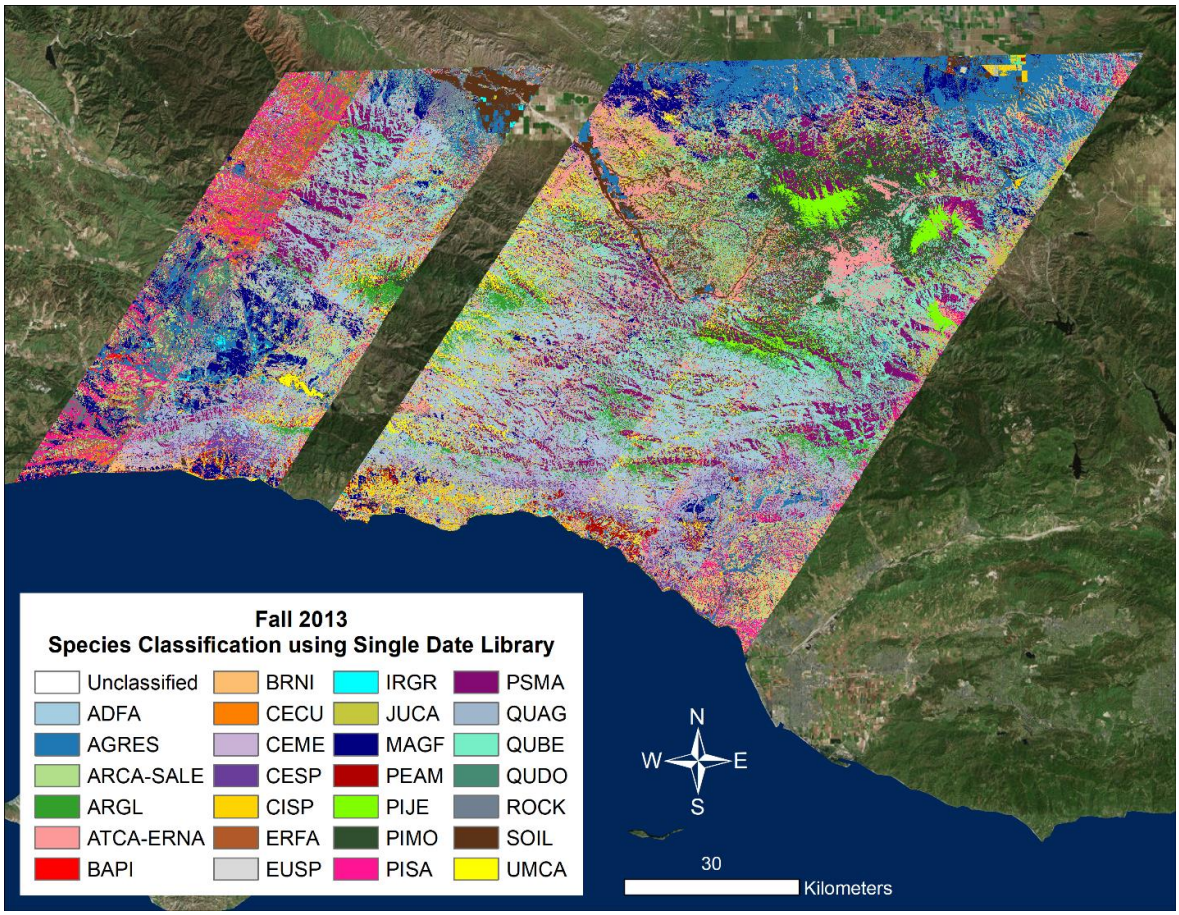


*Figure A.4. Plant species classification using single date spectral library for 2013 fall imagery.*

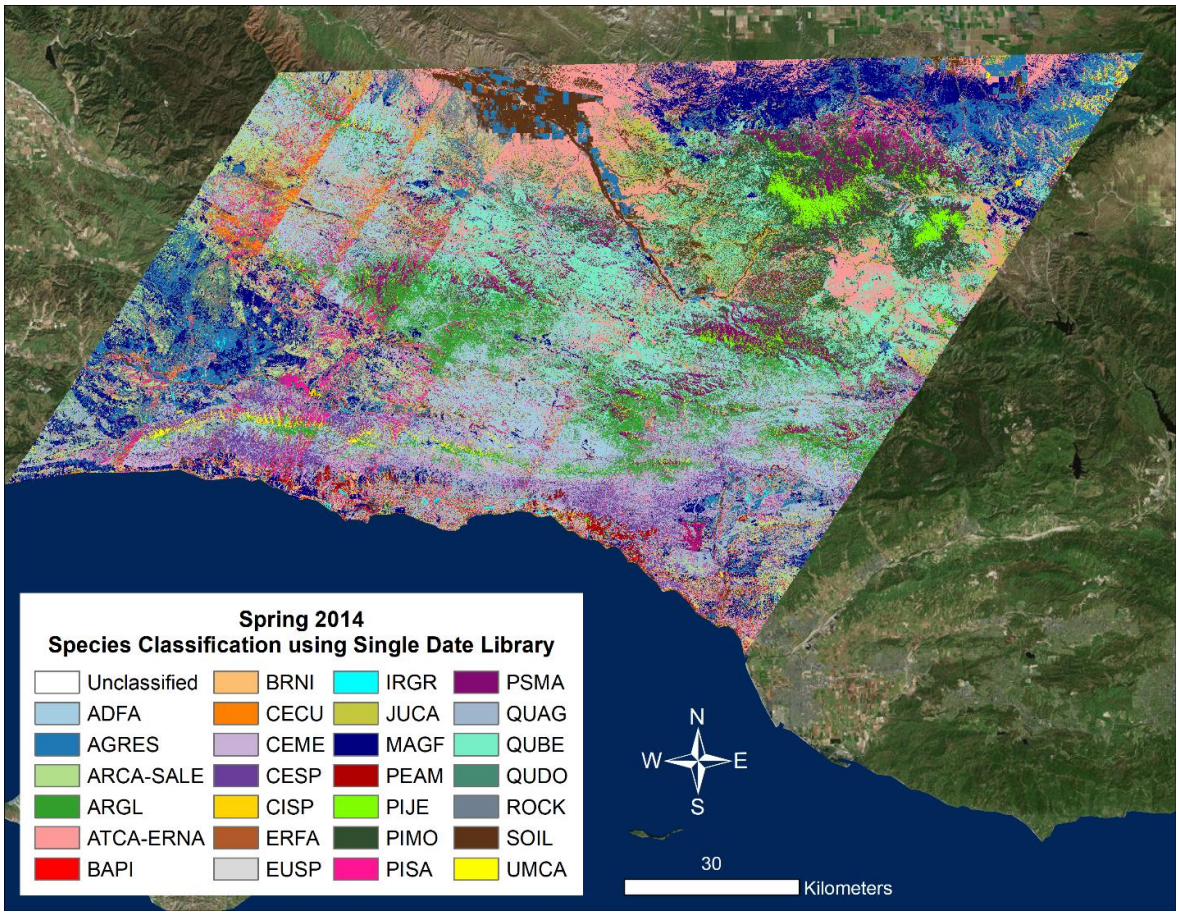


*Figure A.5. Plant species classification using single date spectral library for 2014 spring imagery.*

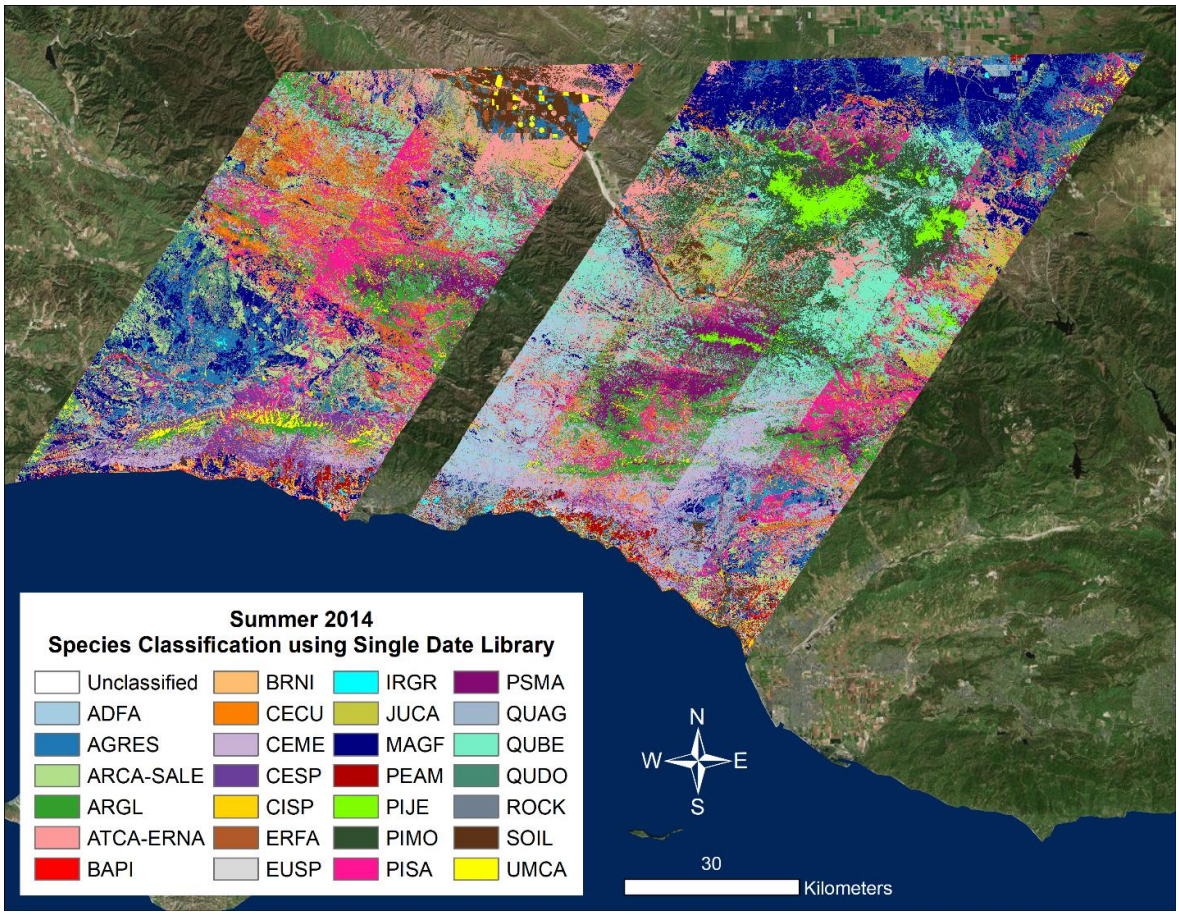


*Figure A.6. Plant species classification using single date spectral library for 2014 summer imagery.*

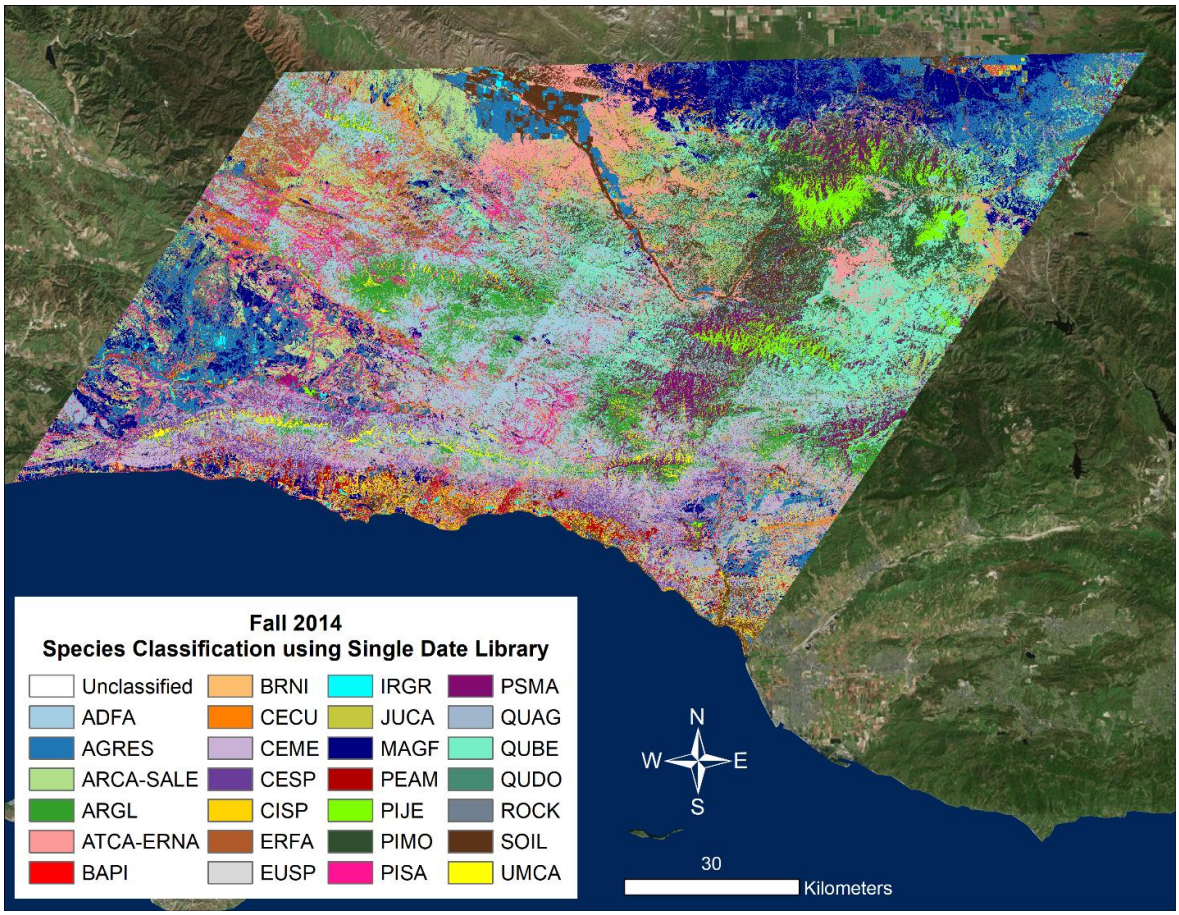


*Figure A.7. Plant species classification using single date spectral library for 2014 fall imagery.*

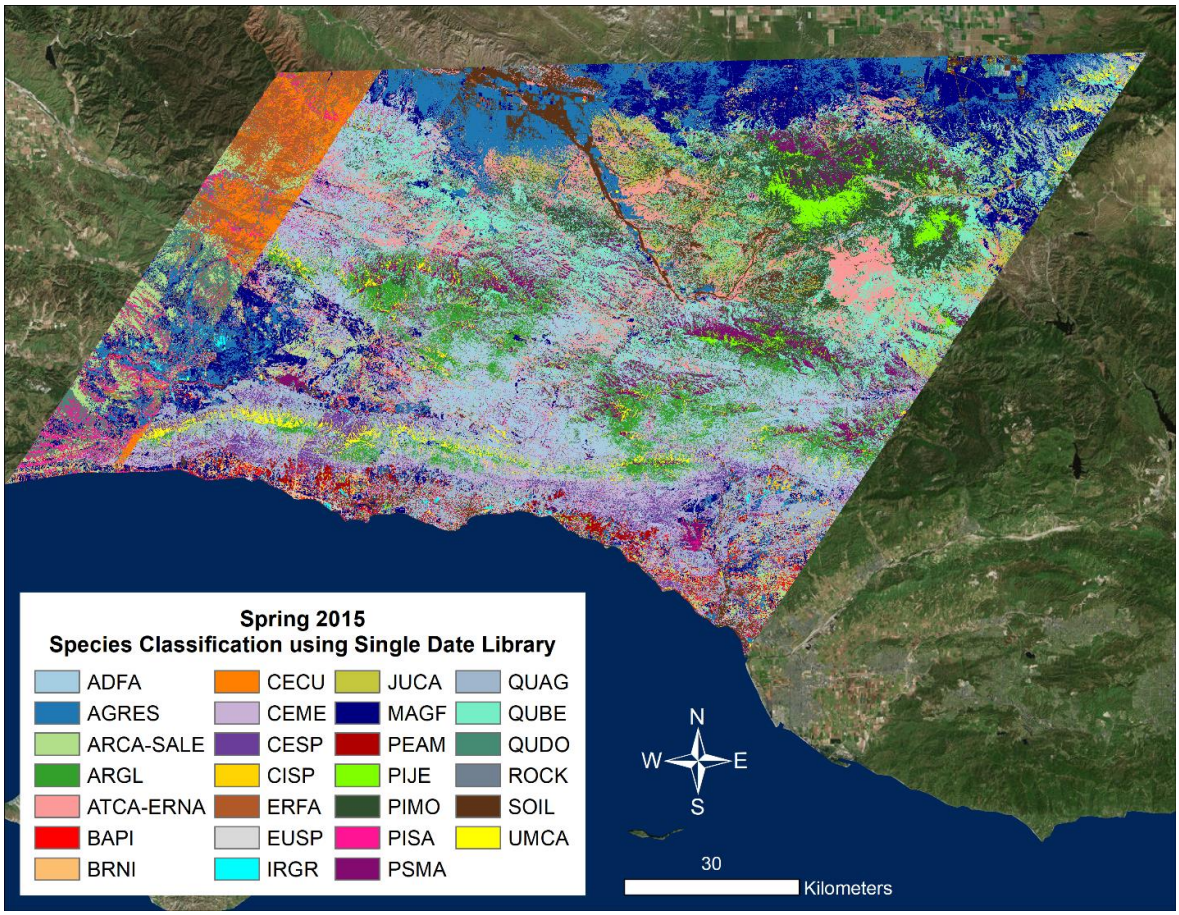


*Figure A.8. Plant species classification using single date spectral library for 2015 spring imagery.*

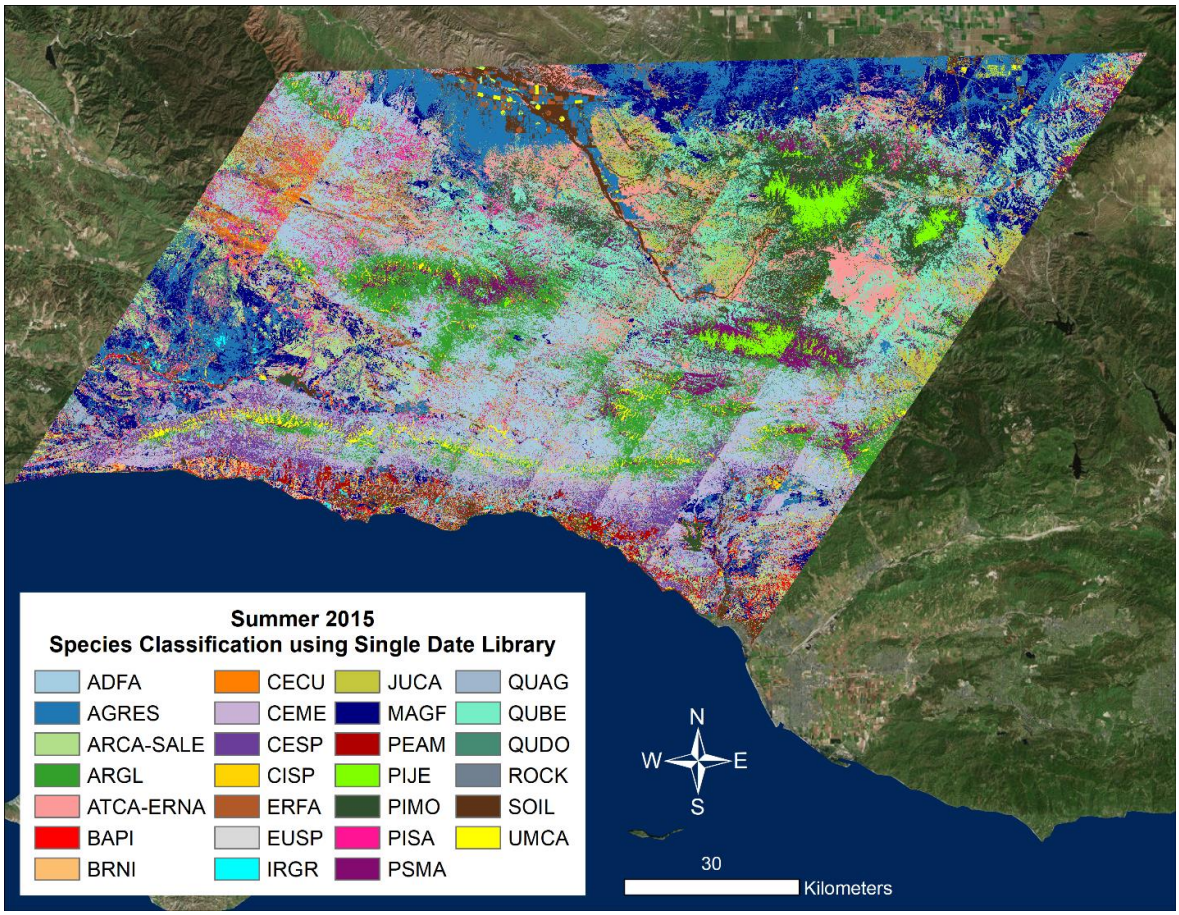


*Figure A.9. Plant species classification using single date spectral library for 2015 summer imagery.*

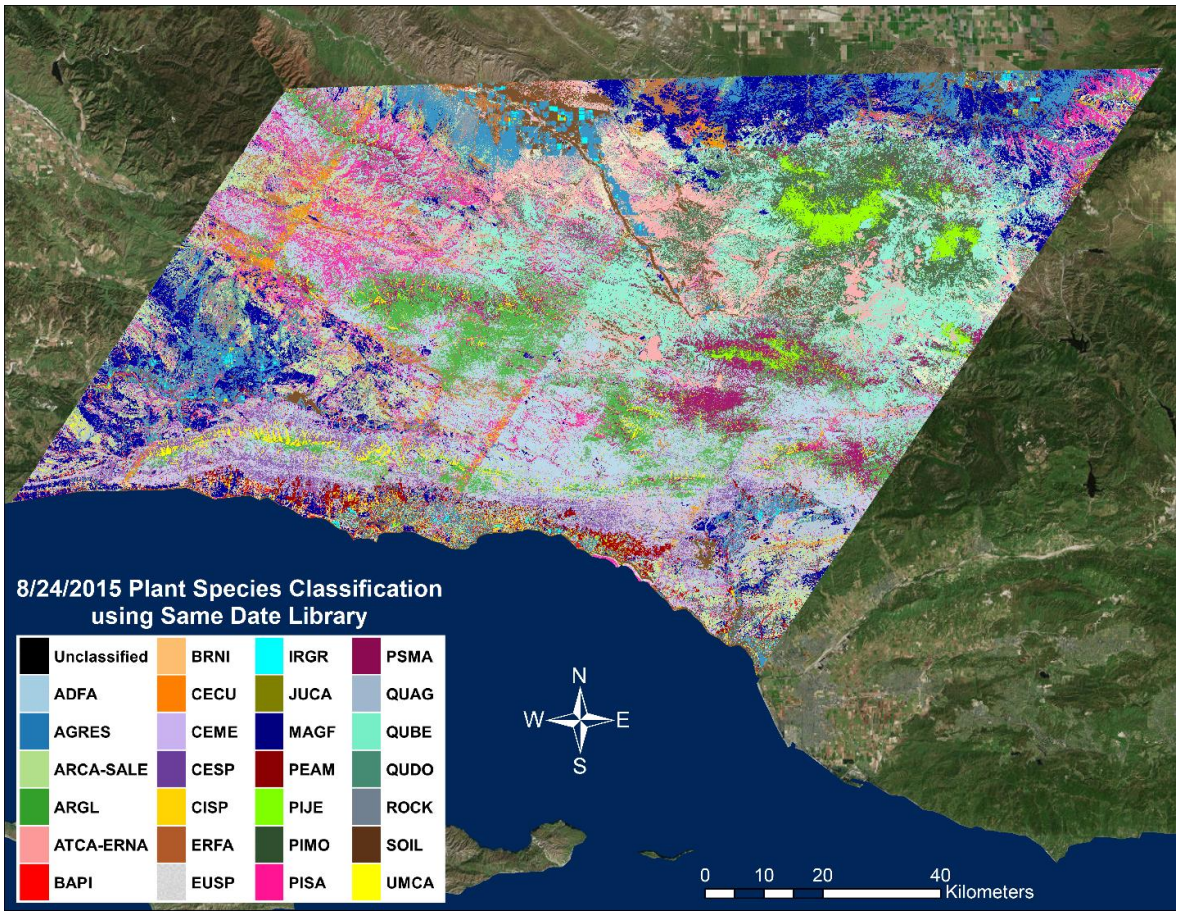


*Figure A.10. Plant species classification using single date spectral library for 2015 fall imagery.*

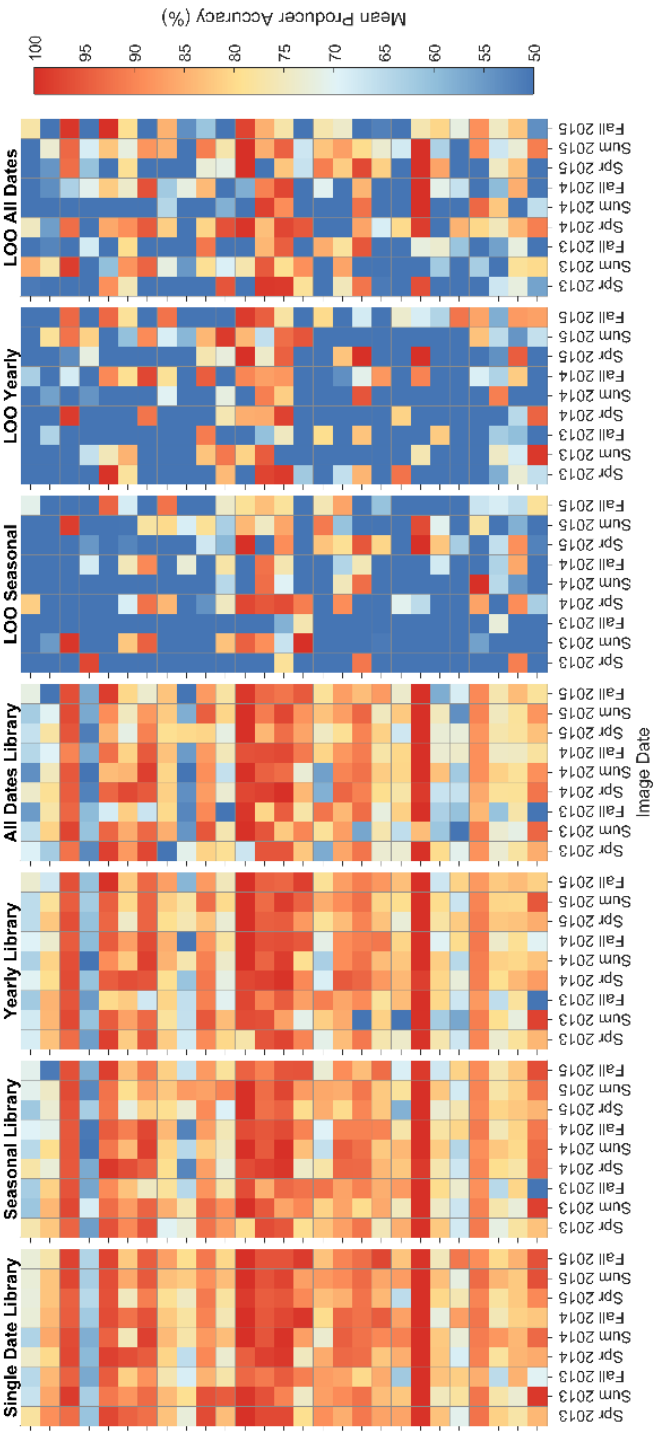


*Figure A.11. Mean producer accuracies for all classes using five spectral libraries on the nine image dates.*

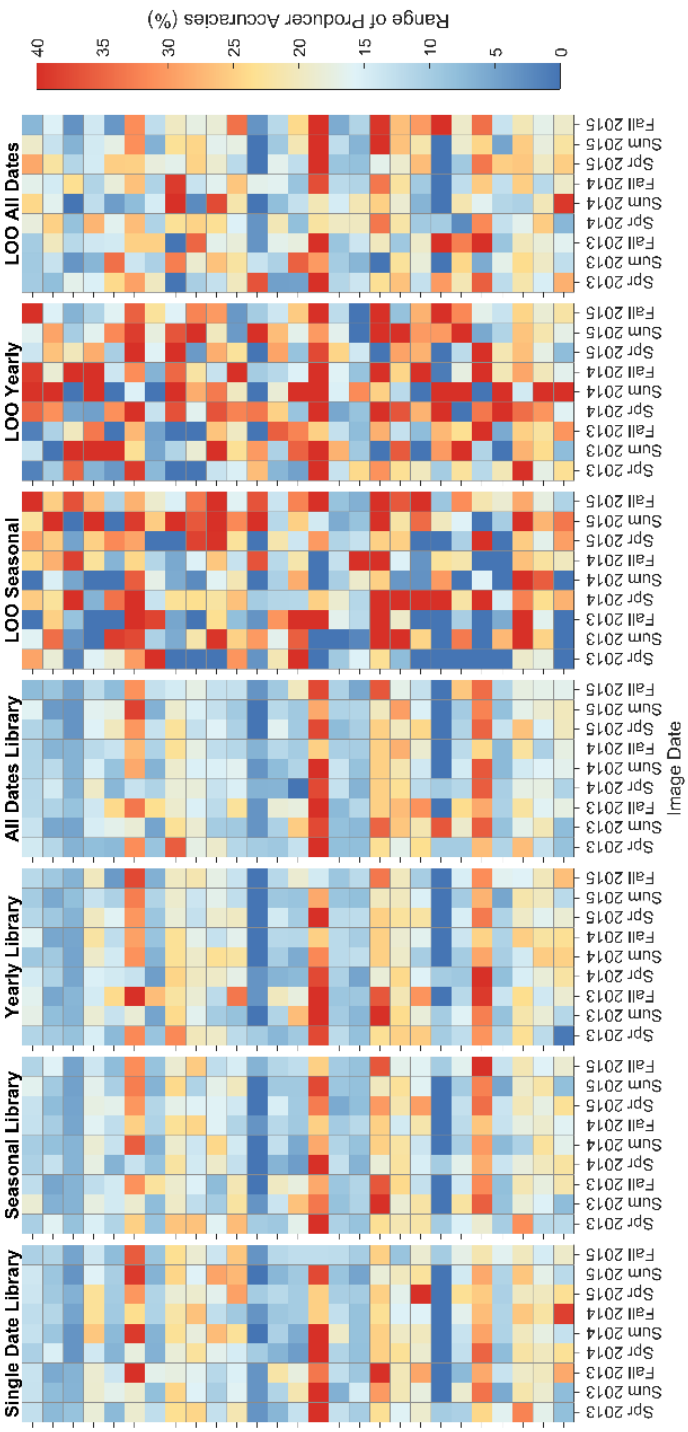


*Figure A.12. Range of producer's accuracies for all classes using five spectral libraries on the nine image dates.*

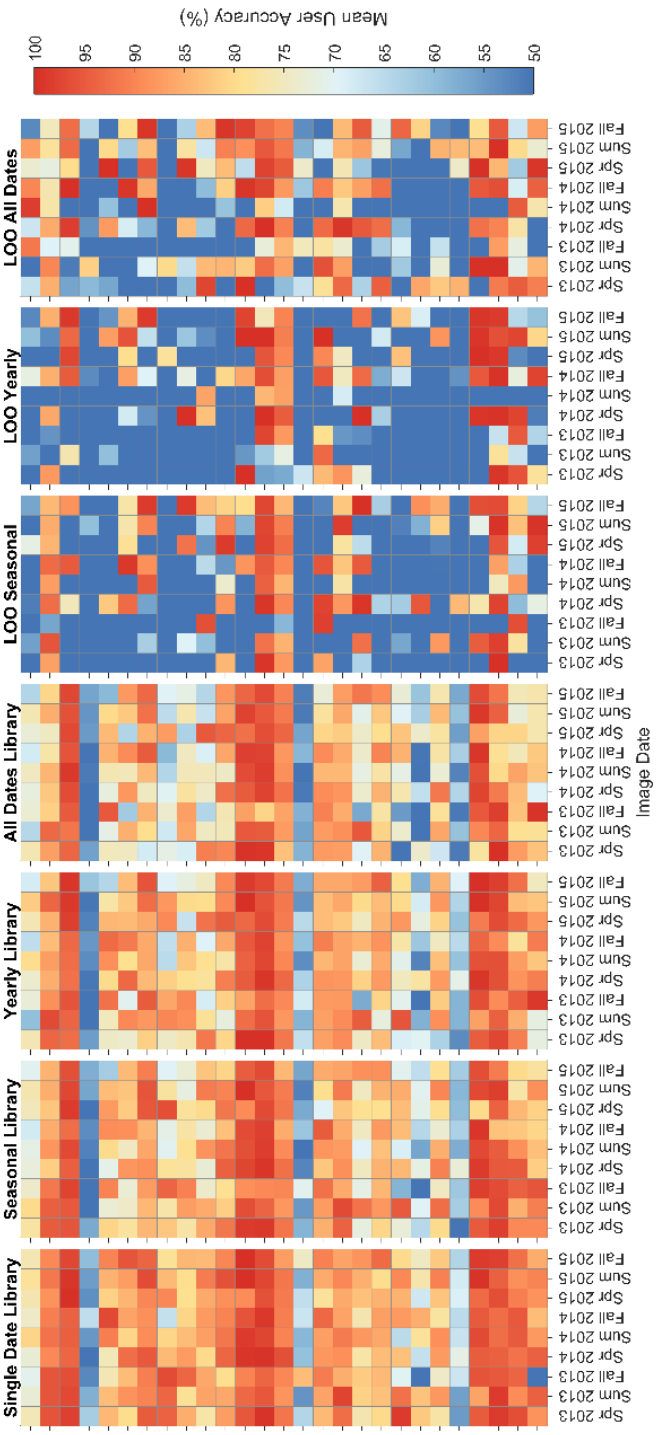


*Figure A.13. Mean user accuracies for all classes using five spectral libraries on the nine image dates.*

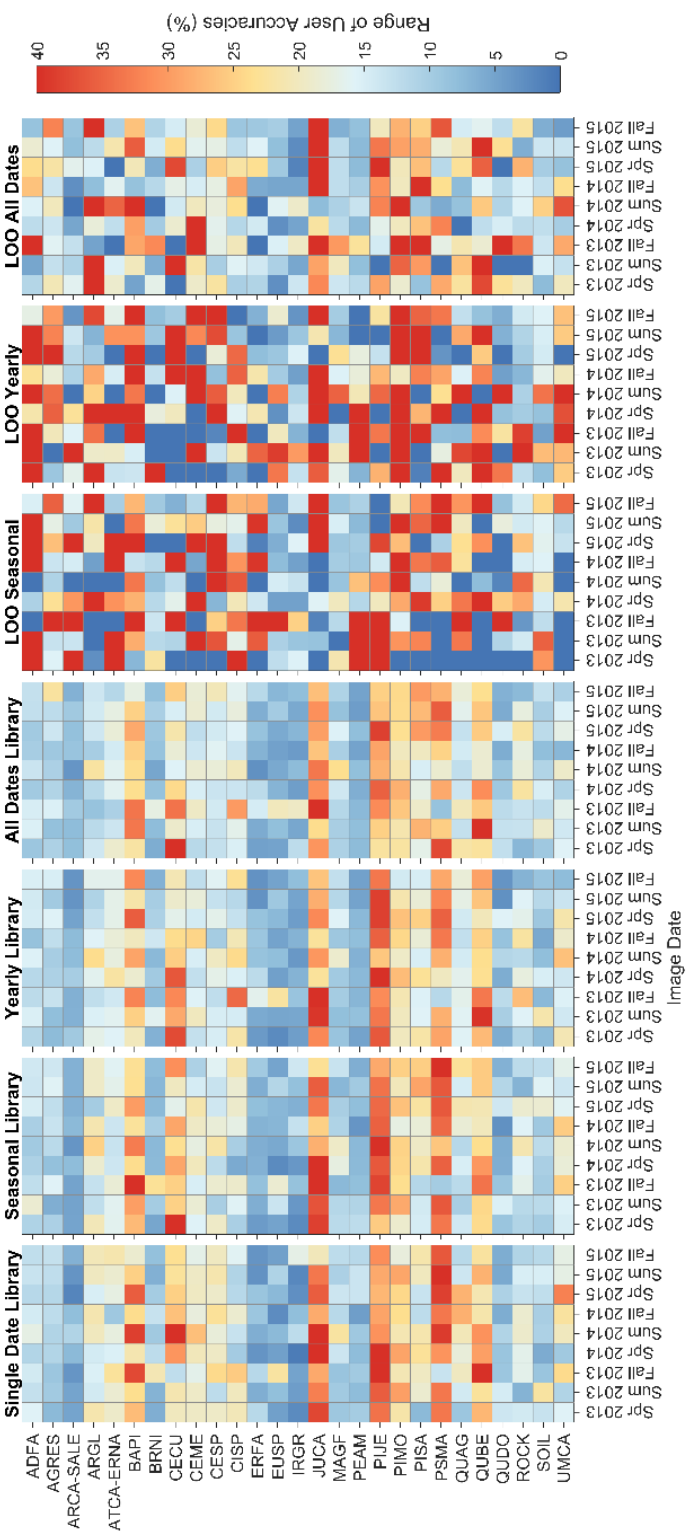


*Figure A.14. Range of user accuracies for all classes using five spectral libraries on the nine image dates.*

*Table A.1. Single date spectral library classification with minimum, mean, maximum overall and kappa classification accuracy calculated from 50 iterations.*

| Library Name | Image Date | Overall | | | Kappa | | |
|---|---|---|---|---|---|---|---|
| | | Min | Mean | Max | Min | Mean | Max |
| Spr-2013 Single Date | Spr 2013 | 83.64 | 85.08 | 86.49 | 0.83 | 0.84 | 0.86 |
| | Sum 2013 | 33.44 | 37.90 | 43.67 | 0.31 | 0.35 | 0.41 |
| | Fall 2013 | 23.44 | 26.23 | 28.31 | 0.20 | 0.23 | 0.25 |
| | Spr 2014 | 36.99 | 40.17 | 45.52 | 0.35 | 0.38 | 0.43 |
| | Sum 2014 | 16.48 | 19.46 | 22.55 | 0.14 | 0.17 | 0.20 |
| | Fall 2014 | 23.49 | 26.58 | 29.19 | 0.21 | 0.24 | 0.26 |
| | Spr 2015 | 32.08 | 36.79 | 40.24 | 0.30 | 0.34 | 0.38 |
| | Sum 2015 | 28.88 | 33.36 | 38.60 | 0.26 | 0.30 | 0.35 |
| | Fall 2015 | 16.72 | 20.51 | 23.94 | 0.15 | 0.19 | 0.22 |
| Sum-2013 Single Date | Spr 2013 | 29.82 | 33.08 | 36.06 | 0.27 | 0.30 | 0.34 |
| | Sum 2013 | 80.13 | 81.79 | 83.51 | 0.79 | 0.81 | 0.83 |
| | Fall 2013 | 23.67 | 26.13 | 28.00 | 0.21 | 0.23 | 0.25 |
| | Spr 2014 | 24.04 | 29.52 | 34.30 | 0.22 | 0.28 | 0.32 |
| | Sum 2014 | 25.22 | 27.31 | 29.84 | 0.23 | 0.25 | 0.27 |
| | Fall 2014 | 25.19 | 29.72 | 34.64 | 0.23 | 0.27 | 0.32 |
| | Spr 2015 | 35.61 | 38.94 | 43.36 | 0.33 | 0.37 | 0.41 |
| | Sum 2015 | 28.83 | 33.47 | 38.50 | 0.26 | 0.31 | 0.36 |
| | Fall 2015 | 21.37 | 26.37 | 31.92 | 0.19 | 0.24 | 0.30 |
| Fall-2013 Single Date | Spr 2013 | 20.13 | 22.79 | 26.25 | 0.17 | 0.20 | 0.23 |
| | Sum 2013 | 22.13 | 26.60 | 30.10 | 0.19 | 0.24 | 0.27 |
| | Fall 2013 | 76.90 | 79.15 | 80.75 | 0.76 | 0.78 | 0.80 |
| | Spr 2014 | 15.49 | 18.17 | 22.61 | 0.13 | 0.15 | 0.20 |
| | Sum 2014 | 12.62 | 16.54 | 21.60 | 0.09 | 0.14 | 0.19 |
| | Fall 2014 | 32.54 | 37.49 | 43.04 | 0.29 | 0.34 | 0.40 |
| | Spr 2015 | 15.88 | 21.83 | 27.81 | 0.13 | 0.19 | 0.25 |
| | Sum 2015 | 21.51 | 26.57 | 31.68 | 0.18 | 0.24 | 0.29 |
| | Fall 2015 | 26.61 | 32.16 | 38.70 | 0.23 | 0.29 | 0.36 |
| Spr-2014 Single Date | Spr 2013 | 7.17 | 9.24 | 13.02 | 0.04 | 0.06 | 0.10 |
| | Sum 2013 | 8.41 | 10.38 | 13.58 | 0.05 | 0.06 | 0.09 |
| | Fall 2013 | 18.92 | 21.88 | 25.06 | 0.16 | 0.19 | 0.22 |
| | Spr 2014 | 83.41 | 84.93 | 87.13 | 0.83 | 0.84 | 0.87 |
| | Sum 2014 | 20.63 | 24.28 | 28.22 | 0.18 | 0.22 | 0.26 |
| | Fall 2014 | 33.55 | 36.00 | 39.02 | 0.31 | 0.34 | 0.37 |
| | Spr 2015 | 37.72 | 40.74 | 43.89 | 0.35 | 0.38 | 0.42 |
| | Sum 2015 | 42.60 | 45.30 | 47.82 | 0.40 | 0.43 | 0.46 |

| | | | | | | | |
|---|---|---|---|---|---|---|---|
| | Fall 2015 | 33.37 | 39.27 | 42.38 | 0.31 | 0.37 | 0.40 |
| Sum-2014 Single Date | Spr 2013 | 18.59 | 22.01 | 24.75 | 0.16 | 0.19 | 0.22 |
| | Sum 2013 | 17.94 | 22.75 | 27.31 | 0.14 | 0.19 | 0.24 |
| | Fall 2013 | 16.39 | 18.16 | 19.61 | 0.13 | 0.15 | 0.16 |
| | Spr 2014 | 24.73 | 29.84 | 33.26 | 0.21 | 0.26 | 0.30 |
| | Sum 2014 | 81.97 | 83.75 | 85.31 | 0.81 | 0.83 | 0.85 |
| | Fall 2014 | 28.79 | 34.67 | 39.57 | 0.25 | 0.31 | 0.36 |
| | Spr 2015 | 32.49 | 36.08 | 39.65 | 0.29 | 0.33 | 0.37 |
| | Sum 2015 | 21.13 | 24.77 | 27.90 | 0.17 | 0.21 | 0.24 |
| | Fall 2015 | 33.08 | 36.82 | 39.39 | 0.29 | 0.33 | 0.36 |
| Fall-2014 Single Date | Spr 2013 | 0.87 | 1.52 | 3.27 | 0.00 | 0.01 | 0.02 |
| | Sum 2013 | 3.15 | 4.00 | 5.67 | 0.02 | 0.03 | 0.04 |
| | Fall 2013 | 7.93 | 9.92 | 11.90 | 0.06 | 0.08 | 0.10 |
| | Spr 2014 | 33.48 | 37.28 | 42.56 | 0.31 | 0.35 | 0.41 |
| | Sum 2014 | 5.70 | 7.46 | 10.21 | 0.04 | 0.06 | 0.09 |
| | Fall 2014 | 82.09 | 84.02 | 85.33 | 0.81 | 0.83 | 0.85 |
| | Spr 2015 | 30.14 | 35.52 | 41.19 | 0.28 | 0.34 | 0.39 |
| | Sum 2015 | 28.91 | 38.86 | 47.00 | 0.27 | 0.37 | 0.45 |
| | Fall 2015 | 43.65 | 49.25 | 55.76 | 0.41 | 0.47 | 0.54 |
| Spr-2015 Single Date | Spr 2013 | 3.50 | 5.51 | 6.75 | 0.02 | 0.04 | 0.05 |
| | Sum 2013 | 7.10 | 10.13 | 12.98 | 0.06 | 0.08 | 0.11 |
| | Fall 2013 | 7.58 | 9.08 | 11.21 | 0.05 | 0.07 | 0.09 |
| | Spr 2014 | 35.13 | 39.20 | 43.41 | 0.33 | 0.37 | 0.41 |
| | Sum 2014 | 13.19 | 15.93 | 19.44 | 0.10 | 0.13 | 0.17 |
| | Fall 2014 | 27.91 | 30.15 | 32.90 | 0.25 | 0.28 | 0.30 |
| | Spr 2015 | 80.02 | 81.70 | 83.50 | 0.79 | 0.81 | 0.83 |
| | Sum 2015 | 28.46 | 34.14 | 38.38 | 0.26 | 0.32 | 0.36 |
| | Fall 2015 | 26.41 | 31.18 | 35.31 | 0.24 | 0.29 | 0.33 |
| Sum-2015 Single Date | Spr 2013 | 6.75 | 8.23 | 11.27 | 0.04 | 0.06 | 0.09 |
| | Sum 2013 | 16.85 | 19.69 | 23.91 | 0.14 | 0.17 | 0.21 |
| | Fall 2013 | 18.89 | 21.07 | 25.00 | 0.16 | 0.18 | 0.22 |
| | Spr 2014 | 35.24 | 41.82 | 49.02 | 0.33 | 0.40 | 0.47 |
| | Sum 2014 | 11.41 | 13.85 | 16.87 | 0.10 | 0.12 | 0.15 |
| | Fall 2014 | 24.29 | 31.88 | 39.98 | 0.21 | 0.29 | 0.36 |
| | Spr 2015 | 29.51 | 35.61 | 42.07 | 0.27 | 0.33 | 0.39 |
| | Sum 2015 | 82.97 | 84.15 | 85.59 | 0.82 | 0.83 | 0.85 |
| | Fall 2015 | 28.96 | 37.33 | 41.55 | 0.27 | 0.35 | 0.39 |
| Fall-2015 Single Date | Spr 2013 | 7.43 | 13.21 | 20.07 | 0.05 | 0.11 | 0.17 |
| | Sum 2013 | 11.99 | 17.52 | 22.39 | 0.09 | 0.14 | 0.20 |
| | Fall 2013 | 12.53 | 15.52 | 18.98 | 0.09 | 0.12 | 0.16 |
| | Spr 2014 | 34.80 | 37.60 | 41.62 | 0.33 | 0.36 | 0.40 |
| | Sum 2014 | 17.08 | 23.11 | 27.80 | 0.15 | 0.20 | 0.25 |

| | | | | | | | |
|---|---|---|---|---|---|---|---|
| | Fall 2014 | 34.59 | 37.91 | 43.48 | 0.32 | 0.35 | 0.41 |
| | Spr 2015 | 28.10 | 32.51 | 36.32 | 0.26 | 0.30 | 0.34 |
| | Sum 2015 | 44.82 | 47.91 | 51.30 | 0.42 | 0.46 | 0.49 |
| | Fall 2015 | 82.08 | 83.34 | 84.65 | 0.81 | 0.83 | 0.84 |

*Table A.2. Multiple date spectral library classification with minimum, mean, maximum overall and kappa classification accuracy calculated from 50 iterations.*

| Library Name | Image Date | Overall | | | Kappa | | |
|---|---|---|---|---|---|---|---|
| | | Min | Mean | Max | Min | Mean | Max |
| Spr-All | Spr 2013 | 80.26 | 81.45 | 82.48 | 0.79 | 0.81 | 0.82 |
| | Sum 2013 | 57.73 | 59.78 | 62.12 | 0.56 | 0.58 | 0.60 |
| | Fall 2013 | 33.05 | 35.49 | 37.74 | 0.30 | 0.33 | 0.35 |
| | Spr 2014 | 81.39 | 82.62 | 84.13 | 0.81 | 0.82 | 0.83 |
| | Sum 2014 | 29.16 | 30.74 | 32.88 | 0.27 | 0.28 | 0.30 |
| | Fall 2014 | 36.36 | 38.98 | 43.21 | 0.34 | 0.37 | 0.41 |
| | Spr 2015 | 76.25 | 78.12 | 79.52 | 0.75 | 0.77 | 0.79 |
| | Sum 2015 | 51.86 | 54.21 | 58.11 | 0.50 | 0.52 | 0.56 |
| | Fall 2015 | 36.43 | 40.16 | 44.19 | 0.34 | 0.38 | 0.42 |
| Sum-All | Spr 2013 | 37.73 | 40.35 | 42.27 | 0.36 | 0.38 | 0.40 |
| | Sum 2013 | 78.35 | 80.25 | 81.60 | 0.77 | 0.79 | 0.81 |
| | Fall 2013 | 30.52 | 33.27 | 35.29 | 0.28 | 0.30 | 0.33 |
| | Spr 2014 | 51.97 | 53.85 | 55.83 | 0.50 | 0.52 | 0.54 |
| | Sum 2014 | 79.54 | 80.98 | 82.67 | 0.79 | 0.80 | 0.82 |
| | Fall 2014 | 61.24 | 63.58 | 65.72 | 0.59 | 0.62 | 0.64 |
| | Spr 2015 | 47.47 | 50.16 | 53.08 | 0.45 | 0.48 | 0.51 |
| | Sum 2015 | 79.96 | 81.23 | 82.34 | 0.79 | 0.80 | 0.82 |
| | Fall 2015 | 54.14 | 56.48 | 59.65 | 0.52 | 0.54 | 0.58 |
| Fall-All | Spr 2013 | 15.02 | 16.30 | 17.30 | 0.13 | 0.14 | 0.15 |
| | Sum 2013 | 31.31 | 35.45 | 38.75 | 0.29 | 0.33 | 0.36 |
| | Fall 2013 | 75.89 | 77.41 | 78.92 | 0.75 | 0.76 | 0.78 |
| | Spr 2014 | 27.47 | 31.96 | 35.44 | 0.25 | 0.30 | 0.33 |
| | Sum 2014 | 15.35 | 16.84 | 20.05 | 0.13 | 0.15 | 0.18 |
| | Fall 2014 | 75.98 | 77.68 | 78.94 | 0.75 | 0.77 | 0.78 |
| | Spr 2015 | 31.71 | 36.47 | 40.81 | 0.29 | 0.34 | 0.39 |
| | Sum 2015 | 45.40 | 48.89 | 51.10 | 0.43 | 0.47 | 0.49 |
| | Fall 2015 | 76.43 | 77.85 | 79.61 | 0.75 | 0.77 | 0.79 |
| 2013-All | Spr 2013 | 76.50 | 78.10 | 79.72 | 0.75 | 0.77 | 0.79 |
| | Sum 2013 | 72.92 | 75.13 | 77.09 | 0.72 | 0.74 | 0.76 |
| | Fall 2013 | 74.03 | 75.30 | 76.56 | 0.73 | 0.74 | 0.75 |

| | | | | | | | |
|---|---|---|---|---|---|---|---|
| | Spr 2014 | 28.45 | 30.78 | 34.21 | 0.27 | 0.29 | 0.32 |
| | Sum 2014 | 13.38 | 15.08 | 18.23 | 0.12 | 0.13 | 0.16 |
| | Fall 2014 | 33.12 | 35.81 | 39.32 | 0.30 | 0.33 | 0.36 |
| | Spr 2015 | 41.75 | 43.10 | 44.91 | 0.39 | 0.41 | 0.42 |
| | Sum 2015 | 31.66 | 33.90 | 36.06 | 0.29 | 0.31 | 0.33 |
| | Fall 2015 | 34.97 | 38.20 | 41.54 | 0.32 | 0.36 | 0.39 |
| 2014-All | Spr 2013 | 27.64 | 29.73 | 31.60 | 0.25 | 0.27 | 0.28 |
| | Sum 2013 | 36.53 | 38.84 | 41.81 | 0.33 | 0.36 | 0.39 |
| | Fall 2013 | 25.27 | 29.22 | 31.00 | 0.23 | 0.27 | 0.29 |
| | Spr 2014 | 81.54 | 83.02 | 84.26 | 0.81 | 0.82 | 0.84 |
| | Sum 2014 | 78.44 | 80.32 | 82.00 | 0.77 | 0.79 | 0.81 |
| | Fall 2014 | 76.20 | 78.21 | 79.72 | 0.75 | 0.77 | 0.79 |
| | Spr 2015 | 55.37 | 57.71 | 60.02 | 0.53 | 0.56 | 0.58 |
| | Sum 2015 | 62.12 | 63.91 | 65.57 | 0.60 | 0.62 | 0.64 |
| | Fall 2015 | 61.00 | 63.15 | 65.80 | 0.59 | 0.61 | 0.64 |
| 2015-All | Spr 2013 | 11.51 | 12.98 | 15.92 | 0.10 | 0.11 | 0.14 |
| | Sum 2013 | 12.43 | 18.37 | 23.03 | 0.10 | 0.16 | 0.20 |
| | Fall 2013 | 19.54 | 21.75 | 24.91 | 0.17 | 0.19 | 0.22 |
| | Spr 2014 | 58.08 | 59.84 | 61.65 | 0.56 | 0.58 | 0.60 |
| | Sum 2014 | 19.88 | 22.84 | 27.04 | 0.18 | 0.21 | 0.25 |
| | Fall 2014 | 54.05 | 56.24 | 58.33 | 0.52 | 0.54 | 0.56 |
| | Spr 2015 | 78.49 | 80.30 | 82.41 | 0.77 | 0.79 | 0.82 |
| | Sum 2015 | 79.74 | 81.33 | 82.49 | 0.79 | 0.80 | 0.82 |
| | Fall 2015 | 78.11 | 79.58 | 81.07 | 0.77 | 0.79 | 0.80 |
| All-Dates | Spr 2013 | 74.46 | 76.09 | 78.20 | 0.73 | 0.75 | 0.77 |
| | Sum 2013 | 73.39 | 76.14 | 77.39 | 0.72 | 0.75 | 0.76 |
| | Fall 2013 | 70.77 | 72.40 | 74.91 | 0.69 | 0.71 | 0.74 |
| | Spr 2014 | 78.32 | 79.75 | 81.02 | 0.77 | 0.79 | 0.80 |
| | Sum 2014 | 74.46 | 76.00 | 77.41 | 0.73 | 0.75 | 0.76 |
| | Fall 2014 | 76.09 | 77.45 | 79.04 | 0.75 | 0.76 | 0.78 |
| | Spr 2015 | 76.81 | 78.23 | 79.45 | 0.76 | 0.77 | 0.78 |
| | Sum 2015 | 76.53 | 78.22 | 79.54 | 0.75 | 0.77 | 0.79 |
| | Fall 2015 | 73.09 | 74.50 | 76.34 | 0.72 | 0.73 | 0.75 |

*Table A.3. Leave one out (LOO) spectral library classification with minimum, mean, maximum overall and kappa classification accuracy calculated from 50 iterations.*

| Library Name | Image Date | Overall | | | Kappa | | |
|---|---|---|---|---|---|---|---|
| | | Min | Mean | Max | Min | Mean | Max |
| LOO-Spr13 | Spr 2013 | 44.64 | 46.22 | 48.64 | 0.42 | 0.44 | 0.46 |
| | Sum 2013 | 73.71 | 75.48 | 76.73 | 0.72 | 0.74 | 0.76 |
| | Fall 2013 | 70.86 | 72.82 | 74.88 | 0.69 | 0.72 | 0.74 |
| | Spr 2014 | 77.79 | 79.11 | 80.80 | 0.77 | 0.78 | 0.80 |
| | Sum 2014 | 74.85 | 76.02 | 77.68 | 0.74 | 0.75 | 0.77 |
| | Fall 2014 | 75.77 | 77.24 | 78.79 | 0.75 | 0.76 | 0.78 |
| | Spr 2015 | 75.38 | 76.78 | 78.13 | 0.74 | 0.76 | 0.77 |
| | Sum 2015 | 75.67 | 77.44 | 78.79 | 0.75 | 0.76 | 0.78 |
| | Fall 2015 | 73.72 | 74.97 | 76.44 | 0.73 | 0.74 | 0.75 |
| LOO-Sum13 | Spr 2013 | 76.55 | 77.65 | 79.61 | 0.75 | 0.77 | 0.79 |
| | Sum 2013 | 56.97 | 59.77 | 61.63 | 0.55 | 0.58 | 0.60 |
| | Fall 2013 | 70.90 | 72.49 | 75.74 | 0.70 | 0.71 | 0.75 |
| | Spr 2014 | 78.23 | 79.81 | 81.10 | 0.77 | 0.79 | 0.80 |
| | Sum 2014 | 74.46 | 76.10 | 77.90 | 0.73 | 0.75 | 0.77 |
| | Fall 2014 | 75.13 | 76.91 | 78.14 | 0.74 | 0.76 | 0.77 |
| | Spr 2015 | 76.73 | 78.30 | 79.84 | 0.76 | 0.77 | 0.79 |
| | Sum 2015 | 77.51 | 78.77 | 80.09 | 0.76 | 0.78 | 0.79 |
| | Fall 2015 | 73.74 | 75.12 | 76.38 | 0.73 | 0.74 | 0.75 |
| LOO-Fall13 | Spr 2013 | 75.77 | 76.89 | 78.03 | 0.75 | 0.76 | 0.77 |
| | Sum 2013 | 73.39 | 75.86 | 77.00 | 0.72 | 0.75 | 0.76 |
| | Fall 2013 | 41.06 | 43.78 | 46.41 | 0.39 | 0.42 | 0.44 |
| | Spr 2014 | 77.92 | 79.94 | 81.87 | 0.77 | 0.79 | 0.81 |
| | Sum 2014 | 75.88 | 77.30 | 78.74 | 0.75 | 0.76 | 0.78 |
| | Fall 2014 | 75.43 | 76.59 | 77.93 | 0.74 | 0.76 | 0.77 |
| | Spr 2015 | 75.63 | 77.57 | 79.03 | 0.74 | 0.76 | 0.78 |
| | Sum 2015 | 76.53 | 78.62 | 80.20 | 0.75 | 0.78 | 0.79 |
| | Fall 2015 | 73.95 | 75.53 | 78.08 | 0.73 | 0.74 | 0.77 |
| LOO-Spr14 | Spr 2013 | 74.46 | 75.78 | 76.94 | 0.73 | 0.75 | 0.76 |
| | Sum 2013 | 74.14 | 76.74 | 78.59 | 0.73 | 0.76 | 0.78 |
| | Fall 2013 | 72.39 | 73.69 | 75.49 | 0.71 | 0.72 | 0.74 |
| | Spr 2014 | 61.51 | 63.59 | 65.72 | 0.60 | 0.62 | 0.64 |
| | Sum 2014 | 74.73 | 76.47 | 77.67 | 0.74 | 0.75 | 0.77 |
| | Fall 2014 | 76.09 | 77.58 | 78.42 | 0.75 | 0.77 | 0.77 |

| | | | | | | | |
|---|---|---|---|---|---|---|---|
| | Spr 2015 | 77.21 | 78.59 | 80.04 | 0.76 | 0.78 | 0.79 |
| | Sum 2015 | 77.28 | 78.65 | 79.76 | 0.76 | 0.78 | 0.79 |
| | Fall 2015 | 73.30 | 74.57 | 76.12 | 0.72 | 0.73 | 0.75 |
| LOO-Sum14 | Spr 2013 | 75.90 | 77.13 | 78.32 | 0.75 | 0.76 | 0.77 |
| | Sum 2013 | 73.18 | 75.90 | 77.48 | 0.72 | 0.75 | 0.76 |
| | Fall 2013 | 72.34 | 73.54 | 75.74 | 0.71 | 0.72 | 0.75 |
| | Spr 2014 | 78.56 | 80.15 | 81.57 | 0.78 | 0.79 | 0.81 |
| | Sum 2014 | 30.98 | 33.54 | 35.00 | 0.29 | 0.31 | 0.33 |
| | Fall 2014 | 75.77 | 77.46 | 78.35 | 0.75 | 0.76 | 0.77 |
| | Spr 2015 | 76.84 | 78.06 | 78.91 | 0.76 | 0.77 | 0.78 |
| | Sum 2015 | 77.06 | 78.21 | 79.87 | 0.76 | 0.77 | 0.79 |
| | Fall 2015 | 73.62 | 74.62 | 75.68 | 0.72 | 0.73 | 0.75 |
| LOO-Fall14 | Spr 2013 | 75.90 | 77.29 | 78.35 | 0.75 | 0.76 | 0.77 |
| | Sum 2013 | 73.39 | 76.08 | 77.62 | 0.72 | 0.75 | 0.77 |
| | Fall 2013 | 72.01 | 73.59 | 75.12 | 0.71 | 0.72 | 0.74 |
| | Spr 2014 | 78.88 | 80.07 | 81.88 | 0.78 | 0.79 | 0.81 |
| | Sum 2014 | 74.82 | 76.37 | 77.78 | 0.74 | 0.75 | 0.77 |
| | Fall 2014 | 57.73 | 59.38 | 61.50 | 0.56 | 0.58 | 0.60 |
| | Spr 2015 | 77.14 | 78.30 | 80.07 | 0.76 | 0.77 | 0.79 |
| | Sum 2015 | 76.74 | 78.28 | 79.61 | 0.76 | 0.77 | 0.79 |
| | Fall 2015 | 72.88 | 74.40 | 76.00 | 0.72 | 0.73 | 0.75 |
| LOO-Spr15 | Spr 2013 | 75.54 | 77.00 | 77.89 | 0.74 | 0.76 | 0.77 |
| | Sum 2013 | 73.82 | 75.99 | 77.83 | 0.73 | 0.75 | 0.77 |
| | Fall 2013 | 71.89 | 73.92 | 76.19 | 0.71 | 0.73 | 0.75 |
| | Spr 2014 | 79.10 | 80.17 | 82.01 | 0.78 | 0.79 | 0.81 |
| | Sum 2014 | 74.91 | 76.51 | 77.94 | 0.74 | 0.75 | 0.77 |
| | Fall 2014 | 75.40 | 76.91 | 78.28 | 0.74 | 0.76 | 0.77 |
| | Spr 2015 | 55.37 | 58.39 | 61.06 | 0.53 | 0.56 | 0.59 |
| | Sum 2015 | 76.15 | 77.43 | 79.54 | 0.75 | 0.76 | 0.79 |
| | Fall 2015 | 73.15 | 74.37 | 75.79 | 0.72 | 0.73 | 0.75 |
| LOO-Sum15 | Spr 2013 | 75.08 | 76.25 | 77.45 | 0.74 | 0.75 | 0.76 |
| | Sum 2013 | 73.50 | 76.29 | 77.61 | 0.72 | 0.75 | 0.77 |
| | Fall 2013 | 71.14 | 72.75 | 74.88 | 0.70 | 0.71 | 0.74 |
| | Spr 2014 | 78.90 | 80.15 | 81.58 | 0.78 | 0.79 | 0.81 |
| | Sum 2014 | 75.83 | 77.21 | 78.79 | 0.75 | 0.76 | 0.78 |
| | Fall 2014 | 75.51 | 77.43 | 78.52 | 0.74 | 0.76 | 0.78 |
| | Spr 2015 | 76.15 | 77.60 | 78.84 | 0.75 | 0.77 | 0.78 |
| | Sum 2015 | 69.41 | 71.27 | 72.76 | 0.68 | 0.70 | 0.72 |
| | Fall 2015 | 72.98 | 74.46 | 75.60 | 0.72 | 0.73 | 0.74 |
| LOO-Fall15 | Spr 2013 | 75.05 | 76.51 | 77.67 | 0.74 | 0.75 | 0.77 |
| | Sum 2013 | 74.03 | 75.80 | 77.62 | 0.73 | 0.75 | 0.77 |
| | Fall 2013 | 70.89 | 72.62 | 75.49 | 0.70 | 0.71 | 0.74 |

| | | | | | | | |
|---|---|---|---|---|---|---|---|
| | Spr 2014 | 78.23 | 79.74 | 81.79 | 0.77 | 0.79 | 0.81 |
| | Sum 2014 | 74.34 | 76.23 | 77.58 | 0.73 | 0.75 | 0.77 |
| | Fall 2014 | 75.19 | 76.94 | 78.12 | 0.74 | 0.76 | 0.77 |
| | Spr 2015 | 75.96 | 77.69 | 79.40 | 0.75 | 0.77 | 0.78 |
| | Sum 2015 | 76.87 | 78.47 | 79.87 | 0.76 | 0.77 | 0.79 |
| | Fall 2015 | 57.76 | 59.03 | 61.45 | 0.56 | 0.57 | 0.60 |

# B. Appendix: Supplementary material for Chapter 3: Plant species' spectral emissivity and temperature using the Hyperspectral Thermal Emission Spectrometer (HyTES) sensor

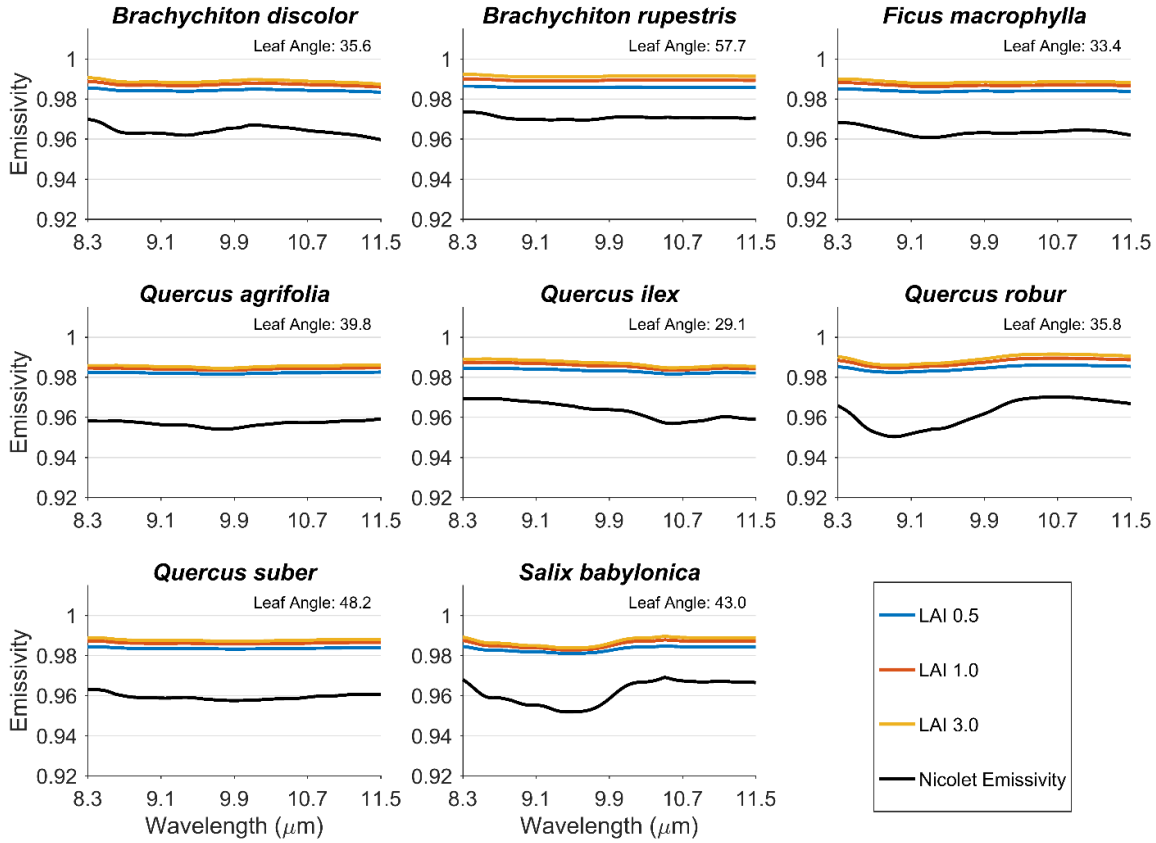


*Figure B.1. Changes in estimated apparent emissivity with changes in Leaf Area Index (LAI).*

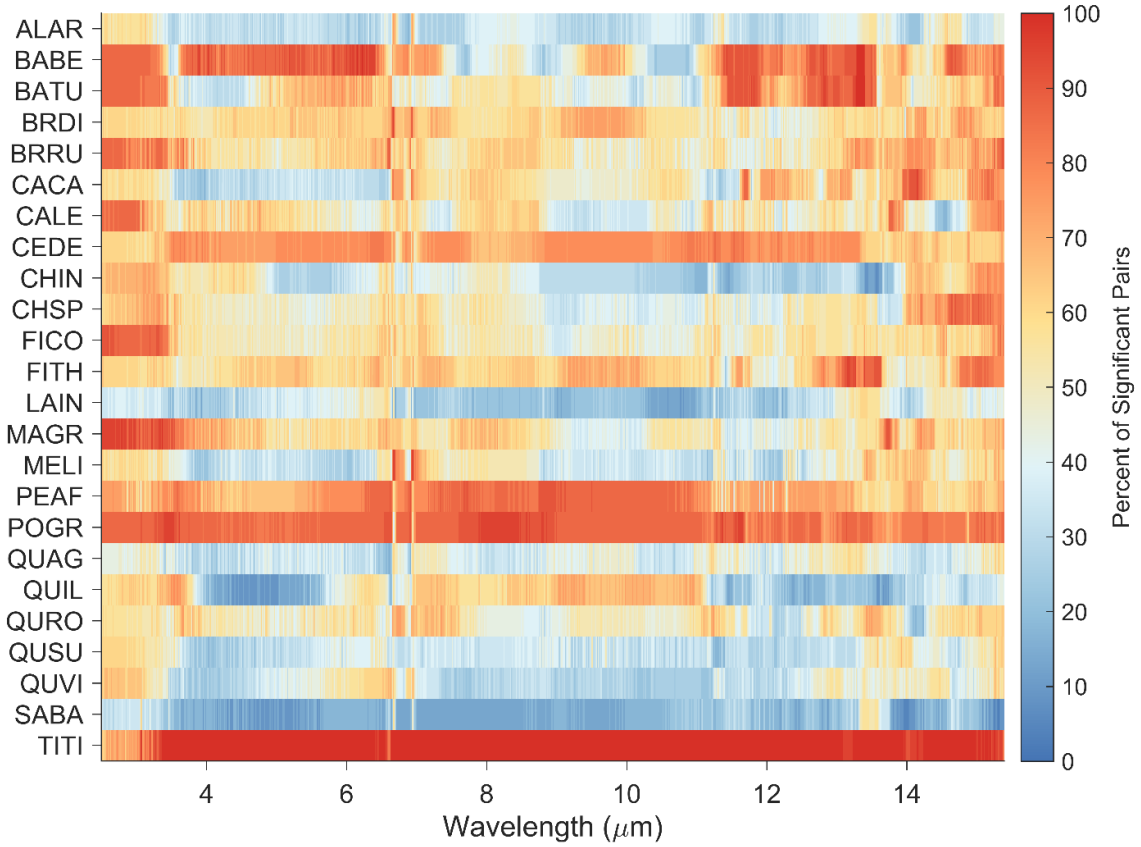


*Figure B.2. Using Mann-Whitney-U tests, the number of significantly different pairs at each wavelength were identified for each plant species using leaf emissivities.*

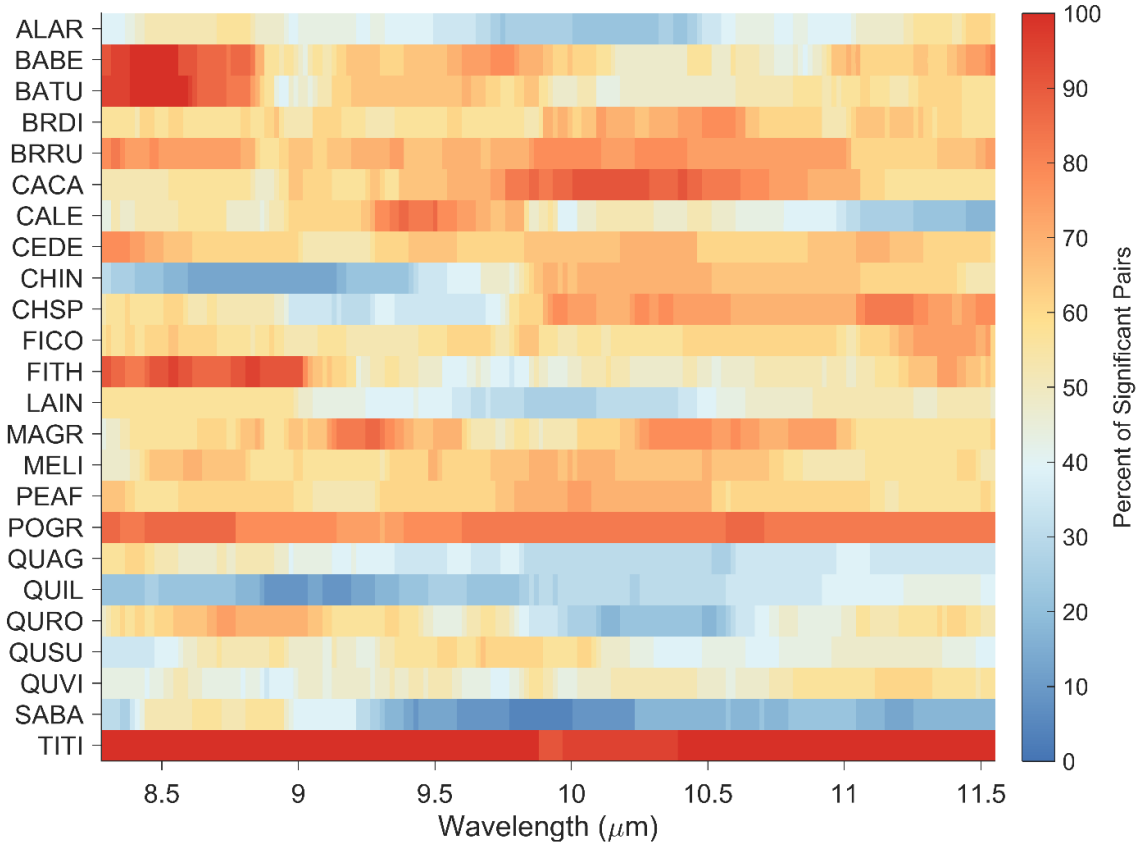


*Figure B.3. Using Mann-Whitney-U tests, the number of significantly different pairs at each wavelength were identified for each plant species using leaf emissivities that have been resampled to HyTES wavelengths.*

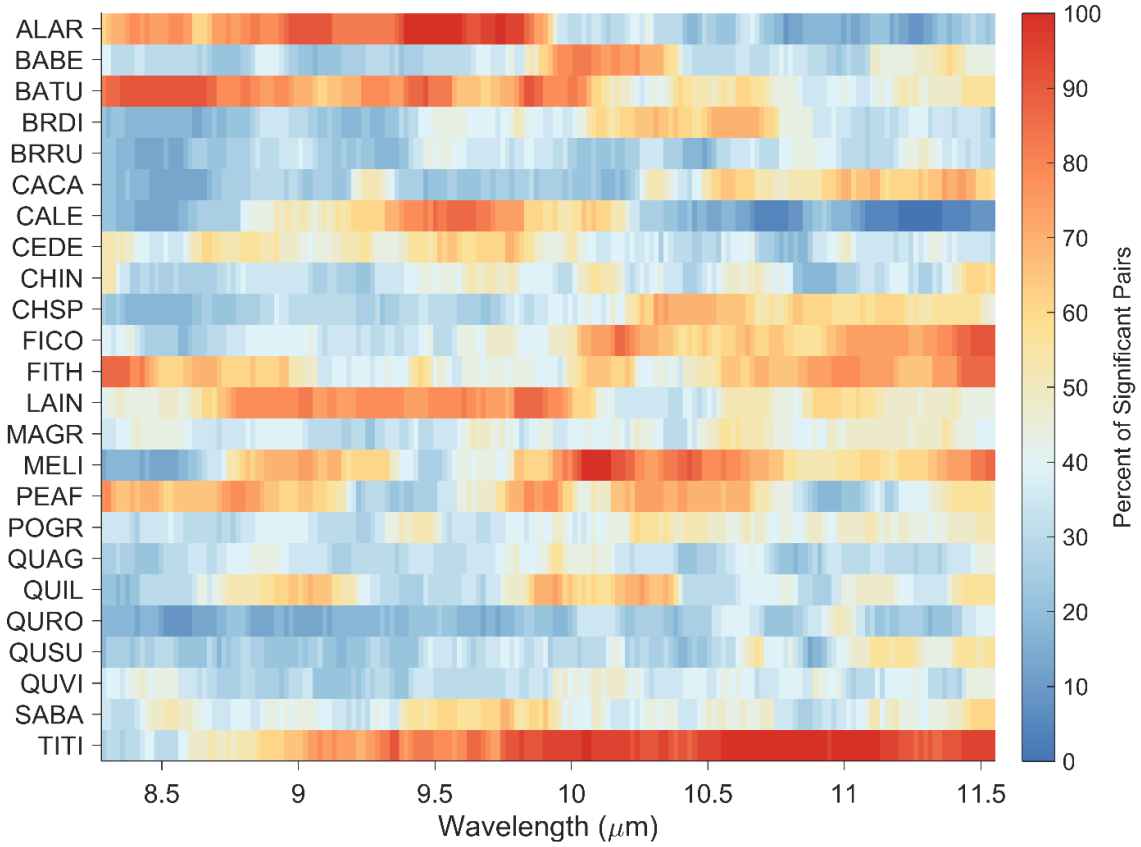


*Figure B.4. Using Mann-Whitney-U tests, the number of significantly different pairs at each wavelength were identified for each plant species using canopy emissivities collected from HyTES 2014 imagery.*

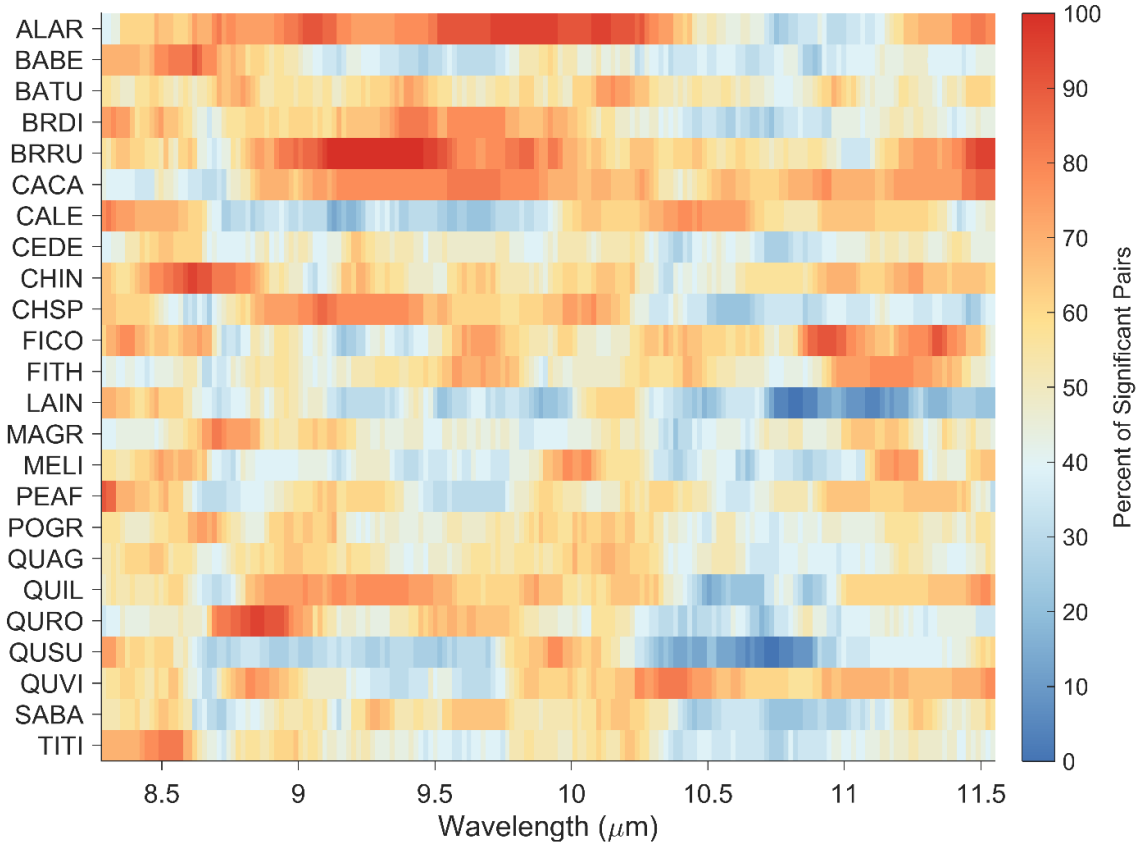


*Figure B.5. Using Mann-Whitney-U tests, the number of significantly different pairs at each wavelength were identified for each plant species using canopy emissivities collected from HyTES 2016 imagery.*

# C. Appendix: ASD FieldSpec 4 Protocol

This protocol is meant to help a user to run an ASD FieldSpec4 specifically, but many features and practices can be applied to other models. This is not meant to replace the FieldSpec4 User Manual or the RS$^3$ User Manual. Please refer to these manuals for more information. You can find documentation for all ASD products (including all versions of spectrometers and RS$^3$ software) here: http://support.asdi.com/Document/Documents.aspx

## C.1 Instrument Overview

This is a simplified version of the FieldSpec 4 instrument overview. For more information, refer to the FieldSpec 4 User Manual pages 2 – 3.

Figure 1.1 shows the front panel of the instrument.

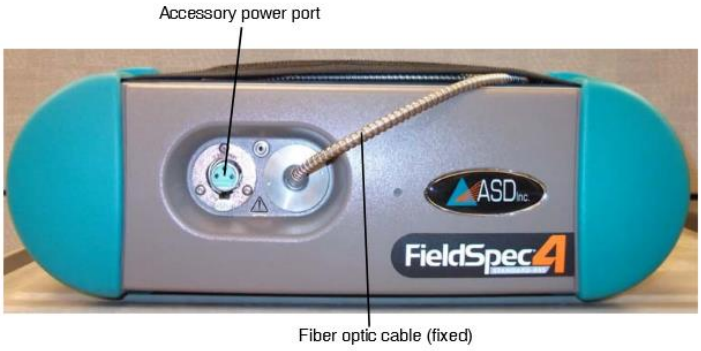


*Figure 1.1: FieldSpec 4 instrument front panel*

Figure 1.2 shows the back panel of the instrument.

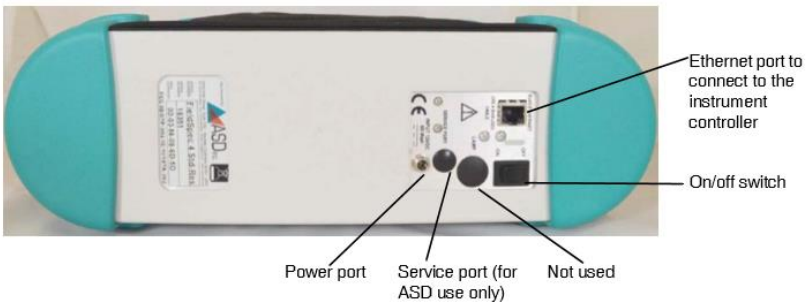


*Figure 1.2: FieldSpec 4 instrument back panel*

## C.2 Setting up the Instrument

Page numbers referenced in this section are from the FieldSpec4 User Manual pages 5 - 6.

1) Provide power to the ASD. There are two ways of providing power to your ASD:
    a) Plugging into an electrical outlet (when using the ASD for indoor or lab work)
        i) Connect the power cable to the back of the instrument and screw into the port.
        ii) Plug power cord into three pronged electrical outlet.
    b) Plugging into an external battery (when using the ASD for outdoor or portable work)
        i) Connect battery power cable to the back of the instrument and screw into the port.
        ii) Attached battery power cable to battery.
        iii) Notes about the batteries and uses:
            (1) Only use the Nickel-Metal Hydride batteries that came with the ASD.
            (2) Expected battery life is ~4 hours. Always charge the second battery to have as a backup in case.
            (3) Instrument will stop collecting spectra when battery drains to about 10 Volts.
            (4) The backpack has two pouches to hold batteries. However, the battery in use should be on the opposite side of the fiber optic cable.
            (5) The $RS^3$ Software will indicate the power status of the battery (found in the bottom left corner of the main window next to the connection status.
    c) To have the best results, 'warm-up' the ASD by plugging in the instrument and turning it on for at least 30 minutes (ASD suggests only 15 minutes, but in my experience that hasn't been enough time). If the surrounding environment is cooler, allow for a longer warm up period. Hint: I will plug in the ASD using Method A for

an hour before heading into the field. Then I will switch to battery power as I pack up for field work.

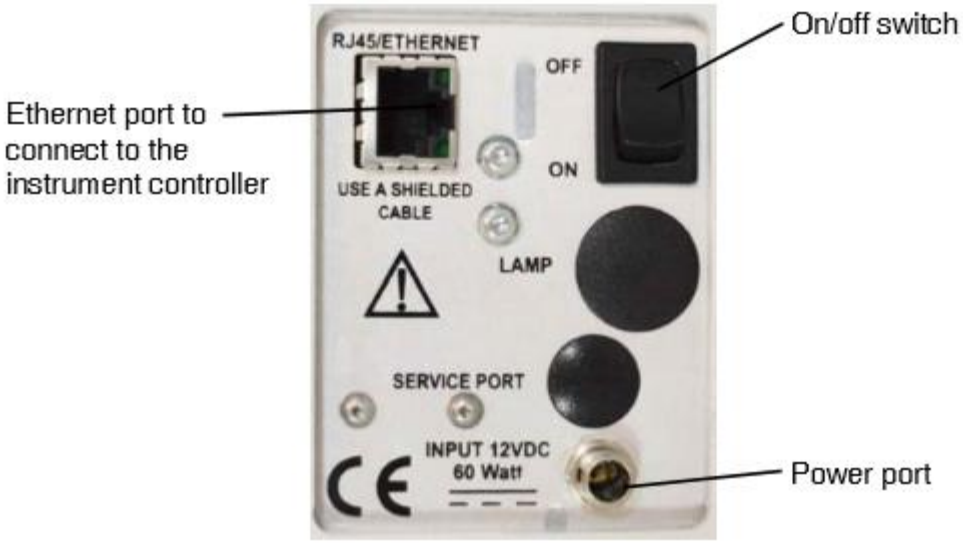


2) Set up connection between the ASD and computer. Connect the Ethernet cable to the computer's Ethernet port and to the back of the instrument. This cable is sensitive and can be harmed easily – so be careful. If you are having connection issues, try unplugging and re-plugging in the Ethernet cable.
3) Connect power to the computer. Obviously if you are in the field you will be using your laptop battery power. Make sure to fully charge your laptop before entering the field. You might want to be a backup battery for your laptop or a way to charge the laptop on the go.
4) Insert fiber optic cable into the pistol grip.
    a) Insert the fiber optic cable through the strain relief spring.
    b) Insert the fiber optic cable all the way through the pistol grip until it clicks. Make sure the fiber optic cable tip is fully seated into the nose of the pistol grip.

c) There is a screw on the top of the pistol grip that you can tighten to hold the fiber optic cable. However, you should NOT have to do this. In my experience if you are having to adjust this screw, your pistol grip is probably broken. Do not adjust the factory set screw at bottom.


5) Turn on the instrument and computer (make sure you've warmed up the instrument).
   a) When turning on the computer, make sure any programs that will drain the battery are closed. This includes Bluetooth and wireless connections, unless you are using these features in the field when collecting.
6) Open $RS^3$ program on the computer. There will be two programs called $RS^3$:
   a) $RS^3$ High Contrast: Use this program if you will be in direct sunlight (outdoor collections) as it maximizes the contrast between items for easy viewing.

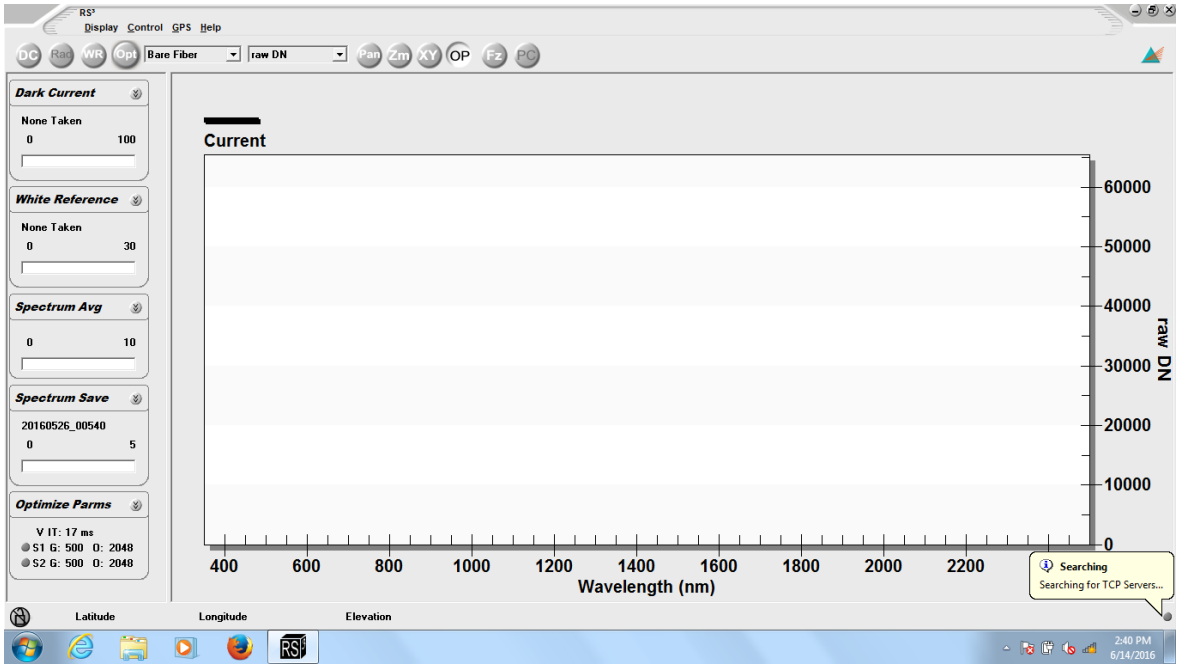


b) RS$^3$: Use this program if you are collecting indoors or if you are hooked up to an electrical outlet.

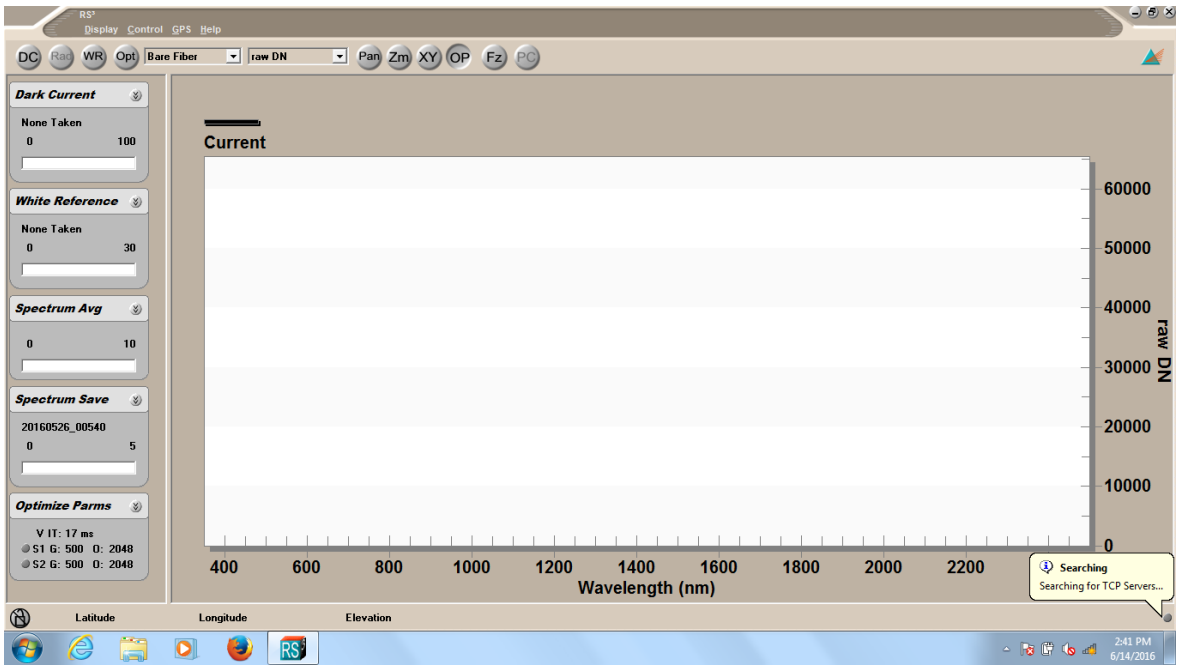


c) Both programs perform the same. The only difference is the GUI screen viewing capabilities.

7) If using an optional light source, turn it on. You will only use this light source if you are working indoors.

### C.3 Setting up the White Reference Panel

Before you can collect spectra, you must optimize and set up a white reference. The white reference is an extremely important part of collecting spectra. The white reference used for calibrating an ASD is a Spectralon® panel. Spectralon Reflectance Material gives the highest diffuse reflectance of any known material or coating over the UV-VIS-NIR region of the spectrum. This is used to tell the ASD what a 100% reflectant surface looks like under current lighting conditions. This panel or disk is quite fragile and VERY expensive, so handle it with care. Any dents, dirt, or debris will affect the spectrum, so try to keep it as clean as possible by wiping it with a very soft cloth. Over time, the spectralon will get dirty enough that it needs a thorough cleaning. There is a special process for cleaning the spectralon panel, so make sure to do your homework before cleaning the surface.


These following instructions are based on fieldwork. For indoor measuring, all you would need to do is place spectralon on sampling surface.

1) Attach spectralon panel to tri-pod. There should be a screw opening on one side of the spectralon panel. Make sure it is very secure so there is no chance of the panel falling off and getting damaged.
2) Adjust the tri-pod to about a height of 80 cm. Make sure to mark down the height of the standard for bookkeeping purposes.
3) Level the spectralon panel using a level bubble. It's important that the spectralon panel is level to ensure correct reflectance.
4) Turn on $RS^3$ and set up program for collection following steps 1 and 2. At step 3 of setting up $RS^3$, you will need to continue with these steps.
5) Hold the pistol grip with the fiber optic about 24 cm away from the panel. Hold the pistol grip as far away from you as possible, because you can impact the spectrum being measured.
6) Optimize and collect white reference using $RS^3$. For more information, refer to Setting up $RS^3$ section.

## C.4 Setting up RS$^3$

1) When opening RS$^3$, the program will automatically detect the connection with the ASD. In the lower right corner of the program there will be a circle that depicts the status of the connection. Nothing in the program will work if the ASD is not connected.
2) Open Control > Save Spectrum.
    a) Update the path name to where you want the spectra to be saved.
    b) Choose a base name that will be used for each spectrum file. I like to include study area and date of collection. The program will add numbers to the end of the base name for each spectrum collected.
    c) Choose the starting spectrum number. At the beginning of a collection start with 000. If the program or instrument freezes or crashes, you can edit which spectrum to restart with here.
    d) Choose the number of files to save with each collection. When you hit SAVE, how many files do you want saved at a time? It really depends on the user's preference. I save 5 files each time I hit save.
    e) Choose the interval between saves. This is the amount of time the program sets between collection of the number of files you designated above. I set this to 00:00:00, but if you want a delay between saving the number of files (to allow the spectra to be more temporally different) you can increase this value. Be warned if you are having highly variable atmospheric conditions you will not want a delay between collections.
    f) Click OK when completed.

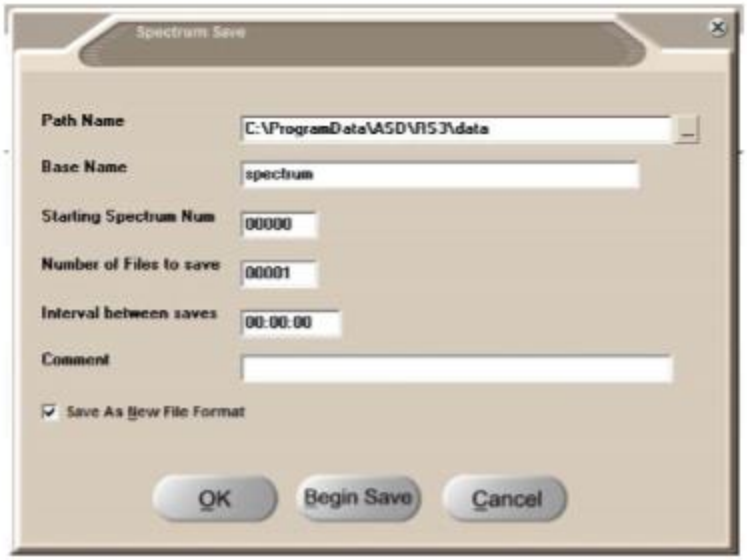


3) With the white reference panel set up and the fiber optic cable pointed at the panel, hit the **Opt** or optimize button to optimize the instrument. This button calibrates the instrument to the current lighting conditions.
    a) The optimization is complete when the Spectrum Avg progress bar resumes. The program will also say in the bottom right corner “Optimization Complete”
    b) The graph will have a spectrum similar to the figure below with the y axis in raw DN or raw Digital Numbers.

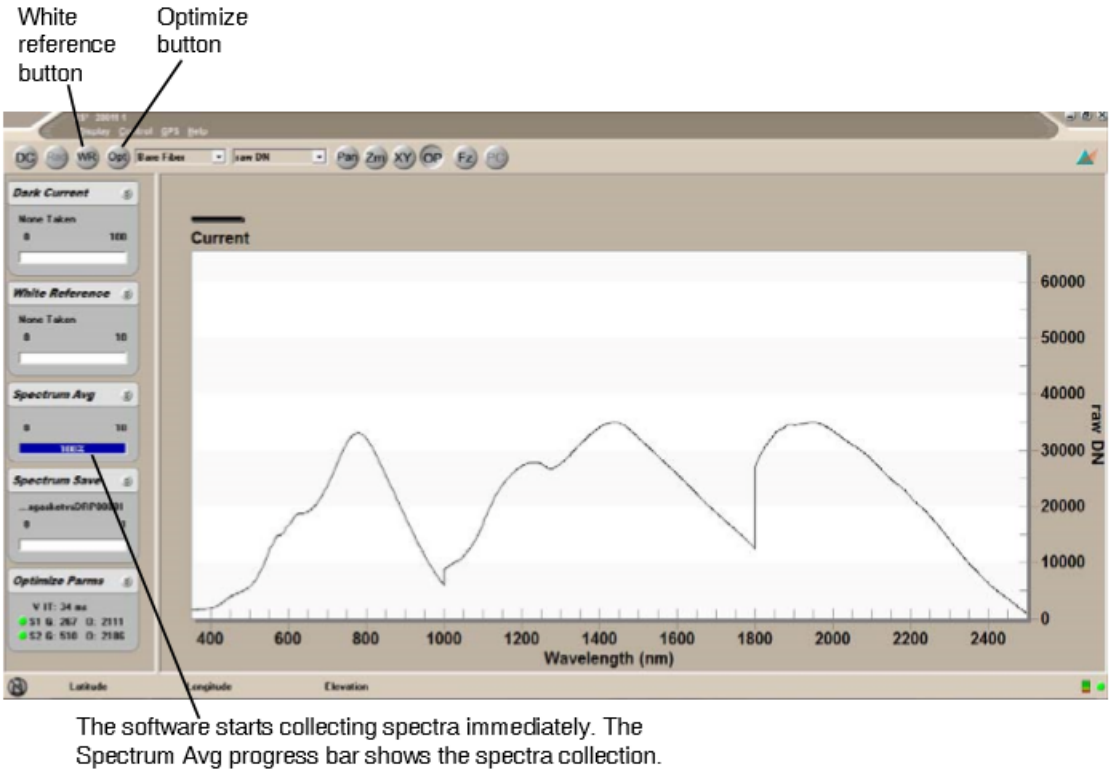


4) When optimization is complete, click **WR** or the white reference button to collect a white reference. The collection of the white reference is telling the ASD that this panel is a 100% reflectant target so that it can be used to calculate reflectance for other surfaces.
    a) HINT: I like to save the white reference spectrum for future analysis. This is a 'just in case' step, but can come in handy if spectra need to be future processed or if you are interested in the atmospheric conditions at the time of collection.
    b) A white reference is only useful when collecting reflectance data. Do not do this step if you are collecting radiance data.
    c) The white reference is complete when the Spectrum Avg progress bar resumes. The program will flip through the steps of the white referencing in the bottom right corner until it says "White Reference Complete".

d) The graph should have a flat line at 100% or 1 depending on your scale. The y-axis will have changed to reflectance. There might be features (like the graph below) with spikes around 1400 and 1800 nm that are highly variable. These are due to water absorption in the atmosphere and cannot be avoided even in perfect sunny cloudless conditions. If you are measuring indoors these water absorption features should not be pronounced or their magnitude much smaller.

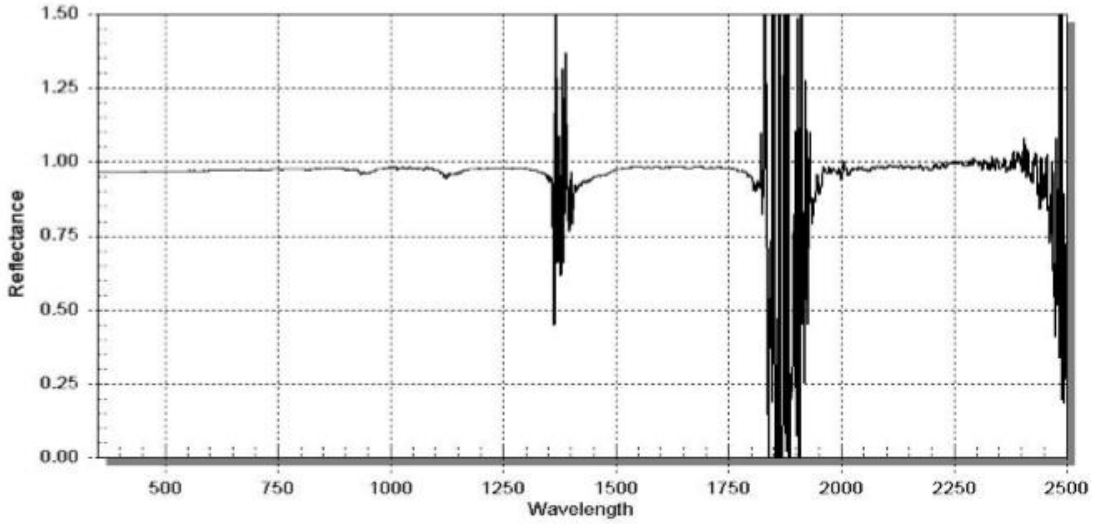


*Figure B.3: Examples of water vapor absorbing light*

5) When you have optimized and collected a white reference, point the end of the fiber optic cable at the sample of interest and hold it there until the spectrum average collection is complete.
6) Hit the space bar on the computer to start saving your spectra. Collect multiple spectra for a sample. In the end you will be visually inspecting your spectra and averaging among the selected spectra.
   a) HINT: I generally save 5 files each time I press the space bar and repeat 5 times for a total of 25 spectra collected for each sample.

b) If you have a delicate sample (some leaves) and you are measuring indoors with a light source, you may not be able to collect that many spectra. The heat load on the sample will quickly change the composition of the sample.

c) The number shown on the Spectrum Save progress is the NEXT file number that will be saved. NOT the file that you just saved.

7) When done collecting samples, simply close the program. Your files will be saved in the directory you specified in Step 2.

## C.5 Sampling Tips and Tricks

### *C.5.1 Field of View*

- The field of view determines the size of the data collection area. When collecting data, be sure that the sample or reference panel is the only object within the field of view.
- **Fore Optics:** There are multiple fore optics that you can attach to the fiber optic that control the field of view. In most cases, the bare fiber (no additional fore optic) will be used for sample collection. The bare fiber provides a 25˚ field of view. There are other fore optics that can decrease the field of view to as little as 1˚.
- **Calculating Field of View:** As a general rule when using the bare fiber, the diameter of the field of view is equal to half the distance the fiber optic cable is from the sample. For example, if the cable is four feet from the sample, the field of view is about two feet wide. See figure below:

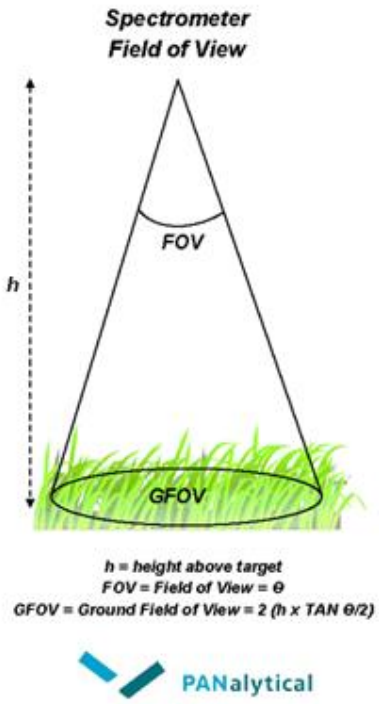


- **Measuring Height:** ALWAYS makes sure to measure the height (if using a tripod) or know approximately at what height you are holding the fiber optic. This is the only way to figure out field of view which is useful for your analysis.

*C.5.2 When to Collect Spectra*

Weather Conditions:

- FYI: This only applies for outdoor collections.
- The atmosphere highly impacts the quality of spectra collected when doing fieldwork. With increasing amounts of water vapor in the air, reflectance in the water vapor regions 1400 and 1800 nm can widen and deepen making retrieval impossible.
- The **best conditions** for measuring spectra is a completely sunny cloud free day. Any amount of clouds can impact your collection and most especially the wispy ones.

- Best conditions are not usually possible, especially for most places in the world. The key to minimize the amount of clouds in the sky and clouds near the sun. NEVER measure spectra when a cloud is obscuring the sun.

Timing:

- **Solar Noon:** The amount of solar radiation that reaches the earth's surface controls the quality of spectra and accuracy. Solar noon is when the sun is at its highest elevation in the sky which results in the largest amount of solar radiation to reach the earth's surface. Solar noon is not at 12pm, but changes which the seasons as the earth rotates around the sun. You will need to look up solar noon for the study area and time of year.
- HINT: I like to use the NOAA Solar Calculator located here: http://www.esrl.noaa.gov/gmd/grad/solcalc/
- **Winter:** During the winter the solar angle is very low, making it more difficult to get quality spectra due to the lower amounts of solar radiation. This causes your time window to be smaller than during the summer. General rule: measure spectra +/- 2 hours of solar noon.
- **Summer:** This is the best season to collect spectra because of high solar angles. A higher solar angle means solar radiation has less atmosphere to go through resulting in more solar radiation at the earth's surface. General rule: measure spectra +/- 3 hours of solar noon.

*C.5.3 Optimization and White Reference*

- **How often should I re-optimize and collect a white reference?** You will need to optimize and collect a white reference fairly often as you collect spectra to ensure that

you are collecting the highest quality. If in doubt, optimize and collect white reference. I optimize and collect a white reference at every new plot when I'm collecting in the field, mainly due to changing atmospheric conditions and changing locations by 10 m. However, optimization and collecting a white reference is time consuming so you will have to work to find a balance between quality and time.

- **How do I know if I should optimize and collect a white reference?** Before collecting a new sample, you should always place your fiber optic over the white reference panel to check on your calibration. When you've just optimized and white referenced your instrument, the reflectance of the white reflectance panel should be at 100% for all wavelengths. The one caveat where this might not be true is the water absorption regions. If the white reflectance panel spectra drifts away from 100% more than 2-3% you should re-optimize and collect a new white reference. Remember any deviation from the 100% white reflectance panel spectra will translate into sample error.
- **Reasons for re-optimization:**
    - If illumination conditions change substantially, such as cloud cover, sun position, moving to another location, you should re-optimize and collect a white reference.
    - Sometimes the lighting conditions will saturate the instrument and the optimization will no longer be valid. Your reflectance of the white reference panel will be over 100% and more likely the instrument/program will give off a warning sound.

- As the sensor warms up and collects spectra the optimization will drift, meaning it will no longer have a 100% reflectance when over the white reference panel. You will have to optimize and collect a white reference more at the beginning as the sensor is warming up.

## C.6 How to Collect Spectra

*C.6.1 Indoors (Lab)*

a) **Pros:** Collecting spectra indoors provides the most controlled atmosphere. Water absorption features in the spectra will be at a minimum. The equipment is set up once and is not moved around throughout sample collection. Sampling is not restricted to plus or minus a few hours around solar noon, because an external light source is set up.

b) **Cons:** However, the downside is many surfaces cannot be transported into the lab (whole trees, roofs, etc.). In addition, if you measure fresh samples such as leaves you need to collect and process them within 48 hours.

c) **Setup:** In the setup show below, the light source is angled at 23˚ and is 23 cm away from sample platform. The pistol grip holding the fiber optic is angled at 27˚ and is 5 cm away from sample platform. You will want to place your sample on a black <5% reflectant background to reduce the background effect on your sampling. Black surfaces are NOT created equal – most will not work as a background surface. Measure the reflectance of your background surface to understand how much it might affect the reflectance of your sample.

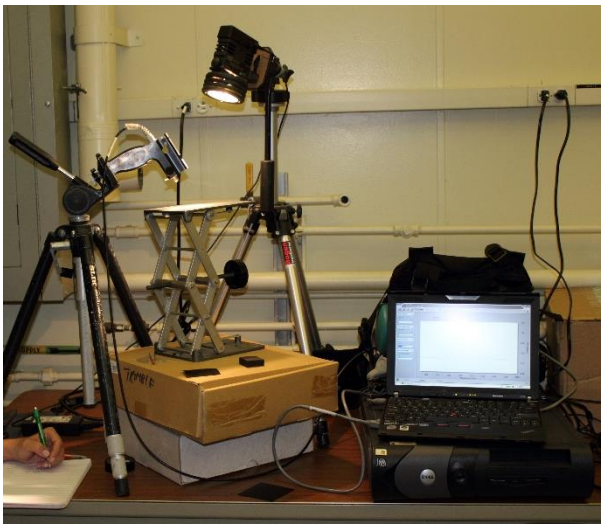

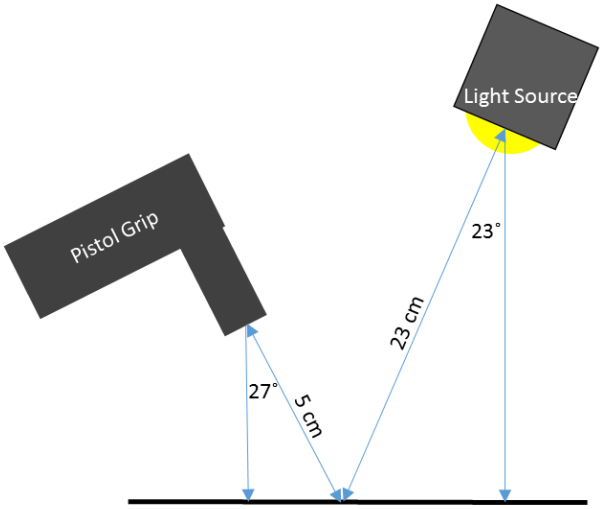


*C.6.2 Outdoors (fieldwork)*

**d) Pros:** You are portable and can move around somewhat easily. You look like a ghost buster. ASD assumes this is the way you will collect spectra in field and has developed accessories to help.

**e) Cons:** You cannot bend over or move things around very well, so you will need an assistant to help you set up the reflectance panel. It is a very heavy set up which you will have to haul around for the entire sampling collection. Climbing up ladders to get

canopy spectra of shrubs or small trees can be dangerous with this on your back – I do not suggest! Instead set ASD on ground as in tri-pod method.

**f) Setup:**

**i)** Use the backpack provided by ASD and clip the instrument into the middle of the backpack (as shown in image).

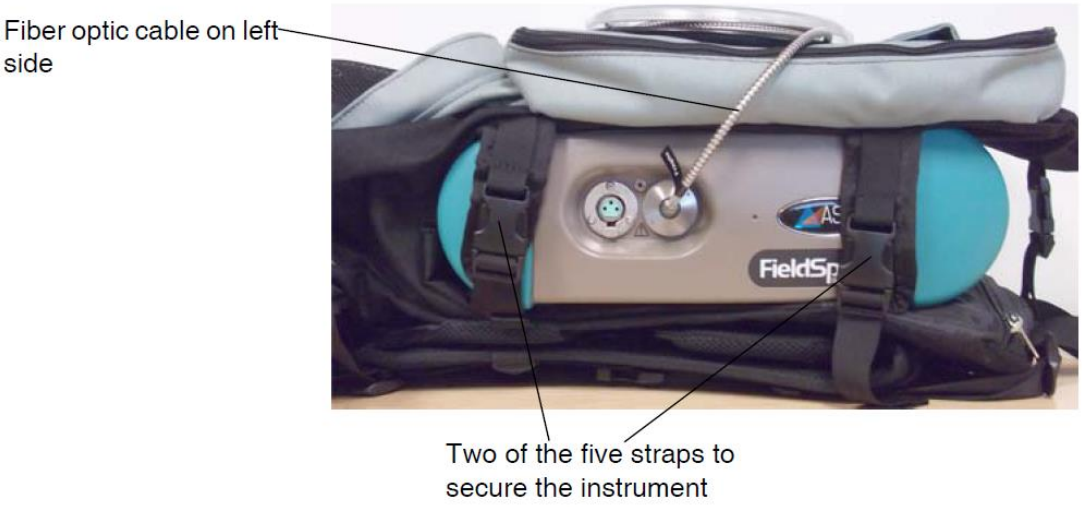


**ii)** Feed battery cable from battery pouch under the cross strap to the power port.

**iii)** Attach laptop carrier to the plastic connectors on the shoulder straps of the backpack.

iv) Place laptop onto carrier, hook up the computer to the instrument, and you are ready to go!

**C.7 Where to Collect Spectra**

Researchers have measured spectra of many surfaces with the only limitation being can you get an ASD in position. However, there are some general guidelines you should follow or keep in mind when choosing sampling locations.

1) Do not sample too close to buildings or trees. Light bounces off surfaces onto other surfaces (ones that you might be interested in sampling). You will find that the spectra you are collecting having building or tree spectral features.
2) Avoid shadows as much as possible. They decrease your overall reflectance and can result in inaccurate spectra.
3) Do not measure with highly variable atmospheric conditions – aka clouds. Clouds of all types will impact your collection more than anything else!
4) You can impact the spectrum collected too! If you hold the fiber optic too close to your body when collecting, reflectance off yourself can impact the sample collection.

## C.8 Typical Spectra

Remember, each surface you measure will be completely different from what is shown below. Use the below example spectra as a gauge to determine if you are measuring correctly.

### *C.8.1 GV, NPV, and Soil*

Note that spectra shown below were collected in a laboratory setting. If collected outside there will be water vapor lines present.

*C.8.2 Spectralon or White Reference*

Notice on this plot that the 1.4, 1.8, and 2.4 µm regions deviate from 100% reflectance significantly. This is due to water vapor absorption, which makes retrievals in these spectral ranges impossible.

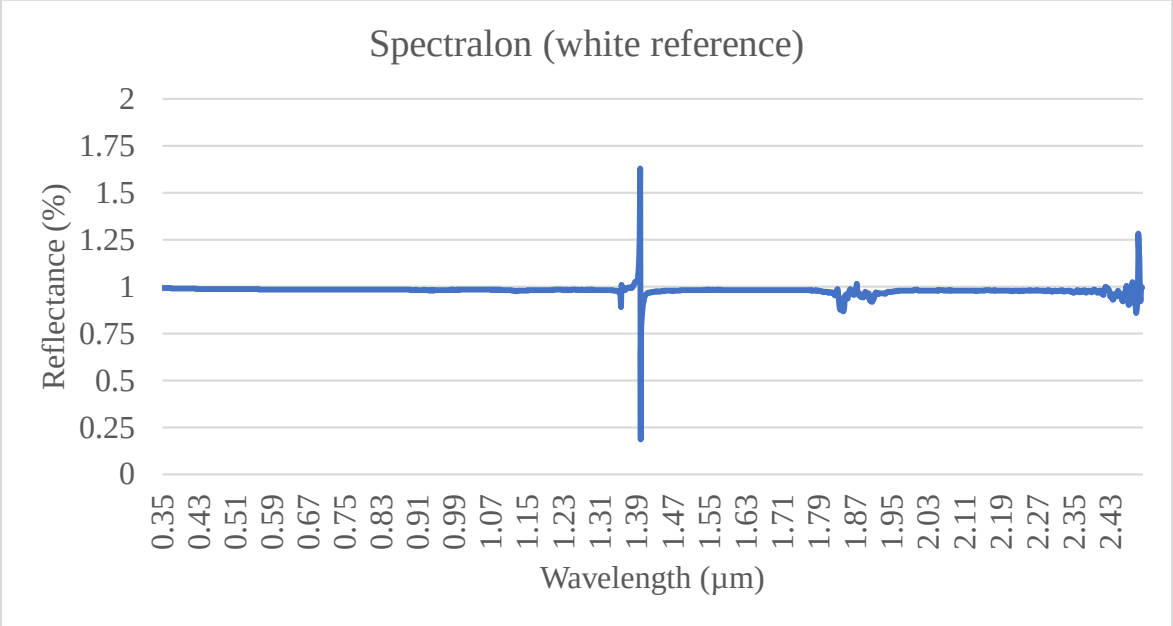

**C.9 Example Data Collection Sheet**

Date: _____ Technician(s): _____

Sky Conditions: _____

Location/Study Site: _____ Solar Noon: _____

File Base Name(s): _____

Folder Containing Files: _____

*Remember: Record the time when Optimization/White Reference is completed

| Time | Surface or Transect | Start File | End File | Notes |
|---|---|---|---|---|
| | | | | |
| | | | | |
| | | | | |
| | | | | |
| | | | | |
| | | | | |
| | | | | |
| | | | | |
| | | | | |
| | | | | |
| | | | | |
| | | | | |
| | | | | |
| | | | | |
| | | | | |
| | | | | |
| | | | | |

## References

Anderson, D.E., Verma, S.B., Rosenberg, N.J., 1984. Eddy correlation measurements of carbon dioxide latent heat and sensible heat fluxes over a crop surface. Boundary-Layer Meteorol. 29, 263–272. https://doi.org/10.1007/BF00119792

Anderson, M., Kustas, W., 2008. Thermal remote sensing of drought and evapotranspiration. Eos (Washington. DC). 89, 233–234. https://doi.org/10.1029/2008EO260001

Anderson, M.C., Norman, J.M., Kustas, W.P., Houborg, R., Starks, P.J., Agam, N., 2008. A thermal-based remote sensing technique for routine mapping of land-surface carbon, water and energy fluxes from field to regional scales. Remote Sens. Environ. 112, 4227–4241. https://doi.org/10.1016/j.rse.2008.07.009

Anderson, M.C., Zolin, C.A., Sentelhas, P.C., Hain, C.R., Semmens, K., Yilmaz, M.T., Gao, F., Otkin, J.A., Tetrault, R., 2016. The Evaporative Stress Index as an indicator of agricultural drought in Brazil : An assessment based on crop yield impacts. Remote Sens. Environ. 174, 82–99. https://doi.org/10.1016/j.rse.2015.11.034

Arshad, M., Ali, A., 2018. Estimation of leaf water content from mid- and thermal-infrared spectra by coupling genetic algorithm and partial least squares regression. J. Appl. Remote Sens. 12. https://doi.org/10.1117/1.JRS.12.022203

Asner, G.P., Brodrick, P.G., Anderson, C.B., Vaughn, N., Knapp, D.E., Martin, R.E., 2016. Progressive forest canopy water loss during the 2012–2015 California drought. Proc. Natl. Acad. Sci. 113, E249–E255. https://doi.org/10.1073/pnas.1523397113

Asner, G.P., Martin, R.E., 2009. Airborne spectranomics: mapping canopy chemical and taxonomic diversity in tropical forests. Front. Ecol. Environ. 7, 269–276. https://doi.org/10.1890/070152

Asner, G.P., Martin, R.E., 2008. Spectral and chemical analysis of tropical forests: Scaling from leaf to canopy levels. Remote Sens. Environ. 112, 3958–3970. https://doi.org/10.1016/j.rse.2008.07.003

Baldridge, A.M., Hook, S.J., Grove, C.I., Rivera, G., 2009. The ASTER spectral library version 2.0. Remote Sens. Environ. 113, 711–715. https://doi.org/10.1016/j.rse.2008.11.007

Bartolome, J.W., Barry, W.J., Griggs, T., Hopkinson, P., 2007. Valley grassland, in: Barbour, M.G., Keeler-Wolf, T., Schoenherr, A.A. (Eds.), Terrestrial Vegetation of California. University of California Press, pp. 367–393. https://doi.org/10.2307/2806144

Bausch, W., Trout, T., Buchleiter, G., 2011. Evapotranspiration adjustements for deficit-irrigated corn: a concept. Irrig. Drain. 60, 682–693. https://doi.org/10.1002/ird.601

Bayarjargal, Y., Karnieli, A., Bayasgalan, M., Khudulmur, S., Gandush, C., Tucker, C.J., 2006. A comparative study of NOAA-AVHRR derived drought indices using change vector analysis. Remote Sens. Environ. 105, 9–22. https://doi.org/10.1016/j.rse.2006.06.003

Bell, T.W., Cavanaugh, K.C., Siegel, D. a., 2015. Remote monitoring of giant kelp biomass and physiological condition: An evaluation of the potential for the Hyperspectral Infrared Imager (HyspIRI) mission. Remote Sens. Environ. 167, 218–228. https://doi.org/10.1016/j.rse.2015.05.003

Bennett, A.C., Mcdowell, N.G., Allen, C.D., Anderson-Teixeira, K.J., 2015. Larger trees suffer most during drought in forests worldwide. Nat. Plants 1, 1–5. https://doi.org/10.1038/nplants.2015.139

Beven, K.J., Kirkby, M.J., 1979. A physically based, variable contributing area model of

basin hydrology. Hydrol. Sci. Bull. 24, 43–69. https://doi.org/10.1080/02626667909491834

Bhuiyan, C., Singh, R.P., Kogan, F.N., 2006. Monitoring drought dynamics in the Aravalli region (India) using different indices based on ground and remote sensing data. Int. J. Appl. Earth Obs. Geoinf. 8, 289–302. https://doi.org/10.1016/j.jag.2006.03.002

Buitrago Acevedo, M.F., Groen, T.A., Hecker, C.A., Skidmore, A.K., 2017. Identifying leaf traits that signal stress in TIR spectra. ISPRS J. Photogramm. Remote Sens. 125, 132–145. https://doi.org/10.1016/j.isprsjprs.2017.01.014

Buitrago, M.F., Groen, T. a., Hecker, C. a., Skidmore, A.K., 2016. Changes in thermal infrared spectra of plants caused by temperature and water stress. ISPRS J. Photogramm. Remote Sens. 111, 22–31. https://doi.org/10.1016/j.isprsjprs.2015.11.003

Buitrago, M.F., Skidmore, A.K., Groen, T.A., Hecker, C.A., 2018. Connecting infrared spectra with plant traits to identify species. ISPRS J. Photogramm. Remote Sens. 139, 183–200. https://doi.org/10.1016/j.isprsjprs.2018.03.013

Burkholder, A., Warner, T.A., Culp, M., Landenburg, R., 2011. Seasonal Trends in Separability of Leaf Reflectance Spectra for Ailanthus altissima and Four Other Tree Species.pdf. Photogramm. Eng. Remote Sensing 77, 793–804. https://doi.org/10.14358/PERS.77.8.793

Calderón, R., Navas-Cortés, J.A., Lucena, C., Zarco-Tejada, P.J., 2013. High-resolution airborne hyperspectral and thermal imagery for early detection of Verticillium wilt of olive using fluorescence, temperature and narrow-band spectral indices. Remote Sens. Environ. 139, 231–245. https://doi.org/10.1016/j.rse.2013.07.031

Canadell, J., Jackson, R.B., Ehleringer, J.B., Mooney, H.A., Sala, O.E., Schulze, E.-D., 1996.

Maximum rooting depth of vegetation types at the global scale. Oecologia 108, 583–595. https://doi.org/10.1007/BF00329030

Carlson, T.N., Riziley, D.A., 1997. On the Relation between NDVI, Fractional Vegetation Cover, and Leaf Area Index. Remote Sens. Environ. 62, 241–252.

Clark, M.L., Roberts, D.A., Clark, D.B., 2005. Hyperspectral discrimination of tropical rain forest tree species at leaf to crown scales. Remote Sens. Environ. 96, 375–398. https://doi.org/10.1016/j.rse.2005.03.009

Cleland, E.E., Chuine, I., Menzel, A., Mooney, H.A., Schwartz, M.D., 2007. Shifting plant phenology in response to global change. Trends Ecol. Evol. 22, 357–365. https://doi.org/10.1016/j.tree.2007.04.003

Coates, A., Dennison, P., Roberts, D., Roth, K., 2015. Monitoring the Impacts of Severe Drought on Southern California Chaparral Species using Hyperspectral and Thermal Infrared Imagery. Remote Sens. 7, 14276–14291. https://doi.org/10.3390/rs71114276

Cohen, W.B., Goward, S.N., 2004. Landsat's Role in Ecological Applications of Remote Sensing. Bioscience 54, 535. https://doi.org/10.1641/0006-3568(2004)054[0535:LRIEAO]2.0.CO;2

Colgan, M.S., Baldeck, C.A., Féret, J. baptiste, Asner, G.P., 2012. Mapping savanna tree species at ecosystem scales using support vector machine classification and BRDF correction on airborne hyperspectral and LiDAR data. Remote Sens. 4, 3462–3480. https://doi.org/10.3390/rs4113462

Cooper, L., 1998. The use of terrain analysis in the evaluation of snow cover over an alpine glacier, in: Lane, S.N., Richards, K.S., Chandler, J.H. (Eds.), Landform Monitoring, Modelling, and Analysis. Wiley, (New York, pp. 385–404.

Costa, J.M., Grant, O.M., Chaves, M.M., 2013. Thermography to explore plant-environment interactions. J. Exp. Bot. 64, 3937–3949. https://doi.org/10.1093/jxb/ert029

Curran, P.J., 1989. Remote sensing of foliar chemistry. Remote Sens. Environ. 30, 271–278. https://doi.org/10.1016/0034-4257(89)90069-2

Davis, F.W., Michaelsen, J., 1995. Sensitivity of fire regime in chaparral ecosystems to climate change, in: J.M., M., W.C., O. (Eds.), Global Change and Mediterranean-Type Ecosystems Volume 117. Springer, New York, NY, pp. 435–456. https://doi.org/https://doi.org/10.1007/978-1-4612-4186-7_21

Delucia, E.H., Schlesinger, W.H., 1991. Resource-use efficiency and drought tolerance in adjacent Great Basin and Sierran Plants. Ecology 72, 51–58.

Delucia, E.H., Schlesinger, W.H., Billings, W.D., 1988. Water Relations and the Maintenance of Sierran Conifers on Hydrothermally Altered Rock. Ecology 69, 303–311.

Dennison, P.E., Roberts, D. a., 2003. The effects of vegetation phenology on endmember selection and species mapping in southern California chaparral. Remote Sens. Environ. 87, 295–309. https://doi.org/10.1016/j.rse.2003.07.001

Dennison, P.E., Roberts, D.A., Thorgusen, S.R., Regelbrugge, J.C., Weise, D., Lee, C., 2003. Modeling seasonal changes in live fuel moisture and equivalent water thickness using a cumulative water balance index. Remote Sens. Environ. 88, 442–452. https://doi.org/10.1016/j.rse.2003.08.015

Diamond, H.J., Karl, T.R., Palecki, M.A., Baker, C.B., Bell, J.E., Leeper, R.D., Easterling, D.R., Lawrimore, J.H., Meyers, T.P., Helfert, M.R., Goodge, G., Throne, P.W., 2013. U.S. climate reference network after one decade of operations: Status and assessment.

Am. Meteorol. Soc. 485–498. https://doi.org/10.1175/BAMS-D-12-00170.1

Dubayah, R., Rich, P.M., 1995. Topographic solar radiation models for GIS. Int. J. Geogr. Inf. Syst. 9, 405–419. https://doi.org/10.1080/02693799508902046

Dubula, B., Tesfamichael, S.G., Rampedi, I.T., Moresi, L.-N., 2016. Assessing the potential of remote sensing to discriminate invasive *Asparagus laricinus* from adjacent land cover types. Cogent Geosci. 1–0. https://doi.org/10.1080/23312041.2016.1154650

Dudley, K.L., Dennison, P.E., Roth, K.L., Roberts, D. a., Coates, A.R., 2015. A multi-temporal spectral library approach for mapping vegetation species across spatial and temporal phenological gradients. Remote Sens. Environ. 167, 121–134. https://doi.org/10.1016/j.rse.2015.05.004

Elvidge, C.D., 1988. Thermal Infrared Reflectance of Dry Plant Materials : 2.5-20.0. Remote Sens. Environ. 26, 265–285.

Fabre, S., Lesaignoux, A., Olioso, A., Briottet, X., 2011. Influence of Water Content on Spectral Reflectance of Leaves in the 3–15 μm Domain. IEEE Geosci. Remote Sens. Lett. 8, 143–147.

Fernandes, M.R., Aguiar, F.C., Silva, J.M.N., Ferreira, M.T., Pereira, J.M.C., 2013. Spectral discrimination of giant reed (Arundo donax L.): A seasonal study in riparian areas. ISPRS J. Photogramm. Remote Sens. 80, 80–90. https://doi.org/10.1016/j.isprsjprs.2013.03.007

Fernandez-manso, A., Quintano, C., Roberts, D.A., 2016. Burn severity influence on post-fire vegetation cover resilience from Landsat MESMA fraction images time series in Mediterranean forest ecosystems. Remote Sens. Environ. 184, 112–123. https://doi.org/10.1016/j.rse.2016.06.015

Fisher, J.B., Tu, K.P., Baldocchi, D.D., 2008. Global estimates of the land-atmosphere water flux based on monthly AVHRR and ISLSCP-II data, validated at 16 FLUXNET sites. Remote Sens. Environ. 112, 901–919. https://doi.org/10.1016/j.rse.2007.06.025

Flowers, T.J., Yeo, A.R., 1986. Ion relations of plants under drought and salinity. Aust. J. Plant Physiol. 13, 75–91. https://doi.org/10.1071/PP9860075

Francois, C., Ottle, C., Prevot, L., 1997. Analytical parameterization of canopy directional emissivity and directional radiance in the thermal infrared. Application on the retrieval of soil and foliage temperatures using two directional measurements. Int. J. Remote Sens. 18, 2587–2621. https://doi.org/10.1080/014311697217495

Fuchs, M., 1990. Infrared Measurement of Canopy Temperature and Detection of Plant Water Stress. Theor. Appl. Climatol. 42, 253–261.

Fuchs, M., Tanner, C.B., 1966. Infrared Thermometry of Vegetation. Agron. J. 58, 597–601.

Garcia, M., Ustin, S.L., 2001. Detection of interannual vegetation responses to climatic variability using AVIRIS data in a coastal savanna in California. IEEE Trans. Geosci. Remote Sens. 39, 1480–1490. https://doi.org/10.1109/36.934079

Gardner, W.R., 1983. Soil properties and efficient water use: an overview, in: Taylor, H.M., Jordan, W.R., Sinclair, T.R. (Eds.), Limitations to Efficient Water Use in Crop Production. American Society of Agronomy, Madison, pp. 45–64.

Gates, D.M., 1968. Transpiration and leaf temperature. Annu. Rev. Plant Physiol. 19, 211–238.

Gates, D.M., Keegan, H.J., Schleter, J.C., Weidner, V.R., 1965. Spectral Properties of Plants. Appl. Opt. 4, 11–20. https://doi.org/10.1364/AO.4.000011

Gates, D.M., Tantraporn, W., 1952. The Reflectivity of Deciduous Trees and Herbaceous

Plants in the Infrared to 25 Microns. Science (80-. ). 115, 613–616.

George, M., Bartolome, J., McDougald, N., Conner, M., Vaughn, C., Markegard, G., 2001. Annual Range Forage Production. Rangel. Manag. Ser. 8018.

Gerhards, M., Rock, G., Schlerf, M., Udelhoven, T., 2016. Water stress detection in potato plants using leaf temperature, emissivity, and reflectance. Int. J. Appl. Earth Obs. Geoinf. 53, 27–39. https://doi.org/10.1016/j.jag.2016.08.004

Gillespie, A., Rokugawa, S., Matsunaga, T., Steven Cothern, J., Hook, S., Kahle, A.B., 1998. A temperature and emissivity separation algorithm for advanced spaceborne thermal emission and reflection radiometer (ASTER) images. IEEE Trans. Geosci. Remote Sens. 36, 1113–1126. https://doi.org/10.1109/36.700995

Glenn, E.P., Brown, J.J., 1998. Effects of soil salt levels on the growth and water use efficiency of Atriplex canescens (Chenopodiaceae) varieties in drying soil. Am. J. Bot. 85, 10–16. https://doi.org/10.2307/2446548

Goodenough, D., Li, J., Asner, G.P., Schaepman, M., Ustin, S.L., Dyk, A., 2006. Combining Hyperspectral Remote Sensing and Physical Modeling for Applications in Land Ecosystems. 2006 IEEE Int. Symp. Geosci. Remote Sens. 2000–2004. https://doi.org/10.1109/IGARSS.2006.518

Grant, O.M., Tronina, Ł., Jones, H.G., Chaves, M.M., 2007. Exploring thermal imaging variables for the detection of stress responses in grapevine under different irrigation regimes. J. Exp. Bot. 58, 815–825. https://doi.org/10.1093/jxb/erl153

Green, R.O., Eastwood, M.L., Sarture, C.M., Chrien, T.G., Aronsson, M., Chippendale, B.J., Faust, J.A., Pavri, B.E., Chovit, C.J., Solis, M., Olah, M.R., Williams, O., 1998. Imaging Spectroscopy and the Airborne Visible / Infrared Imaging Spectrometer (

AVIRIS ). Remote Sens. Environ. 65, 227–248.

Griffin, D., Anchukaitis, K.J., 2014. How unusual is the 2012 – 2014 California drought? Geophys. Res. Lett. 41, 9017–9023. https://doi.org/10.1002/2014GL062433.1.

Guarín, A., Taylor, A.H., 2005. Drought triggered tree mortality in mixed conifer forests in Yosemite National Park, California, USA. For. Ecol. Manage. 218, 229–244. https://doi.org/10.1016/j.foreco.2005.07.014

Guoquan, D., Zhengzhi, L., 1993. The apparent emissivity of vegetation canopies. Int. J. Remote Sens. 14, 183–188. https://doi.org/10.1080/01431169308904329

Hackwell, J.A., Warren, D.W., Bongiovi, R.P., Hansel, S.J., Hayhurst, T.L., Hackwell, J.A., Warren, D.W., Bongiovi, R.P., Hansel, S.J., Hayhurst, T.L., Mabry, D.J., Sivjee, M.G., Skinner, J.W., 1996. LWIR/MWIR imaging hyperspectral sensor for airborne and ground- based remote sensing. Proc. SPIE 2819, Imaging Spectrom. II 2819, 102−107. https://doi.org/10.1117/12.258057

Han, W., Feng, R., Wang, L., Cheng, Y., 2017. A semi-supervised generative framework with deep learning features for high-resolution remote sensing image scene classification. ISPRS J. Photogramm. Remote Sens. 145, 23–43. https://doi.org/10.1016/j.isprsjprs.2017.11.004

Harrison, D., Rivard, B., Sánchez-Azofeifa, A., 2018. Classification of tree species based on longwave hyperspectral data from leaves, a case study for a tropical dry forest. Int. J. Appl. Earth Obs. Geoinf. 66, 93–105. https://doi.org/https://doi.org/10.1016/j.jag.2017.11.009

He, T., Liang, S., Wang, D., Shi, Q., Goulden, M.L., 2015. Estimation of high-resolution land surface net shortwave radiation from AVIRIS data: Algorithm development and

preliminary results. Remote Sens. Environ. 167, 20–30. https://doi.org/10.1016/j.rse.2015.03.021

He, Z., Liu, H., Wang, Y., Hu, J., 2017. Generative adversarial networks-based semi-supervised learning for hyperspectral image classification. Remote Sens. 9. https://doi.org/10.3390/rs9101042

Hellmers, H., Horton, J.S., Juhren, G., J., O., 1955. Root Systems of Some Chaparral Plants in Southern California. Ecology 36, 667–678.

Herold, M., Roberts, D., 2005. Spectral characteristics of asphalt road aging and deterioration: implications for remote-sensing applications. Appl. Opt. 44, 4327–4334. https://doi.org/10.1364/AO.44.004327

Herold, M., Roberts, D.A., Gardner, M.E., Dennison, P.E., 2004. Spectrometry for urban area remote sensing - Development and analysis of a spectral library from 350 to 2400 nm. Remote Sens. Environ. 91, 304–319. https://doi.org/10.1016/j.rse.2004.02.013

Hesketh, M., Sánchez-Azofeifa, G.A., 2012. The effect of seasonal spectral variation on species classification in the Panamanian tropical forest. Remote Sens. Environ. 118, 73–82. https://doi.org/10.1016/j.rse.2011.11.005

Hook, S.J., Johnson, W.R., Abrams, M.J., 2013. NASA's Hyperspectral Thermal Emission Spectrometer, in: Kuenzer, C., Dech, S. (Eds.), Thermal Infrared Remote Sensing: Sensors, Methods, Applications, Remote Sensing and Digital Image Processing. Springer, Dordrecht, pp. 93–115. https://doi.org/10.1007/978-94-007-6639-6

Hook, S.J., Myers, J.J., Thome, K.J., Fitzgerald, M., Kahle, A.B., 2001. The MODIS / ASTER airborne simulator ( MASTER ) a new instrument for earth science studies. Remote Sens. Environ. 76, 93–102.

Hubbert, K.R., Beyers, J.L., Graham, R.C., 2001. Roles of weathered bedrock and soil in seasonal water relations of Pinus Jeffreyi and Arctostaphylos patula. Can. J. For. Res. 31, 1947–1957. https://doi.org/10.1139/cjfr-31-11-1947

Hulley, G.C., Duren, R.M., Hopkins, F.M., Hook, S.J., Vance, N., Guillevic, P., Johnson, W.R., Eng, B.T., Mihaly, J.M., Jovanovic, V.M., Chazanoff, S.L., Staniszewski, Z.K., Kuai, L., Worden, J., Frankenberg, C., Rivera, G., Aubrey, A.D., Miller, C.E., Malakar, N.K., Sánchez Tomás, J.M., Holmes, K.T., 2016. High spatial resolution imaging of methane and other trace gases with the airborne Hyperspectral Thermal Emission Spectrometer (HyTES). Atmos. Meas. Tech. Discuss. 1–32. https://doi.org/10.5194/amt-2016-8

Hulley, G.C., Hook, S.J., 2011. Generating Consistent Land Surface Temperature and Emissivity Products Between ASTER and MODIS Data for Earth Science Research. IEEE Trans. Geosci. Remote Sens. 49, 1304–1315. https://doi.org/10.1109/TGRS.2010.2063034

Idso, S.B., Jackson, R.D., Pinter Jr., P.J., Reginato, R.J., Hatfield, J.L., 1981. Normalizing the stress-degree-day parameter for environmental variability. Agric. Meteorol. 24, 45–55.

Iqbal, A., Ullah, S., Khalid, N., Ahmad, W., Ahmad, I., Sha, M., Hulley, G.C., Roberts, D.A., Skidmore, A.K., 2018. Selection of HyspIRI optimal band positions for the earth compositional mapping using HyTES data. Remote Sens. Environ. 206, 350–362. https://doi.org/10.1016/j.rse.2017.12.005

Ireland, G., Petropoulos, G.P., 2015. Exploring the relationships between post-fire vegetation regeneration dynamics, topography and burn severity: A case study from the Montane

Cordillera Ecozones of Western Canada. Appl. Geogr. 56, 232–248. https://doi.org/10.1016/j.apgeog.2014.11.016

Jackson, R.D., 1986. Remote Sensing of Biotic and Abiotic Plant Stress. Annu. Rev. Phytopathol. 24, 265–287. https://doi.org/10.1146/annurev.py.24.090186.001405

Jackson, R.D., Idso, S.B., Reginato, R.J., Pinter Jr., P.J., 1981. Canopy temperature as a crop water stress indicator. Water Resour. Res. 17, 1133–1138.

Jackson, R.D., Kustas, W.P., Choudhury, B.J., 1988. A reexamination of the crop water stress index. Irrig. Sci. 9, 309–317. https://doi.org/10.1007/BF00296705

Jackson, R.D., Reginato, R.J., Idso, S.B., 1977. Wheat Canopy Temperature: A Practical Tool for evaluating water requirements. Water Resour. Res. 13, 651–656.

Jacob, F., Lesaignoux, A., Olioso, A., Weiss, M., Caillault, K., Jacquemoud, S., Nerry, F., French, A., Schmugge, T., Briottet, X., Lagouarde, J.P., 2017. Reassessment of the temperature-emissivity separation from multispectral thermal infrared data: Introducing the impact of vegetation canopy by simulating the cavity effect with the SAIL-Thermique model. Remote Sens. Environ. 198, 160–172. https://doi.org/10.1016/j.rse.2017.06.006

Jacobsen, A.L., Pratt, R.B., Ewers, F.W., Davis, S.D., Monographs, E., 2007. Cavitation Resistance among 26 Chaparral Species of Southern California. Ecol. Monogr. 77, 99–115.

Jiang, Z., Huete, A.R., Chen, J., Chen, Y., 2006. Analysis of NDVI and scaled difference vegetation index retrievals of vegetation fraction. Remote Sens. Environ. 101, 366–378. https://doi.org/10.1016/j.rse.2006.01.003

Johnson, W.R., Hulley, G., Hook, S.J., 2014. Remote gas plume sensing and imaging with

NASA's Hyperspectral Thermal Emission Spectrometer (HyTES), in: Proc. SPIE 9101, Next-Generation Spectroscopic Technologies VII. https://doi.org/10.1117/12.2049005

Jones, H.G., 2014. Plants and Microclimate: A quantitative approach to environmental plant physiology, Third Edit. ed. Cambridge University Press.

Jones, H.G., 1999. Use of infrared thermometry for estimation of stomatal conductance as a possible aid to irrigation scheduling. Agric. For. Meteorol. 95, 139–149. https://doi.org/10.1016/S0168-1923(99)00030-1

Jones, H.G., Leinonen, I., 2003. Thermal imaging for the study of plant water relations. J. Agric. Meteorol. 59, 205–217.

Jones, H.G., Schofield, P., 2008. Thermal and other remote sensing of plant stress. Gen. Appl. Plant Physiol. 34, 19–32. https://doi.org/10.1.1.399.2918

Jones, H.G., Stoll, M., Santos, T., de Sousa, C., Chaves, M.M., Grant, O.M., 2002. Use of infrared thermography for monitoring stomatal closure in the field: application to grapevine. J. Exp. Bot. 53, 2249–2260. https://doi.org/10.1093/jxb/erf083

Jones, T.G., Coops, N.C., Sharma, T., 2010. Assessing the utility of airborne hyperspectral and LiDAR data for species distribution mapping in the coastal Pacific Northwest, Canada. Remote Sens. Environ. 114, 2841–2852. https://doi.org/10.1016/j.rse.2010.07.002

Kampe, T.U., Johnson, B.R., Kuester, M., Keller, M., 2010. NEON: the first continental-scale ecological observatory with airborne remote sensing of vegetation canopy biochemistry and structure. J. Appl. Remote Sens. 4. https://doi.org/10.1117/1.3361375

Karnieli, A., Bayasgalan, M., Bayarjargal, Y., Agam, N., Khudulmur, S., Tucker, C.J., 2006. Comments on the use of the Vegetation Health Index over Mongolia. Int. J. Remote

Sens. 27, 2017–2024. https://doi.org/10.1080/01431160500121727

Kelly, A.E., Goulden, M.L., 2008. Rapid shifts in plant distribution with recent climate change. Proc. Natl. Acad. Sci. U. S. A. 105, 11823–11826. https://doi.org/10.1073/pnas.0802891105

Kjelgren, R., Montague, T., 1998. Urban tree transpiration over turf and asphalt surfaces. Atmos. Environ. 32, 35–41. https://doi.org/10.1016/S1352-2310(97)00177-5

Kogan, F.N., 1997. Global Drought Watch from Space. Bull. Am. Meteorol. Soc. 78, 621–636. https://doi.org/10.1175/1520-0477(1997)078<0621:GDWFS>2.0.CO;2

Kogan, F.N., 1995. Application of vegetation index and brightness temperature for drought detection. Adv. Sp. Res. 15, 91–100. https://doi.org/10.1016/0273-1177(95)00079-T

Kogan, F.N., 1995. Droughts of the Late 1980s in the United States as Derived from NOAA Polar-Orbiting Satellite Data. Bull. Am. Meteorol. Soc. 76, 655–668. https://doi.org/10.1175/1520-0477(1995)076<0655:DOTLIT>2.0.CO;2

Kogan, F.N., Stark, R., Gitelson, A., Jargalsaikhan, L., Tsooj, S., Stark, R., 2004. Derivation of pasture biomass in Mongolia from AVHRR-based vegetation health indices. Int. J. Remote Sens. 25, 2889–2896. https://doi.org/10.1080/01431160410001697619

Kruse, F. a., Lefkoff, A.B., Boardman, J.W., Heidebrecht, K.B., Shapiro, A.T., Barloon, P.J., Goetz, A.F.H., 1993. The spectral image processing system (SIPS)—interactive visualization and analysis of imaging spectrometer data. Remote Sens. Environ. 44, 145–163. https://doi.org/10.1016/0034-4257(93)90013-N

Kruse, F.A., 2015. Comparative analysis of Airborne Visible/Infrared Imaging Spectrometer (AVIRIS), and Hyperspectral Thermal Emission Spectrometer (HyTES) longwave infrared (LWIR) hyperspectral data for geologic mapping, in: Proc. SPIE 9472,

Algorithms and Technologies for Multispectral, Hyperspectral, and Ultraspectral Imagery XXI. https://doi.org/10.1117/12.2176646

Kuai, L., Worden, J.R., Li, K.F., Hulley, G.C., Hopkins, F.M., Miller, C.E., Hook, S.J., Duren, R.M., Aubrey, A.D., 2016. Characterization of anthropogenic methane plumes with the Hyperspectral Thermal Emission Spectrometer (HyTES): A retrieval method and error analysis. Atmos. Meas. Tech. 9, 3165–3173. https://doi.org/10.5194/amt-9-3165-2016

Kummerow, J., Krause, D., Jow, W., 1977. Root Systems of Chaparral Shrubs. Oecologia 29, 163–177.

LARIAC Product Guide 2006-07, 2006. https://doi.org/http://egis3.lacounty.gov/dataportal/wp-content/uploads/2012/05/ProductGuideFinal.pdf

Lawrence, R., Labus, M., 2003. Early Detection of Douglas-Fir Beetle Infestation with Subcanopy Resolution Hyperspectral Imagery. J. Appl. For. 18, 1–5.

Lee, C.M., Cable, M.L., Hook, S.J., Green, R.O., Ustin, S.L., Mandl, D.J., Middleton, E.M., 2015. An introduction to the NASA Hyperspectral InfraRed Imager (HyspIRI) mission and preparatory activities. Remote Sens. Environ. 167, 6–19. https://doi.org/10.1016/j.rse.2015.06.012

Leinonen, I., Grant, O.M., Tagliavia, C.P.P., Chaves, M.M., Jones, H.G., 2006. Estimating stomatal conductance with thermal imagery. Plant, Cell Environ. 29, 1508–1518. https://doi.org/10.1111/j.1365-3040.2006.01528.x

Leuzinger, S., Körner, C., 2007. Tree species diversity affects canopy leaf temperatures in a mature temperate forest. Agric. For. Meteorol. 146, 29–37.

https://doi.org/10.1016/j.agrformet.2007.05.007

Leuzinger, S., Vogt, R., Körner, C., 2010. Tree surface temperature in an urban environment. Agric. For. Meteorol. 150, 56–62. https://doi.org/10.1016/j.agrformet.2009.08.006

Leuzinger, S., Zotz, G., Asshoff, R., Korner, C., 2005. Responses of deciduous forest trees to severe drought in Central Europe. Tree Physiol. 25, 641–650. https://doi.org/10.1093/treephys/25.6.641

Liu, W.T., Kogan, F.N., 1996. Monitoring regional drought using the vegetation condition index. Int. J. Remote Sens. 17, 2761–2782. https://doi.org/10.1080/01431169608949106

Maherali, H., Pockman, W.T., Jackson, R.B., 2004. Adaptive variation in the vulnerability of woody plants to zylem cavitation. Ecology 85, 2184–2199. https://doi.org/10.1890/02-0538

Mann, M.E., Gleick, P.H., 2015. Climate change and California drought in the 21st century. Proc. Natl. Acad. Sci. 112, 3858–3859. https://doi.org/10.1073/pnas.1503667112

Martin, M.E., Newman, S.., Aber, J.D., Congalton, R.., 1998. Determining Forest Species Composition Using High Spectral Resolution Remote Sensing Data. Remote Sens. Environ. 65, 249–254. https://doi.org/10.1016/S0034-4257(98)00035-2

Maselli, F., Romanelli, S., Bottai, L., Zipoli, G., 2003. Use of NOAA-AVHRR NDVI images for the estimation of dynamic fire risk in Mediterranean areas. Remote Sens. Environ. 86, 187–197. https://doi.org/10.1016/S0034-4257(03)00099-3

Mastrandrea, M.D., Luers, A.L., 2012. Climate change in California: Scenarios and approaches for adaptation. Clim. Change 111, 5–16. https://doi.org/10.1007/s10584-011-0240-4

Mastrandrea, M.D., Tebaldi, C., Snyder, C.W., Schneider, S.H., 2011. Current and future

impacts of extreme events in California. Clim. Change 109, 43–70. https://doi.org/10.1007/s10584-011-0311-6

Meentemeyer, R.K., Moody, A., Franklin, J., 2001. Landscape-scale patterns of shrub-species abundance in California chaparral. Plant Ecol. 156, 19–41. https://doi.org/10.1023/A:1011944805738

Meerdink, S.K., Roberts, D.A., King, J.Y., Roth, K.L., Dennison, P.E., Amaral, C.H., Hook, S.J., 2016. Linking seasonal foliar traits to VSWIR-TIR spectroscopy across California ecosystems. Remote Sens. Environ. 186, 322–338. https://doi.org/10.1016/j.rse.2016.08.003

Meier, F., Scherer, D., 2012. Spatial and temporal variability of urban tree canopy temperature during summer 2010 in Berlin, Germany. Theor. Appl. Climatol. 110, 373–384. https://doi.org/10.1007/s00704-012-0631-0

Miller, P.C., Poole, D.K., 1983. The influence of annual precipitation, topography, and vegetative cover on soil moisture and summer drought in southern California. Oecologia 56, 385–391. https://doi.org/10.1007/BF00379717

Minnich, R. a., 2007. Southern California Conifer Forests, in: Barbour, M.G., Keeler-Wolf, T., Schoenherr, A.A. (Eds.), Terrestrial Vegetation of California. University of California Press, pp. 502–538. https://doi.org/10.1525/california/9780520249554.003.0018

Minnich, R.A., Barbour, M.G., Burk, J.H., Fernau, R.F., Fernaut, R.F., 1995. Sixty Years of Change in Californian Conifer Forests of the San Bernardino Mountains. Conserv. Biol. 9, 902–914. https://doi.org/10.1046/j.1523-1739.1995.09040902.x

Montague, T., Kjelgren, R., 2004. Energy balance of six common landscape surfaces and the

influence of surface properties on gas exchange of four containerized tree species. Sci. Hortic. (Amsterdam). 100, 229–249. https://doi.org/10.1016/j.scienta.2003.08.010

Montandon, L.M., Small, E.E., 2008. The impact of soil reflectance on the quantification of the green vegetation fraction from NDVI. Remote Sens. Environ. 112, 1835–1845. https://doi.org/10.1016/j.rse.2007.09.007

Monteith, J.L., Szeicz, G., 1962. Radiative temperature in the heat balance of natural surfaces. Q. J. R. Meterological Soc. 88, 496–507. https://doi.org/https://doi.org/10.1002/qj.49708837811

Moran, M.S., Clarke, T.R., Inoue, Y., Vidal, A., 1994. Estimating Crop Water deficit using the relation between surface-air temperature and spectral vegetation index. Remote Sens. Environ. 49, 246–263.

Moriondo, M., Good, P., Durao, R., Bindi, M., Giannakopoulos, C., Corte-Real, J., 2006. Potential impact of climate change on fire risk in the Mediterranean area. Clim. Res. 31, 85–95. https://doi.org/10.3354/cr031085

Moritz, M.A., 1997. Analyzing Extreme Disturbance Events : Fire in Los Padres National Forest. Ecol. Appl. 7, 1252–1262.

Mouillot, F., Rambal, S., Joffre, R., 2002. Simulating climate change impacts on fire frequency and vegetation dynamics in a Mediterranean ecosystem. Glob. Chang. Biol. 8, 423–437. https://doi.org/10.1046/j.1365-2486.2002.00494.x

National Academies of Sciences and Medicine, E., 2018. Thriving on Our Changing Planet: A Decadal Strategy for Earth Observation from Space. The National Academies Press, Washington, DC. https://doi.org/10.17226/24938

Neinavaz, E., Darvishzadeh, R., Skidmore, A.K., Groen, T.A., 2016a. Measuring the

response of canopy emissivity spectra to leaf area index variation using thermal hyperspectral data. Int. J. Appl. Earth Obs. Geoinf. 53, 40–47. https://doi.org/10.1016/j.jag.2016.08.002

Neinavaz, E., Skidmore, A.K., Darvishzadeh, R., Groen, T.A., 2016b. Retrieval of leaf area index in different plant species using thermal hyperspectral data. ISPRS J. Photogramm. Remote Sens. 119, 390–401. https://doi.org/10.1016/j.isprsjprs.2016.07.001

Nunez, M., 1980. The Calculation of Solar and Net Radiation in Mountainous Terrain. J. Biogeogr. 7, 173–186.

Oke, R., 1988. The urban energy balance. Prog. Phys. Geogr. Earth Environ. 12, 471–508.

Olioso, A., 1995. Simulating the relationship between thermal emissivity and the normalized difference vegetation index. Int. J. Remote Sens. 16, 3211–3216. https://doi.org/10.1080/01431169508954625

Ollinger, S. V., 2011. Sources of variability in canopy reflectance and the convergent properties of plants. New Phytol. 189, 375–94. https://doi.org/10.1111/j.1469-8137.2010.03536.x

Otkin, J.A., Anderson, M.C., Hain, C.R., Mladenova, I.E., Basara, J.B., Svoboda, M., 2013. Examining Rapid Onset Drought Development Using the Thermal Infrared – Based Evaporative Stress Index. Am. Meteorol. Soc. 14, 1057–1074. https://doi.org/10.1175/JHM-D-12-0144.1

Otkin, J.A., Anderson, M.C., Hain, C.R., Svoboda, M., 2014. Examining the Relationship between Drought Development and Rapid Changes in the Evaporative Stress Index. Am. Meteorol. Soc. 15, 938–956. https://doi.org/10.1175/JHM-D-13-0110.1

Palacios, S.L., Kudela, R.M., Guild, L.S., Negrey, K.H., Torres-Perez, J., Broughton, J.,

2015. Remote sensing of phytoplankton functional types in the coastal ocean from the HyspIRI Preparatory Flight Campaign. Remote Sens. Environ. 167, 269–280. https://doi.org/10.1016/j.rse.2015.05.014

Pavlik, B., 1991. Oaks of California. Cachuma Press: California Oak Foundation.

Paz-Kagan, T., Brodrick, P.G., Vaughn, N.R., Das, A.J., Stephenson, N.L., Nydick, K.R., Asner, G.P., 2017. What mediates tree mortality during drought in the southern Sierra Nevada. Ecol. Appl. 27, 2443–2457. https://doi.org/10.1002/eap.1620

Peñuelas, J., Filella, L., 1998. Visible and near-infrared reflectance techniques for diagnosing plant physiological status. Trends Plant Sci. 3, 151–156. https://doi.org/10.1016/S1360-1385(98)01213-8

Pisek, J., Sonnentag, O., Richardson, A.D., Mõttus, M., 2013. Is the spherical leaf inclination angle distribution a valid assumption for temperate and boreal broadleaf tree species? Agric. For. Meteorol. 169, 186–194. https://doi.org/10.1016/j.agrformet.2012.10.011

Raabe, K., Pisek, J., Sonnentag, O., Annuk, K., 2015. Variations of leaf inclination angle distribution with height over the growing season and light exposure for eight broadleaf tree species. Agric. For. Meteorol. 214–215, 2–11. https://doi.org/10.1016/j.agrformet.2015.07.008

Riaño, D., Chuvieco, E., Ustin, S.L., Zomer, R., Dennison, P.E., Roberts, D.A., Salas, J., 2002. Assessment of vegetation regeneration after fire through multitemporal analysis of AVIRIS images in the Santa Monica Mountains. Remote Sens. Environ. 79, 60–71.

Ribeiro da Luz, B., 2006. Attenuated total reflectance spectroscopy of plant leaves: a tool for ecological and botanical studies. New Phytol. 172, 305–18. https://doi.org/10.1111/j.1469-8137.2006.01823.x

Ribeiro Da Luz, B., Crowley, J.K., 2010. Identification of plant species by using high spatial and spectral resolution thermal infrared (8.0–13.5μm) imagery. Remote Sens. Environ. 114, 404–413. https://doi.org/10.1016/j.rse.2009.09.019

Ribeiro Da Luz, B., Crowley, J.K., 2007. Spectral reflectance and emissivity features of broad leaf plants: Prospects for remote sensing in the thermal infrared (8.0–14.0 μm). Remote Sens. Environ. 109, 393–405. https://doi.org/10.1016/j.rse.2007.01.008

Riley, S.J., DeGloria, S.D., Elliot, R., 1999. A Terrain Ruggedness Index that Qauntifies Topographic Heterogeneity. Intermt. J. Sci. https://doi.org/citeulike-article-id:8858430

Roberts, D. a., Dennison, P.E., Roth, K.L., Dudley, K., Hulley, G., 2015. Relationships between dominant plant species, fractional cover and Land Surface Temperature in a Mediterranean ecosystem. Remote Sens. Environ. 167, 152–167. https://doi.org/10.1016/j.rse.2015.01.026

Roberts, D.A., Gardner, M., Church, R., Ustin, S.L., Scheer, G., 1998. Mapping Chaparral in the Santa Monica Mountains Using Multiple Endmember Spectral Mixture Models. Remote Sens. Environ. 65, 267–279.

Roberts, D.A., Ustin, S.L., Ogunjemiyo, S., Greenberg, J., Dobrowski, Z., Chen, J., Hinckley, T.M., Dobrowski, S.Z., 2004. Spectral and Structural Measures of Northwest Forest Vegetation at Leaf to Landscape Scales. Ecosystems 7, 545–562.

Roberts, D.W., Cooper, S.V., 1989. Concepts and techniques of vegetation mapping. Gen. Tech. Rep. - US Dep. Agric. For. Serv. 90–96.

Rock, G., Gerhards, M., Schlerf, M., Hecker, C.A., Udelhoven, T., Schlerf, M., Werner, W., Udelhoven, T., 2016. Plant species discrimination using emissive thermal infrared imaging spectroscopy. Int. J. Appl. Earth Obs. Geoinf. 53, 16–26.

https://doi.org/10.1016/j.jag.2016.08.005

Rose, K.L., Graham, R.C., Parker, D.R., 2003. Water source utilization by Pinus jeffreyi and Arctostaphylos patula on thin soils over bedrock. Oecologia 134, 46–54. https://doi.org/10.1007/s00442-002-1084-4

Roth, K.L., Dennison, P.E., Roberts, D. a., 2012. Comparing endmember selection techniques for accurate mapping of plant species and land cover using imaging spectrometer data. Remote Sens. Environ. 127, 139–152. https://doi.org/10.1016/j.rse.2012.08.030

Roth, K.L., Roberts, D. a., Dennison, P.E., Peterson, S.H., Alonzo, M., 2015a. The impact of spatial resolution on the classification of plant species and functional types within imaging spectrometer data. Remote Sens. Environ. 171, 45–57. https://doi.org/10.1016/j.rse.2015.10.004

Roth, K.L., Roberts, D.A., Dennison, P.E., Alonzo, M., Peterson, S.H., Beland, M., 2015b. Differentiating plant species within and across diverse ecosystems with imaging spectroscopy. Remote Sens. Environ. 167, 135–151. https://doi.org/10.1016/j.rse.2015.05.007

Ryu, Y., Sonnentag, O., Nilson, T., Vargas, R., Kobayashi, H., Wenk, R., Baldocchi, D.D., 2010. How to quantify tree leaf area index in an open savanna ecosystem: A multi-instrument and multi-model approach. Agric. For. Meteorol. 150, 63–76. https://doi.org/10.1016/j.agrformet.2009.08.007

Salisbury, J.W., 1986. Preliminary Measurements of Leaf Spectral Reflectance in the 8-14 mu-m Region. Int. J. Remote Sens. 7, 1879–1886.

Salisbury, J.W., Milton, N.M., 1988. Thermal Infrared (2.5 to 13.5 um) Direction

Hemispherical Reflectance of Leaves. Photogramm. Eng. Remote Sens. 54, 1301–1304.

Schaaf, A.N., Dennison, P.E., Fryer, G.K., Roth, K.L., Roberts, D. a., 2011. Mapping Plant Functional Types at Multiple Spatial Resolutions Using Imaging Spectrometer Data. GIScience Remote Sens. 48, 324–344. https://doi.org/10.2747/1548-1603.48.3.324

Scherrer, D., Bader, M.K.-F., Körner, C., 2011. Drought-sensitivity ranking of deciduous tree species based on thermal imaging of forest canopies. Agric. For. Meteorol. 151, 1632–1640. https://doi.org/10.1016/j.agrformet.2011.06.019

Schimel, D.S., Pavlick, R., Fisher, J.B., Asner, G.P., Saatchi, S., Townsend, P.A., Miller, C., Frankenberg, C., Hibbard, K., Cox, P., 2014. Observing terrestrial ecosystems and the carbon cycle from space. Glob. Chang. Biol. 21, 1762–1776. https://doi.org/10.1111/gcb.12822

Schoeneweiss, D.F., 1975. Predisposition, stress, and plant disease. Annu. Rev. Phytopathol.

Scholze, M., Knorr, W., Arnell, N.W., Prentice, I.C., 2006. A climate-change risk analysis for world ecosystems. Proc. Natl. Acad. Sci. 103, 13116–13120. https://doi.org/10.1073/pnas.0601816103

Schwartz, M.W., Butt, N., Dolanc, C.R., Holguin, A., Moritz, M.A., North, M.P., Safford, H.D., Stephenson, N.L., Thorne, J.H., van Mantgem, P.J., 2015. Increasing elevation of fire in the Sierra Nevada and implications for forest change. Ecosphere 6, art121. https://doi.org/10.1890/ES15-00003.1

Settle, J.J., Drake, N.A., 1993. Linear mixing and the estimation of ground cover proportions. Int. J. Remote Sensing1 14, 1159–1177. https://doi.org/10.1080/01431169308904402

Sholihah, R.I., Trisasongko, B.H., Shiddiq, D., Iman, L.O.S., Kusdaryanto, S., Manijo, Panuju, D.R., 2016. Identification of Agricultural Drought Extent Based on Vegetation

Health Indices of Landsat Data: Case of Subang and Karawang, Indonesia. Procedia Environ. Sci. 33, 14–20. https://doi.org/10.1016/j.proenv.2016.03.051

Singh, R.P., Roy, S., Kogan, F., 2003. Vegetation and temperature condition indices from NOAA AVHRR data for drought monitoring over India. Int. J. Remote Sens. 24, 4393–4402. https://doi.org/10.1080/0143116031000084323

Snyder, W.C., Wan, Z., 1998. BRDF models to predict spectral reflectance and emissivity in the thermal infrared. IEEE Trans. Geosci. Remote Sens. 36, 214–225. https://doi.org/10.1109/36.655331

Soer, G.J.R., 1980. Estimation of Regional Evapotranspiration and Soft Moisture Conditions Using Remotely Sensed Crop Surface Temperatures. Remote Sens. Environ. 9, 27–45.

Somers, B., Asner, G.P., 2013. Invasive Species Mapping in Hawaiian Rainforests Using Multi-Temporal Hyperion Spaceborne Imaging Spectroscopy. IEEE J. Sel. Top. Appl. Earth Obs. Remote Sens. 6, 351–359. https://doi.org/10.1109/JSTARS.2012.2203796

Somers, B., Asner, G.P., 2012. Hyperspectral time series analysis of native and invasive species in Hawaiian rainforests. Remote Sens. 4, 2510–2529. https://doi.org/10.3390/rs4092510

Somers, B., Asner, G.P., Martin, R.E., Anderson, C.B., Knapp, D.E., Wright, S.J., Van De Kerchove, R., 2015. Mesoscale assessment of changes in tropical tree species richness across a bioclimatic gradient in Panama using airborne imaging spectroscopy. Remote Sens. Environ. 167, 111–120. https://doi.org/10.1016/j.rse.2015.04.016

Sruthi, S., Aslam, M.A.M., 2015. Agricultural Drought Analysis Using the NDVI and Land Surface Temperature Data; a Case Study of Raichur District. Aquat. Procedia 4, 1258–1264. https://doi.org/10.1016/j.aqpro.2015.02.164

Stage, A.R., 1976. An Expression for the Effect of Aspect, Slope, and Habitat Type on Tree Growth. For. Sci. 22, 457–460.

Stage, A.R., Salas, C., 2007. Interactions of Elevation, Aspect, and Slope in Models of Forest Species Composition and Productivity. For. Sci. 53, 486–492.

Stephenson, N.L., 1998. Actual evapotranspiration and deficit: biological meaningful correlates of vegetation distribution across spatial scales. J. Biogeogr. 25, 855–870.

Stuffler, T., Kaufmann, C., Hofer, S., Förster, K.P., Schreier, G., Mueller, a., Eckardt, a., Bach, H., Penné, B., Benz, U., Haydn, R., 2007. The EnMAP hyperspectral imager—An advanced optical payload for future applications in Earth observation programmes. Acta Astronaut. 61, 115–120. https://doi.org/10.1016/j.actaastro.2007.01.033

Swain, D.L., Tsiang, M., Haugen, M., Singh, D., Charland, A., Rajaratnam, B., Diffenbaugh, N.S., 2014. The Extraordinary California Drought of 2013/2014 : Character, Context, and the Role of Climate Change. Am. Meteorol. Soc. 95, S3–S7.

Syphard, A.D., Keeley, J.E., Brennan, T.J., 2011. Factors affecting fuel break effectiveness in the control of large fires on the Los Padres National Forest, California. Int. J. Wildl. Fire 20, 764–775. https://doi.org/10.1071/WF10065

Taghvaeian, S., Comas, L., DeJonge, K.C., Trout, T.J., 2014. Conventional and simplified canopy temperature indices predict water stress in sunflower. Agric. Water Manag. 144, 69–80. https://doi.org/10.1016/j.agwat.2014.06.003

Tane, Z., Roberts, D., Koltunov, A., Sweeney, S., Ramirez, C., 2018a. A framework for detecting conifer mortality across an ecoregion using high spatial resolution spaceborne imaging spectroscopy. Remote Sens. Environ. 209, 195–210. https://doi.org/10.1016/j.rse.2018.02.073

Tane, Z., Roberts, D., Veraverbeke, S., Casas, Á., Ramirez, C., Ustin, S., 2018b. Evaluating Endmember and Band Selection Techniques for Multiple Endmember Spectral Mixture Analysis using Post-Fire Imaging Spectroscopy. Remote Sens. 10, 389. https://doi.org/10.3390/rs10030389

Tanner, C.B., 1963. Plant Temperatures. Agron. J. 55, 210.

Thompson, D.R., Gao, B.-C., Green, R.O., Roberts, D. a., Dennison, P.E., Lundeen, S.R., 2015. Atmospheric correction for global mapping spectroscopy: ATREM advances for the HyspIRI preparatory campaign. Remote Sens. Environ. 167, 64–77. https://doi.org/10.1016/j.rse.2015.02.010

Thomson, S.J., Ouellet-Plamondon, C.M., DeFauw, S.L., Huang, Y., Fisher, D.K., English, P.J., 2012. Potential and Challenges in Use of Thermal Imaging for Humid Region Irrigation System Management. J. Agric. Sci. 4, 103–116. https://doi.org/10.5539/jas.v4n4p103

Ullah, S., Schlerf, M., Skidmore, A.K., Hecker, C., 2012a. Identifying plant species using mid-wave infrared (2.5–6μm) and thermal infrared (8–14μm) emissivity spectra. Remote Sens. Environ. 118, 95–102. https://doi.org/10.1016/j.rse.2011.11.008

Ullah, S., Skidmore, A.K., Groen, T.A., Schlerf, M., 2013. Evaluation of three proposed indices for the retrieval of leaf water content from the mid-wave infrared (2-6 um) spectra. Agric. For. Meteorol. 171–172, 65–71.

Ullah, S., Skidmore, A.K., Naeem, M., Schlerf, M., 2012b. An accurate retrieval of leaf water content from mid to thermal infrared spectra using continuous wavelet analysis. Sci. Total Environ. 437, 145–152.

Ullah, S., Skidmore, A.K., Ramoelo, A., Groen, T. a., Naeem, M., Ali, A., 2014. Retrieval of

leaf water content spanning the visible to thermal infrared spectra. ISPRS J. Photogramm. Remote Sens. 93, 56–64. https://doi.org/10.1016/j.isprsjprs.2014.04.005

Underwood, E., Ustin, S.L., DiPietro, D., 2003. Mapping nonnative plants using hyperspectral imagery. Remote Sens. Environ. 86, 150–161. https://doi.org/10.1016/S0034-4257(03)00096-8

Ustin, S.L., 2013. Remote sensing of canopy chemistry. Proc. Natl. Acad. Sci. U. S. A. 110, 804–5. https://doi.org/10.1073/pnas.1219393110

Ustin, S.L., Roberts, D.A., Gamon, J.A., Asner, G.P., Green, R.O., 2004. Using Imaging Spectroscopy to Study Ecosystem Processes and Properties. Bioscience 54, 523–534.

van Aardt, J., Wynne, R.H., 2007. Examining pine spectral separability using hyperspectral data from an airborne sensor: An extension of field based results. Int. J. Remote Sens. 28, 431–436. https://doi.org/10.1080/01431160500444772

Verbesselt, J., Somers, B., Lhermitte, S., Jonckheere, I., van Aardt, J., Coppin, P., 2007. Monitoring herbaceous fuel moisture content with SPOT VEGETATION time-series for fire risk prediction in savanna ecosystems. Remote Sens. Environ. 108, 357–368. https://doi.org/10.1016/j.rse.2006.11.019

Verhoef, W., 1984. Light scattering by leaf layers with application to canopy reflectance modeling: The SAIL model. Remote Sens. Environ. 16, 125–141. https://doi.org/10.1016/0034-4257(84)90057-9

Verhoef, W., Jia, L., Xiao, Q., Su, Z., 2007. Unified optical-thermal four-stream radiative transfer theory for homogeneous vegetation canopies. IEEE Trans. Geosci. Remote Sens. 45, 1808–1822. https://doi.org/10.1109/TGRS.2007.895844

Verma, S.B., Baldocchi, D.D., Anderson, D.E., Matt, D.R., Clement, R.J., 1986. Eddy fluxes

of CO2, water vapor, and sensible heat over a deciduous forest. Boundary-Layer Meteorol. 36.

Verma, S.B., Kim, J., Clement, R.J., 1989. Carbon dioxide, water vapor, and sensible heat fluxes over a tallgrass praire. Boundary-Layer Meteorol. 46, 53–67.

Vidal, A., Devaux-Ros, C., 1995. Evaluating forest fire hazard with a Landsat TM derived water stress index. Agric. For. Meteorol. 77, 207–224. https://doi.org/10.1016/0168-1923(95)02262-V

Vidal, A., Pinglo, F., Durand, H., Devaux-Ros, C., Maillet, A., 1994. Evaluation of a temporal fire risk index in mediterranean forests from NOAA thermal IR. Remote Sens. Environ. 49, 296–303. https://doi.org/10.1016/0034-4257(94)90024-8

Walther, G., Post, E., Convey, P., Menzel, A., Parmesan, C., Beebee, T.J.C., Fromentin, J., Hoegh-guldberg, O., Bairlein, F., 2002. Ecological responses to recent climate change. Nature 416, 389–395.

Wan, Z., Wang, P., Li, X., 2004. Using MODIS Land Surface Temperature and Normalized Difference Vegetation Index products for monitoring drought in the southern Great Plains, USA. Int. J. Remote Sens. 25, 61–72. https://doi.org/10.1080/0143116031000115328

Wang, D., Liang, S., He, T., Shi, Q., 2015. Estimating clear-sky all-wave net radiation from combined visible and shortwave infrared (VSWIR) and thermal infrared (TIR) remote sensing data. Remote Sens. Environ. 167, 31–39. https://doi.org/10.1016/j.rse.2015.03.022

Wetherley, E.B., McFadden, J.P., Roberts, D.A., 2018. Megacity-scale analysis of urban vegetation temperatures. Remote Sens. Environ. 213, 1–62.

https://doi.org/10.1016/j.rse.2018.04.051

Wetherley, E.B., Roberts, D.A., McFadden, J., 2017. Mapping spectrally similar urban materials at sub-pixel scales. Remote Sens. Environ. 195, 170–183. https://doi.org/10.1016/j.rse.2017.04.013

Willmott, C.J., Matsuura, K., 1995. Smart Interpolation of Annually Averaged Air Temperature in the United States. J. Appl. Meteorol. https://doi.org/10.1175/1520-0450(1995)034<2577:SIOAAA>2.0.CO;2

Willson, C.J., Manos, P.S., Jackson, R.B., 2008. Hydraulic traits are influenced by phylogenetic history in the drought-resistant, invasive genus Juniperus (Cupressaceae). Am. J. Bot. 95, 299–314. https://doi.org/10.3732/ajb.95.3.299

Wong, C., Blevin, W., 1967. Infrared Reflectances of Plant Leaves. Aust. J. Biol. Sci. 20, 501. https://doi.org/10.1071/BI9670501

Xu, L., Baldocchi, D.D., 2004. Seasonal variation in carbon dioxide exchange over a Mediterranean annual grassland in California. Agric. For. Meteorol. 123, 79–96. https://doi.org/10.1016/j.agrformet.2003.10.004

Young, D.J.N., Stevens, J.T., Earles, J.M., Morre, J., Ellis, A., Jirka, A.L., Latimer, A.M., 2017. Long-term climate and competition explain forest mortality patterns under extreme drought. Ecol. Lett. 20, 78–86. https://doi.org/10.1111/ele.12711